Designing up-converting nanomaterials for intracellular cargo dynamics

By

Wilson Tang

Institute for Biomedical Materials & Devices

School of Mathematical and Physical Sciences, Faculty of Science

Supervisors:

Dr. Jiayan Liao & A/Prof Yuen Yee Cheng

This thesis is presented for the degree Master of Science (Research)

August, 2025

CERTIFICATE OF ORIGINAL AUTHORSHIP

I, Wilson Tang, declare that this thesis is submitted in fulfilment of the requirements for the award of Master of Science (Research) in the Maths and Physical Sciences (MaPs) at the University of Technology Sydney.

This thesis is wholly my own work unless otherwise referenced or acknowledged. In addition, I certify that all information sources and literature used are indicated in the thesis.

This document has not been submitted for qualifications at any other academic institution.

This research was supported by an Australian Government Research Training Program (RTP) Scholarship doi.org/10.82133/C42F-K220.

Signature: Production Note:
Signature removed prior to publication.

Date: 12/12/2025

Acknowledgements

First and foremost, I would like to express my sincere gratitude to my supervisor, Dr. Jiayan Liao, for her dedicated guidance and support throughout my studies. Her mentorship has been integral to the development of both my academic skills and scientific thinking. Her diligence and attitude towards research are things that I greatly look up to, which always inspired me to work harder during my studies. Furthermore, I appreciate the valuable advice she has given me during my studies, which was helpful both in and outside of academia.

I would also like to thank Associate Professor Yuen Yee Cheng for her valuable guidance and support in the biological experiments and cell culture work, which formed a key component of my research. A/Prof Yuen Yee Cheng always supported me throughout my studies and gave me research and experimental advice to address problems and challenges which were immeasurable during my research.

I am especially grateful to my colleagues Yuewei Li and Yingfan Li, whose support, collaboration, and shared discussions greatly enriched my experience during this study. As a beginner, Yuewei Li taught me everything I know about optical microscopy, which I would always be grateful for. Furthermore, his insights and approaches towards experimental design are something that I continue to strive for to this day.

I acknowledge all members of the Institute for Biomedical Materials and Devices (IBMD). I extend my thanks to Distinguished Professor Dayong Jin for offering me the initial opportunity to join the IBMD group as a Visiting Student, an experience that played a pivotal role in shaping my research journey. The collaborative and supportive environment fostered within the group, along with the numerous insightful interactions I have had with colleagues, has provided me with many valuable lessons.

I gratefully acknowledge the technical staff at UTS within the Maths and Physical Sciences (MaPs), microstructural analysis unit (MAU) facilities and thank them for their expert assistance and training with the equipment for physical and chemical characterizations. I would also like to thank the technical staff at the School of Life Sciences (SoLS) and microscopy imaging facilities (MIF) for their expert assistance and training on biological experiments and cell microscopy during my studies.

I am deeply thankful to my family and friends for their support during my studies.

Finally, I would like to acknowledge the Australian Government Research Training Program (RTP) Scholarship and the Faculty of Science, MaPs, University of Technology Sydney, for their generous financial and research support, which made this work possible.

Format of Thesis

This thesis is structured as a conventional thesis and is split into six interconnected chapters that collectively explore the synthesis, optical characterization, and intracellular analysis of lanthanide-doped upconversion nanoparticles (UCNPs). Each chapter builds upon the preceding one, forming a cohesive narrative from fundamental principles to experimental applications in biological systems. The overall flow of the thesis is summarized below.

Chapter 1 introduces the background and motivation for this study. This chapter will first outline the fundamental principles, characteristics and applications of upconversion luminescence in lanthanide doped nanomaterials. This is followed up with a brief introduction on nanoparticles and their interactions in biological systems, which will be further explored in the review in chapter 2. Current methods and the significance of single particle tracking within the cell are then discussed in this chapter. The chapter concludes with a clear statement of the thesis aims and a structured outline of the subsequent chapters.

Chapter 2 presents a review of the current literature concerning luminescent materials, with a focus on endoplasmic reticulum targeting luminescent nanoparticles and their potential application. This chapter aims to identify the significance of understanding the mechanism behind nanoparticle trafficking and localization, which this research aims to address.

Chapter 3 details the materials and methods used in this thesis. This chapter will be separated into three major sections which reflect the three major components performed during this thesis. Firstly, the methods used to synthesize inorganic upconverting nanoparticles used in this thesis are outlined. In this section, the surface modification, functionalization and preparation of these nanoparticles for optical characterization and biological experiments are also explored. The second section will describe the development of a custom optical characterization platform tailored for single-particle and cellular studies. This section will discuss the coding and logic behind both scanning confocal and widefield modalities which are integrated with single photon counting and lifetime detection with the system I built. The final experimental section will describe the experiments performed which are related to the interactions between nanoparticles and biological systems.

Chapter 4 will focus on the physical, optical and chemical characteristics of synthesized UCNPs. Morphological control of nanoparticles' size and shape through lattice, precursor and synthesis methods are explored in this chapter. Next, the optical characteristics of single nanoparticles using the home-built characterization system are used to determine the relationship between emitter and sensitizer concentration and single nanoparticle luminescence.

Chapter 5 shifts the focus toward biological interactions by exploring the dynamic behavior of UCNPs within live cells. Firstly, interactions between nanoparticles and biological systems will be explored, along with intracellular localization between live cells and surface-modified nanoparticles. Advanced trajectory analysis using mean square displacement (MSD) is employed to uncover the underlying mechanisms of nanoparticle transport. Population-level analysis is also introduced to classify modes of motion such as active transport and subdiffusion.

Finally, chapter 6 will summarize the previous chapters and provide some additional experimental results performed during this thesis that may be relevant for future work.

Together, these chapters provide a comprehensive exploration of the material, optical, and biological dimensions of UCNPs and set the foundation for future work in nanoparticle-based imaging, diagnostics, and therapeutics.

Publications

Tang, W., Li, Y., Marsh, D.J., Ariotti, N., Cheng, Y.Y., Langford, S.J. and Liao, J., 2025. Design principles and biomedical applications of endoplasmic reticulum-targeting luminescent nanoparticles. Nano Research., 18(6): 94907356. https://doi.org/10.26599/NR.2025.94907356

Statement of Contribution for Chapter 2

	Conceptualization	Investigation	Editing	Manuscript – Original Draft	Supervision	Signature
W.T.	X	X	X	X		Production Note: Signature removed prior to publication.
Y.L.			X			Production Note: Signature removed prior to publication.
D.J.M.			X			Production Note: Signature removed prior to publication.
N.A.			X			Production Note: Signature removed prior to publication.
Y.Y.C.			X			Production Note: Signature removed prior to publication.
S.J.L.			X			Production Note: Signature removed prior to publication.
J.L.	X	X	X	X	X	Production Note: Signature removed prior to publication.

Table of contents

Lists of Acronyms

(In alphabetical order)

AC	Ammonium Chloride
ATP	Adenosine Triphosphate
ATR-FTIR	Attenuated Total Reflectance – Fourier Transform Infrared Spectroscopy
CCD	Charge Coupled Device
CR	Cross-Relaxation
DAMP	Damage Associated Molecular Patterns
DAQ	Data Acquisition Device
DI	De-Ionized
DMSO	Dimethyl Sulfoxide
DNA	Deoxyribonucleic Acid
DS-DNA	Double stranded Deoxyribonucleic Acid
EDC	N-(3-Dimethylaminopropyl)-N′-ethyl carbodiimide hydrochloride
EM	Expectation-Maximization
EMU	Energy migration-based Up-conversion
ER	Endoplasmic Reticulum
ER-LNPs	Endoplasmic Reticulum-Targeting Luminescence Nanoparticles
ESA	Excited State Absorption
ETU	Energy Transfer Up-conversion
FBS	Fetal Bovine Serum
FDA	Food and Drug Administration
HCl	Hydrochloric Acid
HEPES	2-[4-(2-hydroxyethyl)piperazin-1-yl]ethanesulfonic acid
HMM	Hidden Markov Model
ICD	Immunogenic Cell Death
LFA	Lateral Flow Assays

LNPs	Luminescence Nanoparticles
LSW	Lifshitz-Slyozov-Wagner
MES	2-(N-morpholino)ethanesulfonic acid
MOF	Metal Organic Frameworks
MSD	Mean Square Displacement
MSN	Mesoporous Silica Nanoparticles
mRNA	Messenger Ribonucleaic acid
MPA	Multi-Photon Avalanche
MRI	Magnetic Resonance Imaging
NA	Numerical Apeture
NaOH	Sodium Hydroxide
$NaYF_4$	Sodium Yttrium Floride
NH_4F	Ammonium Fluoride
NHS	N-hydroxysuccinimide
NIR	Near-Infrared
NP	Nanoparticle
OA	Oleic Acid
ODE	1-Octadecene
PA	Photon Avalanche
PBS	Phosphate Buffer Serum
PDT	Photodynamic Therapy
PEG	Poly-Ethylene Glycol
PFA	Paraformaldehyde
PLL	Poly-L-Lysine
PS	Penicillin/Streptomycin
PTT	Photothermal Therapy
QY	Quantum Yield
ROS	Reactive Oxygen Species
RPM	Rounds Per Minute
RPMI	Roswell Park Memorial Institute Medium
SEE	Super-linear Excitation Emission

SIM	Structured Illumination Microscopy
SMED	Surface-Migration Emission Depletion
SPAD	Singal Photon Avalanche Diode
SPT	Single Particle Tracking
STED	Stimulated Emission Depletion
STORM	Stochastic Optical Reconstruction Microscopy
SUR	Sufonyl Urea Receptor
TAA	Tumor Antigens
TEM	Transmission Electron Microscopy
THF	Tetrahydrofuran
TNBC	Triple-Negative Breast Cancer Cells
UCL	Up-conversion Luminescence
UCNMs	Up-conversion Nanomaterials
UCNP	Up-conversion Nanoparticles
UCQY	Up-conversion Quantum Yield
UPR	Unfolded Protein Response
UV	Ultra Voilet

Abstract

The advancement of nanotechnology has enabled the development of upconversion nanoparticles (UCNPs), a class of luminescent materials capable of converting low-energy near-infrared light into higher-energy visible or ultraviolet emissions. This unique optical property makes UCNPs highly promising for applications in biomedical imaging, diagnostics, and sensing. However, a deeper understanding of their optical behavior at the single-particle level and their interactions within biological environments remains limited.

This thesis investigates both the fundamental and applied aspects of UCNPs through a combination of synthesis, optical characterization, and computational modeling. It begins by exploring the synthesis of UCNPs with varied dopants, crystal structures, and surface modifications to tune their luminescent and chemical properties. A key part of the project involved building a custom, multi-purpose optical system for high-resolution imaging and single-particle characterization, allowing for precise measurements of luminescence, lifetime, and energy transfer efficiency.

The optical properties of UCNPs were evaluated using techniques such as scanning confocal microscopy, widefield imaging, and photon-counting spectroscopy. These results attempt to predict emission behavior based on dopant combinations and particle environments. In biological contexts, the uptake and movement of UCNPs within living cells were tracked over time. Using statistical tools such as mean square displacement and Hidden Markov Models, the study classified intracellular transport behaviors and explored the mechanisms of vesicle trafficking.

The findings contribute to a better understanding of how UCNPs behave optically and biologically, enabling their optimized use in single-particle imaging, photodynamic therapy, and diagnostic assays. This research lays a strong foundation for the future design of intelligent, responsive nanomaterials for biomedical applications, combining theoretical insight with practical instrumentation and cellular investigation.

Chapter 1. Introduction

Nanomaterials have revolutionized a wide range of scientific and technological domains due to their unique physicochemical properties, which arise from their small size which facilitates high surface-area-to-volume ratios for many technological applications [1]. In recent decades, their application has expanded rapidly across various fields, particularly in therapeutics and diagnostics [2, 3]. For medical application, engineered nanomaterials offer higher spatial resolution, targeted delivery, and minimized systemic toxicity [4, 5].

Despite significant advances in nanomedicine, a fundamental bottleneck remains in our limited understanding of how nanoparticles interact with complex biological systems. Critical aspects such as nanoparticle recognition by the immune system, intracellular trafficking pathways, and long-term biodistribution and excretion remain poorly characterized [6, 7]. The unpredictability of protein corona formation, immune activation, and off-target accumulation poses major challenges to clinical translation [8]. These uncertainties underscore the urgent need for systematic studies that bridge nanomaterial properties with their biological fate and function.

Among the diverse classes of nanomaterials, up conversion nanomaterials (UCNMs) represent a unique subclass that has garnered increasing attention. These materials are capable of converting low-energy near-infrared (NIR) photons into higher-energy visible or ultraviolet emissions via multiphoton processes involving rare-earth ions [9]. Up-conversion nanomaterials are an emerging class of luminescence nanomaterials that display unique optical and physical characteristics that are fundamentally different to traditional fluorescent probes, possessing several key advantages due to their unique optical properties given their high photostability, near-infrared absorption and large anti-stoke shifts [10, 11]. These properties, which facilitates a decrease in phototoxicity, increase in tissue penetration and a significant reduction in background fluorescence are key advantages that display remarkable potential for long-term bioimaging, phototherapy, and disease diagnosis [12]. As such, applying up-converting materials as probes for confocal, widefield and super-resolution microscopy to address fundamental biological questions can be a key towards developing a deeper understanding of complex biological phenomena. However, using these materials as probes to study the intracellular dynamics within the cell remains largely

unexplored. The present thesis will therefore investigate whether UCNPs are suitable for long term tracking of cargo dynamics in live cells and whether the intracellular movement of these cargoes can serve as an indicator of the broader physiological state of the cell over extended periods. This first chapter aims to introduce the audience to the fundamentals of up-conversion and their current applications. Afterwards, a section in this section will be used to discuss basic interactions between nanomaterials and living systems. Afterwards, this chapter will introduce single particle tracking (SPT), a promising method used to study various biological phenomena, not limited to the study performed in this thesis. Finally, this chapter will introduce the aims and objectives of this thesis, as well as the fundamental and transdisciplinary science used to formulate this project. Future chapters will discuss the applications of nanomaterials inside living systems to highlight the urgent need for a deeper understanding of the complex interactions between nanomaterials and living systems, thereby highlighting the immense potential of UCNPs as a fundamental model for studying nanoparticle and cellular interactions. This convergence of optical and functional tunability positions up conversion nanomaterials as a frontier in the design of next-generation nanotechnologies for healthcare applications.

1.1 Fundamentals of Up-conversion nanomaterials

1.1.1. Up-conversion mechanism

Fundamentally, the up-conversion process refers to the anti-Stokes emission of higher-energy photons resulting from the sequential absorption of two or more lower-energy photons, typically in the near-infrared (NIR) region. In contrast to one-photon fluorescence, up conversion relies on nonlinear absorption processes, meaning the emission intensity scales nonlinearly with excitation power ($I \propto P^n$, where n = number of photons absorbed) [13]. This nonlinear optical phenomenon relies on the presence of real, metastable intermediate states, which allow the stepwise excitation of electrons to higher energy levels. Among various luminescent materials, trivalent lanthanide ions (Ln^{3+}) such as Yb^{3+}, Er^{3+}, Tm^{3+}, and Ho^{3+} are especially well-suited for up conversion due to their unique 4f electronic configurations [14]. The $4f^n$ configuration of Ln^{3+} ions split into a dense set of discrete energy levels due to Coulombic repulsion and spin–orbit coupling, with additional minor perturbations from the crystal field [15]. These 4f orbitals are well shielded by the filled 5s and 5p orbitals, resulting in narrow emission bands, high photostability, long

radiative lifetimes, and minimized interaction with the surrounding lattice, which together facilitate efficient up conversion luminescence (UCL)[16]. As such, UCMs are typically UCNPs, ranging from 10 to 50 nanometers and are composed of host lattices such as $NaYF_4$ or Y_2O_2S doped with lanthanide ions [17].

Multiple mechanisms can facilitate up conversion in lanthanide-doped systems, with the most commonly described and experimentally observed being excited state absorption (ESA), energy transfer up conversion (ETU), and photon avalanche (PA)[18]. In ESA, a single ion sequentially absorbs two or more photons, climbing stepwise through energy levels before emitting a photon of higher energy. In contrast, ETU relies on two different ions: a sensitizer and an emitter. The sensitizer—typically Yb^{3+} or Nd^{3+} due to its strong absorption at 980 nm and 808nm respectively, first absorbs NIR photons and then transfers the energy non-radiatively to a neighboring activator ion (e.g., Er^{3+} or Tm^{3+}), which accumulates energy through successive transfers to reach an excited state capable of emitting a visible photon [19]. ETU is particularly efficient due to the large absorption cross-section of sensitizers and the spatial proximity of lanthanide ions in appropriately doped host lattices. In typical systems, a combination of ESA and ETU dominates, resulting in broad up conversion spectra. The multiple excited states inherent to most lanthanide ions yield emissions across a wide range of wavelengths, enabling multicolor or even white-light output from a single nanoparticle [14, 20, 21]. While this diversity is advantageous for applications such as multiplexed bioimaging, it can also lead to unwanted crosstalk or spectral overlap. To address this, researchers often co-dope the system with ions like Mn^{2+}, which can either quench specific transitions or introduce alternative emission pathways through energy exchange processes, thereby tailoring the emission profile to a specific application [22].

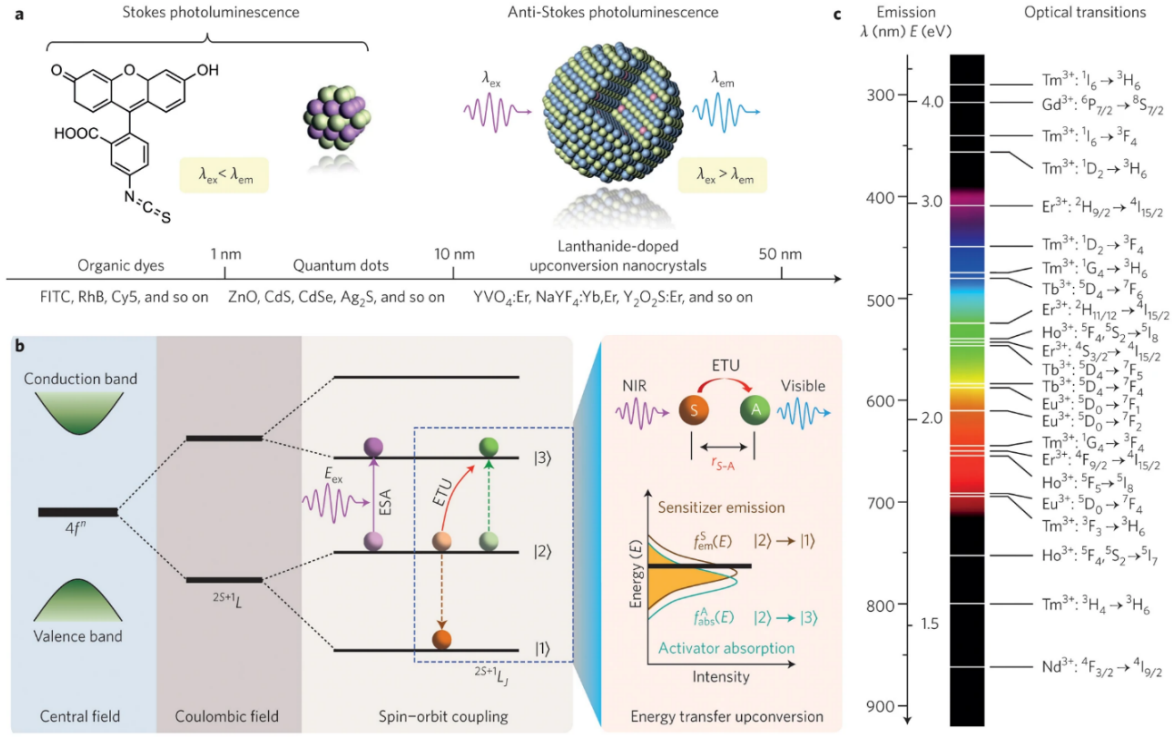

Figure 1.1 Up-Conversion mechanism in lanthanide doped nanoparticles. (a) Different classes of luminescent materials. (b) Up-conversion mechanism via excited state absorption and energy transfer up conversion when electrons are split via Coulomb interactions and spin-orbit coupling. (c) different emissions bands of different lanthanides in different regions.[15]

While the multiphoton absorption of near-infrared wavelengths and visible emissions results in nonlinear scaling of emission intensities, other up conversion mechanisms, namely photon avalanche, can result in extremely high optical nonlinearity [23]. Photon avalanche mechanism is a less commonly observed but highly nonlinear process, involving an initial weak absorption of photons followed by a cascade of energy transfer and cross-relaxation events that dramatically amplify emissions [24]. This mechanism requires a specific arrangement of energy levels and typically occurs in systems with high dopant concentrations under intense excitation. Photon avalanche can be triggered via self-sensitization pathways, for example in highly doped systems containing only Tm^{3+}, resulting in sharp excitation thresholds and extreme optical nonlinearity [25].

Cross-relaxation (CR) is a non-radiative energy-transfer process between sensitizer ions which can result in the quenching or enhancement of differing energy levels. In CR, an ion in an excited state transfers a portion of its energy to a neighboring ion in the ground state, playing a dual role in regulating upconversion efficiency depending on the energy levels involved [26]. In thulium-doped systems, CR is often essential for the population of higher excited states that give rise to blue and ultraviolet emissions. This occurs when the energy provided by ytterbium sensitizers alone is insufficient to access those levels directly [27]. By facilitating energy redistribution among thulium ions, CR enables sequential excitation of higher-lying states. However, when CR predominantly occurs between lower energy states, it can lead to an overpopulation of these intermediate levels [28]. This, in turn, diminishes the population available for higher excited states and results in a reduction in upconversion luminescence efficiency.

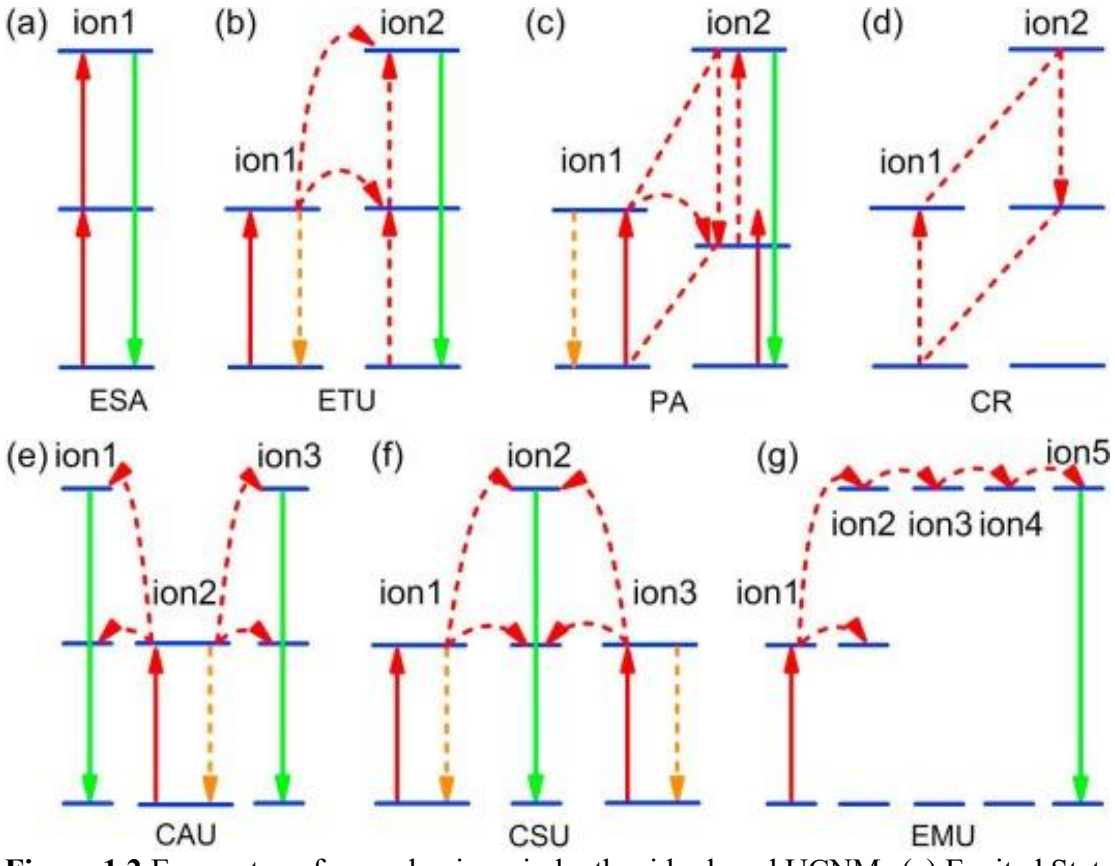

Figure 1.2 Energy transfer mechanisms in lanthanide-doped UCNMs (a) Excited State Absorption (b) Energy transfer upconversion (c) Photon avalanche (d) Cross-relaxation (e) cooperative activation upconversion (f) cooperative sensitization upconversion (g) energy migration upconversion.[18]

1.1.2 Optical characteristics of UCNPs

The optical characteristics of UCNPs are often result of different doping of sensitizers and emitter ions. Sensitizer ions, which are most commonly Yb^{3+} for its large absorption at 976nm, and Nd^{3+} for its ability to absorb 808nm at the NIR-I window [29]. Other than changing the excitation wavelengths through altering sensitizers, the change of emissions wavelengths can occur through doping different emitter lanthanides [30]. As each lanthanide ion possesses a distinct set of 4f–4f transitions, tunable emission across a wide spectral range depends on the chosen dopant. Furthermore, a change in emitter concentration can also result in different emission wavelengths due to increases in cross-relaxation, which changes the distribution of excited electrons, resulting in different emission wavelengths.

Figure 1.3 Different emission wavelengths of different lanthanide doping.[30]

In general, an increase in dopant concentration usually increases cross relaxation which is presented in an increased luminescence emission of lower energy photons, and vice versa, where a lower dopant concentration facilitates brighter photon emission at lower wavelengths and higher energy levels [31]. However, recent reports have suggested the usage of transitional metals such as Cr^{3+} to absorb visible light for down-conversion, lanthanide doped materials given the large absorption cross section of certain transitions metals [32]. These materials are difficult to perform up-conversion emissions due to mismatching absorption wavelengths, as well as the inability to facilitate efficient energy transfer due to their higher rates of transition probability.

Other than emission wavelengths, the luminescent lifetime of UCNPs can be tuned between the microsecond to millisecond range depending on doping concentrations. Decreasing the population or concentration of emitter ions in UCNPs can usually increase radiative lifetimes while increasing the population of emitter ions usually results in a decrease in radiative lifetimes [33]. UCNPs are unique where their radiative lifetimes are magnitudes higher than conventional dyes, which is a result of their non-transition probability which is LaPorte forbidden [34]. However, given that lifetime is inversely proportional to the transition probability, UCNPs often require much higher laser intensities to facilitate multiphoton up-conversion emissions.

Dopant concentration also plays a dual role. While increased concentration of sensitizers and emitters enhances the probability of ETU and cross-relaxation interactions, it simultaneously increases the risk of concentration quenching [31]. At high doping levels, energy migration between ions can lead to non-radiative dissipation at defect sites or surface traps, drastically reducing emission efficiency [35]. This is particularly problematic in ultrasmall nanoparticles, where a high fraction of ions resides near the surface [36].

The photostability of UCNPs is mainly the result of vastly different chemical compositions between fluorescent dyes, which are often composed of carbon-based amphiphilic rings or other organic motifs [37]. The conjugated pi electron systems in carbon based organic materials formed via single and double bonded carbons are easily degraded and disrupted by higher energy photons [38]. Additionally, cleavage via oxygen radicals and other reactive oxygen species (ROS) will result in permanent chemical photobleaching [39]. On the other hand, inorganic host and the 4f-f electronic transitions cannot be disrupted via ROS or high energy photons as they are shielded by outer electrons and crystal lattice respectively [16]. Other inorganic materials with luminescent properties, such as semi-conductor quantum dots, experience photobleaching because of electron trapping into the conductance band [40]. In lanthanide-doped systems, electron trapping becomes infrequent due to the lower energy excitation as well as the inert nature and wide band gap of inert crystal lattices [41].

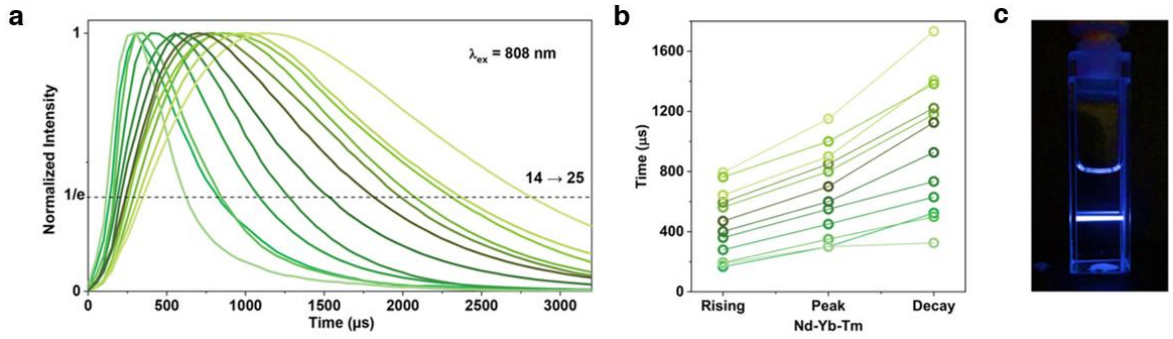

Figure 1.4 Tunable upconversion lifetimes via particle engineering. (a) Nd-Yb-Tm UCNPs with differing sensitizers (Nd, Yb) and emitter (Tm) concentrations. (b) Differing rising, peak and decay times for different concentrations. (c) Photographic representation.[42]

Up conversion systems typically exhibit low up-conversion quantum yield (UCQY), especially under low-intensity excitation [34]. Quantum yield (QY) is a fundamental parameter that characterizes the efficiency of light emission in luminescent materials. It is defined as the ratio of the number of photons emitted to the number of photons absorbed:

$$\text{Quantum Yield (QY)} = \frac{\text{Number of photons emitted}}{\text{Number of photons absorbed}}$$

Given the stepwise excitation of sensitizer and emitter energy transfer upconversion, each transition between excited states is potentially vulnerable to non-radiative relaxation, most notably through multiphonon relaxation [43]. In systems with multiple intermediate energy levels, such as lanthanide doped nanomaterials, an increase in non-radiative decay through phonon relaxation can substantially affect the quantum yield of the material, especially if the energy gap between two excited states is small. The probability of losing that energy to lattice vibrations increases significantly in situations where the energy gap is generally less than 3000–4000 cm^{-1} [44]. This is described by the energy gap law, where smaller gaps lead to higher rates of non-radiative decay via the emission of multiple phonons [45]. The cumulative effect of these non-radiative decay processes across multiple energy levels leads to a substantial reduction in overall quantum yield.

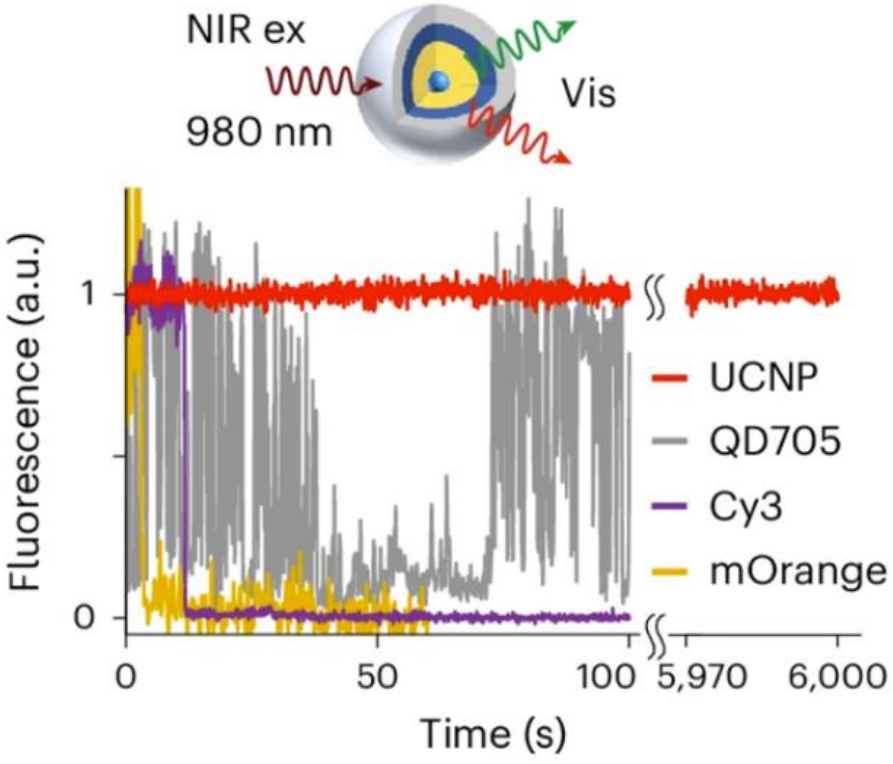

Figure 1.5 Photostability of UCNPs compared to traditional dyes.[46]

1.1.3 Physical characteristics and crystal structure of UCNPs

The physical characteristics and crystal structure of UCNPs are fundamental to their photophysical behavior and functional performance across a wide array of applications. While much of the attention in upconversion research has historically centered on dopant selection and energy transfer mechanisms, the influence of the host lattice and particle morphology is equally critical [47]. The host matrix not only governs phonon dynamics and non-radiative decay pathways but also plays a pivotal role in determining dopant solubility, lattice symmetry, and the nature of crystal field interactions that influence radiative transitions (Figure 1.6) [48]. In addition, surface properties, phase structure, and defect density directly impact luminescence efficiency, stability, and interactions with biological or optical environments [49]. Understanding these structural and physical parameters is essential for engineering UCNPs with tailored properties for applications in bioimaging, phototherapy, sensing, and photonic technologies.

Like all nanomaterials, UCNPs and their interactions with light are significantly attributed to their surface physical characteristics and composition. As such, differing host lattices can

alter the shape, size and optical properties of UCNPs which result in different biological and optical interactions.

Factors such as luminescence and quantum yield are significant optical properties that research aims to optimize to improve their viability in numerous applications, such as improving the detection limit in diagnostics or increasing resolution in super-resolution-based applications [50]. The crystal host is one of the critical factors that can significantly alter the physical characteristics of UCNPs. Host matrices with high phonon energies, such as oxides, result in an increase of vibrational frequence due to the light mass of ions in the host lattice as well as strong ionic or covalent bonding between constituent atoms [51]. Hosts matrices containing higher phonon energies typically increase multiphonon relaxation when excited states are achieved and are therefore more likely to decrease the overall quantum yield.

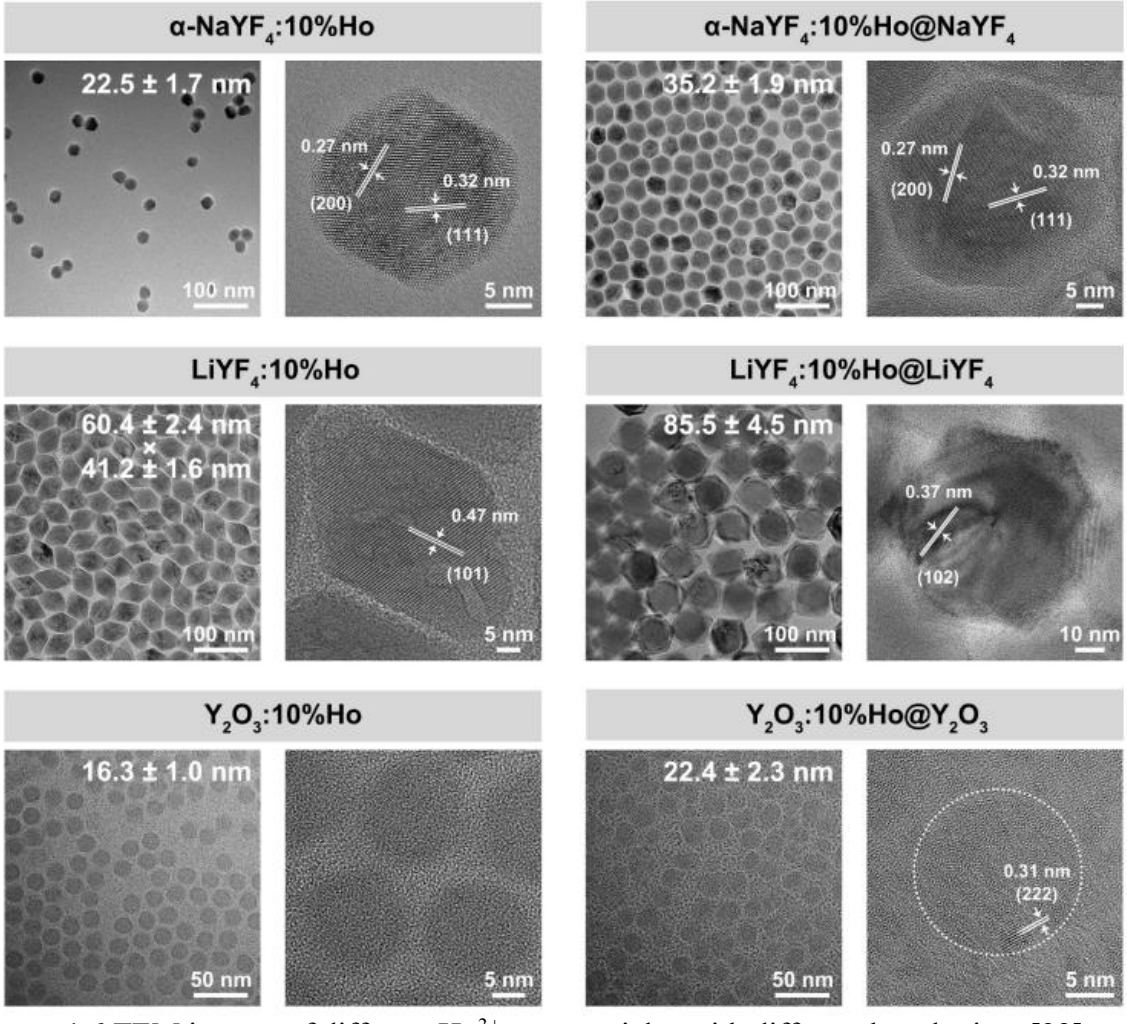

Figure 1.6 TEM images of different Ho^{3+} nanoparticles with different host lattices.[32]

These materials also offer structural compatibility with lanthanide ions, allowing high dopant solubility without phase segregation. Host symmetry and local coordination further affect the intensity and probability of radiative transitions, particularly for parity-forbidden 4f–4f transitions, which are susceptible to changes in crystal field environments [51].To mitigate this, fluoride-based hosts such as $NaYF_4$ are commonly used in UCNP synthesis due to their low maximum phonon energies, which help to suppress non-radiative losses and preserve the long excited-state lifetimes required for efficient upconversion [52]. $NaYF_4$ systems are chemically inert, easily synthesized and generally non-toxic compared to heavy metal nanomaterials. $NaYF_4$ can exist in either a cubic (a) or hexagonal (b) phase depending on the reaction conditions such as temperature and reaction time, which can result in spherical or hexagonal nanoparticles ranging from 5 to 500nm. It is generally recognized that hexagonal phases possess a higher luminescence efficiency due to higher crystal field asymmetry, which allows for the crystal field distortion to enhance 4f-f transitions [47].

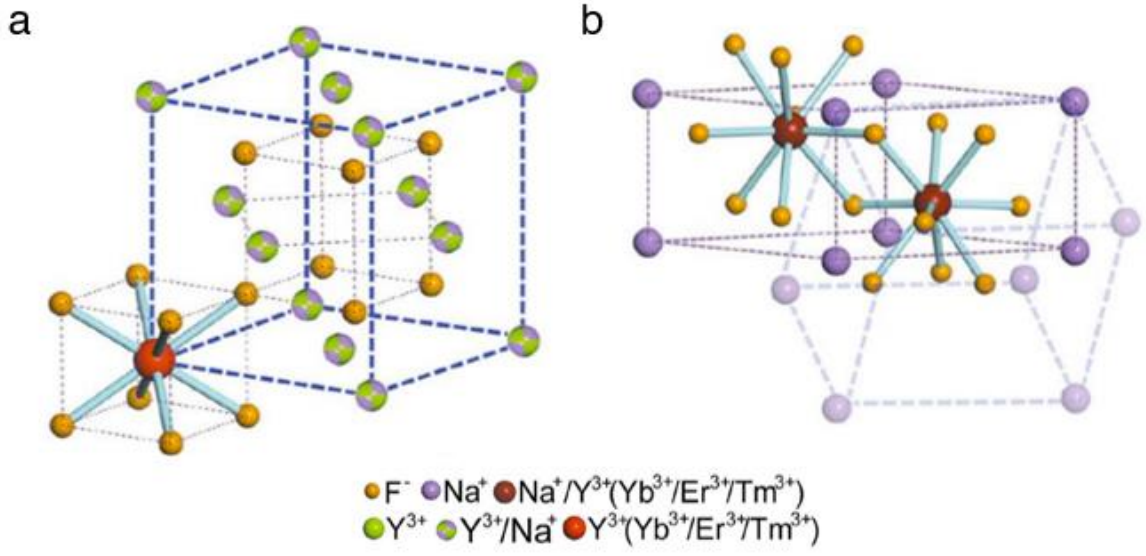

Figure 1.7 Lattice structure of $NaYF_4$ UCNPs in alpha-cubic (a) and beta-hexagonal (b) states.[167]

These structural and compositional factors not only influence fundamental luminescent behavior but also enable tunability in nonlinear optical responses, which are increasingly being leveraged in advanced imaging modalities. By strategically selecting host materials and dopant combinations, it becomes possible to engineer UCNPs with tailored optical behaviors for highly specialized applications [53]. For example, Lutetium doped UCNPs

have recently demonstrated extremely optical nonlinearity by altering the dipole transitions in thulium doped avalanching nanoparticles [54].

As a result of lattice contraction through distorted symmetry via sublattice reconstruction, optical nonlinearity was significantly increased in lutetium and thulium doped UCNPs, which demonstrated a significant increase in lateral and axial resolution through optical scanning microscopy.

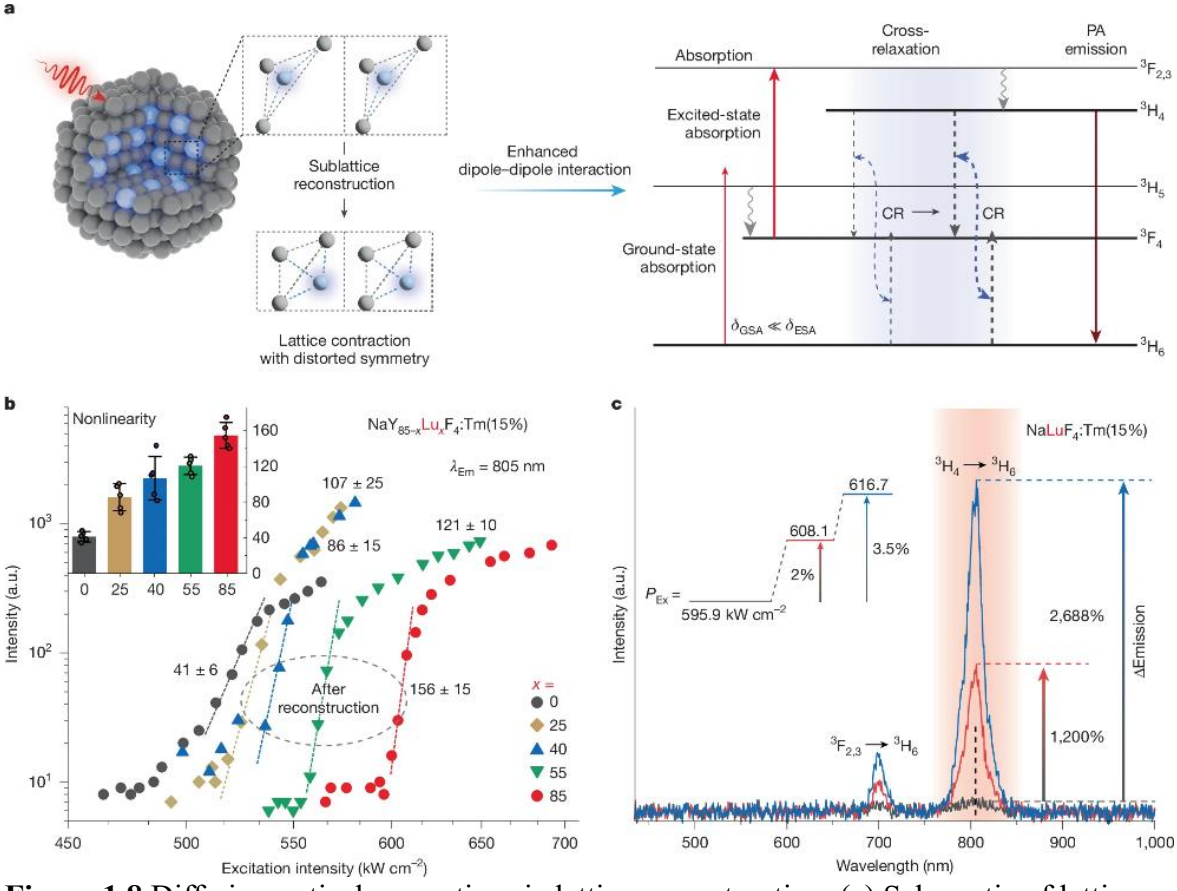

Figure 1.8 Differing optical properties via lattice reconstruction. (a) Schematic of lattice reconstruction enhancing dipole-dipole interactions (b) Increasing Optical nonlinearity after reconstruction (c) Emission wavelengths under slight changes in emission intensities.[54]

Furthermore, recent research has demonstrated that a reduction in defects, specifically hydroxy defects, can significantly increase the luminescence of nanoparticles by reducing non-radiative pathways for optical relaxation [55]. UCL quenching can also occur in water due to non-radiative relaxation between Yb^{3+} ions and water given the matching energies between the stretching vibration energy level of v = 0 to v = 3 in hydroxyl groups and the electron transition energy of Yb3+ ions [32]. As such, method, materials or lattice hosts

which introduce hydroxyl groups or oxygen ions which are prone to forming defects during nanoparticle synthesis can result in lower efficiency UCL. One of the major sources of defects exists at the surface of the nanoparticle, which are formed during the final stages of particle synthesis where surface energy can result in distortions or changes in lattice positions [56]. Given the enhanced surface area to volume ratio in nanoscale materials, surface defects contribute a major role in the quenching in many materials, including UCNPs. As such one of the most classic methods for the reduction of defects is via surface passivation through inert shell formation. The formation of inert shells can significantly reduce the transfer of energy from excited states in lanthanides towards defects as well as potential quenching factors in the environment [57]. In these systems, an active or inert shell surrounds the doped core, isolating the emissive centers from surface quenchers and improving the overall quantum yield. Core–shell designs can also support energy migration-based upconversion (EMU), where excitation energy is relayed through a network of ions before reaching the activator [58]. Taken together, the upconversion process is not defined by a single mechanism but rather by a complex interplay of multiphoton excitation pathways, host-lattice effects, dopant interactions, and nanostructural engineering. A deep understanding of these interdependent factors is essential for rationally designing efficient upconversion nanomaterials for applications ranging from deep-tissue imaging and targeted phototherapy to solar energy harvesting and anti-counterfeiting technologies.

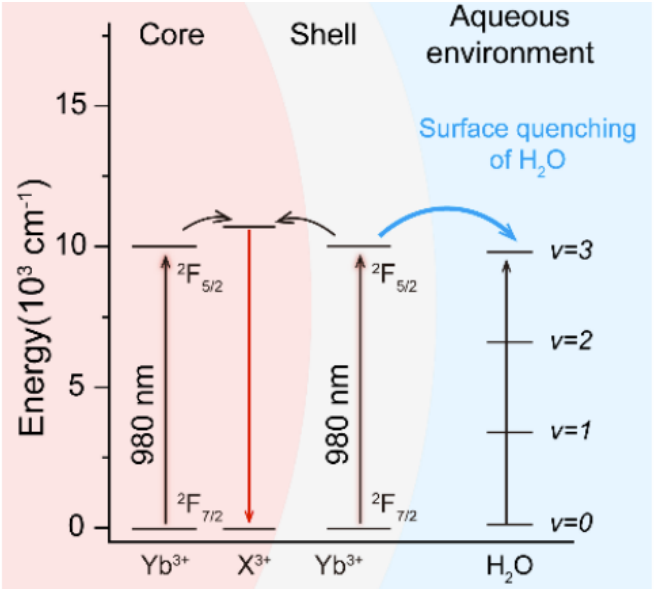

Figure 1.9 Schematic illustration of non-radiative relaxation between UCNPs and hydroxyl groups through surface quenching in an aqueous environment.[32]

1.1.4 Current applications of UCNPs

Given the unique optical properties of UCNPs, these materials have been used extensity in a variety of applications in the fields of energy, fingerprinting, anti-counterfeit materials, diagnostics and bioimaging.

1.1.4.1 Lifetime multiplexing and anti-counterfeit applications

Lifetime multiplexing, which is tunable by dopant concentrations, has been demonstrated to have immense potential for anti-counterfeit materials as well as diagnostic identification [59]. Lifetime multiplexing in upconversion nanoparticles relies on the ability to distinguish luminescent signals based on their decay lifetimes rather than solely their emission spectra. This phenomenon arises because different lanthanide dopants, or varying concentrations of the same dopant, exhibit characteristic excited-state lifetimes. These differences stem from variations in energy transfer processes, cross-relaxation pathways, and non-radiative decay rates, all of which are highly sensitive to dopant type, concentration, and the local crystal field environment [33]. By precisely tuning these parameters during synthesis, it is possible to generate UCNPs with distinct and reproducible temporal luminescence profiles.

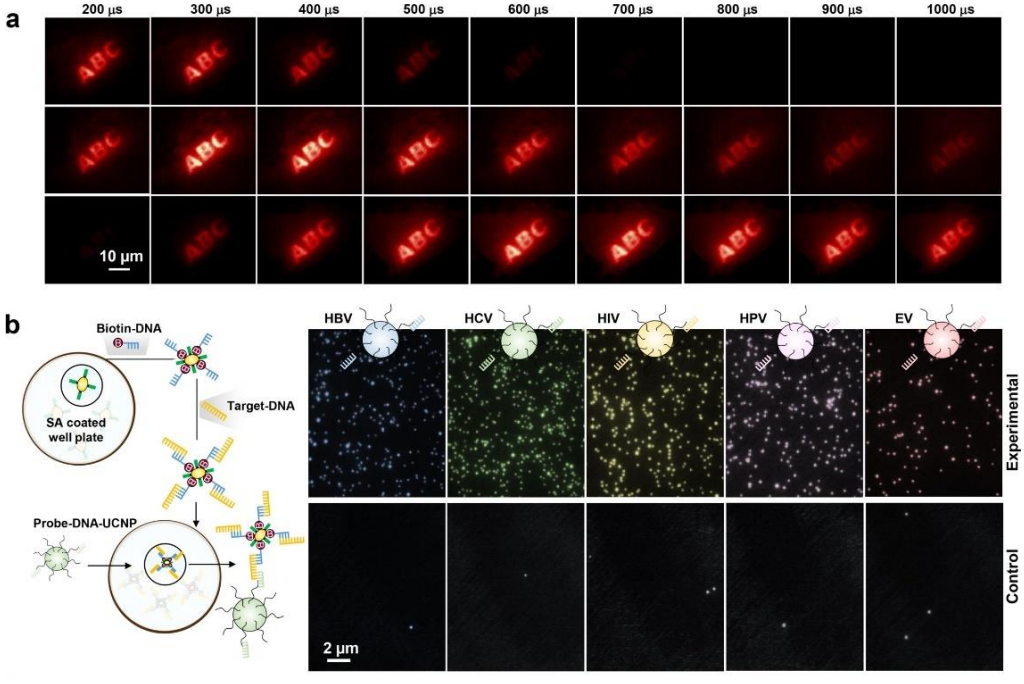

Figure 1.10 Lifetime multiplexing using UCNPs (a) Differing rising-decay fingerprints with UCNPs. (b) Multiplexing through conjugation with DNA using Tm^{3+} UCNPs. [42]

This tunability has significant implications for anti-counterfeit technologies. UCNPs can be embedded into materials to produce unique lifetime-encoded signatures that are not visible under normal lighting and require time-resolved detection for authentication [60]. Such features are difficult to replicate or forge, offering a robust layer of security in labeling or certification.

1.1.4.2 Diagnostics and Lateral flow assays

Lateral flow assays (LFAs) are rapid, portable, and cost-effective diagnostic platforms widely used for point-of-care testing in clinical, environmental, and food safety applications. Based on capillary-driven fluid migration across a porous membrane, LFAs utilize specific molecular recognition events to detect the presence of target analytes, typically producing a visible signal within minutes [61]. Their simplicity, low sample volume requirement, and ease of use have made them indispensable in both resource-limited settings and large-scale screening programs. In LFAs, upconversion nanoparticles offer distinct advantages due to their unique optical properties, particularly their ability to undergo anti-Stokes emission, where they emit shorter-wavelength light upon excitation with NIR light. This characteristic allows for detection with minimal background interference, as biological tissues and common assay substrates typically exhibit little to no autofluorescence under NIR excitation [62].

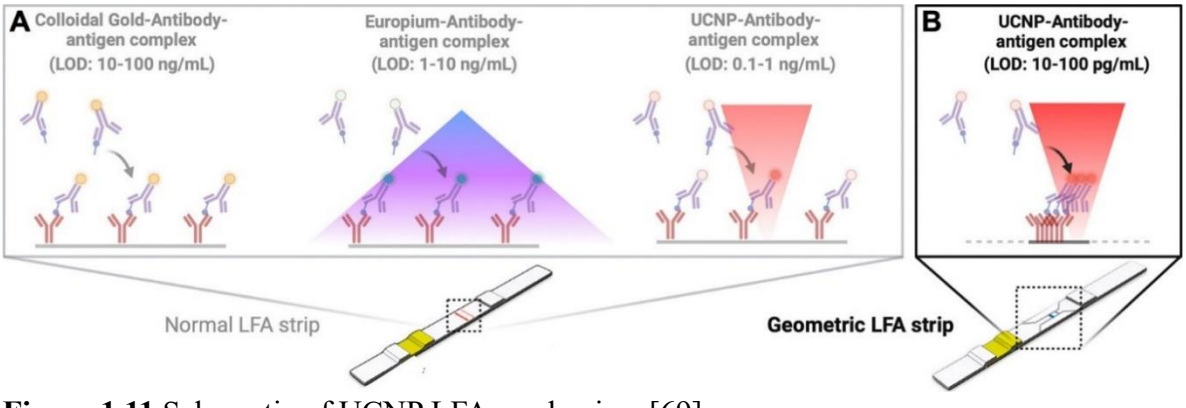

Figure 1.11 Schematic of UCNP LFA mechanism.[69]

The mechanism of UCNP-based LFAs typically involves functionalizing the surface of the nanoparticles with specific biorecognition molecules, such as antibodies or oligonucleotides, which enable selective binding to target analytes [63, 64]. During the

assay, the sample migrates along a nitrocellulose strip via capillary action. If the target is present, it binds to the UCNP-conjugated recognition molecule, and this complex is then captured at a test line that contains a secondary binding agent. Upon NIR excitation, commonly at 980 nm or 808 nm, UCNPs emit visible light, which is detected using a photodetector or a smartphone-based imaging system [65-68].

Compared to traditional fluorophores or gold nanoparticles, UCNPs offer significantly improved sensitivity and signal-to-noise ratio, enabling detection of analytes at much lower concentrations [69]. Additionally, their resistance to photobleaching and chemical degradation enhances assay stability and reproducibility. Because UCNPs can be tuned to emit at different wavelengths or lifetimes depending on their composition, they also allow for multiplexed detection, where multiple targets can be simultaneously identified on the same assay strip [68]. This makes UCNPs a highly promising platform for next-generation point-of-care diagnostics.

1.1.4.3 Photodynamic therapy

Photodynamic therapy (PDT) has become an attractive approach with immense clinical application for cancer and disease therapeutics [70]. As a minimally invasive treatment, PDT utilizes light-activated photosensitizers to generate reactive oxygen species, leading to localized cell damage and apoptosis. PDT offers high spatial selectivity with reduced systemic toxicity, making it an attractive alternative to conventional therapies.

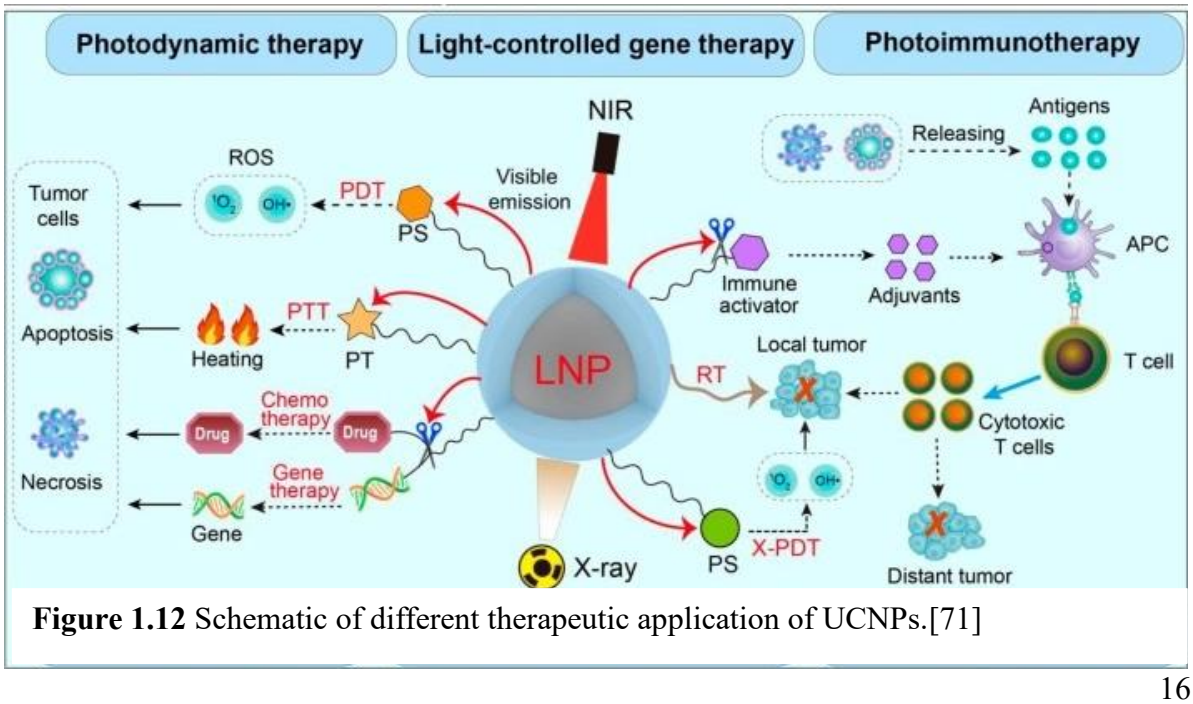

Figure 1.12 Schematic of different therapeutic application of UCNPs.[71]

In PDT, upconversion nanoparticles serve as nanoscale transducers that convert deeply penetrating NIR light into higher-energy visible or ultraviolet photons capable of activating photosensitizers. The mechanism of UCNP-assisted PDT addresses one of the central limitations of conventional PDT, namely, the shallow tissue penetration of visible light, by enabling the excitation of photosensitizers at depth using NIR wavelengths such as 980 nm or 808 nm [72, 73].UCNPs are typically doped with lanthanide ions such as Yb^{3+}, which act as sensitizers absorbing NIR light, and Er^{3+}, Tm^{3+}, or Ho^{3+}, which serve as activators emitting in the visible or UV range. Upon NIR excitation, the absorbed photons undergo sequential energy transfer within the UCNP lattice, resulting in upconverted emission. This emission overlaps with the absorption spectrum of nearby photosensitizer molecules, which are either covalently linked or physically adsorbed onto the UCNP surface [74]. Once activated, these photosensitizers transfer energy to surrounding molecular oxygen, producing cytotoxic reactive oxygen species (ROS), particularly singlet oxygen ($^1O_2$), which induce localized oxidative damage to cellular structures, ultimately leading to cell death for photo-induced chemotherapy and tumor elimination [75].

Recent works have also explored the potential applications of UCNPs for immunogenic cell death for cancer therapy through photoimmunotherapy [168-172]. For example, Through the activation of endogenous iron within the cell, Zhu et al. has demonstrated efficient immunotherapy with ferroptosis and proptosis integration upon NIR radiation [171]. Folic acid molecule functionalization on UCNPs facilitated enhanced tumor targeting through folate receptors, while croconaine molecules enabled iron localization within the lysosome for enhanced ferroptosis. NIR irradiation facilitated UV emissions for the activation of the Fenton reaction for enhanced tumor therapy using UCNPs. In other instances, enhancing targeting through surface labelling of UCNPs has been achieved using methods such as hyaluronic acid, aptamers, membrane encapsulation or small peptides, which are useful alternatives with binding affinities for different applications [168-172].

Several design insights have advanced the efficacy of UCNP-mediated PDT. Surface engineering of UCNPs with mesoporous silica, polymers, or amphiphilic coating enhances biocompatibility and allows for high photosensitizer loading [76-78]. Moreover, doping strategies and energy transfer engineering, such as optimizing sensitizer-to-activator ratios can be fine-tuned to maximize ROS generation. Overall, UCNP-based PDT represents a

promising avenue for non-invasive cancer treatment and localized therapy, offering high spatial control, deeper tissue penetration, and minimized collateral damage due to the low phototoxicity of NIR excitation in healthy tissues.

1.1.4.4 Bioimaging and super-resolution

Similar to photodynamic therapy, in bioimaging, UCNPs offer a powerful alternative to conventional fluorophores due to their unique ability to convert low-energy NIR excitation into visible or ultraviolet emission through a multiphoton absorption process. This anti-Stokes shift allows for imaging with minimal background autofluorescence and reduced photodamage to biological tissues, which are particularly beneficial for in vivo imaging and deep-tissue visualization.

In super-resolution microscopy, UCNPs are increasingly utilized due to their non-linear emission properties and long luminescence lifetimes. Techniques such as stimulated emission depletion (STED) and lifetime-based imaging modalities take advantage of these features. For instance, UCNPs can be depleted selectively in the outer regions of the excitation spot using a secondary beam, as in STED, or distinguished based on decay dynamics in time-gated or lifetime imaging, allowing for sub-diffraction spatial resolution [79].

Additionally, recent advances have demonstrated that single UCNPs can be engineered to exhibit photon emission intermittency (blinking) or nonlinear excitation thresholds, enabling their use in stochastic optical reconstruction microscopy (STORM)-like methods [80]. These blinking dynamics, though not intrinsic to all UCNPs, can be induced through surface modifications, dopant concentration control, or host lattice manipulation [80].

Altogether, UCNPs offer distinct advantages in bioimaging and super-resolution applications, including deep-tissue imaging capability, enhanced signal-to-noise ratios, exceptional photostability, and compatibility with advanced imaging techniques that demand precise spatial and temporal resolution. Their tunability in emission, excitation, and lifetime properties make them highly adaptable tools for next-generation optical imaging.

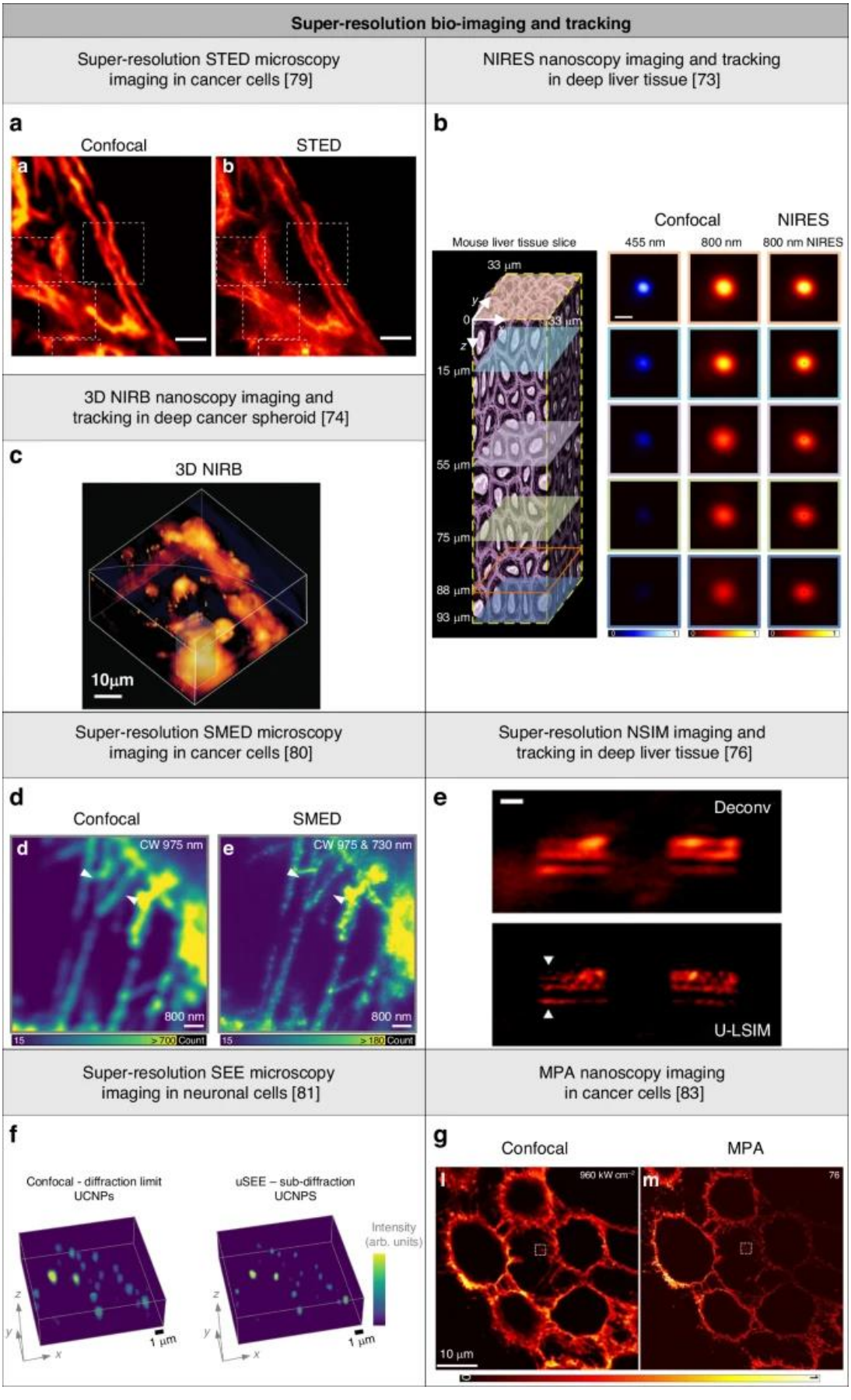
Super-resolution bio-imaging and tracking
Super-resolution STED microscopy imaging in cancer cells [79]
NIRES nanoscopy imaging and tracking in deep liver tissue [73]
a
Confocal
STED
b
Confocal
NIRES
Mouse liver tissue slice
455 nm
800 nm
800 nm NIRES
33 µm
15 µm
55 µm
75 µm
88 µm
93 µm
3D NIRB nanoscopy imaging and tracking in deep cancer spheroid [74]
c
3D NIRB
10µm
Super-resolution SMED microscopy imaging in cancer cells [80]
Super-resolution NSIM imaging and tracking in deep liver tissue [76]
d
Confocal
SMED
CW 975 nm
CW 975 & 730 nm
800 nm
e
Deconv
U-LSIM
Super-resolution SEE microscopy imaging in neuronal cells [81]
MPA nanoscopy imaging in cancer cells [83]
f
Confocal - diffraction limit UCNPs
uSEE – sub-diffraction UCNPS
Intensity (arb. units)
1 µm
g
Confocal
MPA
960 kW cm⁻²
10 µm

Figure 1.13 Bioimaing and super-resolution applications using UCNPs. (a) STED (b) NIRES (c) 3D NIRB (d) SMED (e) NSIM(f) SEE (g) MPA.[81]

1.1.4.5 Persistent luminescence and X-ray imaging

Lanthanide-doped upconversion nanoparticles have gained widespread attention for their ability to convert low-energy near-infrared excitation into visible emission [82]. Beyond traditional upconversion processes, these materials can also be engineered to exhibit functionalities such as persistent luminescence and X-ray-excited emission, both of which significantly expand their utility in biomedical imaging. Persistent luminescence allows for time-delayed photon emission after the excitation source is removed, enabling background-free imaging and prolonged signal monitoring [83]. Meanwhile, X-ray-excited luminescence enables deep-tissue excitation through ionizing radiation, allowing for efficient light generation within optically opaque environments. These advanced luminescent modalities rely on distinct but related mechanisms involving charge carrier dynamics, trap states, and energy transfer to lanthanide ions.

In persistent luminescence, also known as afterglow or long-lasting phosphorescence, the emission persists long after the excitation source has been removed. This process typically requires the presence of charge traps within the host lattices such as defects, vacancies, or intentionally introduced co-dopants that can temporarily store excitation energy [84]. Upon excitation by X-ray, UV, visible, or NIR light, electrons are promoted to higher energy states and subsequently trapped in these long-lived defect states. Over time, thermal energy or low-level background stimulation releases the trapped charge carriers, which then recombine radiatively at luminescent centers such as lanthanide ions (e.g., Er^{3+}, Tm^{3+}, or Dy^{3+}), producing a delayed emission in both a visible and NIR spectrum [85]. In the context of UCNPs, fluoride-based hosts typically lack sufficient trap depth for strong persistent luminescence, so host lattices like garnets or aluminates, which better support charge-trapping, are often used in persistent luminescent materials [86]. However, hybrid systems and core–shell structures can be designed to enable afterglow in UCNPs by introducing trap-rich layers [87].

Lanthanide ions with appropriate electronic configurations, such as Eu^{3+} or Tb^{3+}, can emit strongly under X-ray excitation [82]. Incorporating such ions into UCNP-like nanostructures enables dual-modality probes that can be excited either by NIR or by X-ray

irradiation. X-ray excitation allows for deep tissue imaging due to the high penetration depth of ionizing radiation, while the visible/NIR emission can be detected with high sensitivity [88]. Furthermore, UCNPs doped with elements like Gd^{3+} can serve as contrast agents for magnetic resonance imaging (MRI), enabling multi-modal imaging platforms [89].

Overall, X-ray-activated UCNP systems expand the imaging toolbox for biomedical applications, allowing for high-contrast, background-free imaging in vivo and in deep tissue, especially in scenarios where continuous excitation light is impractical or phototoxic.

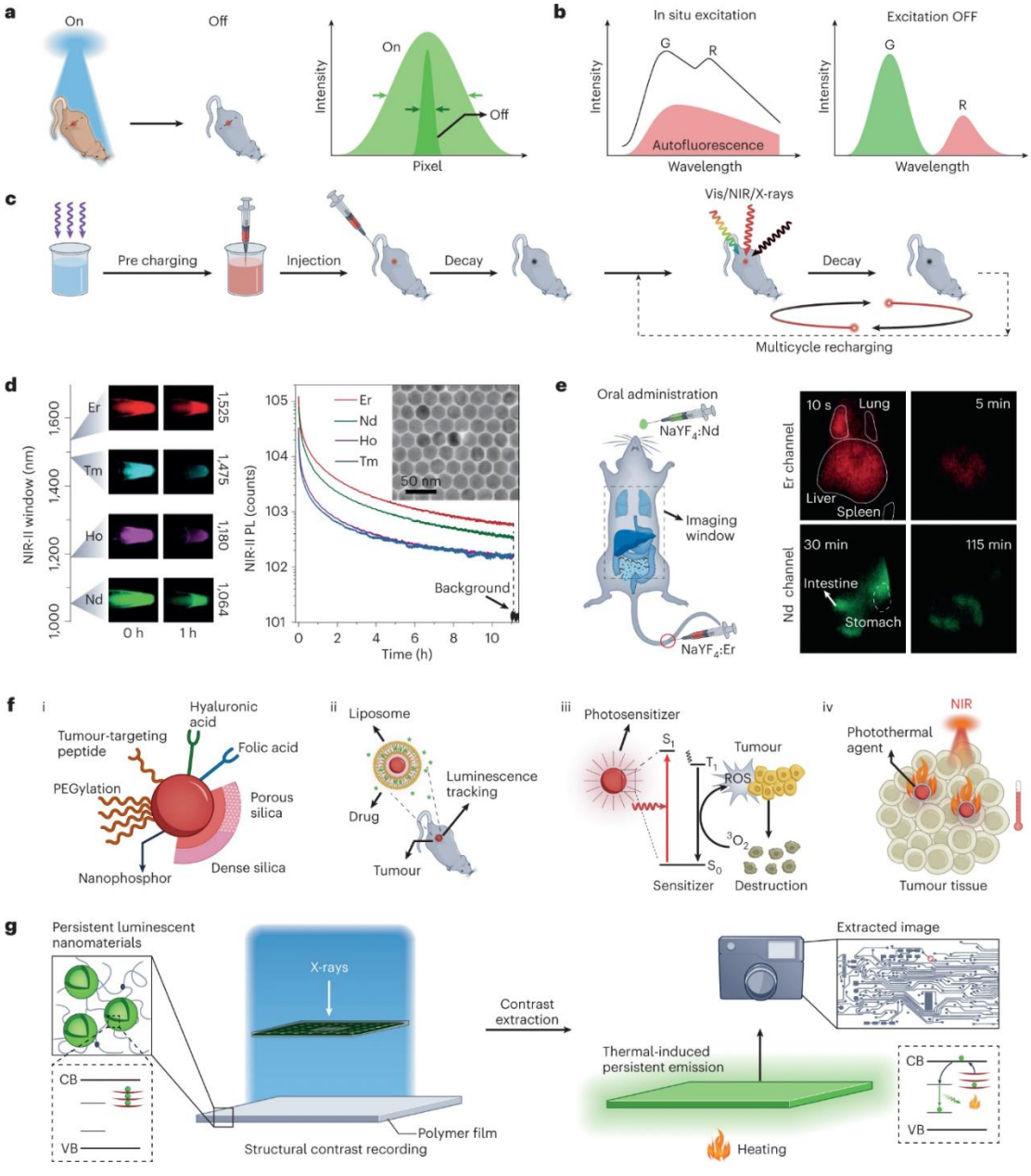

Figure 1.14 Persistent luminescence applications using UCNPs (a) Full resolution imaging using FWHM. (b)Radiometric fluorescence with persistent luminescence. (c) Deep tissue imaging. (d) Persistent luminescence with different lanthanides. (e) Real time tracking using persistent luminescence. (f)Methods for surface functionalization and phototherapy. (g) High resolution X-ray imaging.[83]

1.2 Nanoparticle and the cell

Materials which exist at the nanoscale level possess unique physical and chemical properties that differ greatly from their bulk counterparts. Phenomenon that occurs only at a nanoscale, such as the quantum confinement effect and surface plasmon effect, are a result of materials confined at sizes smaller than the wavelength of light [90, 91]. Furthermore, at a nanoscale, intermolecular forces, such as Van deer Waals forces, electrostatic interactions as well as surface tension, become dominant forces that can significantly influence the physical and chemical properties of nanomaterials [92, 93]. Finally, materials at the nanoscale have significantly higher surface area to volume ratio that inversely increases as size decreases. These properties, along with ingenious strategies to synthesize, modify and structure nanoparticles for tailor-made applications make them a dominant field in recent research.

Particularly, nanoparticles and their clinical applications as therapeutic agents, delivery systems and diagnostics tools have vast potential for revolutionizing medicine.

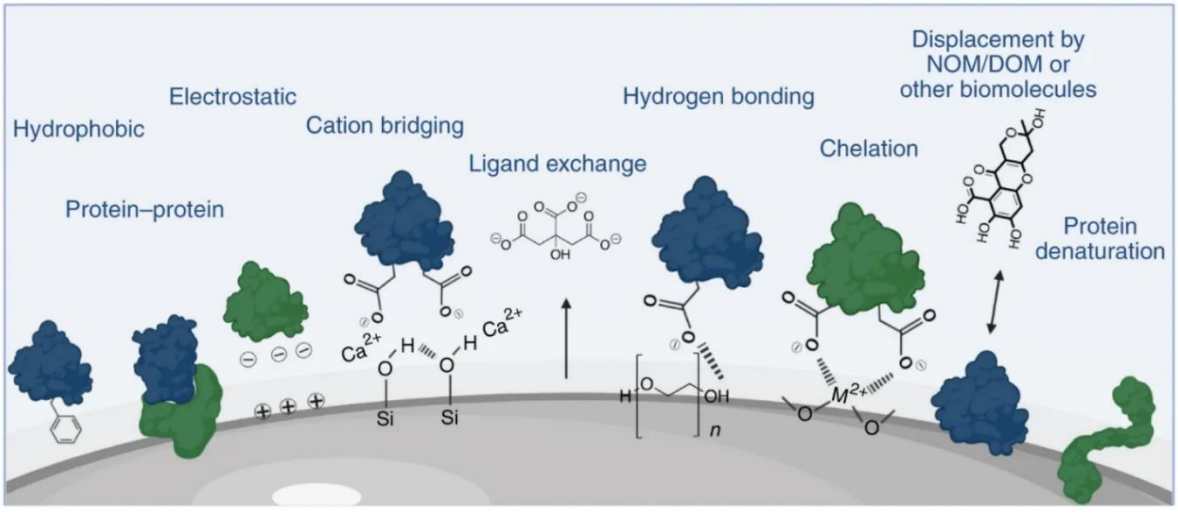

Figure 1.17 Schematic of potential interaction between the nanoparticle surface and proteins.[94]

Fundamentally, nanoparticles as potential strategies for future clinical applications are essentially dependent on nanoparticle-cell interactions, which currently acts as a major bottleneck for future clinical applications [94]. As such, understanding the interactions between the cell and nanoparticles is foundational work that can significantly accelerate clinical applications of nanoparticles. It is therefore imperative to understand and detect nanoparticles and their interactions within the cell at a wide timescale between seconds and days [95].

Nanoparticle endocytosis is the first step between the interactions between cell and the nanoparticle. However, endocytosis is not the first step that occurs between the nanoparticle and a biological environment due to the formation of a protein corona. The protein corona, which is formed via interactions with the surface of the nanomaterial, is often dependent on the chemical and physical characteristics of the nanoparticle surface, such as surface charge and binding affinity [96]. In the majority of cases, common proteins in a living system such as albumin, immunoglobin and fibrinogen can dominate the surface of the nanoparticle**.**

While endocytosis has been extensively studied for decades, its interactions with nanoparticles are still unclear and misunderstood. Namely, interactions between the phospholipid bilayer and its receptors compel nanoparticles and other foreign material to enter the cell only via active transportation [97-99]. In this sense, active transportation of nanoparticles into the cell is facilitated by the cytoskeleton. It has become a challenge in recent years to study how endocytosis can influence the uptake of nanoparticles within the cell. Drug-induced inhibition of endocytic pathways is the standard method in studying nanoparticle cell uptake [100]. However, the major disadvantage of using drug-induced disruption of specific endocytic pathways is the uncertainty of potential side effects of other up-take pathways; that is, drug-induced disruption may affect multiple uptake pathways as well as intracellular trafficking [94]. Cellular interactions with the nanoparticle are further discussed in chapter 2.

1.3 Single particle tracking

1.3.1 Significance and fundamentals

Intrinsically linked with biological function and interaction with living systems, understanding the behavior of molecules in a living system is fundamental towards

understanding the complex mechanisms of biological function. The kinetics of biochemical reactions, such as the rates at which proteins bind and unbind to substrates like DNA, or organelle kinetics-based interactions during cellular mitosis, are crucial interactions that dictate various functions in biological systems [101-103]. Classical biological techniques, such as FISH, FRET and FRAP have been developed to understand these intrinsic interactions at a cellular and single molecular level. However, direct insights into the physical nature and organization of the cellular environment remain unclear today. Single particle tracking (SPT) has become a technique in recent years for monitoring the spatiotemporal dynamics of individual particles within living cells. It serves as a principal methodology for elucidating the complex behaviors of individual proteins or organelles, including their navigation of cellular microenvironments, their interactions with other macromolecules or organelles, and their assembly into functional complexes [104, 105]. A key advantage of SPT over conventional ensemble-based biochemical or imaging techniques is its unique capacity to resolve molecular heterogeneity. Specifically, analysis of individual molecular tracks can reveal diverse binding and unbinding kinetics, spatially dependent variations in protein dynamics, and the viscoelastic properties of the intracellular environment [106, 107]. The application of SPT is broadening to address key questions across cellular biology and biophysics. Through the extraction of multifaceted biophysical

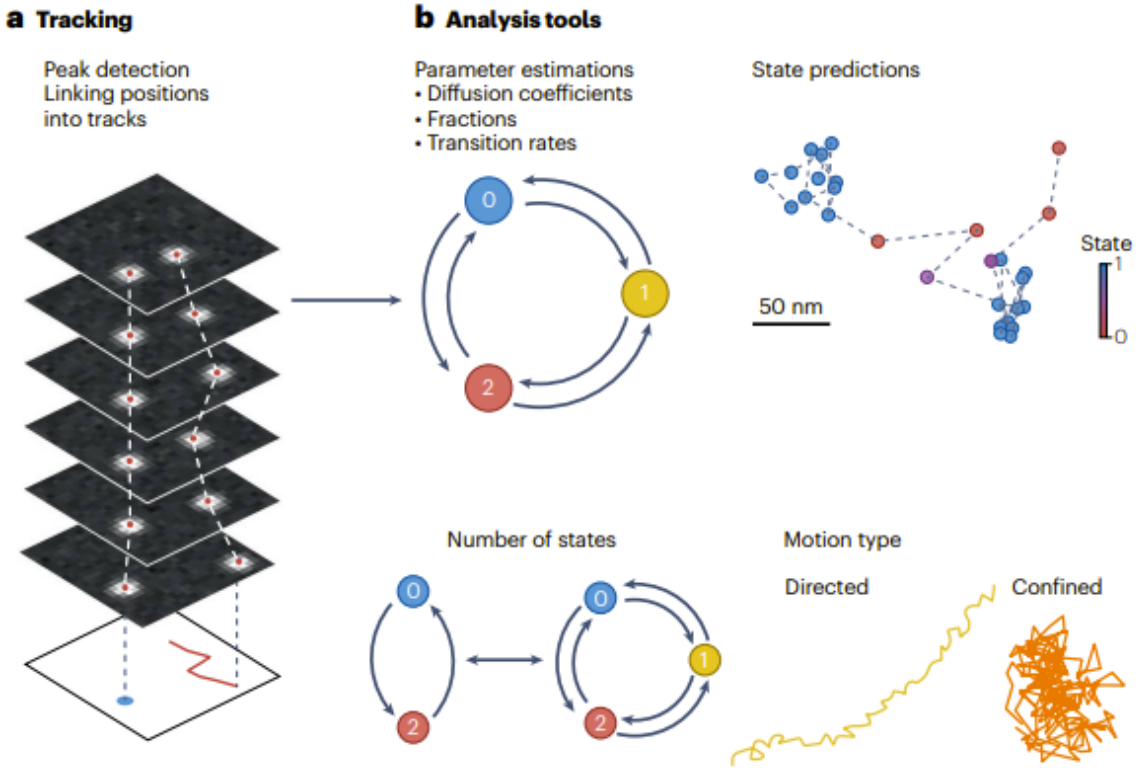

Figure 1.18 Processes to achieve single particle tracking.[108]

information from a single particle or cargo trajectory, distinct diffusion states, binding and unbinding kinetics, and periods of confinement can facilitate the construction of comprehensive, mechanistic models of cellular processes.

The analysis and process to describe certain biological processes using SPT can be described by two processes, the experimental tracking process and analytical process (Fig 1.18). The experimental tracking process, which is dictated by microscopy method, fluorophore selection and biological context, is often selected depending on the context and purpose of the study. In most cases, a scanning or widefield based method is selected with various hardware to choose from depending on the available instruments or resources. Fundamentally, the analytical process needs to mitigate inaccuracies brought in by the experimental process via analytical tools through different calculations and estimations are core themes in SPT [108]. This need to address different inaccuracies brought in by different biological contexts and experimental procedures have resulted in numerous software and methods being developed for SPT. Regardless of what experimental methods are performed, inaccuracies and noise are inevitably bound by physical restrictions. These inaccuracies brought in by the frame rate, diffraction limit, signal to noise ratio, drift, photobleaching and phototoxicity, must be taken into account before analyzing the states and coefficients within biological systems. For example, the diffraction limit often requires predictions and estimations for the localization of singular molecules, as sub 100 nm molecules such as proteins and DNA are vastly smaller than the diffraction limit of approximately 200 nm without super-resolution [80].

1.3.2 Analytical Methods for SPT

With a need to address different tracks in a biological context, numerous analytical techniques have been developed for SPT. For example, the ability to monitor and characterize nanoparticle movement within cells in real time is a critical tool in elucidating mechanisms of cellular uptake, intracellular trafficking, and therapeutic delivery efficiency. This section will analyze modern analytical methods for SPT [109-111].

1.3.2.1 MSD

Among the various analytical tools used to interpret single-particle trajectories, Mean Square Displacement (MSD) analysis has emerged as one of the most widely adopted and informative methods [112, 113]. MSD provides a quantitative measure of particle mobility and can differentiate between key modes of transport such as diffusion, confinement, and active motion. By applying MSD to intracellular tracking data, researchers gain not only kinetic information (e.g., diffusion coefficients) but also mechanistic insight into how nanoparticles navigate the intracellular environment.

MSD is a statistical metric that quantifies the average squared distance a particle travels as a function of time. In the context of intracellular tracking, MSD provides key insights into the dynamic behavior of nanoparticles, vesicles, or organelles within the complex and heterogeneous cellular environment. It is derived from time-lapse imaging data by tracking the positions of individual particles over successive frames. The MSD is mathematically defined as:

$$\mathrm{MSD}(\Delta t) = \langle [\mathbf{r}(t + \Delta t) - \mathbf{r}(t)]^2 \rangle$$

where $\mathbf{r}(t)$ represents the particle's position at time t, and the angular brackets denote an average over all time origins and tracked particles. MSD analysis allows for classification of motion types such as free diffusion, confined diffusion, active transport, and anomalous diffusion, each of which reveals different aspects of the local cellular environment or biological interaction [112].

By segmenting trajectories into motion categories, it becomes possible to quantify the relative contributions of passive and active transport within cells [114]. This analysis provides mechanistic insight into how nanoparticles are trafficked, retained, or exocytosed, which is essential for applications in drug delivery, bioimaging, and nanotoxicology. Additionally, changes in MSD behavior over time or under pharmacological intervention can be used to probe the dynamics of intracellular transport systems.

Despite its utility, MSD analysis presents several technical challenges. Localization noise at short lag times can artificially flatten MSD curves, leading to underestimation of diffusion coefficients [115]. This is particularly problematic for slowly moving or confined particles. At long lag times, trajectory truncation and statistical under sampling can introduce biases due to reduced averaging and increased variability. Additionally, cellular heterogeneity, such as organelle crowding or local viscosity differences, complicated interpretation and necessitate large datasets for statistically robust conclusions [116, 117].

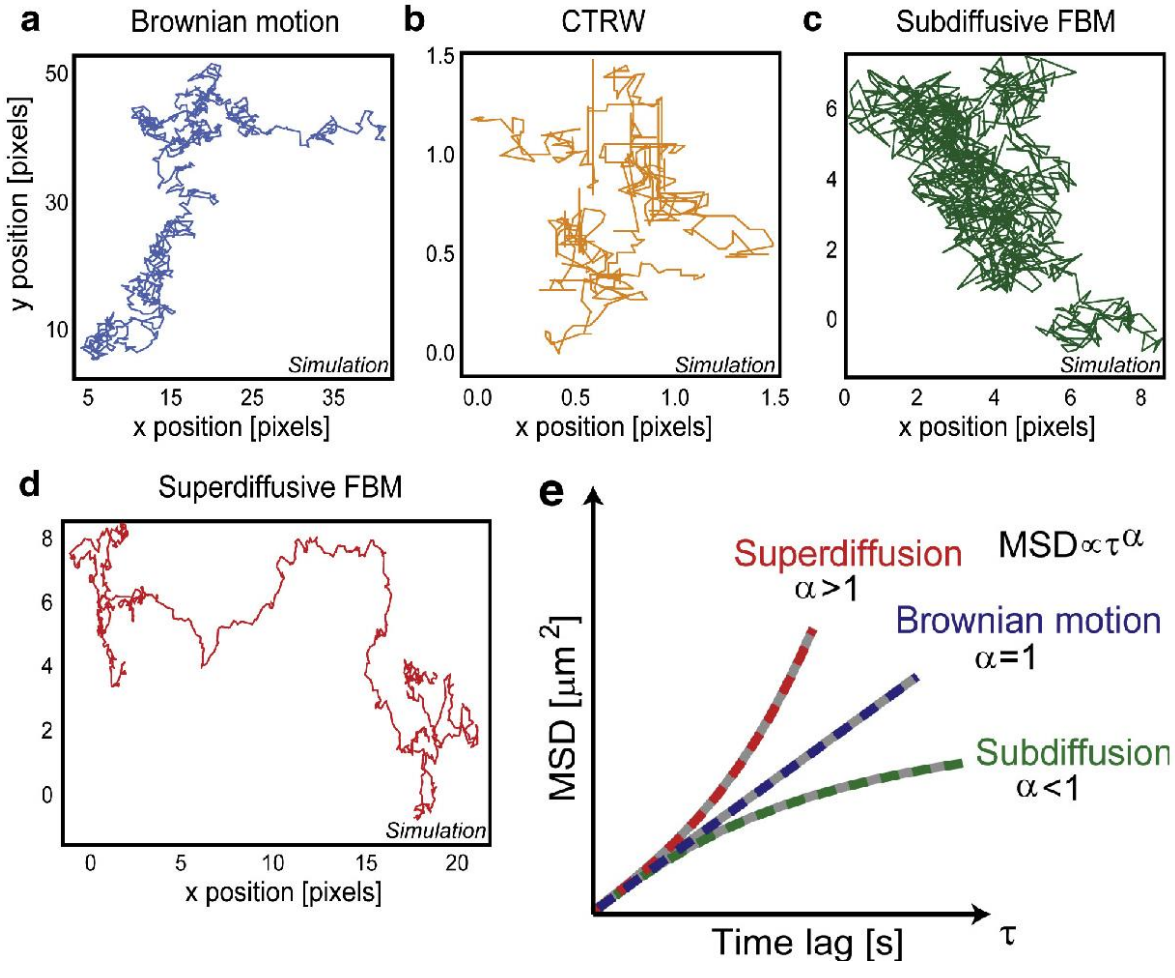

Figure 1.19 Types of diffusive motion (a) Brownian (b) Continous time random walk. (c) Subdiffusive (d) Superdiffusive.[112]

1.3.2.2 Change-point method

Change-point based methods is a powerful approach for elucidating mechanistic differences between experimental conditions. For example, in the analysis of protein-substrate interactions, elevated binding rates may suggest an increase in available binding sites, whereas reduced unbinding rates are indicative of enhanced complex stability [118].

Change-point detection methods identify these transitions by analyzing molecular trajectories within a sliding temporal window to find significant shifts in a locally computed metric, such as the slope of the mean squared displacement or the radius of gyration [119, 120]. While pronounced changes in motion can be identified using a simple threshold, a more rigorous strategy involves a statistical framework that quantifies the confidence level for each putative transition. A fundamental challenge in this approach is the inherent trade-off between detection sensitivity and specificity. Setting a high confidence threshold minimizes the detection of spurious, non-physical transitions but consequently increases the probability of failing to identify genuine transitions, which leads to an underestimation of their rates [121, 122]. Conversely, a low confidence threshold can result in the erroneous detection of transitions. Generally, change-point methodologies are most effective when applied to long trajectories containing hundreds of data points and exhibiting transition frequencies that are low relative to the analysis window size [123]. A principal advantage of these methods is their adaptability, as they do not presuppose a specific underlying model for the different types of motion. However, their reliance on user-specified tuning parameters remains a significant limitation.

1.3.2.3 Jump distance and HMM models

The creation of advanced computational tools, including Hidden Markov Models (HMMs) and machine learning algorithms to classify motion types and quantify state transitions has become a popular method for SPT (Figure 1.19). While MSD analysis remains a widely used and intuitive method for interpreting single-particle tracking data, it often fails to capture the full complexity of intracellular motion. MSD is limited in its ability to resolve transitions between different transport regimes that occur over time within a single trajectory. To overcome these limitations, HMMs offers a more sophisticated and statistically grounded framework. A HMM is a probabilistic model that describes a system which transitions between a finite set of hidden states over time [124]. Each hidden state corresponds to an observable output governed by a specific probability distribution. In the context of particle tracking, the hidden states represent distinct modes of motion (e.g., confined diffusion, free diffusion, active transport), and the observed outputs are the displacements between successive time points [122]. In the case of HMM, it is especially useful for detecting latent biological processes that cannot be directly observed from raw

position data alone. These may include switching between vesicle-associated movement and free cytosolic diffusion, or transitions between confined and actively transported states. The identification of discrete motility states and the dynamic switch between captures the stochastic nature of nanoparticle transport in the crowded and heterogeneous intracellular environment. The likelihood of a sequence of observed displacements is calculated by marginalizing over all possible hidden state sequences. This is typically done using the forward-backward algorithm, which computes the probability of each state at each point given the full observation sequence [124]. Parameter estimation (e.g., diffusion coefficients, velocities, transition rates) is achieved using algorithms such as Expectation-Maximization (EM) or Bayesian inference [125]. Similarly, machine learning algorithms can produce more accurate state transitions, however, understanding the framework behind these classifications can be limited by the black box problem [126].

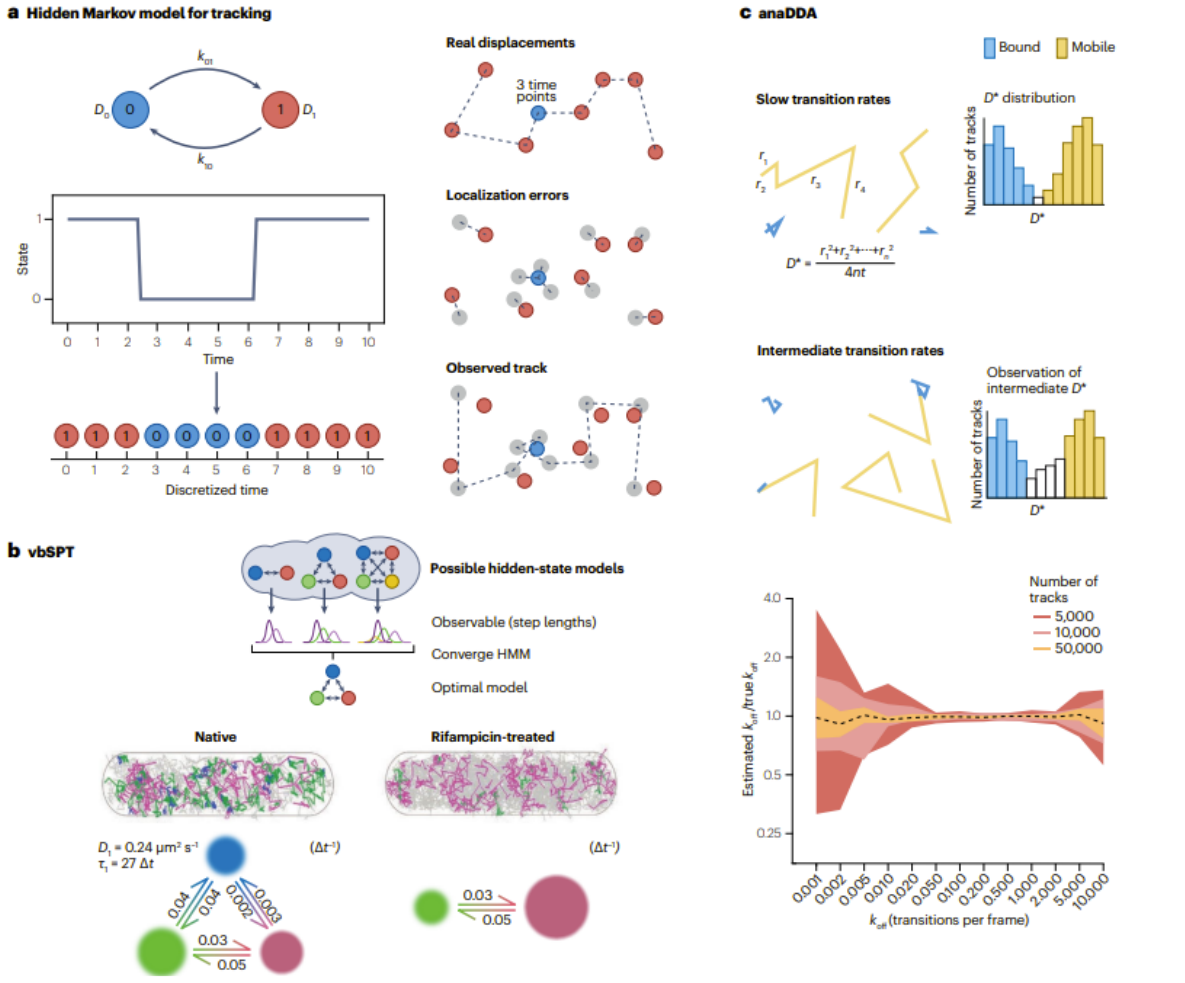

Figure 1.19 Jump distance-based methods for SPT. (a) Hidden Markov model. (b) vbSPT. (c) anaDNA.[108]

Nonetheless, the implementation of HMM poses several challenges. Accurate model fitting depends on sufficient trajectory length and quality, and short or noisy tracks may yield unreliable state assignments. Choosing the correct number of hidden states requires careful validation, as overfitting can produce spurious interpretations while underfitting can mask important biological phenomena [127]. Moreover, the computational cost of fitting HMMs to large datasets can become substantial, particularly when analyzing hundreds to thousands of trajectories [124]. Despite these limitations, HMM remains one of the most effective tools for dissecting complex intracellular transport dynamics. When used in conjunction with other analytical techniques and experimental insights, it provides a robust framework for understanding the stochastic and state-dependent behavior of nanoparticles in living systems.

1.3.3 Applications

Understanding the intracellular dynamics of nanoparticles is essential for the rational design and optimization of nanomaterials for biomedical applications. SPT provides a means of following the trajectory of individual nanoparticles with high spatial and temporal resolution. This approach allows researchers to dissect dynamic behaviors that would be obscured in ensemble-averaged measurements, revealing subpopulations of particles with distinct motion profiles. Applications of intracellular tracking include evaluating nanoparticle targeting, mapping vesicle transport pathways, assessing the impact of particle surface chemistry on cellular processing, and probing intracellular barriers that influence therapeutic efficacy.

1.3.3.1 Membrane Protein Diffusion

The lateral translocation of proteins within the plasma membrane is a biophysical process integral to numerous cellular phenomena, including signal transduction and intercellular communication. Membrane protein diffusion is the lateral movement of proteins within the fluid, two-dimensional environment of the cell's plasma membrane [128-130]. The mobility of membrane proteins is intricately modulated by a confluence of factors, including steric hindrance from macromolecular crowding, dynamic associations with other protein complexes, transient confinement within specialized membrane microdomains, and interactions with the underlying cytoskeletal meshwork [128]. These constraints collectively give rise to complex motional patterns, most notably anomalous subdiffusion,

where the mean squared displacement of a particle scales non-linearly with time, often due to transient trapping or caging effects [131, 132].

The methodology for studying membrane proteins using SPT typically involves the conjugation of a photostable fluorophore to the protein of interest, followed by time-lapse microscopy to record the molecule's position over time [133]. The sequential localization data are then algorithmically linked to reconstruct spatiotemporal trajectories. Afterwards, subsequent quantitative interrogation of these trajectories allows for the classification of motion types revealing the kinetic parameters of transitions between different diffusive states, such as bound versus unbound which decipher the underlying kinetics of molecular interactions directly within their native cellular environment.

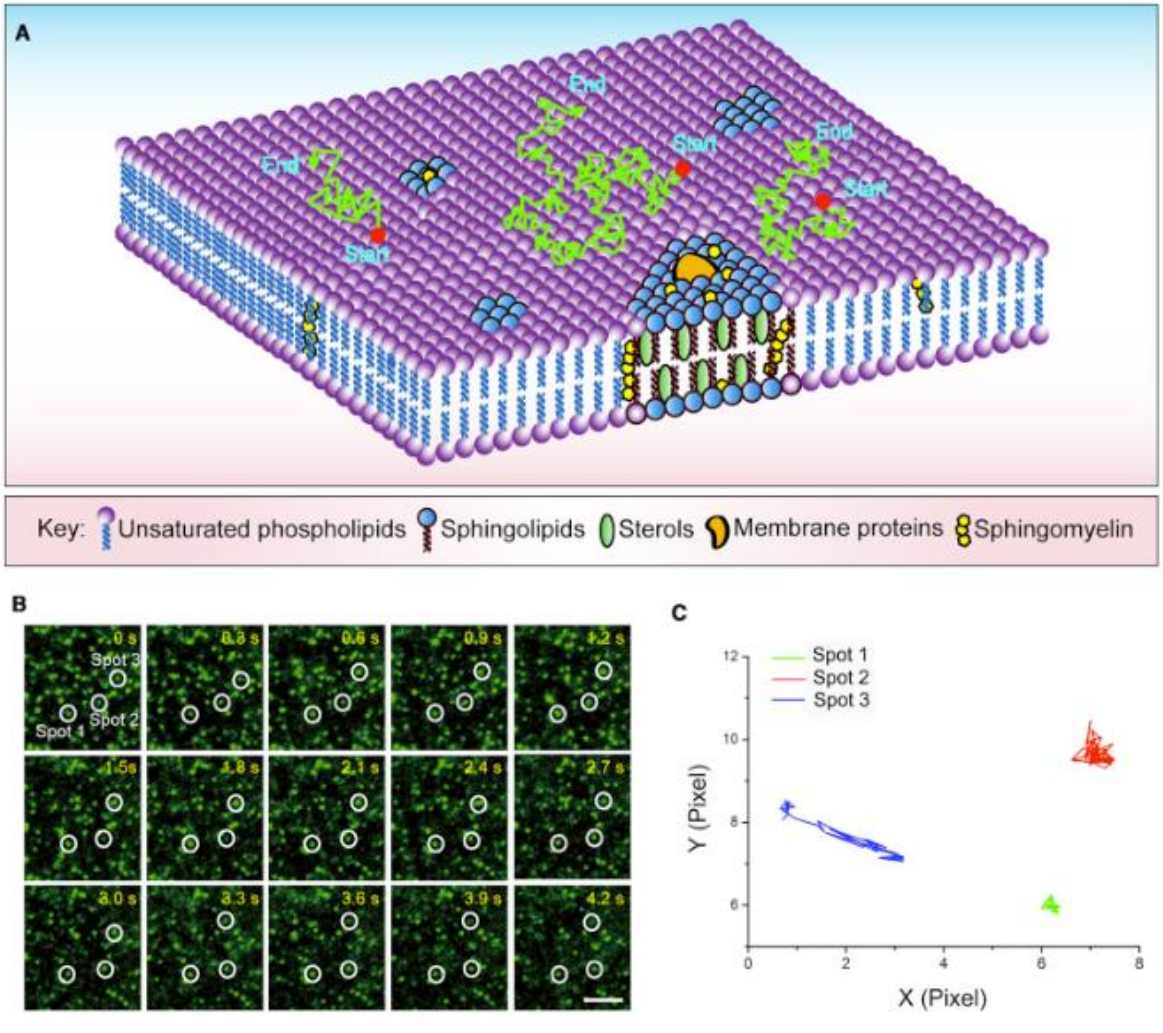

Figure 1.20 SPT for lipid membrane interactions. (a) Schematic illustration of SPT trajectories at a lipid bilayer. (b) Fluorescent spots on the lipid membrane (c) Coordination graph of single molecules.[134]

By tracking single molecules, SPT deconvolutes population averages to reveal co-existing subpopulations with distinct motional properties, such as immobile, confined, and freely diffusing fractions. This capability is crucial for discriminating between different mechanistic models, as multiple distinct biophysical scenarios can produce identical ensemble-averaged behavior. SPT allows for the direct characterization of transient events, such as a receptor entering and exiting a signaling microdomain, providing direct evidence for the "hop diffusion" model where proteins are temporarily corralled by cytoskeletal barriers [135, 136]. Furthermore, the collection of numerous trajectories enables the generation of high-resolution maps of the membrane's biophysical landscape, delineating domains of altered mobility or potential energy [137] (Figure 1.20). Consequently, SPT offers an unprecedented level of mechanistic resolution for investigating the dynamic architecture of the plasma membrane and its regulatory role in protein function.

1.3.3.2 DNA Transcription dynamics

SPT additionally offers a window into millisecond-scale events that constitute transcription initiation and regulation. By observing individual fluorescently labeled transcription factors (TF) or polymerases, single molecule transcription regulation can be observed at a millisecond-level [138, 139]. This approach makes it possible to quantitatively distinguish between the different motional states that define the target search process, as periods of rapid, free diffusion in the nucleoplasm can be clearly separated from segments of slower, constrained motion indicative of non-specific associations with DNA [140, 141]. Crucially,

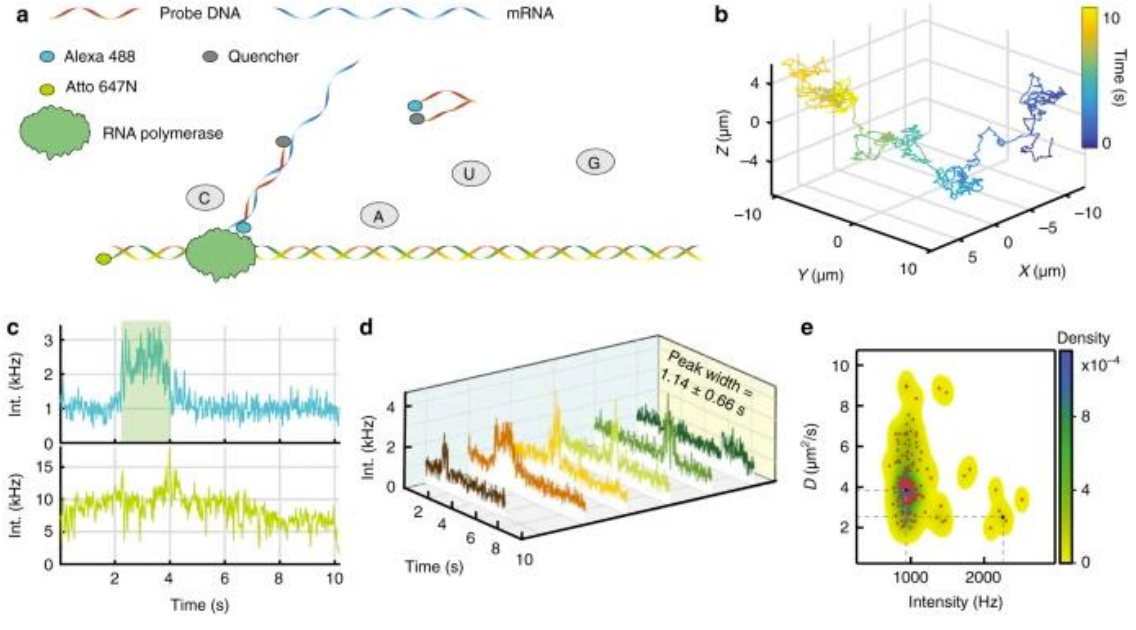

Figure 1.21 Real time tracking of dsDNA transcription (a) Schematic representation. (b) 3D trajectory of dsDNA (c) Intensity of transcription burst between dsDNA (bottom), ssDNA top. (d) Transcription bursts (e) Photon counts of the mRNA channel.[143]

SPT can capture the moment of specific binding, identifying molecules that become transiently immobile upon engaging their cognate DNA target [142]. The direct measurement of the duration and frequency of these key binding events provides a kinetic fingerprint of how these proteins navigate the complex nuclear landscape to execute their function. Furthermore, analysis of DNA transcription dynamics at a single molecular level via FISH can be achieved to observe binding between ssDNA and dsDNA through fluorescence bursts after quencher and fluorophore separation during transcription (Figure 1.21).

1.3.3.3 Cytoplasmic diffusion

The cytoplasmic diffusion of nanomaterials describes the movement of engineered particles, such as quantum dots or drug-delivery vehicles, through the cell's interior which have significant applications for the fields of nanotoxicology [144, 145]. The cytoplasm, which possess a crowded and viscoelastic medium, densely packed with organelles, protein complexes, and a meshwork of cytoskeletal filaments facilitates unique interactions with nanomaterials which can be described and detected via SPT [146-148]. The physical properties of this environment, which can exhibit glass-like characteristics, are actively modulated by the cell's metabolic state [149, 150]. Consequently, the transport of exogenous nanomaterials is often severely hindered , resulting in restricted and sub diffusive motion that reflects upon the physical characteristics present within a living cell [146].

The foremost benefit of using SPT for this purpose is its ability to perform spatially resolved mechanical measurements within a single, living cell, which is impossible with bulk methods that require cell lysis [117, 151]. For example, Zahid, et al. demonstrated differences in diffusive states across different nanoparticle surface modifications through single particle tracking [146]. Coating dependent behavior after osmotic pinosome lysis depicted different interactions between the cytoplasmic region of the cell and the surface of quantum dots (Figure 1.21). SPT can also generate high-resolution maps of the cytoplasm's

physical architecture, identifying regions of higher or lower restriction to movement, which is critical for understanding intracellular transport phenomena [152]. Furthermore, the technique is sensitive enough to detect non-thermal, active fluctuations driven by molecular motors, which contribute significantly to particle motion and reveal the cytoplasm as an active fluid rather than a passive one [153, 154].

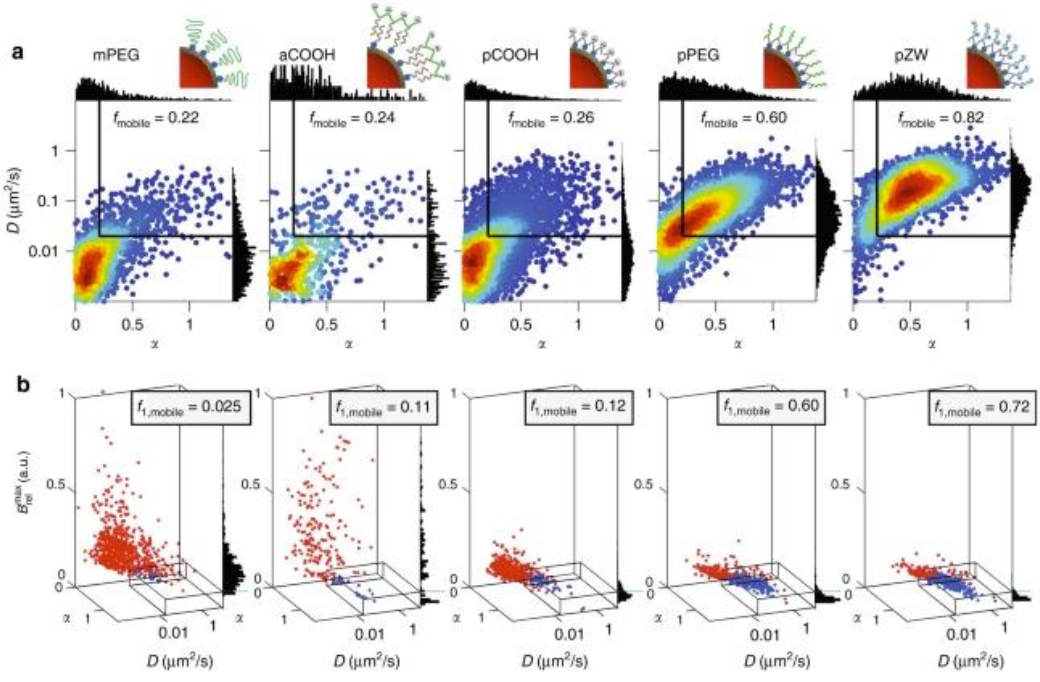

Figure 1.21 Intracellular dynamics and coating differences in quantum dots (a) Diffusion coefficient heat maps. (b) Diffusion coefficient compared to MSD slope α.[146]

1.3.3.4 Live cell intracellular dynamics

The successful application of nanotechnology in medicine hinges on understanding the live intracellular dynamics of nanomaterials. Once internalized, an engineered particle is separated from the typical cytoplasm and reserved within the endomembrane systems, where its fate is determined by a complex interplay of physical barriers and active biological processes [94, 155]. The nanoparticles are subject to constant interaction with cytoskeletal filaments, which is perpetually agitated by ATP-driven forces from molecular motors, creating a non-equilibrium setting that is fundamentally different from a passive fluid, which dictates its ultimate efficacy, localization or potential toxicity [156, 157].

SPT provides an unparalleled method for deciphering a nanoparticle's behavior in real-time as it traverses the cell's interior. Separate from cytoplasmic studies, which involve

nanoparticle escape from endosomal systems, this technique fundamentally observes different modes of transport at the single particle level. SPT can capture moments of sequestration, where a particle's movement abruptly ceases for a prolonged period, which may signify its entrapment within an endosome or lysosome for degradation [158, 159]. By dissecting the trajectory into these distinct behavioral states, SPT reveals the precise mechanisms governing a nanoparticle's intracellular trafficking. For example, DNA-decorated gold nanoparticles allowed dark-field microscopy, which enabled long term observation of gold nanoparticle localization, revealing that localization across different endosomal compartments was dependent on time exposed (Figure 1.22).

The critical contribution of SPT in this field lies in its power to inform the rational design and safety assessment of novel nanomaterials [160]. By directly visualizing how surface modifications alter a particle's mobility and cellular interactions, researchers can iteratively engineer nanocarriers that more effectively evade clearance mechanisms and reach their

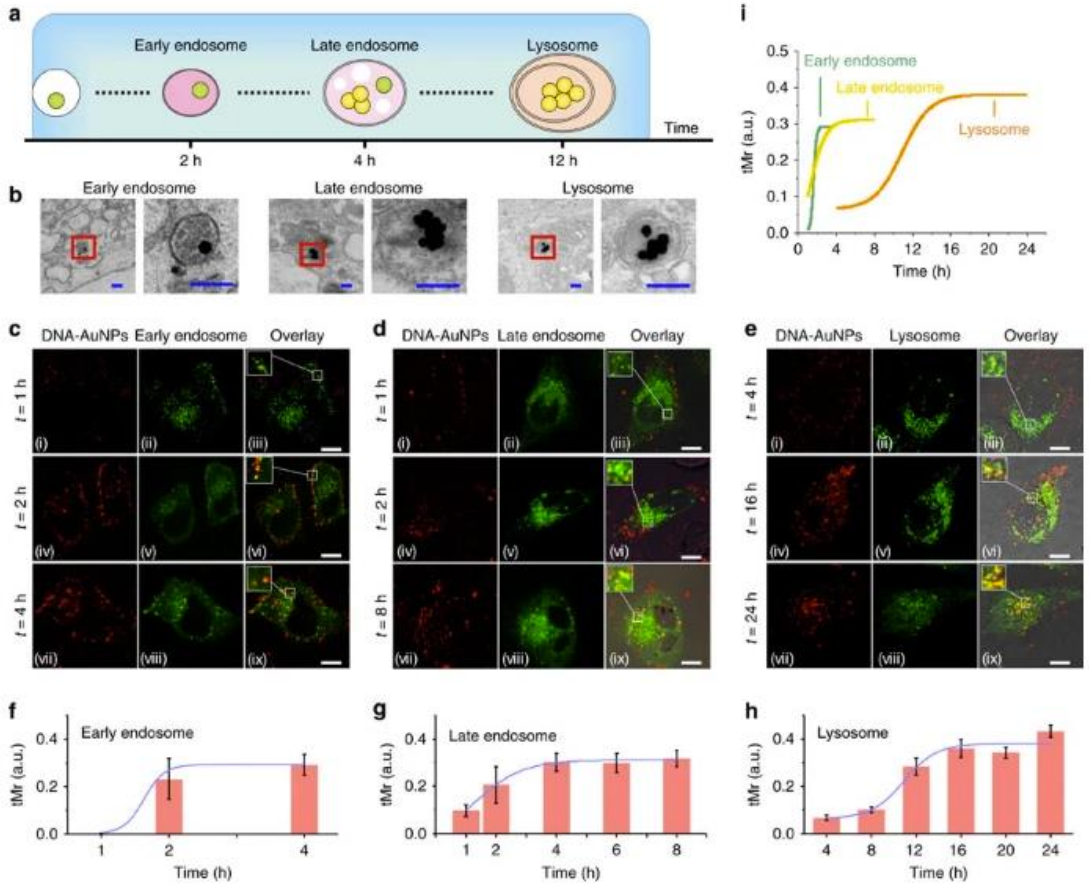

Figure 1.22 Live nanoparticle localization. (a)schematic representation. (b) TEM imaging (c) Early endosome colocalization. (d) Late endosome colocalization. (e) Lysosome colocalization. (f) Early endosome localization over time. (g) Late endosome localization over time. (h) Lysosome localization over time.[166]

intended subcellular targets [161-163]. This approach moves beyond static endpoint assays to provide dynamic, mechanistic feedback. Moreover, SPT serves as a sensitive tool for nanotoxicology by revealing aberrant particle behaviors, such as aggregation within the cytoplasm or disruption of normal organelle transport [164, 165]. Observing these events in live cells offers an early warning of potential cytotoxicity, enabling a more proactive approach to ensuring the biocompatibility of next-generation nanotechnologies.

1.4 Aims and Objectives

With the considerations previously discussed, this thesis will explore the intracellular dynamics and fates using lanthanide doped nanocrystals through the detection and quantification of vesicle dynamics to uncover the molecular mechanisms associated with the long-term distribution and fate of nanoparticles at a subcellular level. As such, the aims of this thesis are 1) The design, synthesis and optimization of up-conversion nanocrystals through lanthanide doping and surface modifications 2) The creation of a home-built microscopy system for optical nanoparticle characterization and cell imaging. 3) the analysis of nanoparticles and their interactions in a cellular environment, with focus on intracellular distribution and dynamics. These studies will demonstrate the plausible and immense potential of lanthanide nanocrystals as tools for multiplexed biological tracking, probing and for understanding the intracellular fate of nanoparticles as well as a potential method for studying long-term subcellular dynamics.

Firstly, the analysis of UCNPs with a focus on emitter and sensitizer concentration with ideal volumetric scaling will be explored. The optical properties of UCNPs without the consideration of surface defects through ideal volumetric scaling, as well as core-shell surface passivation will be observed to understand the intricate mechanism behind the energy transfer at a single nanoparticle level.

Subsequently, the development of a novel method for the detection and quantification of vesicle dynamics will be explored. Using advanced optical methods and novel luminescent nanomaterials, this project seeks to unravel how nanoparticle transportation can be used to explore the cargo dynamics within the cell. The research will offer new insights for future researchers to develop improved biomedical materials for subcellular targeting. Additionally, it provides a novel approach to studying cellular dysfunction at a molecular level through the detection and quantification of vesicle dynamics using luminescent up conversion nanomaterial.

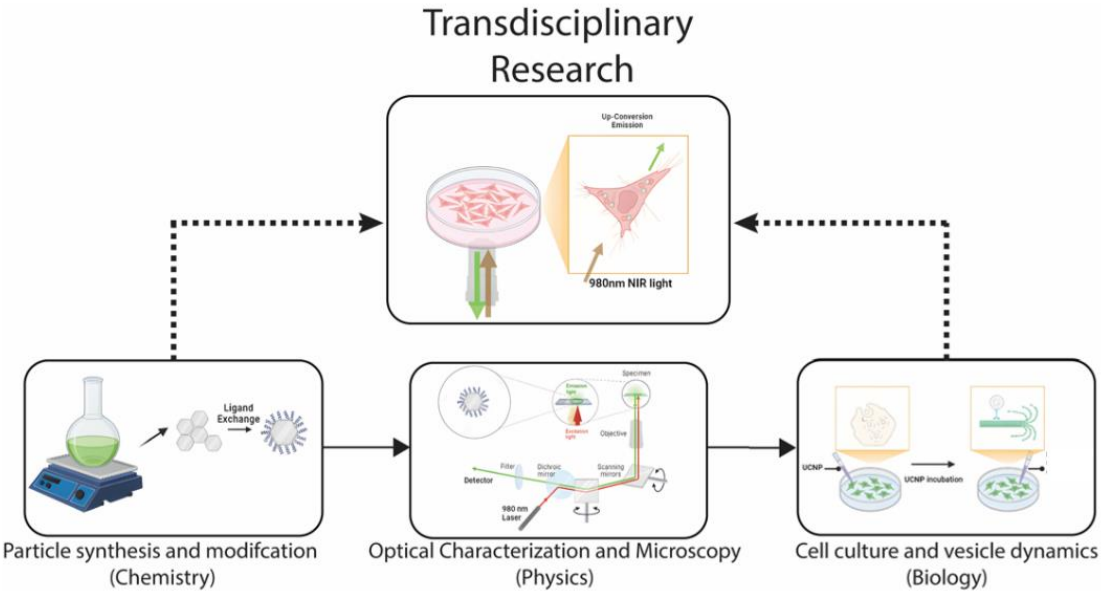

Figure 1.22 Schematic outline of thesis.

1.5 References

[1] Modena, M. M.;Rühle, B.;Burg, T. P.; Wuttke, S. Nanoparticle characterization: what to measure? (2019). *Advanced Materials*.**31**,1901556

[2] Davis, M. E.;Chen, Z.; Shin, D. M. Nanoparticle therapeutics: an emerging treatment modality for cancer (2008). *Nature reviews Drug discovery*.**7**,771-782

[3] Petros, R. A.; DeSimone, J. M. Strategies in the design of nanoparticles for therapeutic applications (2010). *Nature reviews Drug discovery*.**9**,615-627

[4] Mitchell, M. J.;Billingsley, M. M.;Haley, R. M.;Wechsler, M. E.;Peppas, N. A.; Langer, R. Engineering precision nanoparticles for drug delivery (2021). *Nature reviews drug discovery*.**20**,101-124

[5] Poon, W.;Kingston, B. R.;Ouyang, B.;Ngo, W.; Chan, W. C. A framework for designing delivery systems (2020). *Nature nanotechnology*.**15**,819-829

[6] Blanco, E.;Shen, H.; Ferrari, M. Principles of nanoparticle design for overcoming biological barriers to drug delivery (2015). *Nature biotechnology*.**33**,941-951

[7] Dawson, K. A.; Yan, Y. Current understanding of biological identity at the nanoscale and future prospects (2021). *Nature nanotechnology*.**16**,229-242

[8] Wilhelm, S.;Tavares, A. J.;Dai, Q.;Ohta, S.;Audet, J.;Dvorak, H. F.; Chan, W. C. Analysis of nanoparticle delivery to tumours (2016). *Nature reviews materials*.**1**,1-12

[9] Han, S.;Deng, R.;Xie, X.; Liu, X. Enhancing luminescence in lanthanide-doped upconversion nanoparticles (2014). *Angewandte Chemie International Edition*.**53**,11702-11715

[10] Wu, S.; Butt, H. J. Near-infrared-sensitive materials based on upconverting nanoparticles (2016). *Advanced Materials*.**28**,1208-1226

[11] Gu, Z.;Yan, L.;Tian, G.;Li, S.;Chai, Z.; Zhao, Y. Recent advances in design and fabrication of upconversion nanoparticles and their safe theranostic applications (2013). *Advanced Materials*.**25**,3758-3779

[12] Li, X.;Zhang, F.; Zhao, D. Highly efficient lanthanide upconverting nanomaterials: progresses and challenges (2013). *Nano Today*.**8**,643-676

[13] Matias, J.;Komolibus, K.;Kho, K.;Konugolu-Venkata-Sekar, S.; Andersson-Engels, S. Generalised analytical model of the transition power densities of the upconversion luminescence and quantum yield (2023). *Nanoscale Advances*.**5**,3279-3286

[14] Shin, S.;Lim, J. P.;Hong, Y. K.;Kyhm, J.;Hong, A. R.;Kang, G.;Ko, H.;Oh, S. J.; Jang, H. S. Multicolor Fine-Tunable Upconversion Luminescence from a Single Nanoparticle for Full-Color Displays with a Wide Color Gamut (2025). *Advanced Functional Materials*.**35**,2415687

[15] Zhou, B.;Shi, B.;Jin, D.; Liu, X. Controlling upconversion nanocrystals for emerging applications (2015). *Nature nanotechnology*.**10**,924-936

[16] Qin, X.;Liu, X.;Huang, W.;Bettinelli, M.; Liu, X. Lanthanide-activated phosphors based on 4f-5d optical transitions: theoretical and experimental aspects (2017). *Chemical reviews*.**117**,4488-4527

[17] Li, X.;Zhang, F.; Zhao, D. Lab on upconversion nanoparticles: optical properties and applications engineering via designed nanostructure (2015). *Chemical Society Reviews*.**44**,1346-1378

[18] Sun, Q.-C.;Ding, Y. C.;Sagar, D. M.; Nagpal, P. Photon upconversion towards applications in energy conversion and bioimaging (2017). *Progress in Surface Science*.**92**,281-316

[19] Chen, G.;Qiu, H.;Prasad, P. N.; Chen, X. Upconversion nanoparticles: design, nanochemistry, and applications in theranostics (2014). *Chemical reviews*.**114**,5161-5214

[20] Hu, M.;Ma, D.;Liu, C.;Wang, J.;Zhang, Z.; Meng, L. Intense white emission from a single-upconversion nanoparticle and tunable emission colour with laser power (2016). *Journal of Materials Chemistry C*.**4**,6975-6981

[21] Zhong, Y.;Rostami, I.;Wang, Z.;Dai, H.; Hu, Z. Energy migration engineering of bright rare-earth upconversion nanoparticles for excitation by light-emitting diodes (2015). *Advanced Materials*.**27**,6418-6422

[22] Zeng, S.;Yi, Z.;Lu, W.;Qian, C.;Wang, H.;Rao, L.;Zeng, T.;Liu, H.;Liu, H.; Fei, B. Simultaneous realization of phase/size manipulation, upconversion luminescence enhancement, and blood vessel imaging in multifunctional nanoprobes through transition metal Mn2+ doping (2014). *Advanced Functional Materials*.**24**,4051-4059

[23] Szalkowski, M.;Kotulska, A.;Dudek, M.;Korczak, Z.;Majak, M.;Marciniak, L.;Misiak, M.;Prorok, K.;Skripka, A.; Schuck, P. J. Advances in the photon avalanche luminescence of inorganic lanthanide-doped nanomaterials (2025). *Chemical Society Reviews*.

[24] Liang, Y.;Zhu, Z.;Qiao, S.;Guo, X.;Pu, R.;Tang, H.;Liu, H.;Dong, H.;Peng, T.; Sun, L.-D. Migrating photon avalanche in different emitters at the nanoscale enables 46th-order optical nonlinearity (2022). *Nature Nanotechnology*.**17**,524-530

[25] Lee, C.;Xu, E. Z.;Liu, Y.;Teitelboim, A.;Yao, K.;Fernandez-Bravo, A.;Kotulska, A. M.;Nam, S. H.;Suh, Y. D.; Bednarkiewicz, A. Giant nonlinear optical responses from photon-avalanching nanoparticles (2021). *Nature*.**589**,230-235

[26] Fu, X.;Fu, S.;Lu, Q.;Zhang, J.;Wan, P.;Liu, J.;Zhang, Y.;Chen, C.-H.;Li, W.; Wang, H. Excitation energy mediated cross-relaxation for tunable upconversion luminescence from a single lanthanide ion (2022). *Nature Communications*.**13**,4741

[27] Zhan, Q.;Liu, H.;Wang, B.;Wu, Q.;Pu, R.;Zhou, C.;Huang, B.;Peng, X.;Ågren, H.; He, S. Achieving high-efficiency emission depletion nanoscopy by employing cross relaxation in upconversion nanoparticles (2017). *Nature Communications*.**8**,1058

[28] Liu, Y.;Lu, Y.;Yang, X.;Zheng, X.;Wen, S.;Wang, F.;Vidal, X.;Zhao, J.;Liu, D.; Zhou, Z. Amplified stimulated emission in upconversion nanoparticles for super-resolution nanoscopy (2017). *Nature*.**543**,229-233

[29] Wiesholler, L. M.;Frenzel, F.;Grauel, B.;Würth, C.;Resch-Genger, U.; Hirsch, T. Yb, Nd, Er-doped upconversion nanoparticles: 980 nm versus 808 nm excitation (2019). *Nanoscale*.**11**,13440-13449

[30] Zhong, Y.;Tian, G.;Gu, Z.;Yang, Y.;Gu, L.;Zhao, Y.;Ma, Y.; Yao, J. Elimination of photon quenching by a transition layer to fabricate a quenching-shield sandwich structure for 800 nm excited upconversion luminescence of Nd3+-sensitized nanoparticles (2014). *Advanced materials*.**26**,2831-2837

[31] Chen, B.; Wang, F. Combating concentration quenching in upconversion nanoparticles (2019). *Accounts of Chemical Research*.**53**,358-367

[32] Ming, J.;Chen, Y.;Miao, H.;Fan, Y.;Wang, S.;Chen, Z.;Guo, Z.;Guo, Z.;Qi, L.; Wang, X. High-brightness transition metal-sensitized lanthanide near-infrared luminescent nanoparticles (2024). *Nature Photonics*.**18**,1254-1262

[33] Lu, Y.;Zhao, J.;Zhang, R.;Liu, Y.;Liu, D.;Goldys, E. M.;Yang, X.;Xi, P.;Sunna, A.; Lu, J. Tunable lifetime multiplexing using luminescent nanocrystals (2014). *Nature Photonics*.**8**,32-36

[34] Wang, X.;Valiev, R. R.;Ohulchanskyy, T. Y.;Ågren, H.;Yang, C.; Chen, G. Dye-sensitized lanthanide-doped upconversion nanoparticles (2017). *Chemical Society Reviews*.**46**,4150-4167

[35] Huang, F.;Labrador-Paez, L.;Ågren, H.;Wang, L.;Zhang, J.;Pu, R.;Zhan, Q.;Widengren, J.; Liu, H. Transient energy trapping as a size-conserving surface passivation strategy for producing bright ultrasmall upconversion nanoprobes (2023). *Nano Energy*.**105**,108015

[36] Gargas, D. J.;Chan, E. M.;Ostrowski, A. D.;Aloni, S.;Altoe, M. V. P.;Barnard, E. S.;Sanii, B.;Urban, J. J.;Milliron, D. J.; Cohen, B. E. Engineering bright sub-10-nm upconverting nanocrystals for single-molecule imaging (2014). *Nature nanotechnology*.**9**,300-305

[37] Krasley, A. T.;Li, E.;Galeana, J. M.;Bulumulla, C.;Beyene, A. G.; Demirer, G. S. Carbon nanomaterial fluorescent probes and their biological applications (2024). *Chemical Reviews*.**124**,3085-3185

[38] Ravelli, D.;Protti, S.; Fagnoni, M. Carbon–carbon bond forming reactions via photogenerated intermediates (2016). *Chemical reviews*.**116**,9850-9913

[39] Demchenko, A. P. Photobleaching of organic fluorophores: quantitative characterization, mechanisms, protection (2020). *Methods and applications in fluorescence*.**8**,022001

[40] Efros, A. L.; Nesbitt, D. J. Origin and control of blinking in quantum dots (2016). *Nature nanotechnology*.**11**,661-671

[41] Huang, B.;Dong, H.;Wong, K.-L.;Sun, L.-D.; Yan, C.-H. Fundamental view of electronic structures of β-NaYF4, β-NaGdF4, and β-NaLuF4 (2016). *The Journal of Physical Chemistry C*.**120**,18858-18870

[42] Liao, J.;Zhou, J.;Song, Y.;Liu, B.;Chen, Y.;Wang, F.;Chen, C.;Lin, J.;Chen, X.; Lu, J. Preselectable optical fingerprints of heterogeneous upconversion nanoparticles (2021). *Nano Letters*.**21**,7659-7668

[43] Zhou, J.;Wen, S.;Liao, J.;Clarke, C.;Tawfik, S. A.;Ren, W.;Mi, C.;Wang, F.; Jin, D. Activation of the surface dark-layer to enhance upconversion in a thermal field (2018). *Nature Photonics*.**12**,154-158

[44] Johnson, L.; Guggenheim, H. Laser emission at 3 μ from Dy3+ in BaY2F8 (1973). *Applied Physics Letters*.**23**,96-98

[45] Maldovan, M. Phonon wave interference and thermal bandgap materials (2015). *Nature materials*.**14**,667-674

[46] Peng, C. S.;Zhang, Y.;Liu, Q.;Marti, G. E.;Huang, Y.-W. A.;Suedhof, T. C.;Cui, B.; Chu, S. Nanometer-resolution tracking of single cargo reveals dynein motor mechanisms (2025). *Nature Chemical Biology*.**21**,648-656

[47] Quintanilla, M.;Hemmer, E.;Marques-Hueso, J.;Rohani, S.;Lucchini, G.;Wang, M.;Zamani, R. R.;Roddatis, V.;Speghini, A.; Richards, B. S. Cubic versus hexagonal–phase, size and morphology effects on the photoluminescence quantum yield of NaGdF 4: Er 3+/Yb 3+ upconverting nanoparticles (2022). *Nanoscale*.**14**,1492-1504

[48] Ansari, A. A.;Khan, M. M.;Singh, B. P.; Parchur, A. K. Upconversion nanoparticles: influence of the host lattices on crystallographic and luminescent properties (2023). *Journal of Materials Science: Materials in Electronics*.**34**,1625

[49] Schroter, A.; Hirsch, T. Control of luminescence and interfacial properties as perspective for upconversion nanoparticles (2024). *Small*.**20**,2306042

[50] Zheng, W.;Huang, P.;Tu, D.;Ma, E.;Zhu, H.; Chen, X. Lanthanide-doped upconversion nano-bioprobes: electronic structures, optical properties, and biodetection (2015). *Chemical Society Reviews*.**44**,1379-1415

[51] Liu, G. Advances in the theoretical understanding of photon upconversion in rare-earth activated nanophosphors (2015). *Chemical Society Reviews*.**44**,1635-1652

[52] Naccache, R.;Yu, Q.; Capobianco, J. A. The fluoride host: nucleation, growth, and upconversion of lanthanide-doped nanoparticles (2015). *Advanced Optical Materials*.**3**,482-509

[53] Luo, Y.-H.;Wang, J.-W.;Wang, W.;He, X.-T.;Hong, D.-L.;Chen, C.;Xu, T.;Shao, Q.; Sun, B.-W. Bidirectional Photoswitching via Alternating NIR and UV Irradiation on a Core–Shell UCNP–SCO Nanosphere (2018). *Acs Applied Materials & Interfaces*.**10**,16666-16673

[54] Chen, J.;Liu, C.;Xi, S.;Tan, S.;He, Q.;Liang, L.; Liu, X. Optical nonlinearities in excess of 500 through sublattice reconstruction (2025). *Nature*. 1-6

[55] Feng, Y.;Li, Z.;Li, Q.;Yuan, J.;Tu, L.;Ning, L.; Zhang, H. Internal OH− induced cascade quenching of upconversion luminescence in NaYF4: Yb/Er nanocrystals (2021). *Light: Science & Applications*.**10**,105

[56] Bian, W.;Lin, Y.;Wang, T.;Yu, X.;Qiu, J.;Zhou, M.;Luo, H.;Yu, S. F.; Xu, X. Direct identification of surface defects and their influence on the optical characteristics of upconversion nanoparticles (2018). *ACS nano*.**12**,3623-3628

[57] Huang, F.;Bagheri, N.;Wang, L.;Ågren, H.;Zhang, J.;Pu, R.;Zhan, Q.;Jing, Y.;Xu, W.; Widengren, J. Suppression of cation intermixing highly boosts the performance of core–shell lanthanide upconversion nanoparticles (2023). *Journal of the American Chemical Society*.**145**,17621-17631

[58] Wang, X.;Yan, L.;Liu, S.;Zhang, P.;Huang, R.; Zhou, B. Enhancing energy migration upconversion through a migratory interlayer in the core–shell–shell nanostructure towards latent fingerprinting (2020). *Nanoscale*.**12**,18807-18814

[59] Chaudhary, B.;Kshetri, Y. K.; Kim, T.-H. Photocatalysis, Anti-counterfeiting and Optical Thermometry Applications of Upconversion Nanoparticles. In *Upconversion Nanoparticles (UCNPs) for Functional Applications*. Springer, 2023; pp 193-220.

[60] Ren, W.;Lin, G.;Clarke, C.;Zhou, J.; Jin, D. Optical nanomaterials and enabling technologies for high-security-level anticounterfeiting (2020). *Advanced Materials*.**32**,1901430

[61] Wang, Z.;Zhao, J.;Xu, X.;Guo, L.;Xu, L.;Sun, M.;Hu, S.;Kuang, H.;Xu, C.; Li, A. An overview for the nanoparticles-based quantitative lateral flow assay (2022). *Small Methods*.**6**,2101143

[62] Hao, L.;Chen, J.;Li, Q.;Zhang, D.;Huang, Q.;Zhang, H.; Li, S. Recent advances in low-background luminescent nanomaterials-enhanced lateral flow assays for clinical diagnosis (2025). *Interdisciplinary Medicine*.**3**,e20240078

[63] Hou, F.;Sun, S.;Abdullah, S. W.;Tang, Y.;Li, X.; Guo, H. The application of nanoparticles in point-of-care testing (POCT) immunoassays (2023). *Analytical Methods*.**15**,2154-2180

[64] Hlaváček, A.;Farka, Z.;Mickert, M. J.;Kostiv, U.;Brandmeier, J. C.;Horák, D.;Skládal, P.;Foret, F.; Gorris, H. H. Bioconjugates of photon-upconversion nanoparticles for cancer biomarker detection and imaging (2022). *Nature Protocols*.**17**,1028-1072

[65] Ai, Z.;Cai, H.;Liu, C.;Zhao, Y.;Fu, Q.;Fan, N.;Li, Y.;Li, S.;Zhou, S.; Li, C. Ultrasensitive Bi-Mode Lateral-Flow Assay via UCNPs-Based Host-Guest Assembly of Fluorescent-Colorimetric Nanoparticles (2025). *Small*.**21**,2410947

[66] Jin, B.;Yang, Y.;He, R.;Park, Y. I.;Lee, A.;Bai, D.;Li, F.;Lu, T. J.;Xu, F.; Lin, M. Lateral flow aptamer assay integrated smartphone-based portable device for simultaneous detection of multiple targets using upconversion nanoparticles (2018). *Sensors and Actuators B: Chemical*.**276**,48-56
[67] Wang, W.;Ye, Z.;Ma, X.; Guo, J. Smartphone enabled upconversion nanoparticle-based lateral flow strip for ultra-low concentration of methamphetamine detection (2022). *Sensors and Actuators B: Chemical*.**370**,132421
[68] Gong, Y.;Zheng, Y.;Jin, B.;You, M.;Wang, J.;Li, X.;Lin, M.;Xu, F.; Li, F. A portable and universal upconversion nanoparticle-based lateral flow assay platform for point-of-care testing (2019). *Talanta*.**201**,126-133
[69] Zhang, L.;Wen, S.;Khan, J. U.;Liu, Y.;Maddahfar, M.;Zhou, J.; Jin, D. Ultrasensitive Rapid Antigen Test by Geometric Lateral Flow Assays and Highly Doped Upconversion Nanoparticles (2024). *Analytical Chemistry*.**96**,16581-16589
[70] Castano, A. P.;Mroz, P.; Hamblin, M. R. Photodynamic therapy and anti-tumour immunity (2006). *Nature Reviews Cancer*.**6**,535-545
[71] Luo, Z.;Mao, D.;Li, X.;Luo, J.;Gong, C.; Liu, X. Lanthanide-based nanoparticles for cancer phototherapy (2024). *Coordination Chemistry Reviews*.**508**,215773
[72] Hu, J.;Tang, Y. a.;Elmenoufy, A. H.;Xu, H.;Cheng, Z.; Yang, X. Nanocomposite-based photodynamic therapy strategies for deep tumor treatment (2015). *Small*.**11**,5860-5887
[73] Liu, Y.;Meng, X.; Bu, W. Upconversion-based photodynamic cancer therapy (2019). *Coordination chemistry reviews*.**379**,82-98
[74] Lu, S.;Ke, J.;Li, X.;Tu, D.; Chen, X. Luminescent nano-bioprobes based on NIR dye/lanthanide nanoparticle composites (2021). *Aggregate*.**2**,e59
[75] Zhou, Z.;Song, J.;Nie, L.; Chen, X. Reactive oxygen species generating systems meeting challenges of photodynamic cancer therapy (2016). *Chemical society reviews*.**45**,6597-6626
[76] Grüner, M. C.;Arai, M. S.;Carreira, M.;Inada, N.; de Camargo, A. S. Functionalizing the mesoporous silica shell of upconversion nanoparticles to enhance bacterial targeting and killing via photosensitizer-induced antimicrobial photodynamic therapy (2018). *ACS Applied Bio Materials*.**1**,1028-1036
[77] Guan, Y.;Lu, H.;Li, W.;Zheng, Y.;Jiang, Z.;Zou, J.; Gao, H. Near-infrared triggered upconversion polymeric nanoparticles based on aggregation-induced emission and mitochondria targeting for photodynamic cancer therapy (2017). *ACS applied materials & interfaces*.**9**,26731-26739
[78] Yang, S.;Li, N.;Liu, Z.;Sha, W.;Chen, D.;Xu, Q.; Lu, J. Amphiphilic copolymer coated upconversion nanoparticles for near-infrared light-triggered dual anticancer treatment (2014). *Nanoscale*.**6**,14903-14910
[79] Chen, C.;Wang, F.;Wen, S.;Su, Q. P.;Wu, M. C.;Liu, Y.;Wang, B.;Li, D.;Shan, X.; Kianinia, M. Multi-photon near-infrared emission saturation nanoscopy using upconversion nanoparticles (2018). *Nature communications*.**9**,3290
[80] Lee, C.;Xu, E. Z.;Kwock, K. W.;Teitelboim, A.;Liu, Y.;Park, H. S.;Ursprung, B.;Ziffer, M. E.;Karube, Y.; Fardian-Melamed, N. Indefinite and bidirectional near-infrared nanocrystal photoswitching (2023). *Nature*.**618**,951-958
[81] Lamon, S.;Yu, H.;Zhang, Q.; Gu, M. Lanthanide ion-doped upconversion nanoparticles for low-energy super-resolution applications (2024). *Light: Science & Applications*.**13**,252
[82] Ou, X.;Qin, X.;Huang, B.;Zan, J.;Wu, Q.;Hong, Z.;Xie, L.;Bian, H.;Yi, Z.; Chen, X. High-resolution X-ray luminescence extension imaging (2021). *Nature*.**590**,410-415
[83] Liang, L.;Chen, J.;Shao, K.;Qin, X.;Pan, Z.; Liu, X. Controlling persistent luminescence in nanocrystalline phosphors (2023). *Nature Materials*.**22**,289-304
[84] Wei, Y.;Gong, C.;Zhao, M.;Zhang, L.;Yang, S.;Li, P.;Ding, Z.;Yuan, Q.; Yang, Y. Recent progress in synthesis of lanthanide-based persistent luminescence nanoparticles (2022). *Journal of Rare Earths*.**40**,1333-1342
[85] Qin, X.;Wang, J.; Yuan, Q. Synthesis and biomedical applications of lanthanides-doped persistent luminescence phosphors with NIR emissions (2020). *Frontiers in chemistry*.**8**,608578
[86] Ye, H.;Li, Y.;Chen, X.;Du, W.;Song, L.;Chen, Y.;Zhan, Q.; Wei, W. Current Developments in Emerging Lanthanide-Doped Persistent Luminescent Scintillators and Their Applications (2024). *Chemistry–A European Journal*.**30**,e202303661
[87] Qiu, X.;Zhu, X.;Xu, M.;Yuan, W.;Feng, W.; Li, F. Hybrid nanoclusters for near-infrared to near-infrared upconverted persistent luminescence bioimaging (2017). *ACS Applied Materials & Interfaces*.**9**,32583-32590
[88] Rao, L.;Lu, W.;Zeng, T.;Yi, Z.;Wang, H.;Liu, H.; Zeng, S. Sub-10 nm BaLaF 5: Mn/Yb/Er nanoprobes for dual-modal synergistic in vivo upconversion luminescence and X-ray bioimaging (2014). *Journal of Materials Chemistry B*.**2**,6527-6533
[89] Abdukayum, A.;Yang, C.-X.;Zhao, Q.;Chen, J.-T.;Dong, L.-X.; Yan, X.-P. Gadolinium complexes functionalized persistent luminescent nanoparticles as a multimodal probe for near-infrared luminescence and magnetic resonance imaging in vivo (2014). *Analytical chemistry*.**86**,4096-4101
[90] Ghosh, S. K.; Pal, T. Interparticle coupling effect on the surface plasmon resonance of gold nanoparticles: from theory to applications (2007). *Chemical reviews*.**107**,4797-4862
[91] Zhu, S.;Song, Y.;Zhao, X.;Shao, J.;Zhang, J.; Yang, B. The photoluminescence mechanism in carbon dots (graphene quantum dots, carbon nanodots, and polymer dots): current state and future perspective (2015). *Nano research*.**8**,355-381
[92] Luo, D.;Yan, C.; Wang, T. Interparticle forces underlying nanoparticle self-assemblies (2015). *Small*.**11**,5984-6008
[93] Silvera Batista, C. A.;Larson, R. G.; Kotov, N. A. Nonadditivity of nanoparticle interactions (2015). *Science*.**350**,1242477
[94] Rennick, J. J.;Johnston, A. P.; Parton, R. G. Key principles and methods for studying the endocytosis of biological and nanoparticle therapeutics (2021). *Nature nanotechnology*.**16**,266-276
[95] Iannotta, D.;A, A.;Kijas, A. W.;Rowan, A. E.; Wolfram, J. Entry and exit of extracellular vesicles to and from the blood circulation (2024). *Nature nanotechnology*.**19**,13-20
[96] Nel, A. E.;Mädler, L.;Velegol, D.;Xia, T.;Hoek, E. M.;Somasundaran, P.;Klaessig, F.;Castranova, V.; Thompson, M. Understanding biophysicochemical interactions at the nano–bio interface (2009). *Nature materials*.**8**,543-557
[97] Rees, P.;Wills, J. W.;Brown, M. R.;Barnes, C. M.; Summers, H. D. The origin of heterogeneous nanoparticle uptake by cells (2019). *Nature communications*.**10**,2341
[98] Song, E.;Gaudin, A.;King, A. R.;Seo, Y.-E.;Suh, H.-W.;Deng, Y.;Cui, J.;Tietjen, G. T.;Huttner, A.; Saltzman, W. M. Surface chemistry governs cellular tropism of nanoparticles in the brain (2017). *Nature communications*.**8**,15322
[99] Jiang, W.;Kim, B. Y.;Rutka, J. T.; Chan, W. C. Nanoparticle-mediated cellular response is size-dependent (2008). *Nature nanotechnology*.**3**,145-150

[100] Verma, A.;Uzun, O.;Hu, Y.;Hu, Y.;Han, H.-S.;Watson, N.;Chen, S.;Irvine, D. J.; Stellacci, F. Surface-structure-regulated cell-membrane penetration by monolayer-protected nanoparticles (2008). *Nature materials*.**7**,588-595
[101] Saminathan, A.;Zajac, M.;Anees, P.; Krishnan, Y. Organelle-level precision with next-generation targeting technologies (2022). *Nature Reviews Materials*.**7**,355-371
[102] Bath, J.; Turberfield, A. J. DNA nanomachines (2007). *Nature nanotechnology*.**2**,275-284
[103] Sweetlove, L. J.; Fernie, A. R. The role of dynamic enzyme assemblies and substrate channelling in metabolic regulation (2018). *Nature communications*.**9**,2136
[104] Bhatia, D.;Arumugam, S.;Nasilowski, M.;Joshi, H.;Wunder, C.;Chambon, V.;Prakash, V.;Grazon, C.;Nadal, B.; Maiti, P. K. Quantum dot-loaded monofunctionalized DNA icosahedra for single-particle tracking of endocytic pathways (2016). *Nature nanotechnology*.**11**,1112-1119
[105] Niederauer, C.;Nguyen, C.;Wang-Henderson, M.;Stein, J.;Strauss, S.;Cumberworth, A.;Stehr, F.;Jungmann, R.;Schwille, P.; Ganzinger, K. A. Dual-color DNA-PAINT single-particle tracking enables extended studies of membrane protein interactions (2023). *Nature Communications*.**14**,4345
[106] Shen, H.;Tauzin, L. J.;Baiyasi, R.;Wang, W.;Moringo, N.;Shuang, B.; Landes, C. F. Single particle tracking: from theory to biophysical applications (2017). *Chemical reviews*.**117**,7331-7376
[107] Van Heerden, B.;Vickers, N. A.;Krüger, T. P.; Andersson, S. B. Real-Time Feedback-Driven Single-Particle Tracking: A Survey and Perspective (2022). *Small*.**18**,2107024
[108] Simon, F.;Weiss, L. E.; Van Teeffelen, S. A guide to single-particle tracking (2024). *Nature Reviews Methods Primers*.**4**,66
[109] Levi, V.; Gratton, E. Exploring dynamics in living cells by tracking single particles (2007). *Cell biochemistry and biophysics*.**48**,1-15
[110] Ruthardt, N.;Lamb, D. C.; Bräuchle, C. Single-particle tracking as a quantitative microscopy-based approach to unravel cell entry mechanisms of viruses and pharmaceutical nanoparticles (2011). *Molecular therapy*.**19**,1199-1211
[111] Wang, W.; Tao, N. Detection, counting, and imaging of single nanoparticles (2014). *Analytical chemistry*.**86**,2-14
[112] Granik, N.;Weiss, L. E.;Nehme, E.;Levin, M.;Chein, M.;Perlson, E.;Roichman, Y.; Shechtman, Y. Single-particle diffusion characterization by deep learning (2019). *Biophysical journal*.**117**,185-192
[113] Gal, N.;Lechtman-Goldstein, D.; Weihs, D. Particle tracking in living cells: a review of the mean square displacement method and beyond (2013). *Rheologica Acta*.**52**,425-443
[114] Zhang, M.-L.;Ti, H.-Y.;Wang, P.-Y.; Li, H. Intracellular transport dynamics revealed by single-particle tracking (2021). *Biophysics Reports*.**7**,413
[115] Ma, Y.;Wang, X.;Liu, H.;Wei, L.; Xiao, L. Recent advances in optical microscopic methods for single-particle tracking in biological samples (2019). *Analytical and bioanalytical chemistry*.**411**,4445-4463
[116] Waigh, T. A.; Korabel, N. Heterogeneous anomalous transport in cellular and molecular biology (2023). *Reports on Progress in Physics*.**86**,126601
[117] Wirtz, D. Particle-tracking microrheology of living cells: principles and applications (2009). *Annual review of biophysics*.**38**,301-326
[118] Shukron, O.;Seeber, A.;Amitai, A.; Holcman, D. Advances using single-particle trajectories to reconstruct chromatin organization and dynamics (2019). *Trends in Genetics*.**35**,685-705
[119] Saxton, M. J. Single-Particle Tracking Analysis using the Radius of Gyration Tensor, Revisited (2016). *Biophysical Journal*.**110**,487a
[120] Schirripa Spagnolo, C.; Luin, S. Trajectory analysis in single-particle tracking: From mean squared displacement to machine learning approaches (2024). *International Journal of Molecular Sciences*.**25**,8660
[121] Vega, A. R.;Freeman, S. A.;Grinstein, S.; Jaqaman, K. Multistep track segmentation and motion classification for transient mobility analysis (2018). *Biophysical journal*.**114**,1018-1025
[122] Türkcan, S.; Masson, J.-B. Bayesian decision tree for the classification of the mode of motion in single-molecule trajectories (2013). *PloS one*.**8**,e82799
[123] Briane, V.;Vimond, M.;Valades-Cruz, C. A.;Salomon, A.;Wunder, C.; Kervrann, C. A sequential algorithm to detect diffusion switching along intracellular particle trajectories (2020). *Bioinformatics*.**36**,317-329
[124] Slator, P. J.; Burroughs, N. J. A hidden Markov model for detecting confinement in single-particle tracking trajectories (2018). *Biophysical journal*.**115**,1741-1754
[125] Janczura, J.;Balcerek, M.;Burnecki, K.;Sabri, A.;Weiss, M.; Krapf, D. Identifying heterogeneous diffusion states in the cytoplasm by a hidden Markov model (2021). *New Journal of Physics*.**23**,053018
[126] Rudin, C. Stop explaining black box machine learning models for high stakes decisions and use interpretable models instead (2019). *Nature machine intelligence*.**1**,206-215
[127] Slator, P. J.;Cairo, C. W.; Burroughs, N. J. Detection of diffusion heterogeneity in single particle tracking trajectories using a hidden Markov model with measurement noise propagation (2015). *PLoS One*.**10**,e0140759
[128] Lenne, P. F.;Wawrezinieck, L.;Conchonaud, F.;Wurtz, O.;Boned, A.;Guo, X. J.;Rigneault, H.;He, H. T.; Marguet, D. Dynamic molecular confinement in the plasma membrane by microdomains and the cytoskeleton meshwork (2006). *The EMBO journal*.**25**,3245-3256
[129] Niehaus, A. M. S.;Vlachos, D. G.;Edwards, J. S.;Plechac, P.; Tribe, R. Microscopic simulation of membrane molecule diffusion on corralled membrane surfaces (2008). *Biophysical Journal*.**94**,1551-1564
[130] Dennis, J. W.;Nabi, I. R.; Demetriou, M. Metabolism, cell surface organization, and disease (2009). *Cell*.**139**,1229-1241
[131] Oswald, F.;Varadarajan, A.;Lill, H.;Peterman, E. J.; Bollen, Y. J. MreB-dependent organization of the E. coli cytoplasmic membrane controls membrane protein diffusion (2016). *Biophysical journal*.**110**,1139-1149
[132] Woringer, M.;Izeddin, I.;Favard, C.; Berry, H. Anomalous subdiffusion in living cells: bridging the gap between experiments and realistic models through collaborative challenges (2020). *Frontiers in Physics*.**8**,134
[133] Bayle, V.;Fiche, J.-B.;Burny, C.;Platre, M. P.;Nollmann, M.;Martinière, A.; Jaillais, Y. Single-particle tracking photoactivated localization microscopy of membrane proteins in living plant tissues (2021). *Nature Protocols*.**16**,1600-1628
[134] Cui, Y.;Yu, M.;Yao, X.;Xing, J.;Lin, J.; Li, X. Single-particle tracking for the quantification of membrane protein dynamics in living plant cells (2018). *Molecular Plant*.**11**,1315-1327
[135] Ritchie, K.;Shan, X.-Y.;Kondo, J.;Iwasawa, K.;Fujiwara, T.; Kusumi, A. Detection of non-Brownian diffusion in the cell membrane in single molecule tracking (2005). *Biophysical journal*.**88**,2266-2277

[136] Suzuki, K.;Ritchie, K.;Kajikawa, E.;Fujiwara, T.; Kusumi, A. Rapid hop diffusion of a G-protein-coupled receptor in the plasma membrane as revealed by single-molecule techniques (2005). *Biophysical journal*.**88**,3659-3680
[137] Alcor, D.;Gouzer, G.; Triller, A. Single-particle tracking methods for the study of membrane receptors dynamics (2009). *European journal of neuroscience*.**30**,987-997
[138] Gebhardt, J. C. M.;Suter, D. M.;Roy, R.;Zhao, Z. W.;Chapman, A. R.;Basu, S.;Maniatis, T.; Xie, X. S. Single-molecule imaging of transcription factor binding to DNA in live mammalian cells (2013). *Nature methods*.**10**,421-426
[139] Presman, D. M.;Ball, D. A.;Paakinaho, V.;Grimm, J. B.;Lavis, L. D.;Karpova, T. S.; Hager, G. L. Quantifying transcription factor binding dynamics at the single-molecule level in live cells (2017). *Methods*.**123**,76-88
[140] Patange, S.;Ball, D. A.;Karpova, T. S.; Larson, D. R. Towards a 'spot on'understanding of transcription in the nucleus (2021). *Journal of molecular biology*.**433**,167016
[141] Mehta, G. D.;Ball, D. A.;Eriksson, P. R.;Chereji, R. V.;Clark, D. J.;McNally, J. G.; Karpova, T. S. Single-molecule analysis reveals linked cycles of RSC chromatin remodeling and Ace1p transcription factor binding in yeast (2018). *Molecular Cell*.**72**,875-887. e879
[142] Elf, J.;Li, G.-W.; Xie, X. S. Probing transcription factor dynamics at the single-molecule level in a living cell (2007). *Science*.**316**,1191-1194
[143] Hou, S.;Exell, J.; Welsher, K. Real-time 3D single molecule tracking (2020). *Nature communications*.**11**,3607
[144] Trovato, F.; Tozzini, V. Diffusion within the cytoplasm: a mesoscale model of interacting macromolecules (2014). *Biophysical journal*.**107**,2579-2591
[145] Belli, V.;Guarnieri, D.;Biondi, M.;Della Sala, F.; Netti, P. A. Dynamics of nanoparticle diffusion and uptake in three-dimensional cell cultures (2017). *Colloids and Surfaces B: Biointerfaces*.**149**,7-15
[146] Zahid, M. U.;Ma, L.;Lim, S. J.; Smith, A. M. Single quantum dot tracking reveals the impact of nanoparticle surface on intracellular state (2018). *Nature communications*.**9**,1830
[147] Arjona, M. I.;Najafi, J.; Minc, N. Cytoplasm mechanics and cellular organization (2023). *Current opinion in cell biology*.**85**,102278
[148] Hu, J.;Jafari, S.;Han, Y.;Grodzinsky, A. J.;Cai, S.; Guo, M. Size-and speed-dependent mechanical behavior in living mammalian cytoplasm (2017). *Proceedings of the national Academy of Sciences*.**114**,9529-9534
[149] Clegg, J. Properties and metabolism of the aqueous cytoplasm and its boundaries (1984). *American Journal of Physiology-Regulatory, Integrative and Comparative Physiology*.**246**,R133-R151
[150] Yubero, M. L.;Kosaka, P. M.;San Paulo, Á.;Malumbres, M.;Calleja, M.; Tamayo, J. Effects of energy metabolism on the mechanical properties of breast cancer cells (2020). *Communications biology*.**3**,590
[151] Scott, S.;Weiss, M.;Selhuber-Unkel, C.;Barooji, Y. F.;Sabri, A.;Erler, J. T.;Metzler, R.; Oddershede, L. B. Extracting, quantifying, and comparing dynamical and biomechanical properties of living matter through single particle tracking (2023). *Physical Chemistry Chemical Physics*.**25**,1513-1537
[152] Katrukha, E. A.;Mikhaylova, M.;van Brakel, H. X.;van Bergen En Henegouwen, P. M.;Akhmanova, A.;Hoogenraad, C. C.; Kapitein, L. C. Probing cytoskeletal modulation of passive and active intracellular dynamics using nanobody-functionalized quantum dots (2017). *Nature communications*.**8**,14772
[153] Wang, Z.;Wang, X.;Zhang, Y.;Xu, W.; Han, X. Principles and applications of single particle tracking in cell research (2021). *Small*.**17**,2005133
[154] Ariga, T.;Tomishige, M.; Mizuno, D. Experimental and theoretical energetics of walking molecular motors under fluctuating environments (2020). *Biophysical reviews*.**12**,503-510
[155] Gottstein, C.;Wu, G.;Wong, B. J.; Zasadzinski, J. A. Precise quantification of nanoparticle internalization (2013). *ACS nano*.**7**,4933-4945
[156] Bannunah, A. M.;Vllasaliu, D.;Lord, J.; Stolnik, S. Mechanisms of nanoparticle internalization and transport across an intestinal epithelial cell model: effect of size and surface charge (2014). *Molecular pharmaceutics*.**11**,4363-4373
[157] Duan, X.; Li, Y. Physicochemical characteristics of nanoparticles affect circulation, biodistribution, cellular internalization, and trafficking (2013). *Small*.**9**,1521-1532
[158] Baltazar, G. C.;Guha, S.;Lu, W.;Lim, J.;Boesze-Battaglia, K.;Laties, A. M.;Tyagi, P.;Kompella, U. B.; Mitchell, C. H. Acidic nanoparticles are trafficked to lysosomes and restore an acidic lysosomal pH and degradative function to compromised ARPE-19 cells (2012). *PloS one*.**7**,e49635
[159] Wang, X.; Wang, W.-X. Tracking the cellular degradation of silver nanoparticles: Development of a generic kinetic model (2024). *ACS nano*.**18**,13308-13321
[160] Lee, K. J.;Nallathamby, P. D.;Browning, L. M.;Desai, T.;Cherukuri, P. K.; Xu, X.-H. N. Single nanoparticle spectroscopy for real-time in vivo quantitative analysis of transport and toxicity of single nanoparticles in single embryos (2012). *Analyst*.**137**,2973-2986
[161] Jin, H.;Heller, D. A.;Sharma, R.; Strano, M. S. Size-dependent cellular uptake and expulsion of single-walled carbon nanotubes: single particle tracking and a generic uptake model for nanoparticles (2009). *ACS nano*.**3**,149-158
[162] Wu, J. L.;Ji, Q.;Blackadar, C.;Nguyen, L. N.;Lin, Z. P.;Sepahi, Z.;Stordy, B. P.;Granda Farias, A.;Sindhwani, S.; Ngo, W. The pathways for nanoparticle transport across tumour endothelium (2025). *Nature Nanotechnology*. 1-11
[163] Nguyen, L. N.;Lin, Z. P.;Sindhwani, S.;MacMillan, P.;Mladjenovic, S. M.;Stordy, B.;Ngo, W.; Chan, W. C. The exit of nanoparticles from solid tumours (2023). *Nature Materials*.**22**,1261-1272
[164] Baba, K.; Nishida, K. Single-molecule tracking in living cells using single quantum dot applications (2012). *Theranostics*.**2**,655
[165] Luo, Y.;Han, Y.;Hu, X.;Yin, M.;Wu, C.;Li, Q.;Chen, N.; Zhao, Y. Live-cell imaging of octaarginine-modified polymer dots via single particle tracking (2019). *Cell Proliferation*.**52**,e12556
[166] Liu, M.;Li, Q.;Liang, L.;Li, J.;Wang, K.;Li, J.;Lv, M.;Chen, N.;Song, H.; Lee, J. Real-time visualization of clustering and intracellular transport of gold nanoparticles by correlative imaging (2017). *Nature communications*.**8**,15646
[167] Wang, L.;Li, X.;Li, Z.;Chu, W.;Li, R.;Lin, K.;Qian, H.;Wang, Y.;Wu, C.; Li, J. A new cubic phase for a NaYF4 host matrix offering high upconversion luminescence efficiency (2015). *Advanced Materials*.**27**,5528-5533
[168] Bao, W.;Meng, J.;Li, T.;Li, Q.;Liu, H.; Tian, Z. MOFs-Based Nanoinducer Enables Excessive Autophagy for Synergistic Photoimmunotherapy (2025). *Small*. 2503848

[169] Huang, H.;Xiao, Z.;Feng, W.;Song, X.;Chen, L.;Huang, L.;Ding, L.; Chen, Y. Biomimetic nanoimmunotherapy boosts spatiotemporal PANoptosis and reshapes desmoplastic tumor microenvironment (2025). *Cell Reports Medicine*.**6**,

[170] Qin, S.;Wang, Q.;Zhang, Z.;Gu, J.;He, G.;Zeng, F.;Chen, R.;He, B.;Wang, Y.; Wang, M. Metabolic Hijacking by Engineered Probiotics Reprograms Tumor Metabolism and Immune Microenvironment for Self-Reinforcing Photodynamic Immunotherapy (2025). *Journal of the American Chemical Society*.**147**,38180-38194

[171] Zhu, L.;Hu, J.;Wu, X.;Zhang, J.;Xu, X.;Huang, X.;Tian, B.;Zhao, C.-X.;Du, Y.; Wu, L. Programmed enhancement of endogenous iron-mediated lysosomal membrane permeabilization for tumor ferroptosis/pyroptosis dual-induction (2025). *Nature Communications*.**16**,3017

[172] Wang, F.;Xu, W.;Liu, Y.;Zhu, S.;Liu, W.;Bo, S.;Sun, H.;Liu, B.;Sun, Z.; Chu, H. Spatiotemporally Controlled Tumor Photodynamic/Immunotherapy Therapy Based on Upconversion Hybrid Nanosystem (2025). *Advanced Science*. e15052

Chapter 2. Review of current applications for luminescent materials

The contents of this chapter adapted with permission form:

Tang W, et al. Design principles and biomedical applications of endoplasmic reticulum-targeting luminescent nanoparticles. *Nano Research*, 2025, 18(6): 94907356. https://doi.org/10.26599/NR.2025.94907356

2.1 Preamble

The previous chapter highlighted the basic mechanisms of up-conversion materials, the relationship between nanomaterials and living systems as well as a basic outline of the following thesis. However, the significance and importance of developing nanomaterials which can be used to study the movement of cargo at a single cell level is not explored. The following chapter highlights the current application of luminescent nanomaterials and their immense potential for therapeutic and diagnostic tools at a subcellular level. In a context which involves highly specific nanoparticle intracellular targeting, the importance in understanding how intracellular cargo is processed in the cell becomes of vital importance. The presentation of numerous applications and designs for nanoparticles for intracellular applications in this published review article should highlight the importance of understanding the nature and complex mechanisms behind the transportation and intracellular dynamics of nanomaterials.

2.2 Abstract

Luminescent nanoparticles (LNPs) have emerged as a promising approach for enhanced cell labelling and disease diagnosis by leveraging their unique photophysical and surface characteristics. Advanced generations of LNPs, such as quantum dots, dye-loaded nanoparticles and up-converting nanoparticles, exhibit distinct properties and advantages tailored for specialised applications. Consequently, there is a growing focus and demand to develop organelle-specific LNPs to identify, treat and elucidate disease mechanisms. The endoplasmic reticulum (ER) represents one such organelle, playing crucial roles in protein synthesis and modification, calcium homeostasis, lipid trafficking, and regulation of cellular stress. The unfolded protein response, regulated by ER stress, is a clinically

significant pathway within the ER, implicated in cellular dysfunction and disease. The growing understanding of ER stress and the unfolded protein response has led to a rapid emergence of endoplasmic reticulum-targeting LNPs (ER-LNPs) for precise intracellular diagnosis and therapy. This review discusses current advancements and design principles of ER-LNPs, highlights current achievements and applications, and discusses the challenges and interdisciplinarity needed for future development.

KEYWORDS: luminescent nanomaterials; endoplasmic reticulum-targeting; cell labelling; bio-imaging, photodynamic therapy

2.3 Introduction

Rapid progress in nanotechnology has yielded promising improvements in detection limits, drug efficacy, and biocompatibility compared to conventional therapeutics. Precise subcellular delivery of luminescent nanomaterials not only enhances detection capabilities but also increases the precision of drug delivery, making these materials valuable tools in diagnostics and drug efficacy enhancement for preclinical research. Luminescent nanoparticles, or LNPs, have facilitated groundbreaking discoveries, advancing our understanding of complex biological systems at a molecular level [1-6]. In contrast to conventional fluorescent dyes, LNPs are designed to overcome limitations such as low stability, biocompatibility, and monofunctionality by enhancing surface and photophysical properties [7, 8]. The potential for developing advanced therapies and deepening the understanding of intracellular organelle dynamics drives the development of endoplasmic-reticulum targeting LNPs (ER-LNPs). The advancement in particle synthesis and modification have led to the creation of both organic and inorganic-derived LNPs that exhibit precise subcellular localization *in vivo* and *in vitro* (Figure 2.1)[9, 10]. These LNPs offer extensive flexibility, often coupled with enhanced stability, high yield, and the potential for synergistic or combination therapy [11].

Given its numerous functions and substantial localization within the intracellular space, the ER has become one of the key targets for drug therapy. As one of the most prominent membrane-bound organelles in all eukaryotic cells, ER plays a crucial role in cellular functioning and survival [12]. However, the entry and subcellular localization of nanoparticles are influenced by various factors due to complex pathways and mechanisms involved in endocytosis. A collection of nanomaterials with substantially differences sizes

and photophysical properties present new challenges and opportunities for achieving precise subcellular delivery compared to conventional dyes [9, 13, 14]. Currently, the accumulation of nanoparticles in early endosomes and lysosomes significantly hampers intracellular detection and drug delivery efficiency [15, 16].

Typically, the design and selection of nanomaterials for ER-LNPs are developed and optimized based on their biomedical applications such as imaging, diagnosis or therapy. These nanocarriers are engineered to incorporate ligands, protein or genetic material, which help overcome challenges related to instability, non-specificity and insolubility [17]. Further development of many subcellular-specific nanocarrier systems aims to further enhance their efficacy and minimize the drawbacks associated with traditional nanocarrier-based methods for therapy and diagnosis.

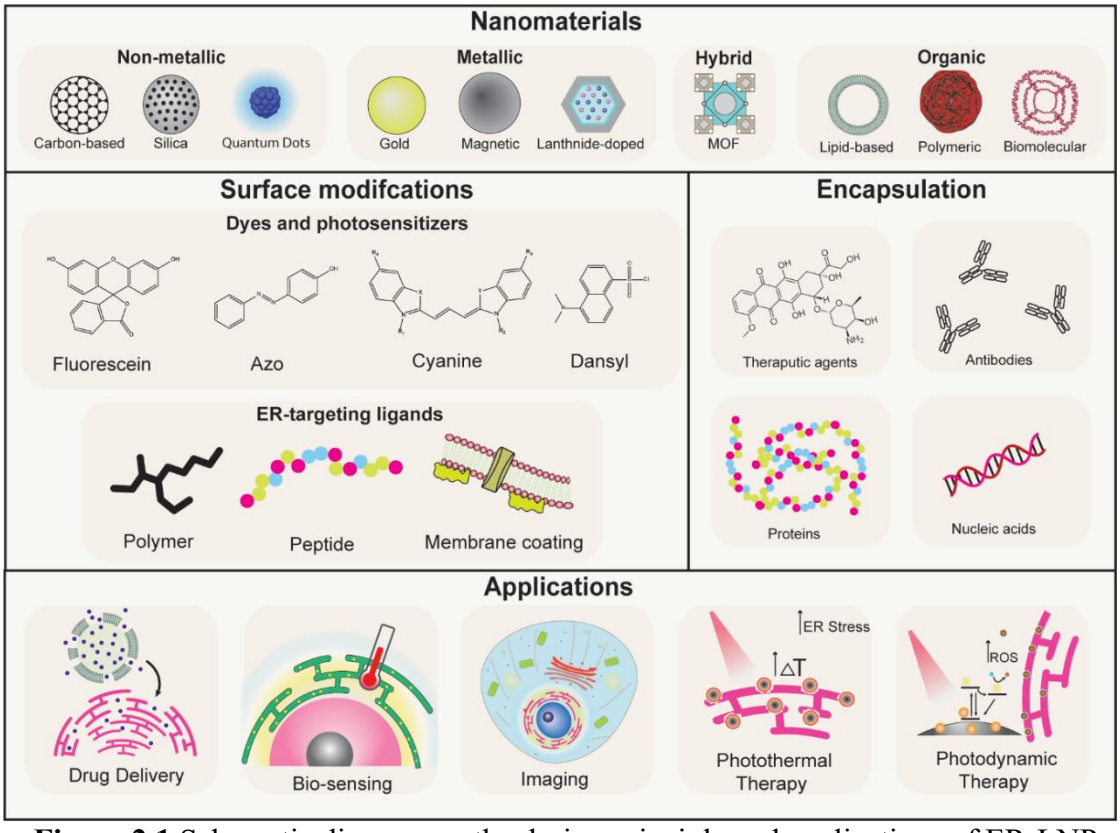

Figure 2.1 Schematic diagram on the design principle and applications of ER-LNPs. The choice of functional materials offers different physical and chemical characteristics appropriate for different applications. Photo-responsive nanomaterials initiate various strategies for intracellular detection and delivery to facilitate combination therapies and diagnostics. ER specifically precisely delivers drugs, treatments and probes a subcellular level for enhanced treatment and diagnosis.

Numerous strategies have been explored to elucidate the mechanism behind precise subcellular delivery. This review will systematically explore the design principles of ER-LNPs, focusing on how these nanomaterials can influence various cellular functions through their distinctive properties to optimize processes for drug delivery, therapy and detection. The clinical implications of ER-associated pathways underscore the significance of current advances in cell imaging, disease diagnostics, and therapy using ER-LNPs. A classification based on composition, structural properties, luminescence and targeting strategies will be discussed, emphasizing the current capabilities of ER-LNPs as candidates for imaging, sensing, and therapeutic applications.

2.4 ER: Cellular Functions and Interactions

The desire for subcellular targeting arises from the need to precisely target specific cellular pathways and functions to maximize efficacy and minimize side effects. As our understanding of individual organelle functionality advances, the specificity required for molecular therapeutics and diagnosis necessitates precision following material entry into the cell. Given its crucial role in regulating cellular stress and protein synthesis essential for cellular survival and proliferation, the ER remains one of the most important yet elusive targets. In essence, ER-specific nanomaterials could manipulate and monitor various cellular functions and pathways, serving as pivotal nanocarriers for specific molecular drugs and probes (Figure 2.2).

Calcium signaling is a ubiquitous cellular response that influences many intracellular interactions through the regulation of cytosolic calcium, involving the storage of intracellular calcium ions within the ER lumen [18]. As ER homeostasis is vital for the regulation of intracellular ions, the ER plays a significant role in managing inflammation-associated cellular dysfunction through to apoptosis in motor neurons. The regulation of intracellular calcium is mediated by a G protein-coupled receptor pathway, which activates inositol 1,4,5-triphosphate receptors through the production of inositol 1,4,5-triphosopahte, with the activation and regulation of intraluminal calcium channels playing a key role during the cell's response to a redox environment [19]. In neuron or muscle cells, the release of calcium into the cytosol functions as an action potential to enable synaptic transmission or muscle contractions, with dysfunction implicated in different neurological diseases. Upon release into the cytoplasm, calmodulin activation through calcium binding

facilitates kinase and phosphatase activity, which are crucial for other metabolic pathways [20]. Furthermore, many ER-associated enzymes, such as binding immunoglobulin protein and calreticulin require calcium binding to activate their function as molecular chaperones.

The significance of calcium fluctuations within the cell underscores the utility of luminescent nanomaterials, which can be used to detect and modulate the distribution and fluctuation of intracellular ions through interactions with ER-associated proteins [21]. Interactions with the plasma membrane, along with different ion, voltage, or receptor channels, can lead to significant fluctuations in cytosolic calcium within neuronal cells [22]. Consequently, nanoparticle-based delivery systems can overcome the instability and insolubility of ion sensitive probes within an intracellular environment to detect or predict cellular stress and survival [23].

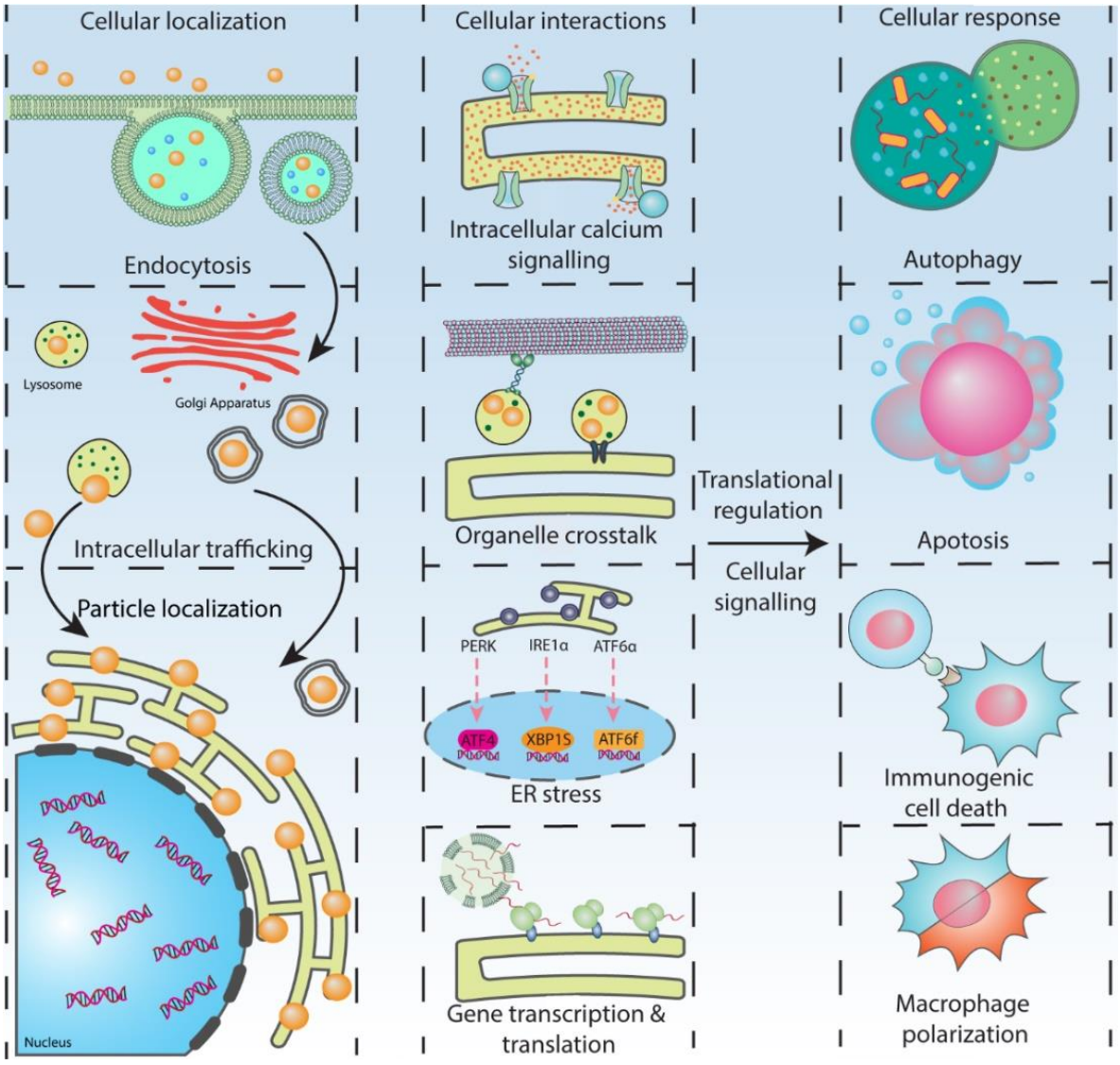

Figure 2.2 Cellular interactions and potential responses. ER-nanoparticle based interactions can trigger and influence several cellular functions, such as intracellular calcium signaling, organelle crosstalk, ER-stress pathway and gene transcription and translation. Ultimately, these interactions can lead to cellular fates and responses that have significant clinical implications

Due to the sensitive nature of proteins, even minute changes in conditions such as pH and temperature can significantly influence their molecular structure and activity. In environments rich in oxygen radicals, reactive oxygen species (ROS) can accumulate and severely damage proteins through the cleavage and oxidation of peptides and amino acid residues, leading to ER stress and activation of the unfolded protein response (UPR) to restore cellular functions [24]. Since ROS generation can induce ER-stressed based programmed cell death, current research focuses on controlling intracellular oxygen levels to prevent hypoxia. Utilizing ER-specific nanoparticles to reduce ROS has shown great therapeutic potential for treating conditions like pulmonary fibrosis, renal dysfunction, neurological diseases, and cancer [25-28]. ER-stress also influences the polarization of M2 macrophages into different subtypes, which can either alleviate or aggravate tissue fibrosis and inflammation [28]. For example, M2a macrophages might promote the progression of renal fibrosis via myofibroblast transition during elevated TGF-B stimulation, whereas M2c subtypes can suppress renal fibrosis by reducing inflammation and enhancing tissue repair. Conversely, damaged proteins can trigger programmed cell death in tumor cells. ER-stress induced apoptosis through ROS presents significant potential for tumor therapy, potentially reducing side effects, overcoming drug resistance, and enhancing tumor elimination. However, with a half-life of less than 50ns, a limited diffusion capabilities not exceeding 20 nm, ROS undergo rapid dissipation in the cellular environment [29]. This limitation makes the ER a critical site for ROS activation due to its protein-rich environment. ER-specific photodynamic strategies have therefore developed to maximize tumor elimination and minimize adverse effects. The classical pathway ROS generation involves two types of reactions: Type I reactions release electrons to a substrate, and Type II reactions transfer electrons to oxygen molecules, both leading to ROS production [30]. ROS generated through photodynamic therapy (PDT) activates ER-stress pathways such as IRE1, ATF6 and PERK which, through protein-induced oxidative damage, can lead to CHOP-activated apoptosis and autophagy through IRE-1 and PERK pathway [24, 31]. Additionally, these

ER stress pathways can induce immunogenic cell death (ICD) through the release of damage-associated molecular patterns (DAMPs), such as calreticulin [32]. A potential *in-situ* tumor vaccine using ER-targeting nanoparticles has been explored, with studies such as those by Liu et al. demonstrating how ER-targeting PDT can induce an antitumor immune response through the generation of tumor antigens (TAAs) and DAMPs, facilitating enhanced dendritic cell maturation [33].

The proximity of the ER to the nucleus also facilitates the delivery of transcription factors activated by specific signal transduction pathways. Transcribed mRNAs are rapidly transported, translated and modified within the ER. Given its strategic location adjacent to the nucleus and the inherent selectivity of nuclear pore complexes, targeting the ER enhances the performance of therapeutic agents aimed at the nucleus or genetic material. Numerous studies have demonstrated that ER-specific nanoparticles possess superior gene silencing, transfection, and gene delivery therapy capabilities compared to traditional lipofectamine [28, 34-38]. Aside from indirect interactions with the nucleus, the ER also organizes a complex distribution network using the cytoskeleton to interact with other organelles such as the lysosomes and mitochondria [39]. Therefore, interactions at protein-protein and lipid-protein contact sites between the ER and other organelles are crucial for maintaining cellular homeostasis and signaling, regulating lipid and ion dynamics [40]. Super-resolution has become an important technique for understanding and imaging cellular and sub-cellular structure so developing nanoprobes capable of breaking the diffraction limit to achieve super-resolved detection of live-cell organelle interactions is a significant research objective. Subcellular-specific biosensing holds immense potential for revealing physiological mechanisms underlying cell growth, metabolism, and disease at the molecular level. For example, cellular stress and dysregulated calcium signaling of Parkinson's Disease have been linked to slower oscillations of calcium concentrations between cytoplasm and ER in neuron cells [41]. Conversely, breast cancer metastasis has been associated with an influx of intra-organelle calcium in the ER via the ORAI-1 pathway [42]. Additionally, environmental factors such as polarity and pH are critical hallmarks of intracellular and oxidative stress that affect cell proliferation and metabolism [43]. ER-specific biosensors are therefore essential for diagnosing and elucidating the intracellular mechanism of various diseases.

While the cellular function of the ER and its relationship with nanomaterials have been studied extensively *in vitro and in vivo*, there is currently a lack of understanding of how ER specific nanomaterials can influence an individual's overall health and metabolism in a clinical setting. Furthermore, the formation of a protein corona when nanomaterials enter the biological environment triggers an immune response that increases non-specific localization and accelerates clearance, potentially reducing therapeutic and diagnostic effectiveness [44]. While the kidney liver and spleen are key organs that play a role in the filtration and circulation of foreign particles, our limited understanding of the long-term effects of nanomaterials remains a key bottleneck that limits potential clinical application. Currently, nanomaterial biocompatibility and stability have been achieved through complex surface modifications without sub-cellular specificity, however, more research is required to understand on how subcellular specificity in nanomaterials differ in circulation or filtration compared to non-organelle specific foreign particles [45].

2.5 Design and Functionality of Nanocarrier Surface Modification

Precise and subcellular delivery of nanoparticles significantly influences their diagnostic and therapeutic potential, improving diagnostic accuracy and drug efficacy while minimizing adverse effects for future clinical applications.

Organelle-specific nanotechnology not only lowers detection limits but also enables synergistic therapy and precise observations, thereby deepening our understanding of molecular interactions at the subcellar level. However, the cell's natural processing systems present major obstacles to developing superior nano-drug delivery systems. The innate physical and chemical barriers within the cell naturally prevent the entry of foreign and invasive materials. Therefore, the entry and intracellular localization of nanoparticles become critical factors determining their therapeutic and diagnostic efficacy. While some viral particles can passively and directly fuse into the cytoplasm through the bilayer of the cell membrane, the internalization of nanomaterials is predominantly processed through various energy-dependent endocytic pathways (Figure 2.3) [45]. Both selective and non-selective uptake of nanoparticles through these pathways occur as the cell naturally engulfs materials from the external environment to receive essential nutrients and signals [45]. Consequently, the cell attempts to eliminate the potentially hazardous nature of foreign

particles by accumulating them in places like the acidic endo-lysosomal system. Endosomes—naturally acidic compartments—physically and chemically prevent foreign material from entering other regions of the cell. These endosomes mature into lysosomes, which process and eliminate potentially hazardous foreign nanomaterials through catalytic enzymes such as lipases, nuclease, and proteases. Nanoparticles delivering drugs often traverse the endosomal and lysosomal pathway, leading to therapeutic degradation under the acidic conditions of late endosomes and lysosomes, which diminished the effectiveness of nanomaterial diagnostics, probing, and drug delivery systems [16 7]. The mechanism underlying the ER-specific targeting through surface modifications and ligands remains elusive. With current theories suggesting three primary strategies (Figure 2.3): receptor-based trafficking, caveolae-mediated endocytosis, and endosomal escape. ER retention via KDEL peptide modification involves COPI and COPII trafficking, where KDEL receptors help transport KDEL materials into the ER lumen. Caveolae and lipid raft-mediated endocytosis can directly target the ER [37, 46, 47], although recent studies suggest that caveosomes may be a byproduct of over-expressed caveolin proteins rather than functional trafficking organelles [48].

Endosomal escape strategies facilitate nanoparticle expulsion from the endosome via mechanisms like membrane fusion, osmosis or the 'proton sponge' effect, which involve manipulating charge and energy on the nanoparticle surface to facilitate varying degrees of lysosomal escape through electrostatic repulsion or membrane fusion in the acidic lysosomal environment [49]. Positively charged nanoparticles have been suggested to be more effective at lysosomal escape compared to their neutrally or negatively charged counterparts [50]. Additionally, the influence of the protein corona on particle targeting and localization post-endocytosis is critically underexplored. Once nanoparticles escape the lysosomal, ER-targeted, surface-modified particles can bind to specific targets as they freely diffuse within the cytoplasm [51-54]. In essence, achieving precise intracellular localization of nanoparticles necessitates surface modifications with ligands such as polymer and peptide, establishing a robust ER localization strategy. Research focusing on subcellular localization outside of lysosomal compartments has become fundamental in enhancing therapeutic delivery and subcellular diagnostics. Particularly, nanoparticle localization in the ER has profound implications for cell biology and medicine, driving significant advances in these fields. The functionality, structure and location of organelle

must be strategically aligned with their intended applications to improve efficacy.

Extensive research has been undertaken to comprehend the interactions of nanoparticles within a subcellular environment for precise particle delivery. However, the specific fate of nanomaterials at the subcellar level remains uncertain due to the diverse pathways affecting their localization and retention [15]. The physical and chemical properties of nanoparticle surfaces play a pivotal role in how they are absorbed and transported within the cell (figure 2.4). Surface modifications alter endocytosis and intracellular trafficking pathways to achieve subcellular localization [55]. The composition and internal structure of the nanoparticle also affect organelle retention [56, 57].Additionally, factors such as shape and core composition significantly influencing organelle-specific retention [16, 51]. A recent

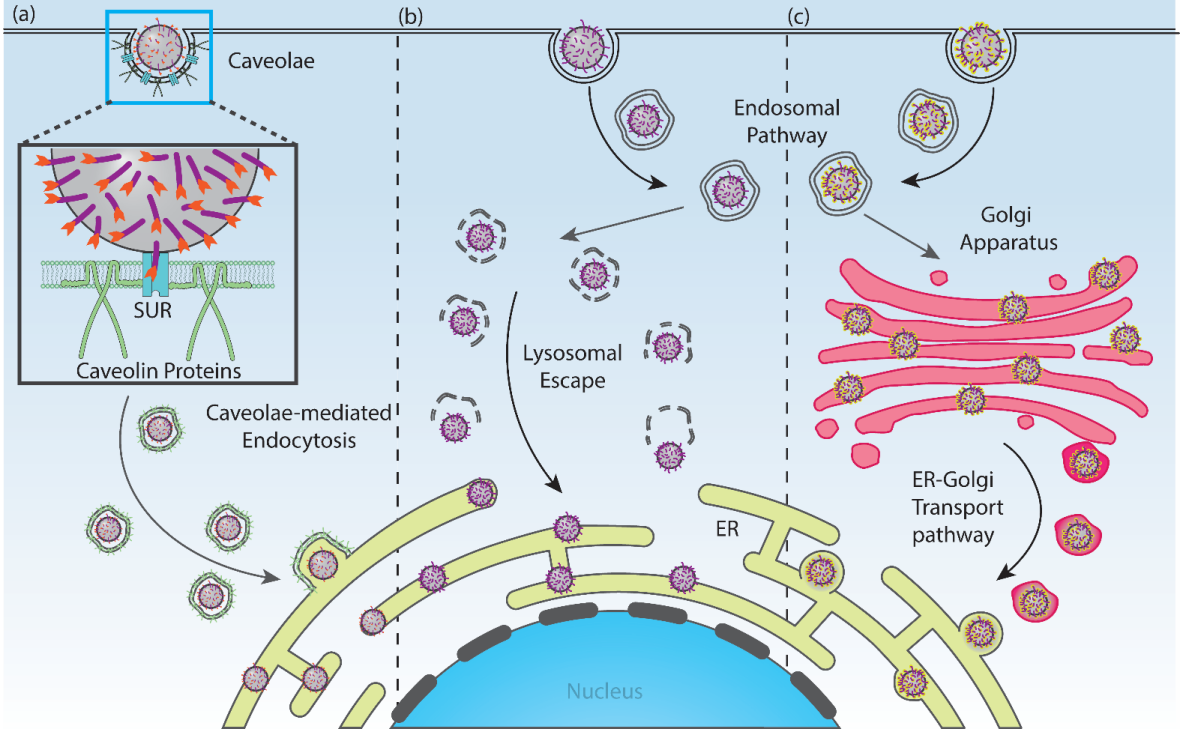

Figure 2.3 Current strategies for ER localization and targeting and their proposed mechanisms. (a) The sulfonyl urea receptor (SUR) receptor is heavily localized on the lipid raft membranes on the surface of the cell membrane; as such, surface modifications with affinity towards proteins such as SUR can induce caveolae-mediated endocytosis for direct uptake into the endoplasmic reticulum. (b) Lysosomal and endosomal escape after non-specific endocytosis facilitates sub-cellular localization. Surface modifications, such as polymer modifications, can induce a change in ion concentration gradient between the endosome and cytoplasm, resulting in membrane rupture, nanoparticle escape and subsequent localization. (c) Some modifications, such as KDEL and cell membrane coatings, can exploit the natural trafficking system of the cell to directly transport nanoparticles into the ER via the COPI/COPII pathway.

study by Shuang et al. underscored the significance of carbon nanodot shape for ER localization and targeting [58]. By altering precursors to create tunable shapes with differing aspect ratios, rod-like carbon nanodots exhibited enhanced cellular uptake and ER localization through active transport. This improved uptake of rod-shaped nanomaterials has been extensively documented, highlighting the critical role of nanoparticle surface aspect ratio in cellular studies [59, 60].

2.5.1 Polymer Modifications

Stability, biocompatibility, and dispersion are critical for nanomaterials within a biological environment. Lipophilic surfactants, typically used during synthesis to maintain the shape and size of inorganic nanoparticles, are often replaced with organic polymers to ensure particle dispersion in an aqueous environment [61]. Polymer-based surface modifications are often the most common methods used to enhance and alter nanoparticle functionality due to the simplicity of surface modification protocols methods through either ligand exchange or organic chemistry linkage such as click or carbodiimide chemistry [62]. Subsequently, one of the earliest approaches for subcellular localization involved polymer-based surface modifications, with the hydrophilic nature of specific polymers facilitating ER-specificity through caveolae-mediated endocytosis [63]. Additionally, it has been recognized that organic polymers introduce superior colloidal stability and biocompatibility which enhances cellular uptake and reduces cytotoxicity facilitated by the polar functional groups within these polymers. Water-soluble
polymers such as PEG, PLA, PAA and other polar co-block polymers enhance nanoparticle dispersion by replacing hydrophobic surfactants used during synthesis [61]. Notably, the length of polymer coatings and their terminal functional groups—carboxylic and primary amine—impact cellular
uptake and viability but also offer opportunities for surface modifications of photosensitizers, dyes and therapeutic agents through click and carbonamide chemistry [64, 65].

The potential and viability of intracellular ER localization through commercially available polymers that provided enhanced intracellular uptake paved the way for simplistic ligand exchange methods. Among these, Diblock and triblock polyether polymers and copolymers like PEG, PEG-PE and Pluronic 127 were among the first to demonstrate live

cell ER localization. Studies in cancerous and non-cancerous A549, MRC and HEK293T cells showed that PEG-PE diblock copolymer micelles specifically localized to the ER [66]. The inhibition of pinocytosis decreased the uptake of PEG micelle but did not affect PEG-PE micelle accumulation highlighting different pathways of entry. Evidence suggesting that difference in entry pathways was dictated by differences in nanoparticle surface chemistry reveals the complex interactions between nanoparticle surface and cellular entry are still not fully understood today.

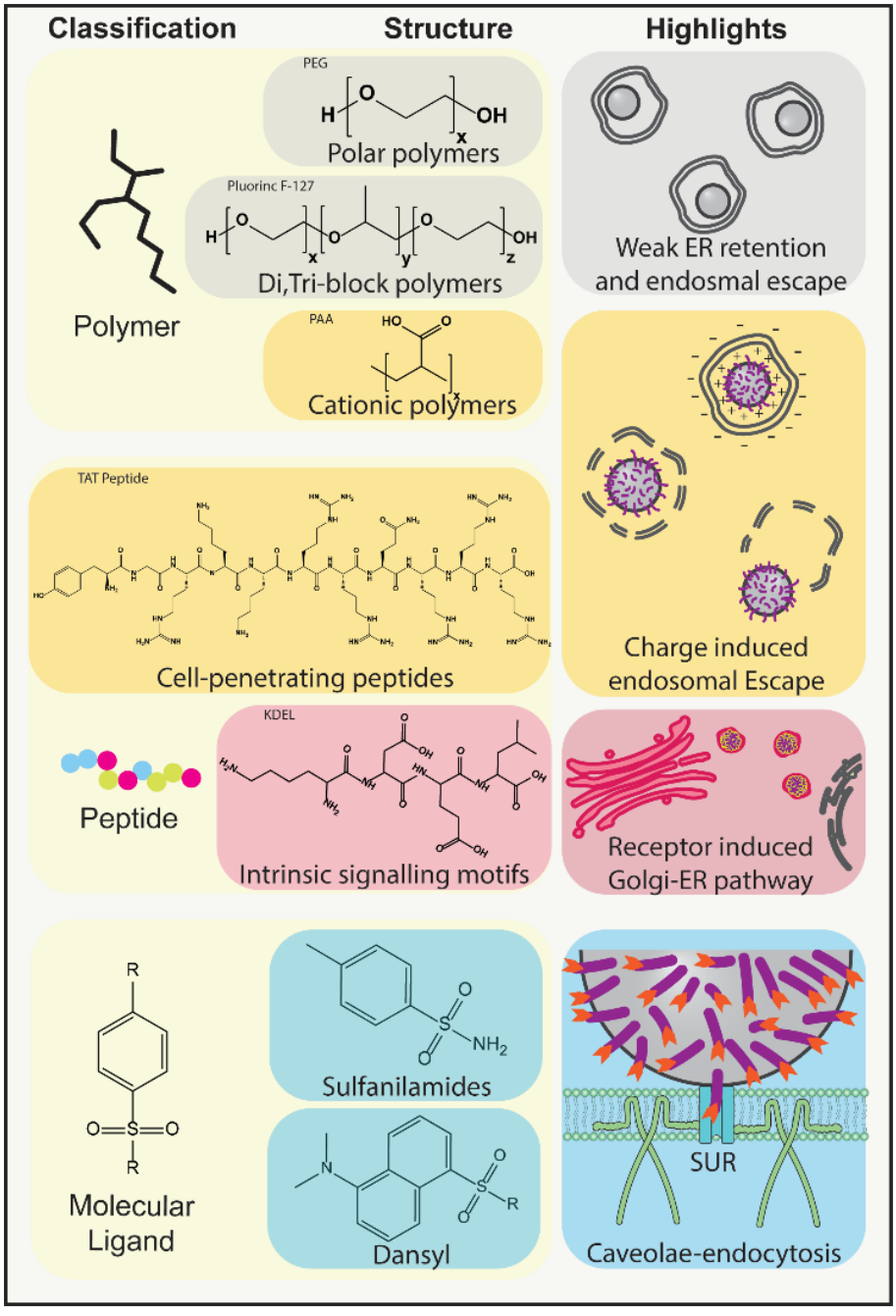

Figure 2.4 The classification and structure of molecular targeting agents and their main characteristics. (a) Polar polymers facilitate endocytosis but possess weak ER retention, however cationic polymers can result in charge induced endosomal escape. (b) Cationic cell penetrating peptides (CPP) facilitate charge induced endosomal rupture, while signaling peptides follow intrinsic pathways through intracellular vesicle trafficking. (c) Molecular binding is facilitated via the binding of the sulfonyl urea receptor (SUR) on the ER through receptor mediated affinity.

One of the leading theories suggests that the accumulation and formation of different protein coronas caused by differences in electrostatic charge and protein affinity of different polymers on the surface of the nanoparticle results in different endocytic pathways [67]. However, non-protein based cellular interactions may also play an important role in the localization of nanomaterials. Pollock et al. designed pH-sensitive phospholipids that complemented the composition of the ER membrane [68], synthesizing liposomes with concentrations of ER membrane phospholipids like phosphatidylcholine, phosphatidylethanolamine, phosphatidylinositol, phosphatidylserine, and cholesterol, which resulted in precise ER delivery. Nanomaterial specificity achieved through complementing lipid-based modifications presents evidence that trafficking of intracellular components is not solely a result of protein-protein based interactions. Instead, intracellular trafficking, and thus intracellular specificity, can be regulated via non-protein-based trafficking through physical and chemical characteristics present in nanomaterials. Subsequently, other properties of polymeric materials, such as lipophilicity and electrophilicity, also enhance ER retention. For instance, Chen Et al. demonstrated that carbon dots synthesized with o-phenylene-diamine (OPD) and lysine facilitated lipid raft-mediated endocytosis for ER retention [69]. Similarly, Shuang et al. synthesized 3 nm laurylamine functionalized quasi-spherical carbon dots that distributed in the ER via lipid raft-mediated and caveolae endocytosis in MCF-7 cells [70]. These studies present evidence that initial endocytosis is one of the critical steps that can influence the intracellular fate of nanoparticles. Active targeting towards the ER via caveolin-mediated endocytosis has been demonstrated to occur via movement along the cytoskeleton via intracellular active transport along the microfilaments. However, localization through passive chemical affinity has also been exploited for enhanced ER localization. Wan et al. utilized comb-like poly(aspartic acid) grafted on PEG polymer micelles, which displayed ER retention facilitated by passive transportation, hypothesizing that the negatively charged carboxyl groups could increase

ER targeting based on the coordination interaction with ER abundant Ca(II) ions [71]. While ER-localization in nanoparticles can be achieved via surface-based modifications, achieving complete ER localization through polymer-based modifications has not yet been realized due to our lack of understanding of the intracellular dynamics and trafficking of nanomaterials. Namely, non-specific endocytosis and interactions which results in localization to the lysosome and recycling endosome are often presented due to the random Brownian motion particles undergo before entering the cell, which influences the time and duration in which the particles are in contact with the cell. As such, Non-specific presentation in mitochondria, lysosomes, and ER suggest that non-specific PEG-induced endocytosis may not be ER-specific but targets membrane-bound organelles more broadly [72].

Inorganic nanoparticles, such as silica quantum dots, modified with the propylene oxide and the PEG-based polymer Pluronic F127, achieved lysosomal evasion and ER localization through caveolae-mediated endocytosis in umbilical vein endothelial cells [63]. Liu et al. suggested that multi-pathway endocytosis could deliver biotinylated dextran amine-conjugated carbonized polymer dots into lysosomes and the ER via endosomes in PC12 and RSC96 neurons, leading to increased non-specific localization [73]. Whilst these strategies suggest that evasion of clathrin-mediated endocytosis might facilitate ER targeting, challenges remain in maintaining ER retention and reducing non-specific or multi-organelle targeting. Evidence indicates that non-specific polymer coating are insufficient for reliable long-term ER retention as intracellular fluctuations can alter particle localization without strong specific binding [74]. Enhanced subcellular targeting thus required receptor-specific binding to enhance long-term ER retention and decrease non-specificity.

2.5.2 Peptide Modifications

Peptide based modifications take inspiration from naturally occurring peptides which offer higher specificity and decrease in non-specific interactions. Furthermore, exploiting the natural pathway and interactions between specific peptides and receptors can result in highly specific, and most importantly, understood pathways to predict and alter the intracellular dynamics and fate of peptide-modified nanoparticles. As such, a majority of current peptides-based modifications for enhanced subcellular specificity originate from

motifs that can be pathological in nature or produced for metabolic or immunological purposes. Peptide conjugation on both organic and inorganic nanomaterials can facilitate ER retention through electrostatic interactions during endocytosis and specific peptide or protein-specific interactions during intracellular trafficking [36, 75]. Precisely controlling the fate of nanoparticles within the cell through naturally occurring pathways using peptide-based interactions can significantly improve therapeutic efficiency and ensure controlled drug release whilst simultaneously reducing immune system activation and inhibiting antagonistic signaling pathways [76].

One such mechanism for peptide-based cellular entry is achieved through the escape of the endomembrane system via the usage of naturally occurring peptides which possess membrane breaking capabilities. Bypassing the acidic compartments of the late endosome and lysosome through escape during the early endosome as well as recycling endosomes can significantly improve therapeutic efficiency by preventing drug and molecular degradation. For example, naturally occurring signal sequences of cell-penetrating peptides (CPPs) which utilize their hydrophobicity, amphipathicity, and cationic nature for achieve high, non-specific cell penetration that can result in ER retention [53, 54, 77-79]. Penetratin, a CPP peptide derived from the first 16 amino acids of the third-alpha helix of the Antennapedia protein homeodomain, was conjugated on lipid polymer hybrid nanovesicles and displayed substantial accumulation in the ER lumen of HEK-293T cells via ATP-dependent endocytosis —a mechanism not achieved by Arg7 and Tat CPPs [80]. While the exact mechanism is currently unknown, it is suggested that the hydrophobic amino acid cores (Met, Trp, Iso, Phe) of the peptide facilitates ER membrane penetration and enable early local disruptions of endosomal membrane structures which interact favourably due to large hydrophobic side chains of tryptophan and phenylalanine amino acids. This ATP-dependent endocytosis suggests that penetratin facilitated ER retention through non-peptide specific, physical interactions.

Precise controlling of nanoparticle fate within the cell is achieved highly specific signaling peptides which induce naturally occurring trafficking pathways. For example, KKXX and KDEL peptides, consisting of lysine-aspartate-glutamate-leucine or lysine-lysine-x-x sequences respectively, specifically target the COPI pathway which enables the retrograde transport from the Golgi apparatus to the ER
through COPI vesicles. KKXX and peptides KDEL bind to pH-dependent KDEL receptors

to form COPI vesicles that deactivate in the neutral pH of the ER [81]. These receptors are activated in the lysosome and Golgi apparatus sub-compartments due to their lower pH, facilitating the formation of COPI vesicle which degrades upon reaching the ER's neutral environment. As such, the usage of KDEL based localization strategies significantly decreases potential localization and storage of nanoparticles inside the lysosome as well as forgoing the requirement for lysosomal escape through exploiting naturally occurring trafficking pathways.

However, the size of the nanoparticle also appears to significantly affect ER retention. For instance, 20 nm gold nanoparticles facilitated ER retention within an hour via KDEL peptides, a feat not replicated with KKXX peptide in 350nm lipid nanoparticles [36, 82]. Acharya et al. demonstrated that ER-targeting nanoparticles exhibited superior gene silencing compared to conventional lipofectamine delivery [36]. Directed retrograde transport through the KDEL motif enhanced silencing of NADPH Oxidase 4 (Nox4) in C2C12 cells, owing to the enhanced uptake and delivery of siRNA. Similarly, a pivotal study showed superior transfection efficacy through virus-like entry mechanisms [37]. Surprisingly, control peptide such as KAAAAK exhibited higher ER retention and lower endosomal retention than KKXX peptide (AAKKAA) after two hours. A plausible explanation for the differing retention level is the size of the PLGA nanoparticles, as the activation of the KDEL receptor via KKXX and KDEL peptides typically mediate the formation of 60 nm COPI vesicles, which was unachievable in the study. Thus, the size of the PLGA nanoparticles might have only facilitated KDEL receptor binding but not the formation of COPI vesicles, disrupting ER retention and increasing endosome accumulation. KDEL-modified PLGA NPs probably accumulated in the ER via a non-specific binding or a non-specific pathway. Smaller KDEL-conjugated gold nanoparticles at 20 nm contributed to rapid ER retention, achieving COPI-mediated endocytosis in Sol8 cells within 60 minutes [83]. Alternative studies utilized KDEL-modified 50 nm up-converting nanoparticles targeting the ER to activate the natural antioxidant defense, including apoptosis in cancer cells [84]. Conflicting research on the intracellular fate of nanoparticles with different physical properties demonstrates more research is required in understanding the indirect and direct effects of size during the nanoparticle transportation via the COPI pathway.

Instead of using generalized peptide sequences, exploiting the cell's own trafficking

network can also be achieved using specific protein sequences which naturally located in specific organelles. Organelle-targeting peptides are proposed to enhance the transport of nanoparticles by increasing their directed delivery to specific organelles [54]. For example, the initial 18 amino acid sequences of human serum albumin (MKWVTFISLLFLFSSAYS) were utilized as a serum albumin signal sequence in 250 nm mesoporous silica nanoparticles (MSNs), which accumulated in the ER of liver macrophages [85]. As integral components of proteins with strong organelle specificity, serum albumin signal sequence enabled targeted trafficking through the natural compartmentalization and transport processes within the cell.

While current prospects on peptide-based localization display immense potential, one of the most poorly understood mechanisms in ER-based localization lies in the ER specificity through the caveolae-mediated endocytosis. Conflicting evidence on caveolae-mediated endocytosis and its subsequent mechanisms due to the misunderstandings on the caveosome has resulted in literature with conflicting and outdated theories for ER based specificity. With only 5% of all endosomes containing caveolae, caveolae-mediated endocytosis only facilitates a minimal amount of endocytosis and membrane trafficking, yet observations through drug-mediated inhibition demonstrates it accounting for higher amounts of nanoparticle intake with specific surface modifications [86]. For example, Pardaxin facilitated the localization of nanoparticles larger than 100 nm within the ER of CT-26 colon carcinoma and B16 melanoma cells [32]. Pardaxin is a 33-amino-acid cationic peptide, originally recognized for its antimicrobial properties through the disruption of zwitterionic lipids in lipid bilayers [87]. Sourced from the Red Sea and Pacific Peacock sole, Pardaxin has recently been shown to induce apoptosis and selectively target the ER [88]. Poly(g-glutamic) lipid nanoparticles modified with Pardaxin demonstrated enhanced ER localization through a caveolae-mediated, virus-like entry that evades lysosomal pathways in CD8 T cells. Without pardaxin surface modifications, these nanoparticles entered cells predominately via micropinocytosis and phagocytosis trafficking. Inspired by the cellular uptake of viral particles, Yuan et al. further explored this phenomenon, showing that virus-like entry along the cytoskeleton, facilitated by caveolin-mediated endocytosis, enhanced transfection efficacy. These studies demonstrate an increase in transfection efficacy when nanoparticles with pardaxin surface modification, perhaps due to the reduction of potential degradation of genetic material via DNAses due to the avoidance of

lysosomal systems due to pardaxin based interactions. While poorly understood, these studies do suggest that the pardaxin cationic polypeptide facilitates critical intracellular interactions that may facilitate trafficking between the endomembrane system towards the ER membrane and the nuclear envelope, thereby increasing transfection efficacy.

Overall, these studies highlight our current lack of understanding of how intrinsic nanomaterial properties such as size can influence the fate and dynamics within the cell. While size, shape and surface chemistry can significantly influence the method and mechanism of initial cellular entry, how these characteristics influence subcellular trafficking and dynamics are still elusive, with misunderstanding and conflicting studies significantly hampering progress in ER-specific localization [45]. Future developments on the influence of physical and chemical characteristics of nanoparticles as well as better understanding of the proposed pathways for subcellar localization are critical for developing effective therapeutic and diagnostic nanomaterials. However, further studies need to address the complex and labor-intensive procedures during synthesis, conjugation and storage of peptides, as well as the effects of the protein corona and the potential for decreased stability in biological environment for future clinical applications.

2.5.3 Ligand Modifications

ER-targeting nanoparticles functionalized by small molecule moieties leverage specific ligand-receptors interactions localized on the ER [89]. ER-specific moieties, first introduced through medication such as glibenclamide, form the base structure for fluorescent dyes such as ER-tracker, which utilize the sulfonamide moiety for localization [90]. Initially utilized as functional groups for fluorescent probes, sulfonamide and its derivatives have become prevalent ER-targeting moieties for both fluorescent probes and nanomaterials. Sulfonamide shows a strong affinity for the subunit of the ATP-sensitive potassium channel, selectively interacting with the sulfonylurea receptor (SUR), which is predominantly located in the ER. Utilizing interactions between SUR receptors and sulphonamide derivatives, various nanoparticle types, including polymer dots, polymeric nanoparticles, and lipid-based nanoparticles, have demonstrated remarkable ER retention using a variety of sulfonamide derivatives [23, 47, 91].

Caveolae-mediated endocytosis is suggested to play a critical role in sulfonamide-based ER specificity, though the precise mechanism remains elusive. It has been shown in cardiac

myocytes that surface Kir 6.2 channels are recycled via caveolae-mediated endocytosis, facilitated by interactions between caveolin three and the SUR receptor [92-94]. A plausible explanation for the increased caveolae-mediated endocytosis and ER specificity of sulphonamide-conjugated nanoparticles is the binding of sulphonamide to SUR within caveolae. For instance, polymeric nanoparticles functionalized with N-tosyl ethylenediamine displayed strong ER retention within one hour but were inhibited by genistein, a caveolar endocytosis inhibitor [91]. Furthermore, 150 nm dodecyl amine-based lipid nanoparticle lipids have succeeded in toluenesulfonyl-derived ER retention within 3 hours via caveolin-controlled endocytosis in HeLa cells [47]. The dansyl moiety, a notable sulfonamide derivative, particularly interesting due to its dual ability to target the ER and provide fluorescence. Studies utilizing dansyl moieties have shown lysosomal escape via electrostatic repulsion, maintaining a positive surface charge under the acidic conditions of the lysosomes [52, 95]. For example, amiloride, an inhibitor of micropinocytosis in HeLa cells, indicated that lysosomal escape was the primary mechanism of ER retention for dansyl-functionalized supramolecular self-assembling nanomaterials [47]. Similarly, dansyl-modified ER-targeting graphene oxide nanoparticles (ER-GO-NPs) and oleic acid-based lipid nanoparticles depicted robust lysosomal localization before achieving ER retention after six hours [95, 96]. Overall, Sulfonamides offers a cheaper alternative with strong localization capabilities compared to polymers and biological materials thus becoming an attractive strategy for ER targeting. Importantly, sulfonamides as smaller moieties offer much higher stability in biological medium without the risk of degradation via proteases, which may lead to decreased localization efficiency in peptides. However, the potential side effects due to the blocking of SUR receptor need to be further studied to understand and enhance ER specificity for increased efficacy [97].

2.5.4 Cell and Organelle Membrane Coatings

Cell and organelle membrane coatings are one of the most advanced methods for clinical camouflage and facilitate highly specific intracellular trafficking. In most conditions, nanoparticles quickly form a protein corona once arriving in a biological environment, which can significantly alter the targeting capabilities through increased non-specific binding and decreasing its ability to escape the endomembrane system and arrive at the ER [98]. Subsequently, cell and membrane coating this address obstacle by forming a pre-

determined protein corona with organelle specific proteins to ensure strong specificity to its targeted intracellular localization. As such, cell and organelle membrane-coated nanoparticles are designed to camouflage and evade immunogenic and intracellular pathways that are unfavorable for therapeutic application. Different coatings on nanoparticles can trigger specific pathways to achieve these desirable outcomes, with cancer cell membrane-coated nanoparticles and ER-coated nanoparticles showing success in ER retention through distinct mechanisms [99, 100]. For instance, Chen et al. designed cancer cell membrane-coated PLAG nanoparticles loaded with Brefeldin A (BFA) to facilitate lysosomal evasion and enhanced ER retention [99]. The cancer cell membrane coating is thought to promote caveolae-related endocytosis, while the use of BFA inhibits vesicle trafficking, reducing nanoparticle escape. Similarly, Zhang et al. explored the subcellar localization of cancer-coated mesoporous silica nanoparticles (MSNs), finding that uptake pathways were shape-dependent [101]. Silica nanorods, which underwent caveolin-mediated endocytosis, demonstrated stronger ER retention compared to nanospheres that entered cells via clathrin-mediated endocytosis in HPSC and BxPC-3 cells. The authors suggested that the preference for different nanomaterial shapes during various endocytosis events might be related to the differences in energic costs associated to structural change of proteins and the cytoskeletons. Additionally, cancer cell coatings on 50 nm hybrid nanoplates promoted COPI-mediated retrograde transportation, resulting in evasion of the lysosomal pathway and strong retention within the ER in MCF-7 cells [100]. However, cell and organelle membrane coatings struggle with stability and can degrade quickly in suboptimal conditions due to their biological nature [102]. Furthermore, exact proteins and coatings between particles with different surface chemistry may significantly impact on the type and quantity of coating due to random protein corona formation, which can ultimately influence its subcellular localization. Whilst membrane coated nanomaterials display immense potential, the storage, design and stability of these coatings as well as understanding their role in intracellular trafficking are still some of the major challenges that will need to be addressed for future clinical applications.

2.6 Nanomaterials: Properties, Functionality and Application

The design and targeting of specific ER-related pathways hinge on the physical and chemical characteristics most suited to a specific application. Nanomaterial luminescence is

desirable for nanoscale tracking, detection, therapy, and super-resolution imaging [103, 104]. Similarly, achieving biological specificity at both cellular and intracellular level is crucial for enhancing therapeutic treatment [105, 106]. The localization of nanoparticles in subcellular compartments like the mitochondria, ER nucleus, and lysosome has shown significant potential for improved tumor therapy, drug delivery and bio detection [106-109]. Current colocalization studies primarily employ light-based optical methods for their simplicity and ease of use. Particle luminescence allows researchers to visualize and confirm the localization of nanoparticles and ensure the delivery of bioactive materials like proteins, nucleic acids, and therapeutics with subcellular precision. Given the importance of nanomaterial luminescence, varying optical characteristics such as quantum yield, emission wavelength and photostability are tailored to specific applications (Table 1). Dye-conjugation and material-based photoluminescence represent two main strategies developed to achieve photosensitivity or photoluminescence in nanomaterials. Fluorescent dyes offer a simple, commercially available strategy with high quantum yield, often with broad spectra and high absorbance. The large surface area and encapsulating capabilities of nanoparticles make the nanoparticle-dye conjugation system a versatile and effective method for creating LNPs suitable for diverse applications [118]. Common conjugation methods utilize EDC/NHS carbodiimide crosslinking chemistry to form covalent bonds between amine and carboxylate functional groups. Organic fluorescent and photosensitive molecules provide a large range of optical and physical characteristics that can both induce and detect chemical changes within the cellular environment for therapeutic and diagnostic applications. As such, they have been frequently used as photosensitizers, biosensors and well organelle probes *in vivo* and *in Vitro*. However, organic fluorescent dyes are prone to photobleaching and possess overlapping emission and excitation wavelengths, rendering them less suitable for long-term exposure in physiological conditions.

Table 1 Summary of fluorescent dyes or photosensitive materials and their properties

Fluorescent Class	Excitation Wavelength	Emission Wavelength	Solubility	Advantages	Application	Ref
Cyanine dyes	500-800nm	550-850nm	Hydrophilic or Lipophilic	NIR excitation, wide range of excitation and emission wavelengths, clinically approved (ICG)	PDT, PTT, Co-localization, deep tissue imaging	[32, 37]
Doxorubicin	480nm	590nm	Hydrophilic	Chemotherapeutic, clinically approved	Chemotherapy	[96]
Dansyl	340nm	550nm	Lipophilic	ER-specificity	Colocalization and ER targeting	[52]
Fluorescein	500-600nm	500-600nm	Lipophilic	High quantum yield	Colocalization and cell labelling	[80, 110]
Naphthalimide	~445nm	533nm	Lipophilic	Photo-inducible DNA damage, pH and metal sensitivity	PDT, Biosensing	[47, 111]
Luminol	N/A	425nm	Hydrophilic	Chemiluminescence with oxidising agent	PDT	[112]
Porphyrin	670nm	~700nm	Lipophilic	NIR excitation, ROS generation, good photostability, variable functionality	PDT, Biosensing	[113-115]
CS NIR	~690nm	~716nm	Hydrophilic or Lipophilic	Optically tuneable hydroxyl group	PDT, deep tissue imaging	[116, 117]

PTT: Photothermal therapy; PDT: Photodynamic therapy; NIR: Near-Infrared; DiD: 1,1'-Dioctadecyl-3,3,3',3'-Tetramethylindodicarbocyanine Perchlorate; ROS: Reactive oxygen species; CS NIR: Chang Shang Near-Infrared Dye.

The host material for ER-LNPs is one of the critical factors that can dictate the efficacy and effectiveness for the desired application. A plethora of materials have demonstrated that unique physical and chemical characteristics dictate the application and efficiency of different nanomaterial hosts (Table 2). In cases where photostability and photobleaching are critical detriments that need to be avoided, often in long-term laser excitation for biosensing or phototherapy, non-organic fluorescence has become an attractive approach to avoid such obstacles. Often, non-organic material fluorescence stems from optical properties in non-organic host materials, where photo-induced degradation cannot disrupt the inorganic bonds of the material [119]. As such, non-organic, host-based luminescence offers differing applications given its higher stability. For example, sub-diffraction microscopy relies on unique, yet tunable optical properties, the instability and rapid photobleaching typical of traditional fluorescent dyes make them poor candidates for sub-diffraction microscopy. Conversely, there is immense potential for LNPs as probes for super-resolution microscopy and intracellular detection due to their enhanced photostability, optical non-linearity and tunable optical switching [120, 121]. Photoluminescent materials like up-converting nanoparticles and quantum dots emit light through physical phenomena such as photon up-conversion and quantum confinement, avoiding photochemical degradation and thus offering significant resistance to photobleaching [122, 123]. These inorganic materials possess innate and unique luminescent properties ideal for phototherapy, bioimaging, labelling and detection [120]. While photoluminescent materials forgo the requirement of dye conjugation, they are limited in size and composition, with less material flexibility and lower carrying capacity, and typically exhibit lower quantum yield.

Besides the use in imaging and diagnosing cellular structures and functions, luminescent nanoparticles also possess exceptional therapeutic potential due to non-invasive and non-hazardous nature of photo-based therapy. The controlled release and activation of therapeutic molecules, facilitated through either photo-stimulated drug release or PDT, are subject of intense research due to their significant clinical potential [124]. Nanomaterials that are inherently responsive to external environment changes, with or without light stimulation, can facilitate the controlled release of therapeutic drugs for tumor therapy [80, 125]. PDT utilizes photosensitizers to generate oxygen radicals that induce oxidative stress at an intracellular level, leading to tumor elimination through apoptosis or ICD [126].

Conversely, the reduction of ROS via light-stimulated therapy can lessen cellular dysfunction and enhance overall cell survival [25]. Thus, photo-triggered therapy has emerged as a compelling research field, offering synergistic, minimally invasive, selective, and versatile strategies for clinical applications.

Photothermal therapy (PTT) features a simple yet precise approach to supplement current clinical cancer therapies through light-induced heat generation. NIR-responsive materials, which penetrate deeper and exhibit lower phototoxicity compared to visible and UV light, enhance the efficacy of photothermal therapy. Unlike conventional radiative heat transfer methods, which feature thermal energy across targeted areas potentially damaging surrounding healthy tissue, laser-generated phototherapy induces non-specific hyperthermia, minimizing damage to adjacent healthy [127]. While the specificity of laser-based PTT minimizes damage towards surrounding healthy tissue, ER-targeting phototherapy aims to maximize intracellular photothermal damage by exploiting its large surface [128-130]. Considering the inflammation-induced angiogenesis and reduced anti-tumor effects following high-temperature photothermal therapy, lower-temperature PTT can induce apoptosis and ICD through ER-stress-based pathways. The temperature-sensitive nature of enzymes, which rapidly unfold and denature at temperatures above 40°C, mean nanoparticle-based ER-specific PTT can trigger heat shock proteins to initiate the unfolded protein response, without precipitating rapid cell death through necrosis [131-133]. Consequently, the necrotic effects of PTT have led to advancements in synergistic PDT and PTT. Synergistic phototherapy is increasingly recognized for its enhanced tumor elimination potential by targeting multiple pathways to facilitate ER-stress induced apoptosis and ICD [32, 134-136]

Table 2 Summary ER targeting nanomaterials and their advantages

Host	Size	Highlights	Application	Ref
Carbon dots	2-10nm	Fluorescent, tunable emissions, Responsive to environmental changes	Imaging, intracellular detection	[137, 138]
Polymer dots	5-50nm	Fluorescent, tunable emissions, Responsive to environmental changes	Imaging, intracellular detection	[139, 140]
Graphene nanoparticles	10-200nm	Complete spectrum absorption for phototherapy	PDT/PTT, combinational therapy	[141]
Quantum dots	2-10nm	High quantum yield, non-bleaching emissions, narrow emission spectrum	Super-resolution imaging, detection, sensing	[1, 142]
Metallic nanoparticles	10-100nm	Strong stability, full spectrum absorption, can facilitate photocatalytic reactions, NIR absorption, potential magnetic properties	PDT/PTT, combinational therapy, imaging	[61]
Lanthanide doped nanoparticles	10-100nm	Up-conversion luminescence for deep tissue penetration, non-blinking and non-photobleaching emissions, multiplexing capabilities, X-ray induced persistent imaging	PDT, super-resolution imaging, nano-thermometry, multiplex imaging	[5, 143, 144]

Silica nanoparticles	10-300nm	High drug loading, good biocompatibility	Drug delivery, combinational therapy, photo-responsive drug delivery, immunotherapy	[145]
Polymeric nanoparticles	50-500nm	Strong solubility, easy lysosomal escape, good biocompatibility, biodegradable	Drug delivery, immunotherapy, combinational therapy, nanoprobe encapsulation	[85]
Lipid nanoparticles	50-200nm	Biodegradable, strong biocompatibility, efficient delivery of hydrophobic and hydrophilic materials	Drug delivery, immunotherapy, combinational therapy	[79, 146, 147]
Peptide and nucleic acid nanostructures	5-200nm	Biodegradable, strong biocompatibility, precise and organized assembly,	Drug delivery and gene delivery	[148, 149]
MOFs	30nm-500nm	Stable encapsulation of enzymes, strong biocompatibility, high surface area	Drug delivery	[150, 151]

PDT: photodynamic therapy; PTT: photothermal therapy; MOFs: Metal organic frameworks

2.6.1 Non-metallic Nanomaterials

Non-metallic nanomaterials encompass a diverse class of compounds with varied physical and chemical properties, presenting potential across multiple domains. For example, carbon-based nanomaterials, including graphene-based nanomaterials, nanodiamonds, and semiconducting polymer dots, are suitable candidates for drug delivery and PDT due to their biocompatibility and stability (Figure 2.5a). An emerging area of development involves sub-20 nm fluorescent carbon-based nanomaterials, which exhibit unique optical properties such as size independence, shorter lifetimes and broader emissions spectra [138]. The synthetic approaches for graphene quantum dots and carbon dots differ significantly, each leading to distinctive features suitable for specific applications. For example, the top-down approach in creating graphene quantum dots allows for scalable production of materials with anisotropic structures [152, 153]. Conversely, the bottom-up synthesis of carbon dots typically yields spherical nanoparticles with varied surface functional groups, enhancing their surface chemistry for better cellular sensing, detection, and therapeutic functions [140, 154]. Anisotropy and high chemical reactivity of aromatics and conjugated alkenes can lead to changes in luminescent intensity or emission wavelength due to fluctuations in energy transfer pathways, triggered by variations in the interaction between the analyte and the nanomaterial's surface. For example, the amination of lauryl amine on carbon dots surfaces allows for pH detection between 6.2 and 7.2 by altering luminescent intensity, a phenomenon influenced by the concentration of lauryl amine [70].Changes in luminescent intensity result from surface quenching through alternative energy transfer pathways, activated by interactions between hydrogen ions and the carboxyl and amine surface groups. Similarly, another study observed shifts in emission wavelength at pH levels ranging from 3.3 to 4.4, attributing these changes to variations in chemical bonds such as C-C/C=C and O-C=O [155]. Direct and real-time observations of precise subcellular stress and hypoxia can be crucial for early disease diagnosis. For instance, tunable carbon dots synthesized using o-phenylenediamine (OPD) and lysine have been employed to detect changes in ER polarity through fluctuating wavelength emissions (figure 2.5b)[69]. In this design, increasing the amount of lysine facilitated n-π^* transitions of C=N and C=O, enhancing absorbance at 315 nm and thereby increasing blue emissions. The addition of lysine is thought to reduce carbonisation, decrease the sp^2 domain within the carbogenic core, and increase OPD polymerization,

leading to a blue-shifted green emission. The fluorescent behavior of these carbon dots is significantly affected by environmental polarity, characterized by a decrease in green emissions and a red shift in emission wavelength. Remarkably, these carbon dots are insensitive to pH or solvent polarity, making them particularly useful in diverse biological environments. They have been utilized to monitor tunicamycin-induced ER stress through altered green/blue fluorescence in hypoxic conditions, which can provide valuable insights into cellular responses to stress. Future studies must further explore the long-term interactions of carbon dots with cells before utilizing them for real-time intracellular chemistry detection [156].

Another class of carbon-based nanoparticles photoluminescent semiconductor nanoparticles consisting of π-conjugated organic polymers termed polymer dots. While they share some similarities with polymeric nanoparticles, namely consisting of organic polymers, polymer dots utilize hydrophilic polymers, resulting in semiconducting

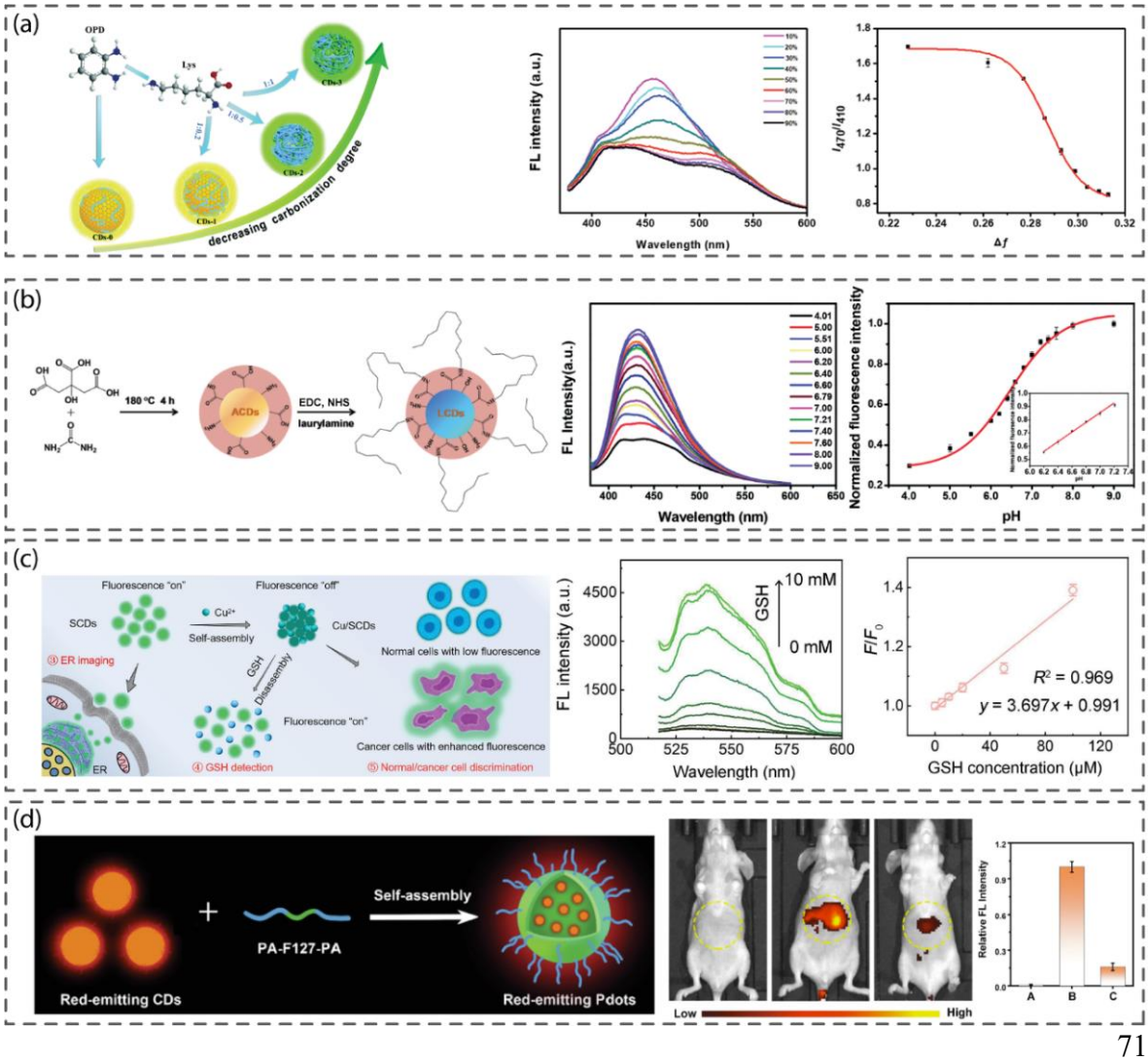

Figure 2.5 Non-metallic nanomaterials and their applications. (a) Schematic representation of carbon dots with tunable emissions dependent on lysine and o-phenylenediamine precursor ratios. Polymer dot fluorescence with different mixtures of water and 1,4-dioxane under 360nm excitation.[69] (b) Depiction of sulphur-doped carbon dots and their intracellular interactions. Fluorescence emission spectra of sulphur-doped carbon dots at differing concentrations of glutathione and its normalized relationship.[159] (c) A representation of the design of self-assembled carbon dot encapsulated polymer dots and the detection of copper in mice injected intraperitoneally with (a) PBS (b) polymer dots (100μg ml^{-1}, 50μL) (c)polymer dots with copper ions (50μM 50μL) [23] (c) Schematic of environmentally responsive ER targeting mesoporous silica nanoparticles. H&E staining depicts the effects of H_2O_2-responsive mesoporous silica nanoparticles releasing melittin (MEL) during pathogen infections. Cal represents cells infected with *C. albicans*, MSN and MSNE represent non-targeting and targeting nanoparticles, respectively, and TPB represents bromobenzyl acid linker.[80]

properties and photoluminescence at the expense of insolubility in water before surface modification. As such, they do not act as effective strategies for drug encapsulation or payload delivery like polymeric nanoparticles and are instead frequently used for bioimaging and biosensing [140]. The luminescent properties of polymer dots are a result of core and surface hybridization via π-conjugated polymers, a phenomenon known as cross-linked-enhanced emission (CEE) [139, 157, 158], which make polymer dots natural candidates as sensor and detectors in biological environments. Their sensitivity to external environment changes, as detected by a shift in luminescent intensity or emission wavelength, rises from fluctuations in energy transfer pathways influenced by interactions between the analyte and the nanoparticle surface. For example, detectable changes in emission intensity due to pH shifts result from surface quenching processes driven by alternative energy transfer pathways. The manipulation of lone pair interactions between carbon double bonds and nitrogen or oxygen can result in different emission wavelengths for carbon-based quantum dots. Huang et al. developed NIR carbon dots encapsulated by polymer dots for *in vivo* copper detection, with the detection of copper ions being observable within 120 seconds and ranging between 0.25 – 9 μM, with a detection limit of 13nM [23]. The chelation of carboxyl groups in the carbon dots with copper ions led to a noticeable decrease in fluorescence intensity, detectable in live cells, zebrafish, and mice models. Polymer dots, which are generally larger in size compared to carbon dots, are limited by the variation of materials that they can detect in a biological environment which

are triggered by ion or molecule specific chemical interactions.

Graphene-based nanomaterials, consisting of a two-dimensional sheet of hexagonally arranged carbon lattices, demonstrate unique physical and chemical characteristics, including a high surface area. These properties confer intrinsic anti-tumor characteristics by increasing oxidative stress and enhancing tumor sensitivity to drug delivery and chemotherapy. Additionally, the energy band gaps of graphene-based nanomaterials allow for strong NIR absorption, facilitating deep tissue penetration for photothermal therapy [137, 160]. However, pure graphene exhibits limited stability and poor solubility in physiological environments due to its lack of hydrophilic functional groups. As such, graphene oxide has become an alternative in nanomedicine applications due to the abundance of hydrophilic functional groups introduced through Hummer's method [141]. The stacking of π bonds in graphene oxide nanoparticles significantly increases drug loading, due to an increased surface area to volume ratio. Moreover, graphene oxide-based nanomaterials can be further reduced to alter their carbon and oxide ratio, enhancing their photothermal properties by increasing NIR absorbance while simultaneously reducing toxicity at the expense of decreased stability in physiological conditions [161]. Metal-doped carbon nanoparticles, as demonstrated by Bao et al., can rapidly elevate tumor temperatures to 60.2 °C, leading to significant tumor volume reduction through necrosis and apoptosis [158, 162]. The NIR photothermal properties, facilitated by the first or second van Hove singularities formed by metal-ion conjugation, enable deep tissue tumor ablation. However, high-temperature, ER-specific PTT has its drawbacks as rapid and non-specific cellular thermal damage can quickly trigger the release of potassium ions from tumor necrosis, reducing anti-tumor activity due to increased CD4 and CD8 T cell dysfunction [163, 164]. Additionally, the inflammatory response of tumor cells during hyperthermia can enhance tumor growth and recurrence through angiogenesis and metastasis [165, 166]. Luminescent graphene nanomaterials also serve as nanocarriers for the delivery of chemotherapeutic drugs, owing to their high stability in intracellular environment. For example an increased expression of ER-stress and apoptosis-associated proteins CHOP and LC3B demonstrated ER-specific delivery of doxorubicin and cisplatin through luminescent graphene nanoparticles, enhancing ER stress-associated apoptosis in lung and triple-negative breast cancer cells [96]. Overall, graphene based nanoparticles possess many physical characteristics attractive for both diagnostic and therapeutic applications, but are limited

due their difficult functionalization as well as to their instability in biological environments that may lead to potential cytotoxicity [167].

Mesoporous silica nanoparticles (MSN) are biodegradable nanomaterials which feature a large surface area to volume ratio, with tunable porosity and size to augment their drug loading capacity [145]. MSN can incorporate additional nanomaterials to create multifunctional nanocomposites with superior biocompatibility across various applications. For instance, Zhao et al. utilized ER-targeting mesoporous silica nanoparticles to combat systemic infection both *in vivo* and *in vitro* [80]. This innovative design facilitated the rapid release of therapeutic peptides upon H_2O_2 exposure by incorporating a peroxide-sensitive bromobenzyl acid linker, making the nanoparticles inherently responsive to pathogen-macrophage interactions. With strong localization in macrophages, the release of melittin peptides inhibited pathogen growth and mitigated cellular dysfunction by reducing pro-inflammatory cytokine production and ER stress, which in turn decreased kidney dysfunction and mortality in mice from systemic fungal infections. With many clinical investigations exploring the immense potential of silica nanoparticles, they remain one of the most promising materials for clinical use due to their biocompatibility, non-toxicity and degradation in a clinical setting [168].

Alternatively, numerous inorganic nanomaterials possess optical properties that are highly applicable to diagnostics and phototherapy. Quantum dots, one of the earliest classes of optical nanomaterials, typically range in size from 1-10 nm. They have become a commercially viable option due to their remarkable optical properties, including high quantum yield, size-tunable and narrow emission spectra, and strong resistance to photobleaching. However, the toxicity of certain quantum dots, particularly those containing heavy metals like cadmium and zinc (e.g., Cadmium-selenium (CdSe) and Zinc-selenium (ZnSe)), can induce cell death through mechanisms like ROS generation and lipid peroxidation. In contrast, silicon quantum dots present a lower toxicity alternative, making them suitable for live cell labelling. The luminescence of quantum dots originates from changes in confinement energy when the band gap of semiconductor materials becomes smaller than their de Broglie wavelength, leading to size-dependent tunable absorption and excitation emissions [157, 169, 170]. This quantum confinement effect facilitates remarkable optical properties, enhancing their utility in super-resolution imaging techniques such as Stimulated Emission Depletion (STED) and Structured Illumination

Microscopy (SIM). Despite their advantages, the broad absorption and blinking properties of quantum dots pose challenges for further development [142]. Interestingly, the stochastic blinking nature of quantum dots facilitates super-resolution imaging by allowing independent and statistical analysis of quantum dot emission states through time-averaging frames over specific period [171]. The optical properties of quantum dots make them excellent probes for studying and observing transportation and interactions between the ER and cytoskeleton in cellular studies, however, the potential toxicity due to heavy metal doping makes them difficult to applied in a clinical setting [172].

The demand for detection and sensing applications emphasizes the need for candidates that are photostable, biocompatible, and highly sensitive to environmental changes. Photoluminescent carbon-based nanomaterials are widely favored for biosensing applications due to their specific optical properties. However, apart from silica nanoparticles, the long-term effects of many non-metallic nanoparticles, as well as potential cytotoxicity during degradation are some of the critical factors that need to be investigated before their translation to clinical applications.

2.6.2 Metallic Nanoparticles

Metallic nanomaterials are remarkably uniform and stable under most biological conditions, boasting unique physical properties that make them suitable for a variety of novel applications. The lattice structure of metallic material significantly influences their physical and chemical properties. While some metallic nanomaterials possess optical properties, most inorganic materials, such as copper NPs, iron oxide NPs, and silica NPs are non-luminescent materials but possess fundamental physical and chemical properties desirable for different applications (Figure 2.6). For instance, magnetic iron nanoparticles are widely used in biomedical imaging due to their paramagnetic properties. Surface-modified iron nanoparticles can accumulate specifically at targeted sites, enhancing their potential for diagnostic and therapeutic purposes. They serve as contrast agents in magnetic resonance imaging (MRI) by reducing the longitudinal spin-lattice relaxation time, which improves image clarity [173]. Moreover, iron nanoparticles facilitate the stimuli-responsive release of therapeutic agents. Given the multi-oxidation state of iron ions, these nanoparticles can be engineered to response to external stimuli such as temperature, magnetic field, or pH changes [174, 175].

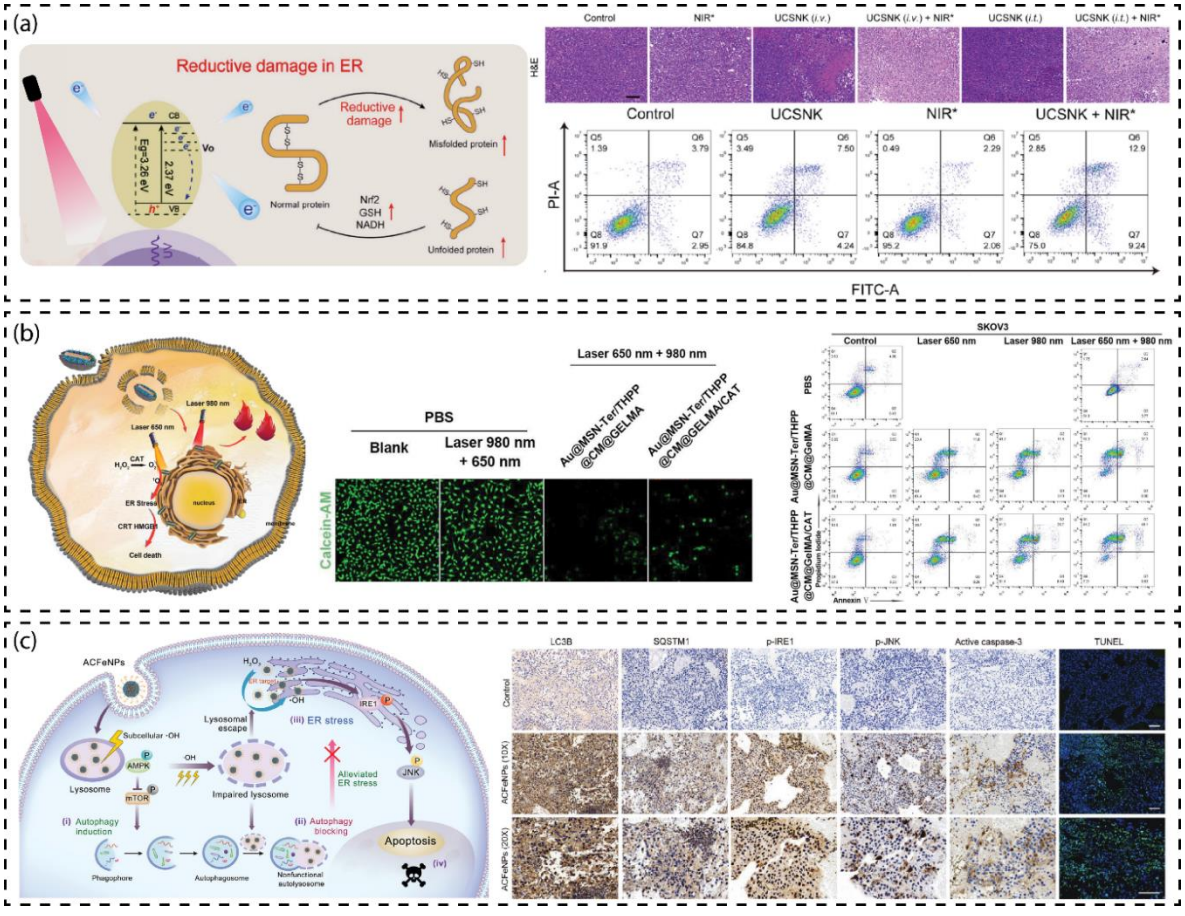

Figure 2.6 Application of ER-specific metallic nanoparticles (a) Representation of the intracellular maladaptation through NIR photodynamic reductive damage of proteins facilitated by electronic interference. H&E staining of tumour cells under different treatments after 14 days. Flow cytometry analysis of 4T1 cells apoptosis through annexin V-FITC.[84] (b) Dual laser synergistic photothermal and photodynamic therapy of gold nanorods with mesoporous silica, tosyl ethylenediamine, cancer membrane coating and porphine in gelatin microgel and surface catalase (Au@MSN-Ter/THPP@CM@GelMA/CAT) for ER stress-activated ICD. Confocal microscopy for SKOV3 cell death analysis (Red: PI, Green: Calcein-AM). Apoptosis analysis through flow cytometry post-treatment and irradiation. Treatment conditions were 48 hours after laser irradiation of 650nm (0.4W/cm2, 5min) and/or 980nm (1W/Cm2, 10 min).[135] (c) Schematic of ACFeNPs and its inhibition of organelle crosstalk to enhance tumor elimination through induced ER stress without alleviation from autophagy using pre-established lysosome impairment. Immunohistochemical staining after three days of ACFeNP exposure in human hepatoma tumors reveals enhanced expression of ER stress and apoptosis markers.[125]

The Fenton reaction exploits the naturally acidic conditions in tumor microenvironments to control drug release and produce ROS. Iron nanoparticles provide exogenous iron ions

that react with naturally occurring hydrogen peroxide from glucose metabolism, facilitating the Fenton reaction. This reaction produces hydroxyl radicals and hydroxide ions, enabling site-specific drug release and targeted organelle damage PDT can employ the Fenton reaction to generate hydroxyl radicals that induce ER stress [125, 176]. The acidic tumor microenvironment and the overexpression of peroxide enhance the selectivity and efficacy of Fenton-based treatments.

Approaches in phototherapy often favor the usage of near-infrared (NIR) wavelengths due to their low phototoxicity and deeper penetration, making luminescent materials such as up-converting nanoparticles and NIR dyes popular choices for photodynamic therapy. For instance, NIR-responsive, ER-targeting PEG polymeric nanoparticles can induce ICD through PDT [114]. The generation of ROS via the conjugated photosensitizer triggered downstream activation of ER stress and UPR. The low half-life of oxygen required high selectivity to enable rapid ROS diffusion across the ER membrane, enhancing the effectiveness of cancer immunotherapy. Yet, other luminescent materials like up-converted nanoparticles also hold potential for future biosensors due to their photostability, deep penetration and low background fluorescence afforded by NIR absorption bands [177, 178].Given the vast potential application of ER-specific PDT, current research aims to further enhance PDT-induced ICD and apoptosis through strategies like starvation therapy [112], autophagy modulation [179], increasing oxygen levels by decreasing oxygen consumption[154] or allowing for oxygen delivery [32, 113]. Considering their close interactions with the endo-lysosomal system, Li et al. demonstrated that disruptions between subcellar interactions could enhance ER-stress-mediated apoptosis [125]. They achieved lysosome destruction using hydroxy radicals generated by the Fenton reaction through ER-specific amorphous core-shell iron nanoparticles. The AMPK/mTOR pathway could not mitigate the resulting ER stress due to lysosomal destruction, which impaired autophagosome and lysosome interactions. This resulted in fully activated apoptosis via the ER stress-induced IRE/JNK pathway without autophagy alleviation.

Copper nanoparticles, facilitate a copper-dependent pathway of programmed cell death deemed knowns as kurtosis [180]. As an essential co-factor for many proteins, excessive copper accumulation within cell disrupts mitochondrial metabolic function through protein-aggregated proteomic stress, leading to ‘cure ptosis’. This mechanism has been exploited to enhance cancer immunotherapy [181]. In related research, Wan et al. developed a

photothermal approach to treat triple-negative breast cancer cells (TNBC) by circumventing the common challenges associated with photothermal therapy [134]. They utilized ER-specific, photothermal, and thermal responsive copper disulphide nanoconstructs to enable the photo-thermally regulated release of the anti-inflammatory agent celecoxib, reducing vascular inflammation while inducing ER stress-mediated ICD. The ER specificity of these nanoconstructs enhanced immune cell recruitment, and the synergistic combination of photothermal therapy and PDT reduced TNBC recurrence and tumor metastasis under NIR-II irradiation.

While typically not luminescence, gold nanoparticles exhibit NIR absorbance optical properties through the surface plasmon resonance effect. This surface effect arises from the matching oscillations between the electronic vibration of gold nanoparticles with NIR wavelengths, which facilitates stronger absorption and scattering intensities. Inert in biological systems, gold nanoparticles possess conduction band electrons that match and resonate with photons to exhibit surface plasmon resonance applicable for dark field plasmonic imaging and NIR photothermal therapy [182, 183]. The aggregation state of gold nanoparticles influences their optical scattering properties, which result in distinct color changes and scattering wavelengths [182]. The optical stability of plasmonic gold nanoparticles (low blinking and photobleaching) makes them suitable for intracellular labelling and detection [184]. ER-targeting plasmonic gold nanoparticles have demonstrated remarkable capabilities for tracing molecular stress during electrical stimulation through surface-enhanced Raman spectroscopy (SERS)[110]. Changes in SERS peaks and Raman spectra, detected by plasmonic nanoparticles, were complementary to protein degradation, cytochrome C release and formational changes in protein structure during electrical stimulation-induced ER stress. Furthermore, plasmonic gold nanoparticles detected fluctuation in tyrosine and tryptophan amino acid Raman spectra during electrically stimulation ER stress. The absorption of light from gold nanoparticles comes with both benefits and challenges, as overheating in non-photothermal applications may damage in influence the detection and results of intracellular plasmonic nanoparticle tracking and detection [185].

Up-converting nanoparticles are lanthanide-doped nanocrystals known for their photon up-conversion capabilities. Consisting of thousands of lanthanide ions in the crystal lattice, these nanocrystals matrix of sensitizer and activator ions enable an anti-stoke shift through

multiphoton absorption. As a result of lanthanide-based photon up-conversion, these nanocrystals do not exhibit photobleaching or blinking. The 4fn electronic configuration of lanthanide ions allows multi-photon excitation through various processes, allowing for the emission of higher energy visible photons after the absorption of multiple NIR photons [186]. Up-converting nanoparticles possess dopant and concentration-dependent tunable emissions and absorption wavelengths, which can be further enhanced through dye sensitization and optical engineering [187-190]. Their nonlinear, nonbleaching and nonblinking emission properties minimize background fluorescence for super-resolution imaging, single particle tracking and in vivo deep tissue imaging [191]. Furthermore, core/shell up-converting nanoparticles can enhance luminescence by reducing surface quenching, as well as introduce multiplexing capabilities in both the NIR-I and NIR-II window through lifetime and luminescence alterations [144, 178, 192-194]. Matching emission and excitation wavelengths between up-converting nanoparticles and photosensitizers enable NIR-based photothermal and PDT through luminescent resonance energy transfer (LRET) [195-199]. In one such study, NIR-responsive up-converting nanoparticles provided a counterintuitive approach to induce apoptosis by reducing ER oxidation and leveraging reductive damage for cancer cell death [84]. Utilizing electronic interference therapy, NIR up-converting nanoparticles facilitated NIR to UV conversion, allowing for the separation of electrons from tin oxide into ER for reductive damage that induced the breakdown of protein disulphide bonds. Photogenerated electrons from the reduction of Sn^{2+} to Sn^{4+} produced an ~190 ps excited-state relaxation process, observed via transient absorption spectroscopy as the protein disulphide bonds were reduced within the ER. The upregulation of the intracellular redox homeostasis regulator NRF factor demonstrated that the accumulation of misfolded proteins within the ER and subsequent cell apoptosis was a result of nanoparticle-based light-induced ER maladaptation. Future applications can potentially apply lanthanide doped nanocrystals with multiplexing or persistent luminescence properties for direct, long term intracellular tracking in order to eliminate phototoxicity and autofluorescence and to study the inner trafficking and distribution of inorganic nanocrystals [200, 201].

Metal-organic frameworks (MOF), popular for their high surface area and tunable size and porosity, are another class of metallic nanomaterials that enable precise enzyme delivery to targeted sites, reducing enzyme aggregation, degradation, and enhancing

specificity. These frameworks protect enzymes from harsh external environments, such as lysosomes and proteases, and promote cellular uptake and endosomal escape for improved delivery [150, 151]. Furthermore, MOFs show potential as contrasting agents and biosensors due to their ability to carry metallic ions with paramagnetic properties. The delivery of metallic ions into the cellular environment can act as catalytic artificial enzymes which interact with the intracellular ions to reduce oxidative stress. For example, Ruthenium nanozyme carrying MOFs demonstrated reduced oxidative stress in brain tissues after ER localization, with a reduction of neuroinflammation and MMPs expression after a one-time intravenous administration [27]. The biological applications of MOF remain critically understudied due difficulties in maintaining stability in biological environments, as well as the potential to contain trace heavy metals after degradation which can induce cytotoxicity [202, 203].

2.6.3 Organic Nanoparticles

Organic nanoparticles and their respective derivatives have become a class of nanomaterials that have already been approved by the American Food and Drug Administration (FDA) for use as vaccines and drug carriers [204]. Exhibiting superior biocompatibility compared to inorganic counterparts, organic nanoparticles possess fewer unique physical and chemical properties and are typically less stable in biological conditions. Despite these challenges, lipid nanoparticles have emerged as highly successful nanomaterials for clinical and therapeutic applications (Figure 2.7). Their success in a clinical setting is attributed to their self-assembling nature and the diverse array of designs developed over the past decade. Their biocompatibility, low toxicity, and ability to encapsulate hydrophobic drugs make lipid and polymeric nanoparticles favored candidates for drug and gene delivery [146]. As a central role player for signaling, homeostasis, protein transcription and intracellular quality control, precise ER delivery enhances the therapeutic efficacy of drugs and genetic materials directly occurring within the ER. Additionally, lipid-based nanoparticles facilitate endosomal escape through endocytosis once they enter the cell to enhance biocompatibility. Endosomal escape can occur through lysosomal degradation due to the ionizability of lipids at low pH or through endosomal fusion, which is modulated by the energic costs and topological transformation of the endosomal membrane during the fusion and fusion-pore formation [49, 147].

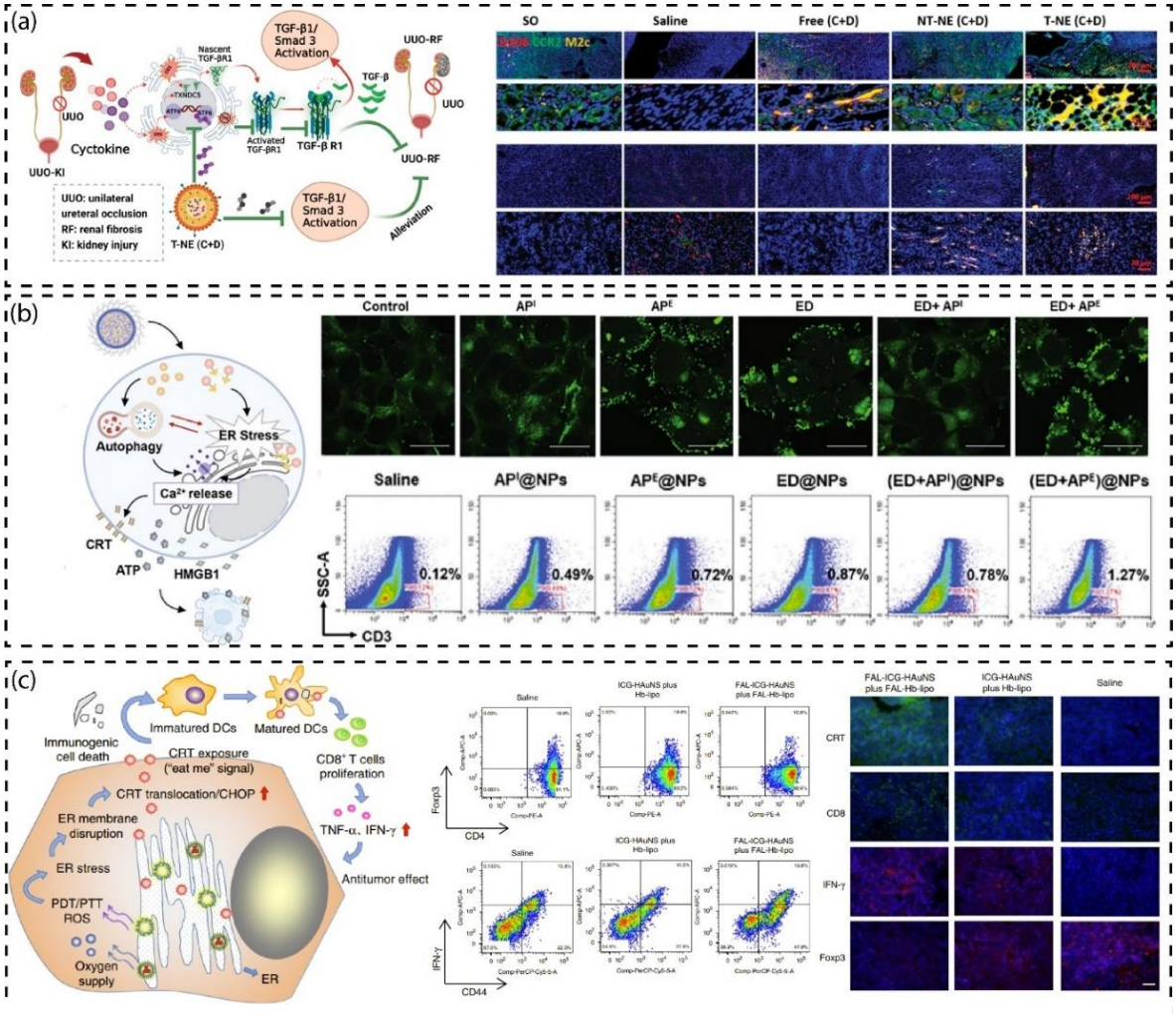

Figure 2.7 Organic nanoparticle applications (a) Schematic of renal fibrosis alleviation through Ceapin 7 and Dexamethasone delivery to the ER for TGF-B1/Smad 3 for controlled macrophage polarisation. Immunofluorescent staining of M2c macrophages in left (top) and right (bottom) kidney **(b)** ER-specific immunogenic cell death is enhanced through autophagy activation through elevated Ca^{2+} release. CLSM depicts LC3 expression in different treatment groups, Api:3-methyadenine, Ape: rapamycin, ED: p-toluene sulfonyl modified doxorubicin. Loaded in PLGA nanoparticles. Flow cytometry analysis of CD3+ and CD8+ T cell maturation after treatment.[179] **(c)** Synergistic photodynamic and PTT through simultaneous exposure of hollow gold nanoparticles (ICG-HAuNS) and haemoglobin-encapsulated lipid nanoparticles (Hb-lipo). Flow cytometry of activated and regulated T cells after treatment with and without ER targeting moiety pardaxin (FAL). Immunofluorescent staining of CD8+ T cells, interferon (IFN)-γ, Foxp3+ T cells after treatment. Scale bar 50 μm.[32]

Advances in lipid design and synthesis have introduced unique structural features such as chain length, saturation, and head group, which dictates the morphology and functional

properties of the assembled nanoparticle. Lipid nanoparticle self-assembly is driven by the undesirable interactions between the aqueous environment and the non-polar domain of lipid molecules [205]. The non-polar domains of lipid molecules will assemble and encapsulate non-polar domains to avoid unfavorable interactions and form a surface layer based on the domains that are more favored in an aqueous environment. Different classes of lipid nanoparticles are defined by their internal structure. To enhance the solubility and delivery of lipophilic hydrophobic molecules, liposomes were one of the first approaches to enhance the delivery of unstable drug molecules. Typically composed of phospholipids and emulsifiers, liposomes possess a lipid bilayer to encapsulate hydrophilic molecules in the aqueous interior and localized hydrophobic drugs in its membrane sections, with sizes varying greatly depending on the application [206]. On the other hand, solid lipid nanoparticles represent a new generation composed of solid lipids, offering enhanced stability, higher loading capacity, and higher biocompatibility. Possessing a solid lipid core matrix for enhanced loading capacity, solid lipid nanoparticles can offer controlled release and higher compatibility but are unable to deliver hydrophilic drugs without an aqueous interior.

For instance, a pivotal study by Li et al. designed ER-selective PDT and PTT to precisely target pathways inducing ICD and apoptosis, without facilitating necrosis [32]. This approach involved the simultaneous delivery of indocyanine green-modified hollow gold nanoparticles and hemoglobin-encapsulated liposomes, providing sufficient oxygen supply for ROS production and inducing a persistent imbalance of intracellular calcium between the ER and cytoplasm, thereby perpetuating ER stress. The sustained ER stress led to the continuous release of damage-associated molecular patterns (DAMPs), triggering ICD as evidenced by the increased expression of multiple ER stress protein markers. Increased fluorescence of surface-exposed calreticulin (CRT) and enhanced HMGB1 translocation from the nucleus were attributed to the DAMP-promoted ICD effect from PDT. CHOP and CRT translocation induced dendritic cell maturation, which resulted in the production of CD8+ T cells, increasing TNF-α and INF-γ proteins for an enhanced anti-tumor effect. By minimizing the obstacles from the physical characteristics of both organic and inorganic material, combinational therapy utilizing the advantages of both inorganic and organic nanomaterials has immense potential for future clinical applications.

Organic polymer-based nanoparticles are flexible in physical and chemical properties,

providing superior solubility and strong shielding capabilities [85]. Composed of copolymers, these nanoparticles introduce diverse physical and chemical characteristics. They are highly biocompatibility due to their solubility, low toxicity, chemical inertness and non- immunogenic nature. Notably, their effective lysosomal escape makes them highly desirable for precise intracellular drug delivery. Several mechanisms facilitate the lysosomal escape of polymeric nanoparticles. The 'proton sponge' effect, for instance, involves the rupturing of endosomal and lysosomal membranes during osmolysis as the polymers experience varying pH levels. Protonation of the polymers, as they move to more acidic cellular compartments, induces the transport of negative ions to maintain charge balance, leading to osmotic swelling and membrane rupture for particle escape. Alternatively, membrane destabilization is attributed to membrane damages at localized regions of contact, which facilitates endosomal escape [207]. Like lipid nanoparticles, the assembly of polymers is thermodynamically favored in specific environments, enhancing drug loading capacity and efficiency [205]. Electrostatic interactions between negatively charged molecules such as nucleic acids and positively charged polymers enhance delivery and particle stability in biological environments. Increasing the drug delivery efficiency of non-soluble molecules through enhanced solubility, as well as avoiding the degradation of drugs through polymer coating are the critical advantages of polymeric nanoparticles that make them appealing for future clinical use.

Lipid-polymer hybrid nanoparticles have become a novel approach that features advantages from both materials. Luo et al. derived a therapeutic approach by modulating TFG-B1 and Smad 3 using stress inhibitors and glucocorticoids delivered directly to the ER using nanoemulsions [28]. The M2c subtype macrophages inhibited cytokines production and reduced disease progression by suppressing the macrophage-to-myofibroblast transition. Furthermore, stress-induced macrophage polarization has been shown to regulate pulmonary fibrosis through chronic inflammation, potentially leading to irreversible lung damage or death [208, 209]. Their loaded ER-targeting micelles are responsive to high ROS levels with the ER stress inhibitor KIRA6 and the anti-inflammatory drug Dexamethasone, which reduced cytokine storms and restored ER homeostasis to prevent acute lung injury and pulmonary fibrosis (Figure 2.6). The repolarization of macrophages through inhibiting oxidative and ER stress can also enhance tumor immunotherapy [210]. KIRA6 inhibition of the IRE-XBP1 pathway reprogramed M2-tumour-associated macrophages in hypoxic

conditions by increasing glycolysis and decreasing fatty acid oxidation, facilitating the sensitization of anti-PD1 immunotherapy. Overall, while lipid-polymer hybrid nanoparticles are more complex in nature in comparison to polymeric or lipid nanoparticles, making them more difficult to manufacture, the polymeric characteristics of the particles increase structural integrity and drug delivery efficacy and capacity, while the outer lipid layer significantly enhances biocompatibility makes them a compelling advancement over conventional lipid and polymer nanoparticles [211].

Degradation of organic nanoparticles after cell entry avoids potential toxicity from bioaccumulation as well reducing damaging during kidney and liver accumulation, which apart from silica nanoparticles, are characteristics that have not been vigorously studied in non-organic nanoparticles [44]. Due to high biocompatibility and their organic nature, understanding the long-term effects of organic nanoparticles are significantly less difficult compared to non-organic nanoparticles that may contain heavy metals or materials which are extremely non-reactive. Furthermore, controlled drug release during the degradation of organic nanoparticles makes them suitable candidates of highly specific therapeutic applications. As such, organic nanoparticles and silica nanoparticles remain as some of the most promising candidates for future clinical applications, supported by numerous clinical trials demonstrating their safety and efficacy, as well as FDA approved treatments such as the COVID vaccine. The circulation and degradation of non-organic particles must be further understood to facilitate potential clinical use.

Innovative nanostructures utilizing peptides, nucleic acids, and organic frameworks have also emerged as novel strategies for a variety of applications [148, 150, 212]. The inherent stability and compatibility of these biologically derived materials in intracellular environments, along with the dynamic properties of peptides and nucleic acids, allow for the creation of highly precise nanostructures with tailored functionalities. From primary to quaternary structures, the self-assembly process of nucleic acids and peptides follows similar classifications, albeit with vastly different properties. The complementation of nucleic acid base pairs through hydrogen bonding modulates the structure of primary and secondary structures, while steric and geometrical hindrance dictates the tertiary and quaternary structures of nucleic acids [149]. Similarly, hydrogen bonding contributes to the secondary structure of peptides, while disulphide bonds and steric hindrance contribute to the tertiary and quaternary structure of peptide nanostructures [213]. The biocompatibility

and controllable nature of peptide and protein self-assembly have made them novel strategies for developing nanomaterials for biomedical applications. However, the complexity, stability and manufacturing of biological nanostructures requires further investigation before potential clinical translation.

2.7 Closing Remarks and Future Directions

This review outlines the current prospects and applications of ER-LNPs for precise intracellular diagnostics and disease treatment. The innovations in ER-LNPs largely stem from their potential to enhance drug delivery, phototherapy, and specific intracellular labelling and detection. The design principles behind these nanoparticles show that core characteristics, such as material composition, luminescence, and targeting strategies, are interchangeable yet tailored to meet specific application needs. The stringency of optical properties such as photostability, absorption, and emission wavelengths vary greatly depending on the optical method and material.

Present strategies highlight three mechanisms for achieving ER-specificity: lysosomal escape, lysosomal evasion via caveolae-mediated endocytosis, and direct endosomal trafficking through peptide signaling. However, many areas remain critically unexplored, such as the formation of a protein corona on the outer surface of nanomaterials within biological environments. Nonetheless, the applications for ER-LNPs are highly diverse, depending on the nanomaterial composition. The differing properties with various luminescent nanomaterials allowed ER-LNPs to act as tools for in vivo and in vitro sensors and vessels for ER-specific PDT and drug delivery. ER-specific intracellular detection showcases the potential for disease diagnostics through minor subcellular fluctuations. Furthermore, ER-specific PDT and drug delivery revealed increased therapeutic effectiveness, significantly influenced by nanoparticle luminescence which ensures that drug efficacy and delivery are enhanced by selective ER targeting.

While *in vivo* and *in vitro* studies demonstrate immense potential of ER-LNPs, major challenges still need to be addressed in the future for effective clinical applications. Namely, combinational targeting through dual cell and organelle specific targeting will require more complex surface modifications to reduce non-specific cell targeting in clinical trials. Furthermore, it is currently uncertain how subcellular specificity can influence nanoparticle degradation and circulation. Currently, the relationship between ER stress

pathways and the localization of nanoparticles inside or surrounding the membrane of the ER has also not been elucidated. With changes in circulation and degradation due to lysosomal escape and enhanced ER localization, long term cytotoxicity within clinical trials needs to be addressed. Furthermore, as the major organs for the filtration of foreign materials, toxicity due to kidney and liver accumulation is one of the critical bottlenecks for advanced clinical applications. Subsequently, how ER specificity can induce kidney or liver damage needs to be further investigated. With an abundance of endoplasmic reticulum in hepatocytes involved in hormone and lipid synthesis as well as detoxification, the effects of ER-LNPs on normal liver metabolism and function need to be further investigated. As such, The accumulation of nanoparticles within the liver is one of the major bottlenecks that need to be addressed before advanced clinical applications [214].

Advancements in biotechnology, chemistry, and pharmacology promise a bright future for LNPs in ER-specific applications. Although current strategies show immense potential for ER-specific therapeutics, there remains a vast untapped potential within the detection and observation of subcellular interactions using luminescent nanoprobes. Furthermore, understanding the distribution, degradation, and ultimate fate of nanomaterials are crucial factors that currently bottleneck the clinical viability of nanotherapeutics. The future clinical viability of these therapies will hinge on a deeper understanding of the core interactions between cellular systems and foreign nanomaterials, underscoring the importance of studying the localization and trafficking of intracellular materials through advanced optical methods.

2.8 References

[1] Michalet, X.;Pinaud, F. F.;Bentolila, L. A.;Tsay, J. M.;Doose, S.;Li, J. J.;Sundaresan, G.;Wu, A. M.;Gambhir, S. S.; Weiss, S. Quantum dots for live cells, in vivo imaging, and diagnostics. Science 2005, 307, 538-544.

[2] Lowe, A. R.;Siegel, J. J.;Kalab, P.;Siu, M.;Weis, K.; Liphardt, J. T. Selectivity mechanism of the nuclear pore complex characterized by single cargo tracking. Nature 2010, 467, 600-603.

[3] Howes, P. D.;Chandrawati, R.; Stevens, M. M. Bionanotechnology. Colloidal nanoparticles as advanced biological sensors. Science 2014, 346, 1247390.

[4] Fan, Z.;Sun, L.;Huang, Y.;Wang, Y.; Zhang, M. Bioinspired fluorescent dipeptide nanoparticles for targeted cancer cell imaging and real-time monitoring of drug release. Nat Nanotechnol 2016, 11, 388-394.

[5] Zhou, J.;Del Rosal, B.;Jaque, D.;Uchiyama, S.; Jin, D. Advances and challenges for fluorescence nanothermometry. Nat Methods 2020, 17, 967-980.

[6] Wang, F.;Wen, S.;He, H.;Wang, B.;Zhou, Z.;Shimoni, O.; Jin, D. Microscopic inspection and tracking of single upconversion nanoparticles in living cells. Light Sci Appl 2018, 7, 18007.

[7] He, J.;Li, C.;Ding, L.;Huang, Y.;Yin, X.;Zhang, J.;Zhang, J.;Yao, C.;Liang, M.;Pirraco, R. P.;Chen, J.;Lu, Q.;Baldridge, R.;Zhang, Y.;Wu, M.;Reis, R. L.; Wang, Y. Tumor Targeting Strategies of Smart Fluorescent Nanoparticles and Their Applications in Cancer Diagnosis and Treatment. Adv Mater 2019, 31, e1902409.

[8] Pratiwi, F. W.;Kuo, C. W.;Chen, B. C.; Chen, P. Recent advances in the use of fluorescent nanoparticles for bioimaging. Nanomedicine (Lond) 2019, 14, 1759-1769.

[9] Huang, J.;Leshuk, T.; Gu, F. Emerging nanomaterials for targeting subcellular organelles. Nano Today 2011, 6, 478-492.

[10] Saminathan, A.;Zajac, M.;Anees, P.; Krishnan, Y. Organelle-level precision with next-generation targeting technologies. Nature Reviews Materials 2022, 7, 355-371.

[11] Chen, W. H.;Luo, G. F.; Zhang, X. Z. Recent Advances in Subcellular Targeted Cancer Therapy Based on Functional Materials. Adv Mater 2019, 31, e1802725.

[12] Schwarz, D. S.; Blower, M. D. The endoplasmic reticulum: structure, function and response to cellular signaling. Cell Mol Life Sci 2016, 73, 79-94.

[13] Oh, N.; Park, J. H. Endocytosis and exocytosis of nanoparticles in mammalian cells. Int J Nanomedicine 2014, 9 Suppl 1, 51-63.

[14] Decelle, J.;Veronesi, G.;Gallet, B.;Stryhanyuk, H.;Benettoni, P.;Schmidt, M.;Tucoulou, R.;Passarelli, M.;Bohic, S.;Clode, P.; Musat, N. Subcellular Chemical Imaging: New Avenues in Cell Biology. Trends Cell Biol 2020, 30, 173-188.

[15] Patel, S.;Kim, J.;Herrera, M.;Mukherjee, A.;Kabanov, A. V.; Sahay, G. Brief update on endocytosis of nanomedicines. Adv Drug Deliv Rev 2019, 144, 90-111.

[16] Sahay, G.;Querbes, W.;Alabi, C.;Eltoukhy, A.;Sarkar, S.;Zurenko, C.;Karagiannis, E.;Love, K.;Chen, D.;Zoncu, R.;Buganim, Y.;Schroeder, A.;Langer, R.; Anderson, D. G. Efficiency of siRNA delivery by lipid nanoparticles is limited by endocytic recycling. Nature Biotechnology 2013, 31, 653-658.

[17] Bedard, P. L.;Hyman, D. M.;Davids, M. S.; Siu, L. L. Small molecules, big impact: 20 years of targeted therapy in oncology. Lancet 2020, 395, 1078-1088.

[18] Monteith, G. R.;Prevarskaya, N.; Roberts-Thomson, S. J. The calcium–cancer signalling nexus. Nature Reviews Cancer 2017, 17, 373-380.

[19] Fujii, S.;Ushioda, R.; Nagata, K. Redox states in the endoplasmic reticulum directly regulate the activity of calcium channel, inositol 1, 4, 5-trisphosphate receptors. Proceedings of the National Academy of Sciences 2023, 120, e2216857120.

[20] Ma, H.;Groth, R. D.;Cohen, S. M.;Emery, J. F.;Li, B.;Hoedt, E.;Zhang, G.;Neubert, T. A.; Tsien, R. W. γCaMKII shuttles Ca2+/CaM to the nucleus to trigger CREB phosphorylation and gene expression. Cell 2014, 159, 281-294.

[21] Hebert, D.;Simons, J.;Peterson, J.; Helenius, A. Calnexin, calreticulin, and Bip/Kar2p in protein folding. In Cold Spring Harbor symposia on quantitative biology; Cold Spring Harbor Laboratory Press, 1995; pp 405-415.

[22] Lovisolo, D.;Gilardino, A.; Ruffinatti, F. A. When neurons encounter nanoobjects: spotlight on calcium signalling. International journal of environmental research and public health 2014, 11, 9621-9637.

[23] Huang, H.;Li, S.;Chen, B.;Wang, Y.;Shen, Z.;Qiu, M.;Pan, H.;Wang, W.;Wang, Y.; Li, X. Endoplasmic reticulum-targeted polymer dots encapsulated with ultrasonic synthesized near-infrared carbon nanodots and their application for in vivo monitoring of Cu2+. Journal of Colloid and Interface Science 2022, 627, 705-715.

[24] Zhang, K.; Kaufman, R. J. From endoplasmic-reticulum stress to the inflammatory response. Nature 2008, 454, 455-462.

[25] Luo, L.;Luo, Z.;Zhang, J.;Liu, X.;Huang, J.;Wang, S.;Yin, H.;Guo, X.;Hu, Y.; Lu, Y. Preventing acute lung injury from progressing to pulmonary fibrosis by maintaining ERS homeostasis through a multistage targeting nanomicelle. Nano Today 2023, 48, 101719.

[26] Jiang, M.;Li, X.;Zhang, J.;Lu, Y.;Shi, Y.;Zhu, C.;Liu, Y.;Qin, B.;Luo, Z.;Du, Y.;Luo, L.;Peng, L.; You, J. Dual Inhibition of Endoplasmic Reticulum Stress and Oxidation Stress Manipulates the Polarization of Macrophages under Hypoxia to Sensitize Immunotherapy. ACS Nano 2021, 15, 14522-14534.

[27] Bai, Q.;Han, Y.;Khan, S.;Wu, T.;Yang, Y.;Wang, Y.;Tang, H.;Li, Q.; Jiang, W. A Novel Endoplasmic Reticulum-targeted Metal-Organic Framework–Confined Ruthenium (Ru) Nanozyme Regulation of Oxidative Stress for Central Post-Stroke Pain. Advanced Healthcare Materials 2023, 2302526.

[28] Luo, L.;Wang, S.;Hu, Y.;Wang, L.;Jiang, X.;Zhang, J.;Liu, X.;Guo, X.;Luo, Z.; Zhu, C. Precisely Regulating M2 Subtype Macrophages for Renal Fibrosis Resolution. ACS nano 2023.

[29] Winterbourn, C. C. Reconciling the chemistry and biology of reactive oxygen species. Nature chemical biology 2008, 4, 278-286.

[30] Garcia-Diaz, M.;Huang, Y.-Y.; Hamblin, M. R. Use of fluorescent probes for ROS to tease apart Type I and Type II photochemical pathways in photodynamic therapy. Methods 2016, 109, 158-166.

[31] Tabas, I.; Ron, D. Integrating the mechanisms of apoptosis induced by endoplasmic reticulum stress. Nat Cell Biol 2011, 13, 184-190.

[32] Li, W.;Yang, J.;Luo, L.;Jiang, M.;Qin, B.;Yin, H.;Zhu, C.;Yuan, X.;Zhang, J.;Luo, Z.;Du, Y.;Li, Q.;Lou, Y.;Qiu, Y.; You, J. Targeting photodynamic and photothermal therapy to the endoplasmic reticulum enhances immunogenic cancer cell death. Nat Commun 2019, 10, 3349.

[33] Liu, X.;Liu, Y.;Li, X.;Huang, J.;Guo, X.;Zhang, J.;Luo, Z.;Shi, Y.;Jiang, M.;Qin, B.;Du, Y.;Luo, L.; You, J. ER-Targeting PDT Converts Tumors into In Situ Therapeutic Tumor Vaccines. ACS Nano 2022, 16, 9240-9253.

[34] Qin, B.;Yuan, X.;Jiang, M.;Yin, H.;Luo, Z.;Zhang, J.;Zhu, C.;Li, X.;Shi, Y.;Luo, L.;Du, Y.; You, J. Targeting DNA to the endoplasmic reticulum efficiently enhances gene delivery and therapy. Nanoscale 2020, 12, 18249-18262.

[35] Yin, H.;Yuan, X.;Luo, L.;Lu, Y.;Qin, B.;Zhang, J.;Shi, Y.;Zhu, C.;Yang, J.;Li, X.;Jiang, M.;Luo, Z.;Shan, X.;Chen, D.; You, J. Appropriate Delivery of the CRISPR/Cas9 System through the Nonlysosomal Route: Application for Therapeutic Gene Editing. Adv Sci (Weinh) 2020, 7, 1903381.

[36] Wang, G.;Norton, A. S.;Pokharel, D.;Song, Y.; Hill, R. A. KDEL peptide gold nanoconstructs: promising nanoplatforms for drug delivery. Nanomedicine 2013, 9, 366-374.

[37] Yuan, X.;Qin, B.;Yin, H.;Shi, Y.;Jiang, M.;Luo, L.;Luo, Z.;Zhang, J.;Li, X.;Zhu, C.;Du, Y.; You, J. Virus-like Nonvirus Cationic Liposome for Efficient Gene Delivery via Endoplasmic Reticulum Pathway. ACS Cent Sci 2020, 6, 174-188.

[38] Shi, Y.;Zhu, C.;Liu, Y.;Lu, Y.;Li, X.;Qin, B.;Luo, Z.;Luo, L.;Jiang, M.;Zhang, J.;Guan, G.;Zheng, C.; You, J. A Vaccination with Boosted Cross Presentation by ER-Targeted Antigen Delivery for Anti-Tumor Immunotherapy. Adv Healthc Mater 2021, 10, e2001934.

[39] De Brito, O. M.; Scorrano, L. Mitofusin 2 tethers endoplasmic reticulum to mitochondria. Nature 2008, 456, 605-610.

[40] Naón, D.;Hernández-Alvarez, M. I.;Shinjo, S.;Wieczor, M.;Ivanova, S.;Martins de Brito, O.;Quintana, A.;Hidalgo, J.;Palacín, M.; Aparicio, P. Splice variants of mitofusin 2 shape the endoplasmic reticulum and tether it to mitochondria. Science 2023, 380, eadh9351.

[41] Ham, S. J.;Yoo, H.;Woo, D.;Lee, D. H.;Park, K. S.; Chung, J. PINK1 and Parkin regulate IP(3)R-mediated ER calcium release. Nat Commun 2023, 14, 5202.

[42] Yang, S.;Zhang, J. J.; Huang, X. Y. Orai1 and STIM1 are critical for breast tumor cell migration and metastasis. Cancer Cell 2009, 15, 124-134.

[43] Schwarz, M.;Meyer, C. E.;Loser, A.;Lossow, K.;Hackler, J.;Ott, C.;Jager, S.;Mohr, I.;Eklund, E. A.;Patel, A. A. H.;Gul, N.;Alvarez, S.;Altinonder, I.;Wiel, C.;Maares, M.;Haase, H.;Hartlova, A.;Grune, T.;Schulze, M. B.;Schwerdtle, T.;Merle, U.;Zischka, H.;Sayin, V. I.;Schomburg, L.; Kipp, A. P. Excessive copper impairs intrahepatocyte trafficking and secretion of selenoprotein P. Nat Commun 2023, 14, 3479.

[44] Chen, Y.;Wang, S.; Zhang, F. Near-infrared luminescence high-contrast in vivo biomedical imaging. Nature Reviews Bioengineering 2023, 1, 60-78.

[45] Rennick, J. J.;Johnston, A. P. R.; Parton, R. G. Key principles and methods for studying the endocytosis of biological and nanoparticle therapeutics. Nat Nanotechnol 2021, 16, 266-276.

[46] Shi, Y.;Wang, S.;Wu, J.;Jin, X.; You, J. Pharmaceutical strategies for endoplasmic reticulum-targeting and their prospects of application. Journal of Controlled Release 2021, 329, 337-352.

[47] Ghosh, C.;Nandi, A.; Basu, S. Lipid Nanoparticle-Mediated Induction of Endoplasmic Reticulum Stress in Cancer Cells. ACS Appl Bio Mater 2019, 2, 3992-4001.

[48] Parton, R. G.; Howes, M. T. Revisiting caveolin trafficking: the end of the caveosome. J Cell Biol 2010, 191, 439-441.

[49] Zheng, L.;Bandara, S. R.;Tan, Z.; Leal, C. Lipid nanoparticle topology regulates endosomal escape and delivery of RNA to the cytoplasm. Proc Natl Acad Sci U S A 2023, 120, e2301067120.

[50] Hoshyar, N.;Gray, S.;Han, H.; Bao, G. The effect of nanoparticle size on in vivo pharmacokinetics and cellular interaction. Nanomedicine 2016, 11, 673-692.

[51] Sabourian, P.;Yazdani, G.;Ashraf, S. S.;Frounchi, M.;Mashayekhan, S.;Kiani, S.; Kakkar, A. Effect of physico-chemical properties of nanoparticles on their intracellular uptake. International Journal of Molecular Sciences 2020, 21, 8019.

[52] Ghosh, C.;Nandi, A.; Basu, S. Supramolecular self-assembly of triazine-based small molecules: targeting the endoplasmic reticulum in cancer cells. Nanoscale 2019, 11, 3326-3335.

[53] Vhora, I.;Patil, S.;Bhatt, P.; Misra, A. Protein–and peptide–drug Conjugates: An emerging drug delivery technology. Advances in protein chemistry and structural biology 2015, 98, 1-55.

[54] Yu, Q.;Wu, G.;Zhang, T.;Zhao, X.;Zhou, Z.;Liu, L.;Chen, W.; Alvarez, P. J. Targeting specific cell organelles with different-faceted nanocrystals that are selectively recognized by organelle-targeting peptides. Chemical Communications 2020, 56, 7613-7616.

[55] Malhotra, K.;Kumar, B.;Piunno, P. A.; Krull, U. J. Cellular Uptake of Upconversion Nanoparticles Based on Surface Polymer Coatings and Protein Corona. ACS Applied Materials & Interfaces 2024, 16, 35985-36001.

[56] Parvez, S.;Karole, A.; Mudavath, S. L. Transport mechanism of hydroxy-propyl-beta-cyclodextrin modified solid lipid nanoparticles across human epithelial cells for the oral absorption of antileishmanial drugs. Biochimica et Biophysica Acta (BBA)-General Subjects 2022, 1866, 130157.

[57] Yue, Z.-G.;Wei, W.;Lv, P.-P.;Yue, H.;Wang, L.-Y.;Su, Z.-G.; Ma, G.-H. Surface charge affects cellular uptake and intracellular trafficking of chitosan-based nanoparticles. Biomacromolecules 2011, 12, 2440-2446.

[58] Xing, Y.;Du, S.;Liu, A.;Gao, Z.;Zhou, Q.;Xuan, Y.;Zhao, Y.;Chen, X.; Zhang, S. Shape Control of Carbon Nanoparticles via Simple Anion-Directed Strategy for Precise Endoplasmic Reticulum-Targeted Imaging. Angewandte Chemie (International ed. in English) 2023, e202311008-e202311008.

[59] Fu, L.;Shi, B.;Wen, S.;Morsch, M.;Wang, G.;Zhou, Z.;Mi, C.;Sadraeian, M.;Lin, G.; Lu, Y. Aspect ratio of PEGylated upconversion nanocrystals affects the cellular uptake in vitro and in vivo. Acta Biomaterialia 2022, 147, 403-413.

[60] Xie, X.;Liao, J.;Shao, X.;Li, Q.; Lin, Y. The effect of shape on cellular uptake of gold nanoparticles in the forms of stars, rods, and triangles. Scientific reports 2017, 7, 3827.

[61] Erathodiyil, N.; Ying, J. Y. Functionalization of inorganic nanoparticles for bioimaging applications. Acc Chem Res 2011, 44, 925-935.

[62] Feng, L.;Zhu, C.;Yuan, H.;Liu, L.;Lv, F.; Wang, S. Conjugated polymer nanoparticles: preparation, properties, functionalization and biological applications. Chemical Society Reviews 2013, 42, 6620-6633.

[63] Shen, P.;Ohta, S.;Inasawa, S.; Yamaguchi, Y. Selective labeling of the endoplasmic reticulum in live cells with silicon quantum dots. Chem Commun (Camb) 2011, 47, 8409-8411.

[64] Zhang, F.;Lees, E.;Amin, F.;Rivera Gil, P.;Yang, F.;Mulvaney, P.; Parak, W. J. Polymer-coated nanoparticles: a universal tool for biolabelling experiments. Small 2011, 7, 3113-3127.

[65] Zhang, L.;Cao, C.;Kaushik, N.;Lai, R. Y.;Liao, J.;Wang, G.;Ariotti, N.;Jin, D.; Stenzel, M. H. Controlling the Biological Behaviors of Polymer-Coated Upconverting Nanoparticles by Adjusting the Linker Length of Estrone Ligands. Biomacromolecules 2022, 23, 2572-2585.

[66] Wang, J.;Fang, X.; Liang, W. Pegylated phospholipid micelles induce endoplasmic reticulum-dependent apoptosis of cancer cells but not normal cells. ACS Nano 2012, 6, 5018-5030.

[67] Han, S.;da Costa Marques, R.;Simon, J.;Kaltbeitzel, A.;Koynov, K.;Landfester, K.;Mailänder, V.; Lieberwirth, I. Endosomal sorting results in a selective separation of the protein corona from nanoparticles. Nature Communications 2023, 14, 295.

[68] Pollock, S.;Antrobus, R.;Newton, L.;Kampa, B.;Rossa, J.;Latham, S.;Nichita, N. B.;Dwek, R. A.; Zitzmann, N. Uptake and trafficking of liposomes to the endoplasmic reticulum. FASEB J 2010, 24, 1866-1878.

[69] Shuang, E.;Mao, Q.-X.;Wang, J.-H.; Chen, X.-W. Correction: Carbon dots with tunable dual emissions: from the mechanism to the specific imaging of endoplasmic reticulum polarity. Nanoscale 2021, 13, 3307-3307.

[70] Shuang, E.;Mao, Q.-X.;Yuan, X.-L.;Kong, X.-L.;Chen, X.-W.; Wang, J.-H. Targeted imaging of the lysosome and endoplasmic reticulum and their pH monitoring with surface regulated carbon dots. Nanoscale 2018, 10, 12788-12796.

[71] Wan, J.;Sun, L.;Wu, P.;Wang, F.;Guo, J.;Cheng, J.; Wang, C. Synthesis of indocyanine green functionalized comblike poly (aspartic acid) derivatives for enhanced cancer cell ablation by targeting the endoplasmic reticulum. Polymer Chemistry 2018, 9, 1206-1215.

[72] Lin, H.;Yue, Y.;Maidana, D. E.;Bouzika, P.;Atik, A.;Matsumoto, H.;Miller, J. W.; Vavvas, D. G. Drug Delivery Nanoparticles: Toxicity Comparison in Retinal Pigment Epithelium and Retinal Vascular Endothelial Cells. Semin Ophthalmol 2016, 31, 1-9.

[73] Liu, Y.;Liu, J.;Zhang, J.;Li, X.;Lin, F.;Zhou, N.;Yang, B.; Lu, L. A brand-new generation of fluorescent nano-neural tracers: biotinylated dextran amine conjugated carbonized polymer dots. Biomater Sci 2019, 7, 1574-1583.

[74] Sahay, G.;Gautam, V.;Luxenhofer, R.; Kabanov, A. V. The utilization of pathogen-like cellular trafficking by single chain block copolymer. Biomaterials 2010, 31, 1757-1764.

[75] Delehanty, J. B.;Boeneman, K.;Bradburne, C. E.;Robertson, K.;Bongard, J. E.; Medintz, I. L. Peptides for specific intracellular delivery and targeting of nanoparticles: implications for developing nanoparticle-mediated drug delivery. Ther Deliv 2010, 1, 411-433.

[76] Chatterjee, S.;Kon, E.;Sharma, P.; Peer, D. Endosomal escape: A bottleneck for LNP-mediated therapeutics. Proceedings of the National Academy of Sciences 2024, 121, e2307800120.

[77] Cerrato, C. P.; Langel, Ü. An update on cell-penetrating peptides with intracellular organelle targeting. Expert Opinion on Drug Delivery 2022, 19, 133-146.

[78] Foerg, C.; Merkle, H. P. On the biomedical promise of cell penetrating peptides: limits versus prospects. Journal of pharmaceutical sciences 2008, 97, 144-162.

[79] Kang, J. Y.;Kim, S.;Kim, J.;Kang, N.-G.;Yang, C.-S.;Min, S.-J.; Kim, J. W. Cell-penetrating peptide-conjugated lipid/polymer hybrid nanovesicles for endoplasmic reticulum-targeting intracellular delivery. Journal of Materials Chemistry B 2021, 9, 464-470.

[80] Zhao, Y.;Liu, S.;Shi, Z.;Zhu, H.;Li, M.; Yu, Q. Pathogen infection-responsive nanoplatform targeting macrophage endoplasmic reticulum for treating life-threatening systemic infection. Nano Research 2022, 15, 6243-6255.

[81] Wilson, D. W.;Lewis, M. J.; Pelham, H. R. pH-dependent binding of KDEL to its receptor in vitro. J Biol Chem 1993, 268, 7465-7468.

[82] Sneh-Edri, H.;Likhtenshtein, D.; Stepensky, D. Intracellular targeting of PLGA nanoparticles encapsulating antigenic peptide to the endoplasmic reticulum of dendritic cells and its effect on antigen cross-presentation in vitro. Mol Pharm 2011, 8, 1266-1275.

[83] Hallock, K. J.;Lee, D.-K.;Omnaas, J.;Mosberg, H. I.; Ramamoorthy, A. Membrane composition determines pardaxin's mechanism of lipid bilayer disruption. Biophysical journal 2002, 83, 1004-1013.

[84] Chen, L.;Jiang, X.;Lv, M.;Wang, X.;Zhao, P.;Zhang, M.;Lv, G.;Wu, J.;Liu, Y.;Yang, Y.;Chen, J.; Bu, W. Reductive-damage-induced intracellular maladaptation for cancer electronic interference therapy. Chem 2022, 8, 866-879.

[85] Moreno-Vega, A.-I.;Gomez-Quintero, T.;Nunez-Anita, R.-E.;Acosta-Torres, L.-S.; Castaño, V. Polymeric and ceramic nanoparticles in biomedical applications. Journal of Nanotechnology 2012, 2012.

[86] Shvets, E.;Bitsikas, V.;Howard, G.;Hansen, C. G.; Nichols, B. J. Dynamic caveolae exclude bulk membrane proteins and are required for sorting of excess glycosphingolipids. Nature communications 2015, 6, 6867.

[87] Ting, C.-H.;Huang, H.-N.;Huang, T.-C.;Wu, C.-J.; Chen, J.-Y. The mechanisms by which pardaxin, a natural cationic antimicrobial peptide, targets the endoplasmic reticulum and induces c-FOS. Biomaterials 2014, 35, 3627-3640.

[88] Liu, Y.;Jia, H.-R.;Han, X.; Wu, F.-G. Endoplasmic reticulum-targeting nanomedicines for cancer therapy. Smart Materials in Medicine 2021, 2, 334-349.

[89] Wang, C.;Yan, Q.;Liu, H.-B.;Zhou, X.-H.; Xiao, S.-J. Different EDC/NHS activation mechanisms between PAA and PMAA brushes and the following amidation reactions. Langmuir 2011, 27, 12058-12068.

[90] de Jong, F.;Pokorny, J.;Manshian, B.;Daelemans, B.;Vandaele, J.;Startek, J. B.;Soenen, S.;Van der Auweraer, M.;Dehaen, W.; Rocha, S. Development and characterization of BODIPY-derived tracers for fluorescent labeling of the endoplasmic reticulum. Dyes and Pigments 2020, 176, 108200.

[91] Zhang, X.;Wan, J.;Mo, F.;Tang, D.;Xiao, H.;Li, Z.;Jia, J.; Liu, T. Targeting Bone Tumor and Subcellular Endoplasmic Reticulum via Near Infrared II Fluorescent Polymer for Photodynamic-Immunotherapy to Break the Step-Reduction Delivery Dilemma. Advanced Science 2022, 9, 2201819.

[92] Sun, W.; Hu, K. Role for SUR2A in coupling cardiac K(ATP) channels to caveolin-3. Cell Physiol Biochem 2010, 25, 409-418.

[93] Garg, V.;Jiao, J.; Hu, K. Regulation of ATP-sensitive K+ channels by caveolin-enriched microdomains in cardiac myocytes. Cardiovasc Res 2009, 82, 51-58.

[94] Huo, J. Y.;Feng, Y. L.;Chen, Y. T.;Yang, B.;Zhi, Y. T.;Wang, H. J.; Yang, H. Q. Caveolin-3 negatively regulates endocytic recycling of cardiac K(ATP) channels. Am J Physiol Cell Physiol 2023, 325, C1106-C1118.

[95] Pandey, S.;Patil, S.;Ballav, N.; Basu, S. Spatial targeting of Bcl-2 on endoplasmic reticulum and mitochondria in cancer cells by lipid nanoparticles. Journal of Materials Chemistry B 2020, 8, 4259-4266.

[96] Pandey, S.;Nandi, A.;Basu, S.; Ballav, N. Inducing endoplasmic reticulum stress in cancer cells using graphene oxide-based nanoparticles. Nanoscale Adv 2020, 2, 4887-4894.

[97] Patton, B. L.;Zhu, P.;ElSheikh, A.;Driggers, C. M.; Shyng, S.-L. Dynamic duo: Kir6 and SUR in KATP channel structure and function. Channels 2024, 18, 2327708.

[98] Wheeler, K. E.;Chetwynd, A. J.;Fahy, K. M.;Hong, B. S.;Tochihuitl, J. A.;Foster, L. A.; Lynch, I. Environmental dimensions of the protein corona. Nature Nanotechnology 2021, 16, 617-629.

[99] Chen, L.;Liu, C.;Xiang, Y.;Lyu, J.;Zhou, Z.;Gong, T.;Gao, H.;Li, L.; Huang, Y. Exocytosis blockade of endoplasmic reticulum-targeted nanoparticle enhances immunotherapy. Nano Today 2022, 42, 101356.

[100] Qiu, C.;Han, H.-H.;Sun, J.;Zhang, H.-T.;Wei, W.;Cui, S.-H.;Chen, X.;Wang, J.-C.; Zhang, Q. Regulating intracellular fate of siRNA by endoplasmic reticulum membrane-decorated hybrid nanoplexes. Nature Communications 2019, 10, 2702.

[101] Zhang, W.;Yu, M.;Xi, Z.;Nie, D.;Dai, Z.;Wang, J.;Qian, K.;Weng, H.;Gan, Y.; Xu, L. Cancer cell membrane-camouflaged nanorods with endoplasmic reticulum targeting for improved antitumor therapy. ACS applied materials & interfaces 2019, 11, 46614-46625.

[102] Fang, R. H.;Kroll, A. V.;Gao, W.; Zhang, L. Cell membrane coating nanotechnology. Advanced materials 2018, 30, 1706759.

[103] Ni, J. S.;Li, Y.;Yue, W.;Liu, B.; Li, K. Nanoparticle-based Cell Trackers for Biomedical Applications. Theranostics 2020, 10, 1923-1947.

[104] He, J.;Li, C.;Ding, L.;Huang, Y.;Yin, X.;Zhang, J.;Zhang, J.;Yao, C.;Liang, M.;Pirraco, R. P.;Chen, J.;Lu, Q.;Baldridge, R.;Zhang, Y.;Wu, M.;Reis, R. L.; Wang, Y. Tumor Targeting Strategies of Smart Fluorescent Nanoparticles and Their Applications in Cancer Diagnosis and Treatment. Advanced Materials 2019, 31, 1902409.

[105] Patra, J. K.;Das, G.;Fraceto, L. F.;Campos, E. V. R.;Rodriguez-Torres, M. D. P.;Acosta-Torres, L. S.;Diaz-Torres, L. A.;Grillo, R.;Swamy, M. K.;Sharma, S.;Habtemariam, S.; Shin, H. S. Nano based drug delivery systems: recent developments and future prospects. J Nanobiotechnology 2018, 16, 71.

[106] Zhao, Z.;Ukidve, A.;Kim, J.; Mitragotri, S. Targeting Strategies for Tissue-Specific Drug Delivery. Cell 2020, 181, 151-167.

[107] Rajendran, L.;Knolker, H. J.; Simons, K. Subcellular targeting strategies for drug design and delivery. Nat Rev Drug Discov 2010, 9, 29-42.

[108] Di, X.;Wang, D.;Zhou, J.;Zhang, L.;Stenzel, M. H.;Su, Q. P.; Jin, D. Quantitatively Monitoring In Situ Mitochondrial Thermal Dynamics by Upconversion Nanoparticles. Nano Lett 2021, 21, 1651-1658.

[109] Di, X.;Wang, D.;Su, Q. P.;Liu, Y.;Liao, J.;Maddahfar, M.;Zhou, J.; Jin, D. Spatiotemporally mapping temperature dynamics of lysosomes and mitochondria using cascade organelle-targeting upconversion nanoparticles. Proc Natl Acad Sci U S A 2022, 119, e2207402119.

[110] Zhang, C.;Qi, G.;Kong, J.;Diao, X.;Ju, X.;Wang, J.;Dong, S.; Jin, Y. Label-Free Single-Cell SERS Detection and Fluorescence Imaging of Molecular Responses to Endoplasmic Reticulum Stress under Electrical Stimulation. Anal Chem 2023, 95, 17716-17725.

[111] Oshchepkov, A. S.;Oshchepkov, M. S.;Oshchepkova, M. V.;Al-Hamry, A.;Kanoun, O.; Kataev, E. A. Naphthalimide-based fluorescent polymers for molecular detection. Advanced Optical Materials 2021, 9, 2001913.

[112] Zhang, H.;Liu, Y.;Cao, Y.;Song, P.;Li, W.;Lv, Z.;Song, S.;Wang, Y.; Zhang, H. A Porous Organic Framework-Based Nanoplatform for Directional Destruction on Endoplasmic Reticulum to Enhance Tumor Immunotherapy. Advanced Functional Materials 2023, 33, 2307175.

[113] Qian, Y.;Wang, M.;Xie, Y.;Sun, Q.;Gao, M.; Li, C. Rationally Integrated Precise ER-Targeted and Oxygen-Compensated Photodynamic Immunostimulant for Immunogenicity-Boosted Tumor Therapy. Advanced Healthcare Materials 2023, 2301728.

[114] Deng, H.;Zhou, Z.;Yang, W.;Lin, L.-s.;Wang, S.;Niu, G.;Song, J.; Chen, X. Endoplasmic reticulum targeting to amplify immunogenic cell death for cancer immunotherapy. Nano Letters 2020, 20, 1928-1933.

[115] Paolesse, R.;Nardis, S.;Monti, D.;Stefanelli, M.; Di Natale, C. Porphyrinoids for chemical sensor applications. Chemical reviews 2017, 117, 2517-2583.

[116] Yuan, L.;Lin, W.;Zhao, S.;Gao, W.;Chen, B.;He, L.; Zhu, S. A unique approach to development of near-infrared fluorescent sensors for in vivo imaging. Journal of the American Chemical Society 2012, 134, 13510-13523.

[117] Wang, W.;Zhang, Y.;Wang, Z.;Liu, X.;Lu, S.; Hu, X. A native drug-free macromolecular therapeutic to trigger mutual reinforcing of endoplasmic reticulum stress and mitochondrial dysfunction for cancer treatment. ACS nano 2023, 17, 11023-11038.

[118] del Rosal, B.;Jia, B.; Jaque, D. Beyond Phototherapy: Recent Advances in Multifunctional Fluorescent Nanoparticles for Light-Triggered Tumor Theranostics. Advanced Functional Materials 2018, 28, 1803733.

[119] Ming, J.;Chen, Y.;Miao, H.;Fan, Y.;Wang, S.;Chen, Z.;Guo, Z.;Guo, Z.;Qi, L.; Wang, X. High-brightness transition metal-sensitized lanthanide near-infrared luminescent nanoparticles. Nature Photonics 2024, 18, 1254-1262.

[120] Jin, D.;Xi, P.;Wang, B.;Zhang, L.;Enderlein, J.; van Oijen, A. M. Nanoparticles for super-resolution microscopy and single-molecule tracking. Nat Methods 2018, 15, 415-423.

[121] Lee, C.;Xu, E. Z.;Kwock, K. W.;Teitelboim, A.;Liu, Y.;Park, H. S.;Ursprung, B.;Ziffer, M. E.;Karube, Y.; Fardian-Melamed, N. Indefinite and bidirectional near-infrared nanocrystal photoswitching. Nature 2023, 618, 951-958.

[122] Lu, Y.;Zhao, J.;Zhang, R.;Liu, Y.;Liu, D.;Goldys, E. M.;Yang, X.;Xi, P.;Sunna, A.; Lu, J. Tunable lifetime multiplexing using luminescent nanocrystals. Nature Photonics 2014, 8, 32-36.

[123] Zhou, J.;Chizhik, A. I.;Chu, S.; Jin, D. Single-particle spectroscopy for functional nanomaterials. Nature 2020, 579, 41-50.

[124] Dai, Y.;Bi, H.;Deng, X.;Li, C.;He, F.;Ma, P.;Yang, P.; Lin, J. 808 nm near-infrared light controlled dual-drug release and cancer therapy in vivo by upconversion mesoporous silica nanostructures. J Mater Chem B 2017, 5, 2086-2095.

[125] Li, H.;Zhang, H.;He, X.;Zhao, P.;Wu, T.;Xiahou, J.;Wu, Y.;Liu, Y.;Chen, Y.; Jiang, X. Blocking Spatiotemporal Crosstalk between Subcellular Organelles for Enhancing Anticancer Therapy with Nanointercepters. Advanced Materials 2023, 2211597.

[126] Feng, Z.;Wang, H.;Wang, S.;Zhang, Q.;Zhang, X.;Rodal, A. A.; Xu, B. Enzymatic assemblies disrupt the membrane and target endoplasmic reticulum for selective cancer cell death. Journal of the American Chemical Society 2018, 140, 9566-9573.

[127] Gai, S.;Yang, G.;Yang, P.;He, F.;Lin, J.;Jin, D.; Xing, B. Recent advances in functional nanomaterials for light–triggered cancer therapy. Nano today 2018, 19, 146-187.

[128] Wang, K.;Xiang, Y.;Pan, W.;Wang, H.;Li, N.; Tang, B. An endoplasmic reticulum-targeted organic photothermal agent for enhanced cancer therapy. Chinese Chemical Letters 2022, 33, 793-797.

[129] Lu, M.;Christensen, C. N.;Weber, J. M.;Konno, T.;Laubli, N. F.;Scherer, K. M.;Avezov, E.;Lio, P.;Lapkin, A. A.;Kaminski Schierle, G. S.; Kaminski, C. F. ERnet: a tool for the semantic segmentation and quantitative analysis of endoplasmic reticulum topology. Nat Methods 2023, 20, 569-579.

[130] Jung, H. S.;Han, J.;Lee, J.-H.;Lee, J. H.;Choi, J.-M.;Kweon, H.-S.;Han, J. H.;Kim, J.-H.;Byun, K. M.; Jung, J. H. Enhanced NIR radiation-triggered hyperthermia by mitochondrial targeting. Journal of the American Chemical Society 2015, 137, 3017-3023.

[131] Gao, G.;Jiang, Y. W.;Guo, Y.;Jia, H. R.;Cheng, X.;Deng, Y.;Yu, X. W.;Zhu, Y. X.;Guo, H. Y.; Sun, W. Enzyme-mediated tumor starvation and phototherapy enhance mild-temperature photothermal therapy. Advanced Functional Materials 2020, 30, 1909391.

[132] Yi, X.;Duan, Q. Y.; Wu, F. G. Low-Temperature Photothermal Therapy: Strategies and Applications. Research (Wash D C) 2021, 2021, 9816594.

[133] Richter, K.;Haslbeck, M.; Buchner, J. The heat shock response: life on the verge of death. Mol Cell 2010, 40, 253-266.

[134] Wan, G.;Chen, X.;Chen, J.;Gou, R.;Wang, H.;Liu, S.;Zhang, M.;Chen, H.;Wang, D.; Zhang, Q. Endoplasmic reticulum-targeted NIR-II phototherapy combined with inflammatory vascular suppression elicits a synergistic effect against TNBC. Biomaterials Science 2023, 11, 1876-1894.

[135] Ma, X.;Zhou, W.;Zhang, R.;Zhang, C.;Yan, J.;Feng, J.;Rosenholm, J. M.;Shi, T.;Shen, X.; Zhang, H. Minimally invasive injection of biomimetic Nano@ Microgel for in situ ovarian cancer treatment through enhanced photodynamic reactions and photothermal combined therapy. Materials Today Bio 2023, 20, 100663.

[136] Hua, X.-W.;Bao, Y.-W.;Zeng, J.; Wu, F.-G. Ultrasmall all-in-one nanodots formed via carbon dot-mediated and albumin-based synthesis: multimodal imaging-guided and mild laser-enhanced cancer therapy. ACS Applied Materials & Interfaces 2018, 10, 42077-42087.

[137] Feng, Z.;Adolfsson, K. H.;Xu, Y.;Fang, H.;Hakkarainen, M.; Wu, M. Carbon dot/polymer nanocomposites: From green synthesis to energy, environmental and biomedical applications. Sustainable Materials and Technologies 2021, 29, e00304.

[138] Tao, S.;Feng, T.;Zheng, C.;Zhu, S.; Yang, B. Carbonized polymer dots: a brand new perspective to recognize luminescent carbon-based nanomaterials. The Journal of Physical Chemistry Letters 2019, 10, 5182-5188.

[139] Wu, C.; Chiu, D. T. Highly fluorescent semiconducting polymer dots for biology and medicine. Angewandte Chemie International Edition 2013, 52, 3086-3109.

[140] Zhu, S.;Song, Y.;Zhao, X.;Shao, J.;Zhang, J.; Yang, B. The photoluminescence mechanism in carbon dots (graphene quantum dots, carbon nanodots, and polymer dots): current state and future perspective. Nano research 2015, 8, 355-381.

[141] Cui, G.;Wu, J.;Lin, J.;Liu, W.;Chen, P.;Yu, M.;Zhou, D.; Yao, G. Graphene-based nanomaterials for breast cancer treatment: promising therapeutic strategies. Journal of Nanobiotechnology 2021, 19, 1-30.

[142] Gil, H. M.;Price, T. W.;Chelani, K.;Bouillard, J.-S. G.;Calaminus, S. D.; Stasiuk, G. J. NIR-quantum dots in biomedical imaging and their future. Iscience 2021, 24.

[143] Wen, S.;Zhou, J.;Zheng, K.;Bednarkiewicz, A.;Liu, X.; Jin, D. Advances in highly doped upconversion nanoparticles. Nature communications 2018, 9, 2415.

[144] Liao, J.;Jin, D.;Chen, C.;Li, Y.; Zhou, J. Helix shape power-dependent properties of single upconversion nanoparticles. The journal of physical chemistry letters 2020, 11, 2883-2890.

[145] Huang, Y.;Li, P.;Zhao, R.;Zhao, L.;Liu, J.;Peng, S.;Fu, X.;Wang, X.;Luo, R.; Wang, R. Silica nanoparticles: Biomedical applications and toxicity. Biomedicine & Pharmacotherapy 2022, 151, 113053.

[146] Mitchell, M. J.;Billingsley, M. M.;Haley, R. M.;Wechsler, M. E.;Peppas, N. A.; Langer, R. Engineering precision nanoparticles for drug delivery. Nat Rev Drug Discov 2021, 20, 101-124.

[147] Editorial Let's talk about lipid nanoparticles. Nat. Rev. Mater. 2021, 6, 99.

[148] Gazit, E. Self-assembled peptide nanostructures: the design of molecular building blocks and their technological utilization. Chemical Society Reviews 2007, 36, 1263-1269.

[149] Ramezani, H.; Dietz, H. Building machines with DNA molecules. Nat Rev Genet 2020, 21, 5-26.

[150] Li, B.;Wen, H. M.;Cui, Y.;Zhou, W.;Qian, G.; Chen, B. Emerging multifunctional metal–organic framework materials. Advanced Materials 2016, 28, 8819-8860.

[151] Dutta, S.;Kim, J.;Hsieh, P. H.;Hsu, Y. S.;Kaneti, Y. V.;Shieh, F. K.;Yamauchi, Y.; Wu, K. C. W. Nanoarchitectonics of biofunctionalized metal–organic frameworks with biological macromolecules and living cells. Small Methods 2019, 3, 1900213.

[152] Li, W.;Kaminski Schierle, G. S.;Lei, B.;Liu, Y.; Kaminski, C. F. Fluorescent Nanoparticles for Super-Resolution Imaging. Chem Rev 2022, 122, 12495-12543.

[153] Ozyurt, D.;Al Kobaisi, M.;Hocking, R. K.; Fox, B. Properties, Synthesis, and Applications of Carbon Dots: A Review. Carbon Trends 2023, 100276.

[154] Ding, H.;Yu, S.-B.;Wei, J.-S.; Xiong, H.-M. Full-color light-emitting carbon dots with a surface-state-controlled luminescence mechanism. ACS nano 2016, 10, 484-491.

[155] Zhu, Z.;Liu, C.;Song, X.-M.;Mao, Q.; Ma, T. Carbon Dots as an Indicator of Acid–Base Titration and a Fluorescent Probe for Endoplasm Reticulum Imaging. ACS Applied Bio Materials 2021, 4, 3623-3629.

[156] Lin, F.;Jia, C.; Wu, F.-G. Carbon dots for intracellular sensing. Small Structures 2022, 3, 2200033.

[157] Fu, M.;Ehrat, F.;Wang, Y.;Milowska, K. Z.;Reckmeier, C.;Rogach, A. L.;Stolarczyk, J. K.;Urban, A. S.; Feldmann, J. Carbon dots: a unique fluorescent cocktail of polycyclic aromatic hydrocarbons. Nano letters 2015, 15, 6030-6035.

[158] Bao, Y.-W.;Hua, X.-W.;Li, Y.-H.;Jia, H.-R.; Wu, F.-G. Endoplasmic reticulum-targeted phototherapy using one-step synthesized trace metal-doped carbon-dominated nanoparticles: Laser-triggered nucleolar delivery and increased tumor accumulation. Acta Biomaterialia 2019, 88, 462-476.

[159] Wang, Z.;Xu, K.-F.;Wang, G.;Durrani, S.;Lin, F.; Wu, F.-G. “One stone, five birds”: ultrabright and multifaceted carbon dots for precise cell imaging and glutathione detection. Chemical Engineering Journal 2023, 457, 140997.

[160] Yang, K.;Zhang, S.;Zhang, G.;Sun, X.;Lee, S. T.; Liu, Z. Graphene in mice: ultrahigh in vivo tumor uptake and efficient photothermal therapy. Nano Lett 2010, 10, 3318-3323.

[161] Hashemi, M.;Omidi, M.;Muralidharan, B.;Smyth, H.;Mohagheghi, M. A.;Mohammadi, J.; Milner, T. E. Evaluation of the photothermal properties of a reduced graphene oxide/arginine nanostructure for near-infrared absorption. ACS applied materials & interfaces 2017, 9, 32607-32620.

[162] Bao, Y. W.;Hua, X. W.;Chen, X.; Wu, F. G. Platinum-doped carbon nanoparticles inhibit cancer cell migration under mild laser irradiation: Multi-organelle-targeted photothermal therapy. Biomaterials 2018, 183, 30-42.

[163] Liu, Z.-g.; Jiao, D. Necroptosis, tumor necrosis and tumorigenesis. Cell stress 2020, 4, 1.

[164] Eil, R.;Vodnala, S. K.;Clever, D.;Klebanoff, C. A.;Sukumar, M.;Pan, J. H.;Palmer, D. C.;Gros, A.;Yamamoto, T. N.; Patel, S. J. Ionic immune suppression within the tumour microenvironment limits T cell effector function. Nature 2016, 537, 539-543.

[165] Yue, Y.;Li, F.;Li, Y.;Wang, Y.;Guo, X.;Cheng, Z.;Li, N.;Ma, X.;Nie, G.; Zhao, X. Biomimetic Nanoparticles Carrying a Repolarization Agent of Tumor-Associated Macrophages for Remodeling of the Inflammatory Microenvironment Following Photothermal Therapy. ACS Nano 2021, 15, 15166-15179.

[166] Fiedler, U.;Reiss, Y.;Scharpfenecker, M.;Grunow, V.;Koidl, S.;Thurston, G.;Gale, N. W.;Witzenrath, M.;Rosseau, S.;Suttorp, N.;Sobke, A.;Herrmann, M.;Preissner, K. T.;Vajkoczy, P.; Augustin, H. G. Angiopoietin-2 sensitizes endothelial cells to TNF-alpha and has a crucial role in the induction of inflammation. Nat Med 2006, 12, 235-239.

[167] Ou, L.;Song, B.;Liang, H.;Liu, J.;Feng, X.;Deng, B.;Sun, T.; Shao, L. Toxicity of graphene-family nanoparticles: a general review of the origins and mechanisms. Particle and fibre toxicology 2016, 13, 1-24.

[168] Janjua, T. I.;Cao, Y.;Yu, C.; Popat, A. Clinical translation of silica nanoparticles. Nature Reviews Materials 2021, 6, 1072-1074.

[169] Thureja, D.;Imamoglu, A.;Smolenski, T.;Amelio, I.;Popert, A.;Chervy, T.;Lu, X.;Liu, S.;Barmak, K.;Watanabe, K.;Taniguchi, T.;Norris, D. J.;Kroner, M.; Murthy, P. A. Electrically tunable quantum confinement of neutral excitons. Nature 2022, 606, 298-304.

[170] Zhang, Q.;Wang, R.;Feng, B.;Zhong, X.; Ostrikov, K. K. Photoluminescence mechanism of carbon dots: triggering high-color-purity red fluorescence emission through edge amino protonation. Nat Commun 2021, 12, 6856.

[171] Dertinger, T.;Colyer, R.;Iyer, G.;Weiss, S.; Enderlein, J. Fast, background-free, 3D super-resolution optical fluctuation imaging (SOFI). Proceedings of the National Academy of Sciences 2009, 106, 22287-22292.

[172] Bhatia, D.;Arumugam, S.;Nasilowski, M.;Joshi, H.;Wunder, C.;Chambon, V.;Prakash, V.;Grazon, C.;Nadal, B.;Maiti, P. K.;Johannes, L.;Dubertret, B.; Krishnan, Y. Quantum dot-loaded monofunctionalized DNA icosahedra for single-particle tracking of endocytic pathways. Nat Nanotechnol 2016, 11, 1112-1119.

[173] Yang, Y.;Liu, Y.;Song, L.;Cui, X.;Zhou, J.;Jin, G.;Boccaccini, A. R.; Virtanen, S. Iron oxide nanoparticle-based nanocomposites in biomedical application. Trends in Biotechnology 2023.

[174] Yang, M.;Li, J.;Gu, P.; Fan, X. The application of nanoparticles in cancer immunotherapy: Targeting tumor microenvironment. Bioact Mater 2021, 6, 1973-1987.

[175] Dadfar, S. M.;Roemhild, K.;Drude, N. I.;von Stillfried, S.;Knüchel, R.;Kiessling, F.; Lammers, T. Iron oxide nanoparticles: Diagnostic, therapeutic and theranostic applications. Advanced drug delivery reviews 2019, 138, 302-325.

[176] Ranji-Burachaloo, H.;Gurr, P. A.;Dunstan, D. E.; Qiao, G. G. Cancer Treatment through Nanoparticle-Facilitated Fenton Reaction. ACS Nano 2018, 12, 11819-11837.

[177] Mi, C.;Guan, M.;Zhang, X.;Yang, L.;Wu, S.;Yang, Z.;Guo, Z.;Liao, J.;Zhou, J.;Lin, F.;Ma, E.;Jin, D.; Yuan, X. High Spatial and Temporal Resolution NIR-IIb Gastrointestinal Imaging in Mice. Nano Lett 2022, 22, 2793-2800.

[178] Liao, J.;Yang, L.;Wu, S.;Yang, Z.;Zhou, J.;Jin, D.; Guan, M. NIR-II emissive properties of 808 nm-excited lanthanide-doped nanoparticles for multiplexed in vivo imaging. Journal of Luminescence 2022, 242, 118597.

[179] Shen, X.;Deng, Y.;Chen, L.;Liu, C.;Li, L.; Huang, Y. Modulation of Autophagy Direction to Enhance Antitumor Effect of Endoplasmic-Reticulum-Targeted Therapy: Left or Right? Advanced Science 2023, 2301434.

[180] Tsvetkov, P.;Coy, S.;Petrova, B.;Dreishpoon, M.;Verma, A.;Abdusamad, M.;Rossen, J.;Joesch-Cohen, L.;Humeidi, R.; Spangler, R. D. Copper induces cell death by targeting lipoylated TCA cycle proteins. Science 2022, 375, 1254-1261.

[181] Guo, B.;Yang, F.;Zhang, L.;Zhao, Q.;Wang, W.;Yin, L.;Chen, D.;Wang, M.;Han, S.; Xiao, H. Cuproptosis Induced by ROS Responsive Nanoparticles with Elesclomol and Copper Combined with αPD-L1 for Enhanced Cancer Immunotherapy. Advanced Materials 2023, 35, 2212267.

[182] Liu, M.;Li, Q.;Liang, L.;Li, J.;Wang, K.;Li, J.;Lv, M.;Chen, N.;Song, H.;Lee, J.;Shi, J.;Wang, L.;Lal, R.; Fan, C. Real-time visualization of clustering and intracellular transport of gold nanoparticles by correlative imaging. Nat Commun 2017, 8, 15646.

[183] Ghosh, S. K.; Pal, T. Interparticle coupling effect on the surface plasmon resonance of gold nanoparticles: from theory to applications. Chemical reviews 2007, 107, 4797-4862.

[184] Liu, M.;Wang, F.;Zhang, X.;Mao, X.;Wang, L.;Tian, Y.;Fan, C.; Li, Q. Tracking endocytosis and intracellular distribution of spherical nucleic acids with correlative single-cell imaging. Nature Protocols 2021, 16, 383-404.

[185] Jauffred, L.;Samadi, A.;Klingberg, H.;Bendix, P. M.; Oddershede, L. B. Plasmonic heating of nanostructures. Chemical reviews 2019, 119, 8087-8130.

[186] Zhou, B.;Shi, B.;Jin, D.; Liu, X. Controlling upconversion nanocrystals for emerging applications. Nat Nanotechnol 2015, 10, 924-936.

[187] Liao, J.;Yang, Z.;Wu, H.;Yan, D.;Qiu, J.;Song, Z.;Yang, Y.;Zhou, D.; Yin, Z. Enhancement of the up-conversion luminescence of Yb 3+/Er 3+ or Yb 3+/Tm 3+ co-doped NaYF4 nanoparticles by photonic crystals. Journal of Materials Chemistry C 2013, 1, 6541-6546.

[188] Liao, J.;Yang, Z.;Lai, S.;Shao, B.;Li, J.;Qiu, J.;Song, Z.; Yang, Y. Upconversion emission enhancement of NaYF4: Yb, Er nanoparticles by coupling silver nanoparticle plasmons and photonic crystal effects. The Journal of Physical Chemistry C 2014, 118, 17992-17999.

[189] Liao, J.;Yang, Z.;Wu, H.;Lai, S.;Qiu, J.;Song, Z.;Yang, Y.; Yin, Z. Continuous modification of upconversion luminescence of fluorescent dye in the crystalline colloidal arrays. Colloid and Polymer Science 2014, 292, 613-617.

[190] Garfield, D. J.;Borys, N. J.;Hamed, S. M.;Torquato, N. A.;Tajon, C. A.;Tian, B.;Shevitski, B.;Barnard, E. S.;Suh, Y. D.; Aloni, S. Enrichment of molecular antenna triplets amplifies upconverting nanoparticle emission. Nature Photonics 2018, 12, 402-407.

[191] Mi, C.;Zhang, X.;Yang, C.;Wu, J.;Chen, X.;Ma, C.;Wu, S.;Yang, Z.;Qiao, P.; Liu, Y. Bone disease imaging through the near-infrared-II window. Nature Communications 2023, 14, 6287.

[192] Yang, Y.;Chen, Y.;Pei, P.;Fan, Y.;Wang, S.;Zhang, H.;Zhao, D.;Qian, B.-Z.; Zhang, F. Fluorescence-amplified nanocrystals in the second near-infrared window for in vivo real-time dynamic multiplexed imaging. Nature nanotechnology 2023, 18, 1195-1204.

[193] Fan, Y.;Wang, P.;Lu, Y.;Wang, R.;Zhou, L.;Zheng, X.;Li, X.;Piper, J. A.; Zhang, F. Lifetime-engineered NIR-II nanoparticles unlock multiplexed in vivo imaging. Nature nanotechnology 2018, 13, 941-946.

[194] Liao, J.;Zhou, J.;Song, Y.;Liu, B.;Chen, Y.;Wang, F.;Chen, C.;Lin, J.;Chen, X.; Lu, J. Preselectable optical fingerprints of heterogeneous upconversion nanoparticles. Nano Letters 2021, 21, 7659-7668.

[195] Liu, B.;Li, C.;Xing, B.;Yang, P.; Lin, J. Multifunctional UCNPs@PDA-ICG nanocomposites for upconversion imaging and combined photothermal/photodynamic therapy with enhanced antitumor efficacy. J Mater Chem B 2016, 4, 4884-4894.

[196] Liu, F.;He, X.;Lei, Z.;Liu, L.;Zhang, J.;You, H.;Zhang, H.; Wang, Z. Facile Preparation of Doxorubicin-Loaded Upconversion@Polydopamine Nanoplatforms for Simultaneous In Vivo Multimodality Imaging and Chemophotothermal Synergistic Therapy. Advanced Healthcare Materials 2015, 4, 559-568.

[197] Yan, S.;Zeng, X.;Tang, Y. a.;Liu, B.-F.;Wang, Y.; Liu, X. Activating Antitumor Immunity and Antimetastatic Effect Through Polydopamine-Encapsulated Core–Shell Upconversion Nanoparticles. Advanced Materials 2019, 31, 1905825.

[198] Sun, M.;Xu, L.;Ma, W.;Wu, X.;Kuang, H.;Wang, L.; Xu, C. Phototherapy: Hierarchical Plasmonic Nanorods and Upconversion Core–Satellite Nanoassemblies for Multimodal Imaging-Guided Combination Phototherapy (Adv. Mater. 5/2016). Advanced Materials 2016, 28, 897-897.

[199] Ng, C. W.;Li, J.; Pu, K. Recent progresses in phototherapy-synergized cancer immunotherapy. Advanced Functional Materials 2018, 28, 1804688.

[200] Pei, P.;Chen, Y.;Sun, C.;Fan, Y.;Yang, Y.;Liu, X.;Lu, L.;Zhao, M.;Zhang, H.; Zhao, D. X-ray-activated persistent luminescence nanomaterials for NIR-II imaging. Nature Nanotechnology 2021, 16, 1011-1018.

[201] Wang, T.;Wang, S.;Liu, Z.;He, Z.;Yu, P.;Zhao, M.;Zhang, H.;Lu, L.;Wang, Z.; Wang, Z. A hybrid erbium (III)–bacteriochlorin near-infrared probe for multiplexed biomedical imaging. Nature Materials 2021, 20, 1571-1578.

[202] Abánades Lázaro, I.;Chen, X.;Ding, M.;Eskandari, A.;Fairen-Jimenez, D.;Giménez-Marqués, M.;Gref, R.;Lin, W.;Luo, T.; Forgan, R. S. Metal–organic frameworks for biological applications. Nature Reviews Methods Primers 2024, 4, 42.

[203] Sun, H.;Li, Y.;Yu, S.; Liu, J. Metal-organic frameworks (MOFs) for biopreservation: From biomacromolecules, living organisms to biological devices. Nano Today 2020, 35, 100985.

[204] Bobo, D.;Robinson, K. J.;Islam, J.;Thurecht, K. J.; Corrie, S. R. Nanoparticle-based medicines: a review of FDA-approved materials and clinical trials to date. Pharmaceutical research 2016, 33, 2373-2387.

[205] Dilliard, S. A.; Siegwart, D. J. Passive, active and endogenous organ-targeted lipid and polymer nanoparticles for delivery of genetic drugs. Nat Rev Mater 2023, 8, 282-300.

[206] Tenchov, R.;Bird, R.;Curtze, A. E.; Zhou, Q. Lipid Nanoparticles horizontal line From Liposomes to mRNA Vaccine Delivery, a Landscape of Research Diversity and Advancement. ACS Nano 2021, 15, 16982-17015.

[207] Pei, D.; Buyanova, M. Overcoming endosomal entrapment in drug delivery. Bioconjugate chemistry 2018, 30, 273-283.

[208] Lawson, W. E.;Cheng, D.-S.;Degryse, A. L.;Tanjore, H.;Polosukhin, V. V.;Xu, X. C.;Newcomb, D. C.;Jones, B. R.;Roldan, J.; Lane, K. B. Endoplasmic reticulum stress enhances fibrotic remodeling in the lungs. Proceedings of the National Academy of Sciences 2011, 108, 10562-10567.

[209] Guo, Y.;Liu, Y.;Zhao, S.;Xu, W.;Li, Y.;Zhao, P.;Wang, D.;Cheng, H.;Ke, Y.; Zhang, X. Oxidative stress-induced FABP5 S-glutathionylation protects against acute lung injury by suppressing inflammation in macrophages. Nature Communications 2021, 12, 7094.

[210] Jiang, M.;Li, X.;Zhang, J.;Lu, Y.;Shi, Y.;Zhu, C.;Liu, Y.;Qin, B.;Luo, Z.; Du, Y. Dual inhibition of endoplasmic reticulum stress and oxidation stress manipulates the polarization of macrophages under hypoxia to sensitize immunotherapy. ACS nano 2021, 15, 14522-14534.

[211] Gajbhiye, K. R.;Salve, R.;Narwade, M.;Sheikh, A.;Kesharwani, P.; Gajbhiye, V. Lipid polymer hybrid nanoparticles: a custom-tailored next-generation approach for cancer therapeutics. Molecular Cancer 2023, 22, 160.

[212] Wilner, O. I.; Willner, I. Functionalized DNA nanostructures. Chemical reviews 2012, 112, 2528-2556.

[213] Stites, W. E. Protein− protein interactions: interface structure, binding thermodynamics, and mutational analysis. Chemical reviews 1997, 97, 1233-1250.

[214] Ngo, W.;Ahmed, S.;Blackadar, C.;Bussin, B.;Ji, Q.;Mladjenovic, S. M.;Sepahi, Z.; Chan, W. C. Why nanoparticles prefer liver macrophage cell uptake in vivo. Advanced Drug Delivery Reviews 2022, 185, 114238.

Chapter 3. Materials and Methods

This chapter will explore the experimental methods; characterization procedures and sample preparation performed in this thesis. Materials, as well as commercial instruments will be listed with their respective experimental procedures. Furthermore, three sections separated by the chemical, optical and biological experimental procedures performed by the author will be highlighted in this section.

3.1 Chemicals, reagents and consumables

Reagents and chemicals used in this thesis were purchased via Sigma-Aldrich unless specified. Reagents used include: Yttrium (III) chloride hexahydrate (YCl3·6H2O, 99.99%), Ytterbium (III) chloride hexahydrate (YbCl3·6H2O, 99.9%), Thulium (III) chloride hexahydrate (TmCl3·6H2O, 99.99%), Erbium (III) chloride hexahydrate (ErCl3·6H2O, 99.9%),Sodium Hydroxide (NaOH, 99%), NaF (99%), Oleic Acid (OA, Technical grade 90%), 1-Octadecene (Technical grade 90%), Ammonium fluoride (NH_4F, 98%), Methanol (99.9%), Cyclohexane (97%), Tetrahydrofuran (THF, 99.9%), Poly-L-lysine (PLL) solution, Rhodamine B (95%) , Sulfo-n-hydroxysulfosuccinimide (Sulfo-NHS, 98%), 1-Ethyl-3-(3-dimethylaminopropyl)carbodiimide (EDC, 97%), MES buffer (99%), Borate buffer (Powder pack). Ethanol (99.5%) was purchased from Chemsupply. All chemical reagents were used without additional purification. The author acknowledges Dr. Jiayan Liao for providing RAFT polymer B12, which represents *tri*block terpolymers, poly(poly (ethylene glycol) methyl ether methacrylate)-*block*-polymethacrylic acid-*block*-polyethylene glycol methacrylate phosphate ($PPEGMEMA_{15}$-*b*-$PMAA_{12}$-*b*-$PEGMP_3$).

Consumables and Miscellaneous include: Pipettes, Pipette tips, TEM copper grids, Glass slides, Cover slips, Centrifuge test tubes, (1.5ml, 2ml, 15ml), Freezer, Teflon rare-earth stir bars, Argon gas tank, Glass bottles.

3.2 Commercial Instruments

Instrumentation and consumables used for the preparation and characterization of nanomaterials described in this thesis are listed below: Malvern Zetasizer Nano ZS90 ATA

Scientific, Nicolet FT-IR 6700 ATR-FTIR, JEOL F2000 TEM, Heating mantle (Room temperature to 400 °C), Two-neck Round Bottom Flask, Three-neck Round Bottom Flask, Eppendorf Bench top Centrifuge 5424, LSE Vortex mixer, Thermometer, Ultra-sonic bath, Schlenk line, Analytical scale, Vacuum oven, Teflon-lined Autoclave, Fume hood.

3.3 Synthesis, functionalization and characterization of UCNPs

3.3.1 Nanoparticle synthesis

3.3.1.1 Coprecipitation

The co-precipitation of lanthanide UCNPs was performed according to previous literature [1, 2]. In a typical coprecipitation procedure, 1 mmol of combined RECl3 (RE = Y, Yb, Er, Tm), where the amount of rare earth chlorides adds up to 1 mmol total is mixed thoroughly with 6 ml of oleic acid and 15 ml of 1-octadecence in a 50 ml two-neck round-bottom flask. Under a fume hood, lanthanide oleate complexes were formed after the solution became transparent after vigorous stirring 160°C with argon gas pumping. The solution was then cooled to room temperature before adding a solution of 100 mg NaOH and 148mg of NH4Cl dissolved in methanol. Remaining precipitates in the container were flushed again with methanol into the mixture. The solution was then stirred for 20 minutes at 50°C under inert conditions through argon gas pumping. The mixture was then heated to 100°C to facilitate the evaporation of residual water and methanol for 30 minutes. Additionally, the solution underwent vacuum pump to ensure the complete removal of water and methanol for 10 minutes. The mixture was then heated rapidly to 300°C under slow stirring for 90 minutes before rapid cooling to room temperature.

The removal of excess unreacted reagents was achieved through centrifugation. For 6ml of UCNP solution after synthesis, the supernatant was discarded after centrifugation at 8500 rpm for 8 minutes. The nanocrystals were then washed by adding 3 ml of cyclohexane and sonicated for 2 minutes. 1 ml of oleic acid was then added into the washed nanocrystals and further sonicated before adding 10ml of ethanol. The solution was sonicated again for 2 minutes before centrifugation. The washing step was repeated three times in total before redispersing in cyclohexane and frozen at -20°C.

3.3.1.2 Shell Pre-cursor

Shell Pre-cursor was synthesized with a similar method as co-precipitation. Shell precursor synthesis followed the steps for co-precipitation expect the removal of water and methanol was performed at 130°C for 40 minutes to ensure complete removal of water and methanol. Vacuum pumping was performed for an additional 10 minutes before rapid cooling to room temperature.

3.3.1.3 Core-shell synthesis

Epitaxial growth method was achieved with 3 ml of oleic acid, 8 ml of 1-octadecene and 0.2 mmol of washed nanoparticles. Using a three-neck round-bottom flask, the above mixture was heated to 150°C for 30 minutes to remove residual water, methanol and cyclohexane before rising the temperature to 300°C under argon atmosphere. Afterwards, a 0.15 ml shell-precursor solution was injected into the mixture at 300°C every two minutes. The thickness of the shell was determined by the amount and duration of pre-cursor injected into the solvent, which could be calculated using quantity, volume, and surface area of the nanoparticles as well as the volume of the desired core-shell structure. After the injection, the reaction was left at 300°C for 10 minutes before rapidly cooling down to room temperature. Core-shell nanoparticles were washed using the same procedure as stated above and stored at -20°C.

3.3.3 Sample preparation

3.3.3.1 Glass slide sample preparation

Washed UCNPs dispersed in cyclohexane were sonicated before carefully dropped onto a cover slide with differing concentrations based on experiments. The cover slide was then placed onto a microscope slide using scotch tape or by covering the sides with nail polish to ensure no leakage of immersion oil. Nanoparticle samples did not degrade over 2 years and were stored at room temperature.

3.3.3.2 TEM

10 μL of prepared nanoparticles (100 ug/mL) were dropped onto a copper grid and dried before being examined under a transmission electron microscope.

3.4 Optics setup and software design

Optical microscopy remains a cornerstone of the investigation of sub-micron structures and nanoscale luminescence, with its versatility extending across various imaging modalities. Among the many configurations, widefield and confocal microscopy represent two principal approaches, each offering distinct advantages depending on the imaging requirements and sample characteristics. This section outlines the foundational concepts of optical microscopy and details the specific optical pathways, illumination schemes, and detection strategies involved in both widefield and confocal systems, with emphasis on their relevance to UCNP imaging.

3.4.1 Optical Components

Optical components include: 976 nm butterfly laser (BL976-PAG900- 976nm), temperature controller (Thorlabs CLD1015), data acquisition device (DAQ) (National instruments NI USB-6353), 10X objective lens (Olympus PLN 10X objective), 100X objective lens (Olympus PLN 100X objective 1.4A), charged coupled device (CCD) (Manta MG-809C IRC), 950 nm long pass dichroic mirror (DML950R), single photon avalanche diode (SPAD) (Excelcitas SPCM-AQRH), spectrometer (Ocean optics QE Pro) , pizeo controller (BPC303), Concave lens kit (LSB04-B), 800 nm bandpass (FBH800-40), 950 nm long pass (FEL0950). PM100D Energy Meter was used for power measurements.

Components for microscope assembly were purchased from Thorlabs. Components include: kinematic mirror mounts (KM100), pedestal posts (RS1P), clamping forks (CF125,CF175), lens tubes (SM30L10), XY translation mounts (ST1XY-S,CXY1A), cage plates (CP35, CP36) , cage cubes (C6WR), kinematic platform (B4C), Optic mounts (FFM1), construction rods (ER series)), Z-Axis translation mount (SM1ZA), motorized stage (MDT630B), manual stage (MT1), screws (SH6M series), post, post holders and post clamps (MSP, PH RA and TR series).

3.4.2 Setup outline Custom multi-purpose optical instrumentation

The custom microscope system is depicted in figure 3.1 and figure 3.2. The polarize maintaining laser 976 nm butterfly laser utilized a temperature controller which was controlled via a DAQ, which was further controlled using custom LABVIEW software with

a personal computer. The laser was spatially filtered using a pinhole and collimated with a 10X objective lens. A 950 nm LP was used to filter out any residual lasing. A 950 nm long pass dichroic mirror was used to reflect the laser into the objective lens and pass photons between 300 nm to 850 nm into the SPAD or spectrometer. A focusing lens was used to focus the photons into the CCD, SPAD or spectrometer, which was determined using a flip mirror. Piezo controller outputs were used to find the sample and SPAD inputs were both received and processed by the DAQ device. Finally, a brightfield illuminator with a phase ring and focusing lens was used to focus the sample using the CCD.

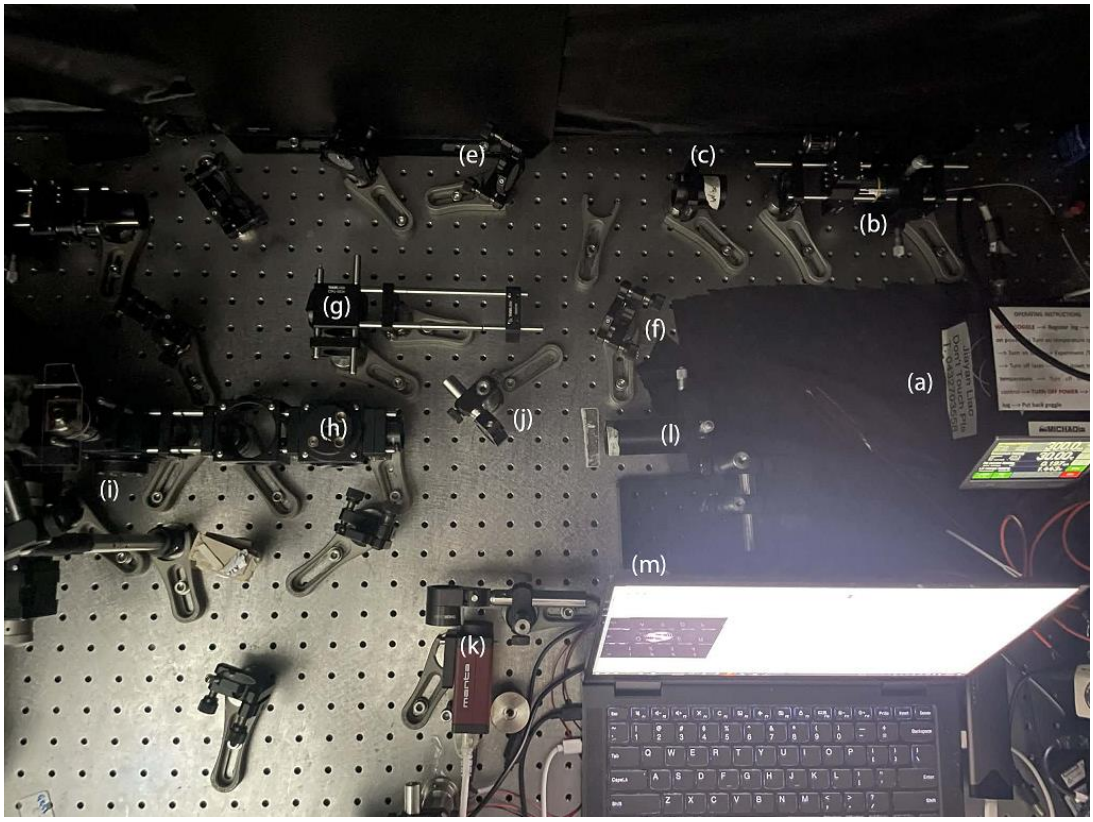

Figure 3.1 Panoramic view of home-built optical characterization device. (a) Laser controller. (b) 10x objective lens for collimation. (c) 900 nm filter. (d) Neutral density filter. (e), (f), (g) Silver mirror. (h) Dichotic mirror. (i) Stage and objective lens. (j) Flip mirror. (k) CCD. (L)Acquisition panel with pinhole (m) personal computer.

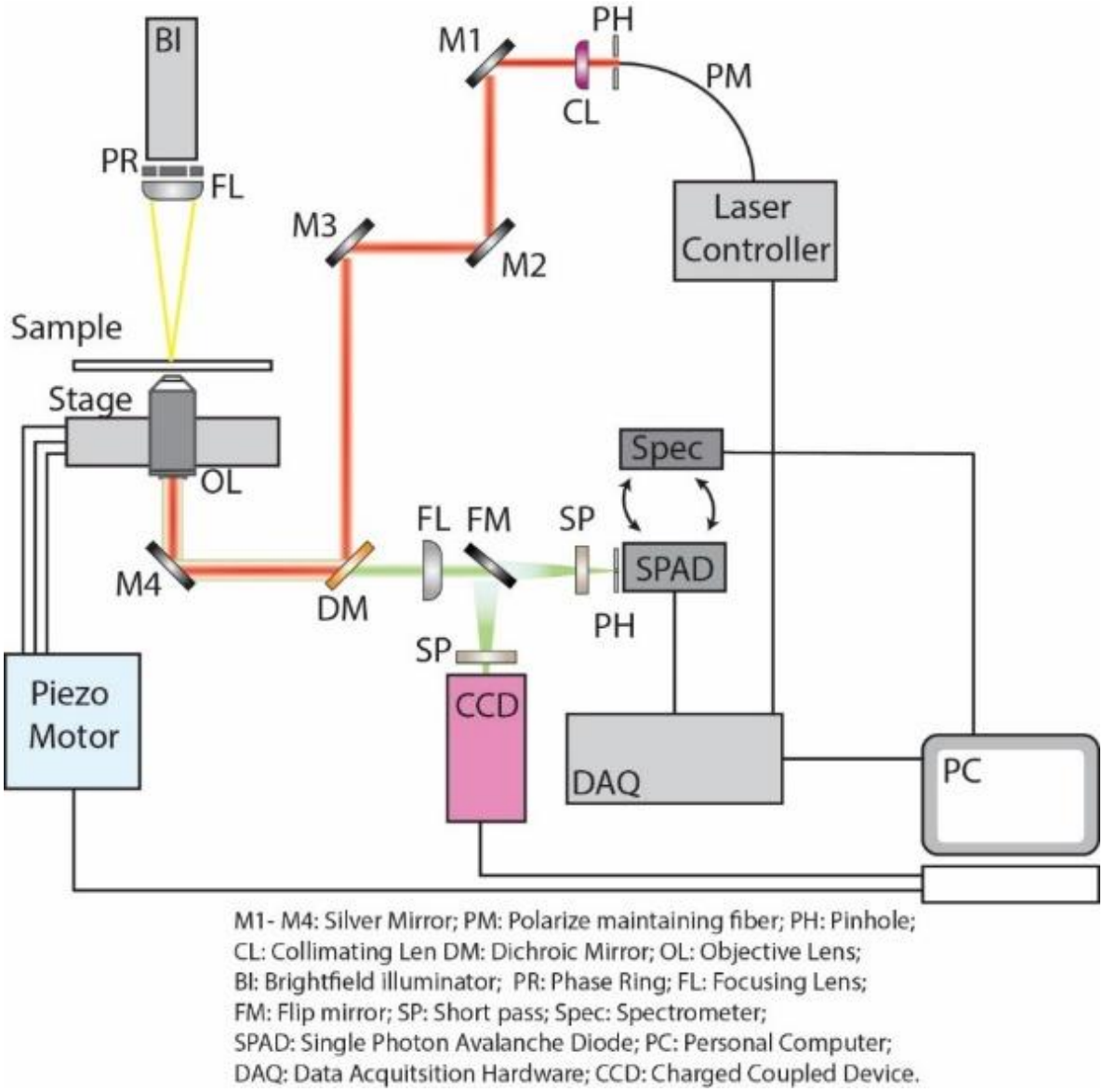

Figure 3.2 Schematic illustration of the home-built characterization device.

3.4.2 Widefield microscopy

Widefield microscopy is characterized by the uniform illumination of the entire sample area, typically achieved through Koehler illumination, which produces a collimated beam incident on the specimen. In this configuration, the condenser lens system is aligned such that the light source is imaged at the back focal plane of the objective, resulting in evenly distributed excitation across the field of view. For coherent laser excitation, such as in the case of UCNP excitation, the Gaussian intensity distribution of the laser remains unchanged unless modified by a beam-shaping element [3]. While a top-hat or flat-top beam shaper can be employed to homogenize the intensity profile, in this system such diffusers were intentionally omitted to preserve maximal laser power. Instead, control over the laser spot size was achieved using a defocusing lens placed at the phase conjugate plane. Adjusting the axial position of this lens introduced controlled divergence or convergence of the beam, thereby modifying the illumination profile at the sample plane (Figure 3.3). This flexibility proved particularly advantageous for bulk UCNP characterization, where a broader excitation area was desirable to maximize signal integration without the need for raster scanning. Although widefield imaging lacks optical sectioning capability and is susceptible to out-of-focus background, it offers superior acquisition speed and simplicity, making it well-suited for rapid screening, spectral measurements, and static single-particle analyses [4].

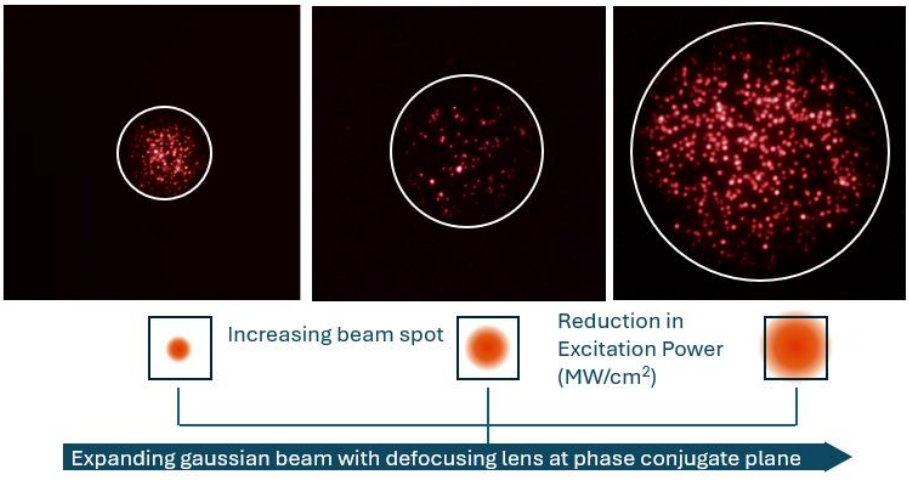

Figure 3.3 Gaussian beam expansion and field of view observation with home-built microscope. An increase in beam spot results in an increase in field of view at the expense of decreased power density.

3.4.3 Confocal microscopy

Confocal microscopy provides optical sectioning by rejecting out-of-focus light through the use of a spatial pinhole in the detection pathway. Unlike widefield systems, confocal microscopy utilizes point illumination and spatially filters the emitted light, enabling high-resolution imaging with enhanced axial discrimination. In the standard configuration, a laser beam is focused on a diffraction-limited spot on the sample by a high numerical aperture objective. The fluorescence or upconversion emission from the focal volume is collected by the same objective and directed through a pinhole aperture before reaching the detector [5, 6]. This pinhole eliminates light originating from planes above and below the focal plane, thus enhancing contrast and resolution in thick or heterogeneous samples.

In this project, confocal imaging was essential for high-fidelity single-particle measurements of UCNPs. The point-scanning mechanism enabled isolation of individual particles while suppressing background signals from aggregates or the substrate. Due to the non-linear nature of upconversion luminescence, where emission intensity is dependent on excitation power density, the confocal configuration offered an additional advantage, as the laser beam's tight focus naturally increased the power density at the focal point, thereby enhancing upconversion efficiency and signal detectability at the single-particle level [7].

Moreover, the integration of precise scanning stages and programmable laser modulation allowed for flexible control over spatial and temporal parameters, including excitation dwell time and pixel resolution. Together, these features enabled quantitative mapping of luminescence intensity, saturation behavior, and photostability across individual particles. Confocal microscopy thus served as a critical tool in evaluating the intrinsic optical properties of UCNPs, resolving heterogeneities otherwise obscured in ensemble measurements.

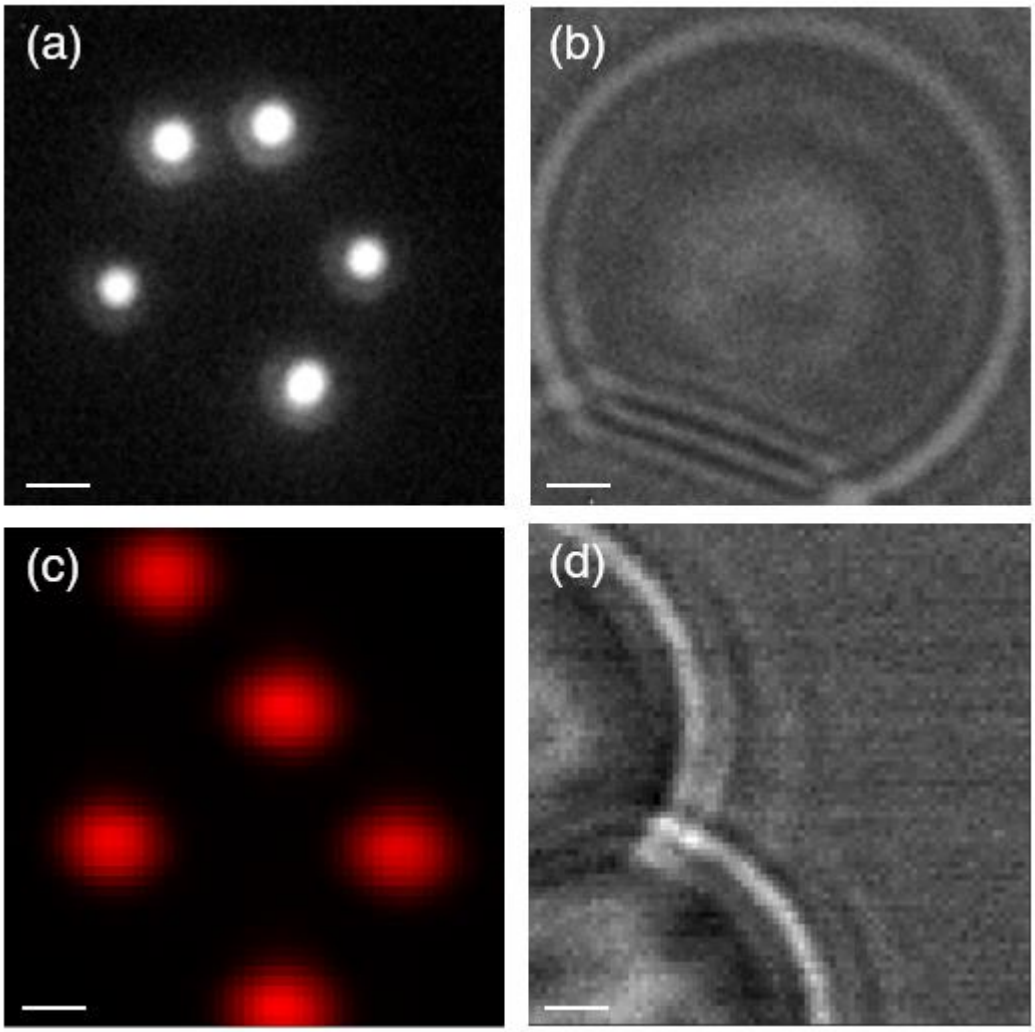

Figure 3.4 Widefield and confocal microscopy. (a) Widefield imaging of UCNPs (20%Tm,40%Yb NaYF4), scale bar: 500 nm. (b) Widefield imaging of 5 um Microbeads, scale bar: 500 nm. (c) Confocal imaging of UCNPs (20%Tm,40%Yb $NaYF_4$), scale bar: 250 nm (d) Confocal scanning imaging of 5 um microbeads. Scale bar: 500 nm.

3.4.4 Principles and implementation for programmable optical instrumentation

The precise control of optical instrumentation is critical for accurate and reproducible characterization of upconversion nanoparticles, particularly when measuring parameters such as luminescence intensity and lifetime. Unlike commercially available microscope systems with fixed or proprietary control architectures, the system developed in this project was designed to be modular, fully programmable, and highly customizable to accommodate

the unique requirements of UCNP characterization. Central to this system is the integration of hardware control and data acquisition via a LabVIEW based graphical programming environment, interfaced with a National Instruments DAQmx system for real-time analog and digital signal generation and synchronization.

At the core of the system is a principle of time and event resolved control over both excitation and detection pathways (Figure 3.5). The DAQ device serves as a bridge between the LabVIEW interface and the physical components of the optical setup, which are mainly the laser, piezo motor, and photodetector. Analog output channels from the DAQ device are used to modulate laser intensity, while digital output lines are employed for synchronized timing pulses for pulse laser modulation and initiate data acquisition windows.

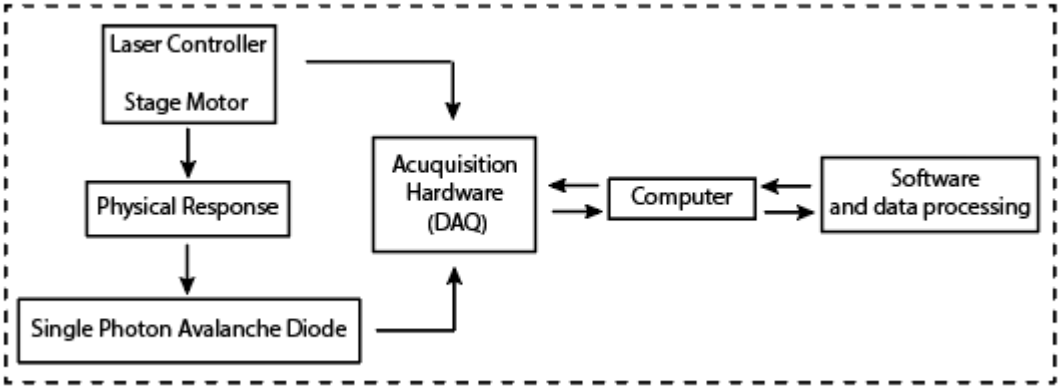

Figure 3.5 Schematic illustration of hardware and software interface interactions. A closed loop of control, acquisition, and analysis. The laser controller and stage motor generate optical signals from UCNPs, and the resulting luminescence signals are detected by the single photon avalanche diode. This signal is transferred to the data acquisition hardware, which interfaces with the computer, which deals with data processing.

LabVIEW provides a high-level programming interface that enables precise sequencing of experimental routines, including the control of excitation pulse durations, dwell times at specific scanning coordinates, or synchronization of laser excitation with photon detection (Figure 3.6). LabVIEW software is designed to control DAQ devices designed by National Instruments and is a graphical programming language that facilitates automated data

acquisition and instrument control. LabVIEW programs contain a virtual instrument that consists of two interfaces, a front panel (Figure 3.7) with controls and indicators, which the user controls when the program is running, and a block diagram where functions and structures are wired together to form the executable code (Figure 3.8 & Figure 3.9). Using a producer-consumer architecture, data acquisition and control processes can be decoupled, allowing for real-time streaming and analysis of photon counts, fluorescence decay curves, or spatial emission patterns. This architecture is particularly valuable when acquiring high temporal resolution data, such as single-particle luminescence traces or time-resolved emission profiles, where latency and timing jitter can degrade measurement fidelity.

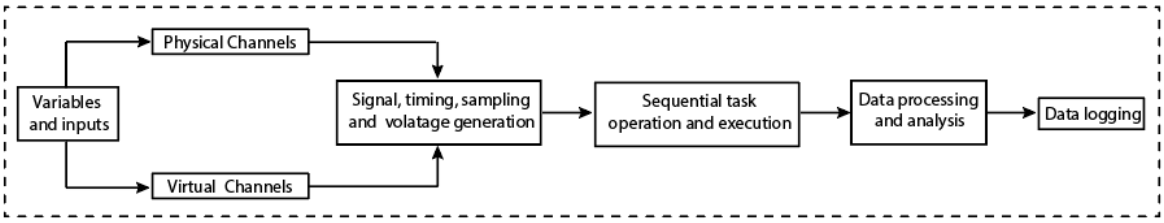

Figure 3.6 Illustration of LabVIEW logic. LabVIEW logic is built from interconnected functional blocks featuring physical and virtual channels. Each block performs a specific task, and it executes only when all required input data becomes available. Once a block finishes its operation, the resulting output data flows to the next connected block, allowing the entire program to run as a network of data driven operations.

The system's flexibility also allows for dynamic protocol switching and feedback-based control. For example, laser scanning parameters can be altered in real-time based on incoming signal intensity, or acquisition can be paused and resumed based on signal thresholds or external triggers. This programmability enables complex experimental protocols such as saturation curve measurements, repeated excitation-recovery cycles, or lifetime mapping, all of which are critical for fully characterizing the nonlinear and long-lived photophysical behavior of UCNPs [8].

Through the combined use of LabVIEW and DAQmx, this custom-built optical system offers a robust and extensible platform for high-precision control and measurement in optical nanomaterial research. It enables seamless integration of diverse hardware

components, allowing for tailored experimental design, and provides the temporal and spatial control necessary for probing UCNPs at both the bulk and single-particle level.

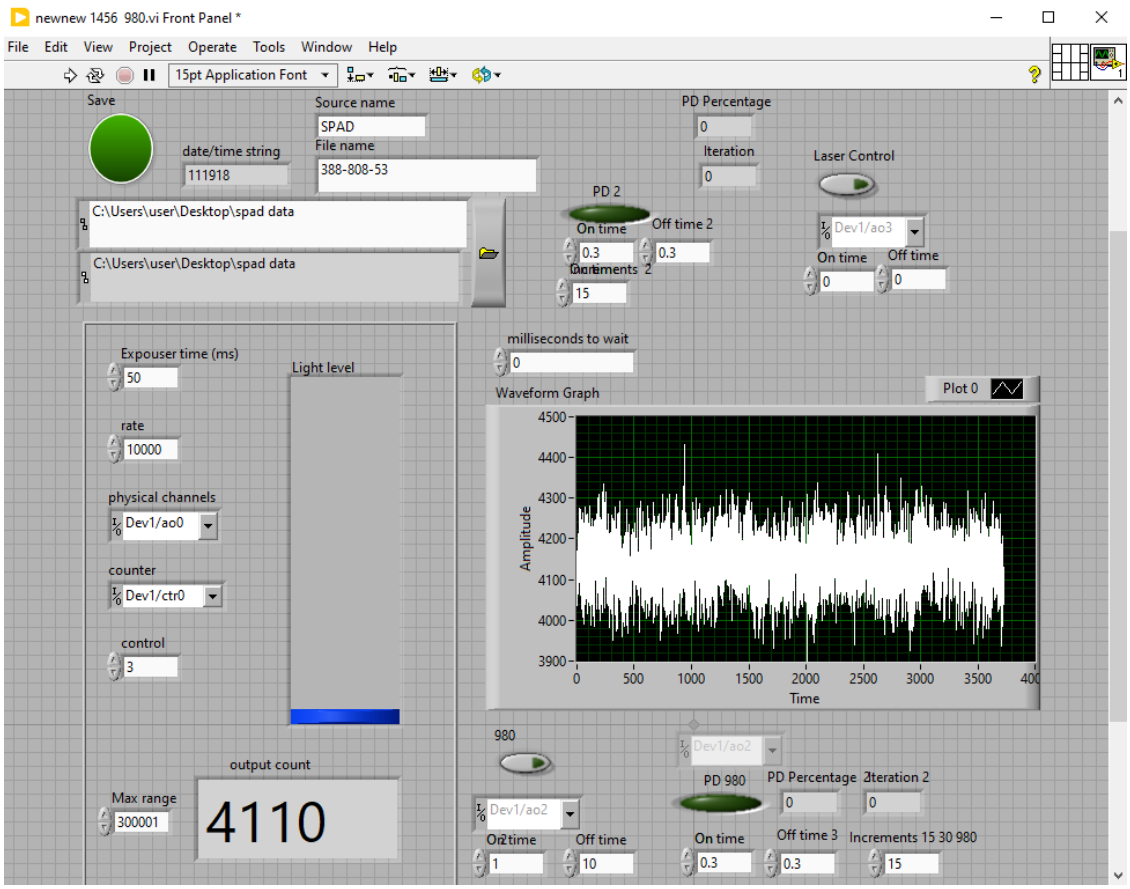

Figure 3.7 Front Panel of LabVIEW software for single particle photon counting. The front panel in LabVIEW serves as the graphical user interface of a virtual instrument and functions as the space where users interact with the program yet is directly to the underlying block diagram. It contains controls and indicators that allow users to provide input, adjust parameters, and observe outputs generated during execution.

3.4.5 Single particle photon counting

Single particle photon counting was achieved with custom LabVIEW code, which dictates the positioning of the sample, single photon counting through SPAD, as well as laser intensity control for power dependence experiments. The first function within the LabVIEW software enables laser control which outputs the laser intensity by changing the voltage given to the laser which is placed within a sub-VI (Figure 3.8). Duration of the laser is programmed in a case structure which allows tunable duration on the front panel.

The second function designed within a while structure receives signals from the SPAD at a given rate and accumulates photon counts in each interval depending on exposure time, which is then exported to a text file (Figure 3.9). The main purpose behind single particle photon counting instead of ensemble or powder-based counting is a result of the Gaussian distribution of the laser. In a normal microscope setup, regardless of whether the laser is collimated or convergent at the back focal plane, the Gaussian distribution of a laser will result in disproportionate values caused by surrounding nanoparticles absorbing laser intensities lower than the maximum laser intensity received in the middle. Given that UCNPs can display non-linear optical responses and saturate at higher laser intensities, outer nanoparticles can result in inaccurate data measurements. In circumstances like this, the only way to ensure that particle luminescent recants are accurate is to guarantee that either the quantity of particles remains the same and are distributed evenly during data acquisition, or that only a single particle receives the maximum laser intensity (which is calibrated by hand using the piezo controller). Single particle photon counting was therefore done with a collimated laser at the back focal plane to form a small focused gaussian laser spot on the sample.

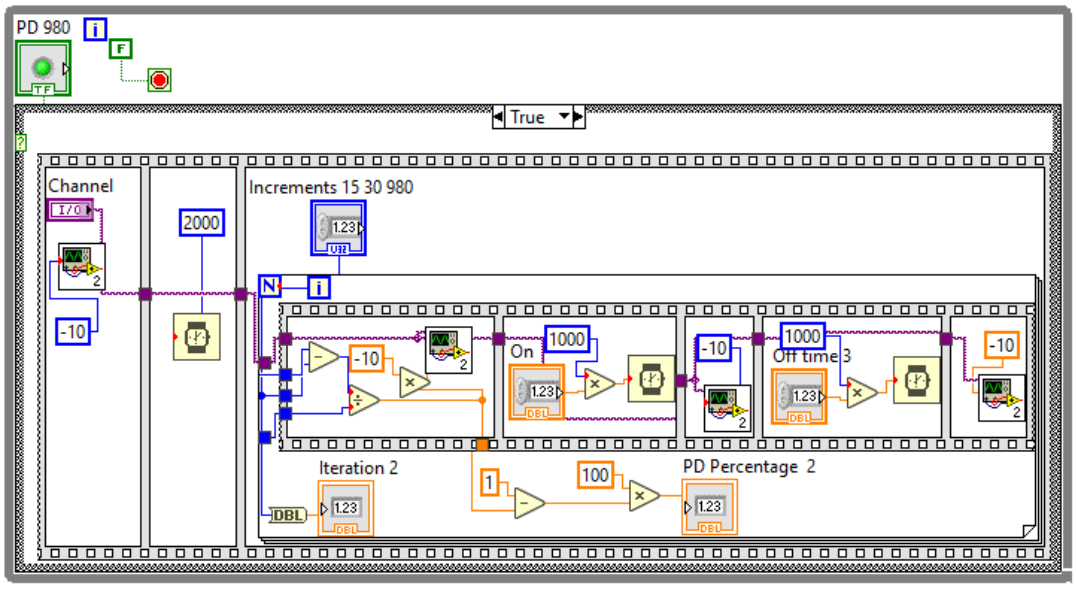

Figure 3.8 Laser intensity and timing control. In a closed loop system, a change in laser power occurs with changing voltage, which changes based on the increments "*n*", which represents the loop number. The orange boxes represent tunable values available on the front panel of the LabVIEW program.

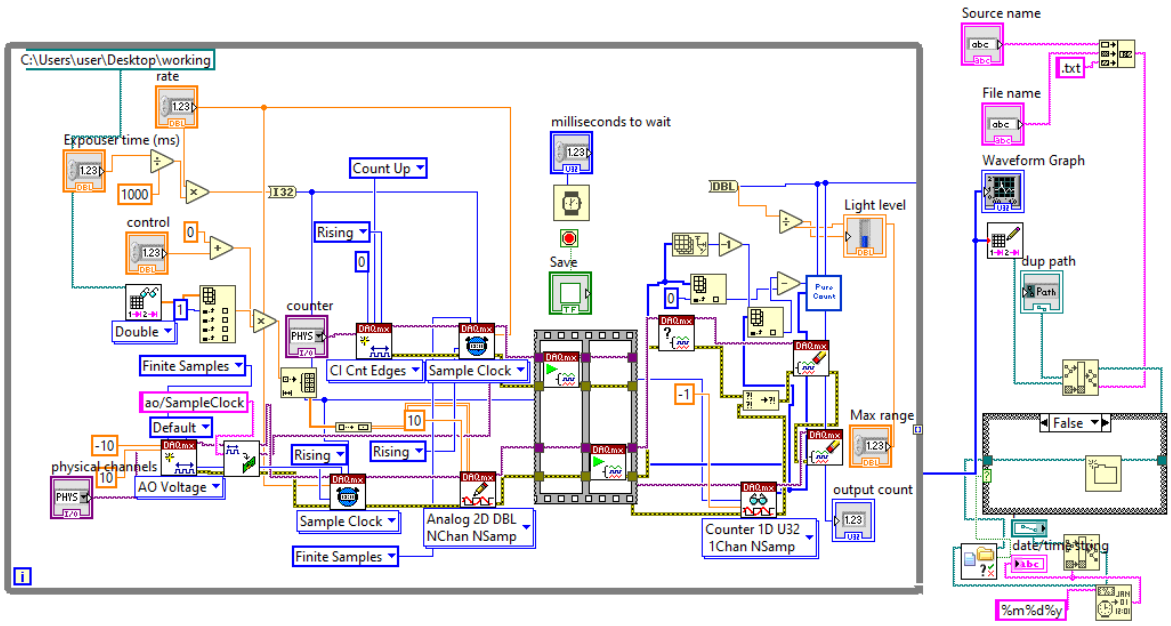

Figure 3.9 Hardware timing, sequential timing and data acquisition. In addition to tunable values for controlling laser on off time, photon counts and the waveform graph in the front panel and are saved within the computer.

3.4.6 Single nanoparticle lifetime measurements

Similar to single particle photon counting, nanoparticle lifetime measurements were acquired using the same methodology with modified programs to control data acquisition. However, differing from the previous program, where some data points are omitted for the sake of speed and processing, every photon is counted during lifetime measurements given the required sensitivity for single particle lifetime experiments. To ensure that the measurements are accurate, the lifetime experiment is repeated and observed with a pulsed laser in mind. These lifetime measurements are then fitted using a custom MATLAB code to illustrate the lifetime fitting across multiple lifetime measurements.

3.4.7 Up-conversion spectroscopy

Up-conversion spectroscopy was performed using QEpro, to ensure that the focusing lens remains aligned with the optic fiber, the outer optic fiber (Fiber not connected to a pinhole) was switched between photon counting and spectrophotometer experiments. Furthermore,

given the limited sensitivity of the spectrometer, nanoparticle ensembles were prepared for spectrophotometer experiments.

3.5 UCNPs under biological conditions – Methods and procedures

3.3.2 Surface modification of nanoparticles

3.3.2.1. Ligand exchange

Hydrophilic nanoparticles were obtained through ligand exchange with PEG di-block copolymer. 10 mg of nanoparticles were redispersed in 1 mL of THF with 15 mg of polymer and shaken for 12 hours at room temperature. The polymer coated UCNPs were washed using a mixture of THF and water three times, with the ratio of THF gradually reduced in subsequent washing cycles until the particles were completely dispersed in water. The final solution was stored at 4°C in 0.2 ml of de-ionized water [9].

3.3.2.2. PLL and Rhodamine bioconjugation

The formation of positively charged nanoparticles was achieved through the conjugation of poly-lysine. 0.5 ml of 0.1% PLL solution was added along with 0.3 ml of de-ionized water and sonicated for 2 minutes. Afterwards, the solution was shaken at room temperature for 40 minutes before being washed twice with DI water via centrifugation.

Rhodamine B conjugation was achieved via EDC-NHS carbonamide linking (Figure 3.10). Carbonamide activation was achieved when 0.5 mg of Rhodamine B was added in 1 ml of MES buffer with 5 mg of EDC and 5 mg of NHS and shaken at 4°C for 15 minutes under darkness to prevent photodegradation. PLL conjugated UCNPs were then added into the solution and further shaken for 2 hours at 4°C. The Rhodamine-PLL-UCNP was then washed at least three times with DI water via centrifugation and stored in dark conditions at 4°C [10].

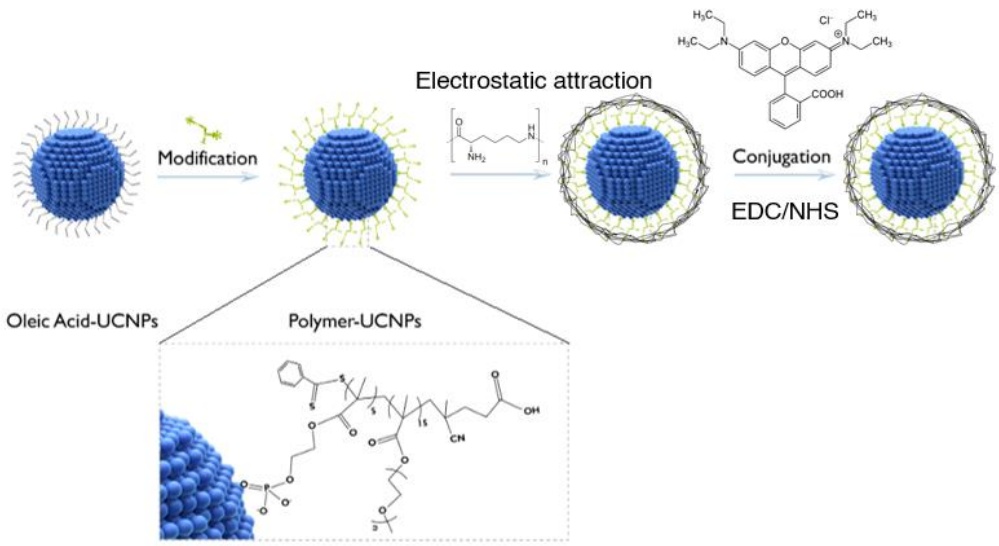

Figure 3.10 Schematic illustration of surface modification of UCNPs. UCNPs first undergo ligand exchange from Oleic Acid-UCNPs with the polymer triblock terpolymers, poly(poly (ethylene glycol) methyl ether methacrylate)-block-polymethacrylic acid-block-polyethylene glycol methacrylate phosphate (PPEGMEMA15-b-PMAA12-b-PEGMP3 (provided by Dr. Jiayan Liao). Afterwards, electrostatic attraction between carboxylic acid groups with poly-l-lysine facilitates a PLL coating. Rhodamine dye is then conjugated using EDC NHS.

3.3.2.3. Protein Corona formation

Hydrophilic UCNPs were incubated in sterile RPMI with 10% FBS for 30 minutes. The particles were then recovered via slow-speed centrifugation and used immediately for further experiments [11].

3.3.3.3 DLS & Zeta potential

Dynamic light scattering and zeta potential experiments were performed on a Malvern Zetasizer. Hydrodynamic size, and zeta potential experiments were performed with nanoparticles in a solution de-ionized water (100 ug/ml) using a quartz Zetasizer cuvette.

3.3.3.4. ATR-FTIR

Attenuated total reflectance – Fourier transform infrared spectroscopy (ATR-FTIR) was performed using a Nicolet FT-IR 6700. After centrifugation at 15000 rpm for 30 minutes for UCNPs, supernatant was removed and dried using a vacuum dehydrator. Approximately 10 mg of dehydrated powder UCNPs was used for FTIR analysis.

3.5.1 Cell culture

Experimental investigations for nanoparticle interactions with living cells involved HeLa, BV2, A549 and COLO-794 cell lines under the same conditions. Cell culture was performed in a T25 flask grown in RPMI 1640 cell culture medium with 10% fetal bovine serum (FBS) and 1% Penicillin-Streptomycin (PS). When stored, cell lines were stored in -80℃ until being thawed for usage. Cell lines were warmed in a 37c bath incubator before being centrifuged for 1500 RPM for 5 minutes. The supernatant was removed to remove all DMSO, leaving behind the cell pellet. 5ml of RPMI containing the previous materials were added and mixed thoroughly before placing into the T25 flask and placed inside a 37℃ incubator. Medium was replaced every 72 hours and checked for confluency. Under confluent conditions, medium was removed and washed with PBS before 1ml of trypsin was added for 5 minutes before RPMI containing FBS was added to neutralize the remaining trypsin. Most of the medium containing the cell suspension was removed for experiments from the flask before adding fresh medium to culture cells. For long term storage, 100uL DMSO was added into 1mL of medium containing 1 x 10^6 cells before being frozen at -80°C.

3.5.2 Fixed cell UCNP imaging

50,000 cells were seeded in a 35 mm imaging dish (CG 1.0, sterile) incubated in 1 mL RPMI containing 10% FBS and 1% PS overnight. Afterwards, PBS was used three times to wash and remove the medium before fixing cells in a 4% paraformaldehyde solution. UCNPs were added and incubated for 4 hours to observe fixed particle localization. Afterwards, UCNPs were washed using TRIS buffer gently three times to remove excess nanoparticles. Nanoparticle and cell microscopy was performed using the home-built widefield microscope [12].

3.5.3 Cytotoxic Assays

2,500 cells were seeded in a 96-well plate for cytotoxicity assays. After 24 hours, nanoparticles with differing conditions and concentrations were added to each well. After 72 hours, 10 μL of Alamar blue stock solution was added to each well and kept in the

incubator for 4 more hours. A microplate reader was then used to read the absorbance at 560 nm to determine the cell viability compared with the control.

3.5.4 Co-localization studies

Colocalization studies were conducted using a Tie2 widefield microscope with Rhodamine conjugated UCNPs for fluorescent widefield imaging and lysotracker Deep Red. 50,000 cells were seeded in a 35 mm imaging dish (CG 1.0, sterile) incubated in 1 mL RPMI containing 10% FBS and 1% PS overnight. Afterwards, sterilized UCNPs (50 ug/ml) were added into the medium and incubated for 4 hours. HEPES was then used three times to wash and remove the excess UCNPs. Afterwards, 200 nM Lysotracker was added for 30 minutes prior to imaging and washed three times using HEPES.

3.5.5 Cell TEM imaging

Cell plating procedure was similar to colocalization studies, with an increase to 500,000 cells being seeded in a 6 well plate in 1mL RPMI with 10% FBS and 1% PS overnight. The nanoparticle incubation procedure (200ug/ml) was identical to co-localization studies. After washing with HEPES, cells were fixed in a 2.5% glutaraldehyde solution in 0.1M Sorensen's phosphate buffer. Afterwards, cells were further fixed in 0.5% osmium tetroxide carefully washed with Sorenson's buffer, and then further fixed in a 2% uranyl acetate 50% ethanol solution. The solution was then washed 3 times with Sorenson's buffer to remove all previous solutions and reduce artifacts. Cells were then scraped using a rubber-policemen and pelleted at 3000 RPM for 5 minutes. The supernatant was then removed, and 2% melted agar was added into the tube to form a small gel, before being cut and placed into 70% ethanol for dehydration. Dehydration from 70%, 90%, 95% and 100% ethanol was done twice for 10 minutes before being embedded in epoxy resin. Capsules were first further dehydrated in a 50% propylene oxide and 50% Epoxy resin solution for 2hours before transferring the pellet into 100% epoxy resin solution. After polymerization, sections were cut using an ultramicrotome (Leica ultraacut microtome) and placed onto copper TEM grids before being examined under TEM.

3.5.6 Intracellular cargo tracking

Intracellular cargo tracking was performed with cells seeded in the procedure, the same as co-localization studies omitting the addition of Lysotracker. Co-localization analysis used ImageJ Plugin JaCoP [13]. Nanoparticle tracking was performed using home-built microscope system. Tracking analysis was performed using ImageJ Trackmate Plugin [14].MSD analysis used custom Matlab software as well as software MSDanalyzer [15]. In this thesis, HMM was applied to single-particle trajectories of UCNPs tracked within live cells using the package HMM-Bayes [16]. Each trajectory was modeled as a time series of two-dimensional displacements, with the goal of inferring underlying dynamic states and their temporal transitions. The number of hidden states was determined empirically using a Bayesian Information Criterion (BIC) and were optimally modeled using two to four motility states.

3.6 References

[1] Liu, D.;Xu, X.;Du, Y.;Qin, X.;Zhang, Y.;Ma, C.;Wen, S.;Ren, W.;Goldys, E. M.; Piper, J. A. Three-dimensional controlled growth of monodisperse sub-50 nm heterogeneous nanocrystals (2016). *Nature communications*.**7**,10254

[2] Wang, F.;Deng, R.; Liu, X. Preparation of core-shell NaGdF4 nanoparticles doped with luminescent lanthanide ions to be used as upconversion-based probes (2014). *Nature protocols*.**9**,1634-1644

[3] Chen, C.;Wang, F.;Wen, S.;Su, Q. P.;Wu, M. C.;Liu, Y.;Wang, B.;Li, D.;Shan, X.; Kianinia, M. Multi-photon near-infrared emission saturation nanoscopy using upconversion nanoparticles (2018). *Nature communications*.**9**,3290

[4] Liu, Q.;Zhang, Y.;Peng, C. S.;Yang, T.;Joubert, L.-M.; Chu, S. Single upconversion nanoparticle imaging at sub-10 W cm− 2 irradiance (2018). *Nature photonics*.**12**,548-553

[5] Li, X.;Wang, Y.;Shi, J.;Zhao, Z.;Wang, D.;Chen, Z.;Cheng, L.;Lu, G.-H.;Liang, Y.; Dong, H. Large-area near-infrared emission enhancement on single upconversion nanoparticles by metal nanohole array (2024). *Nano Letters*.**24**,5831-5837

[6] Wang, Y.;Liu, B.;Ding, L.;Chen, C.;Shan, X.;Wang, D.;Tian, M.;Song, J.;Zheng, Z.; Xu, X. Multi-Photon Super-Linear Image Scanning Microscopy Using Upconversion Nanoparticles (2024). *Laser & Photonics Reviews*.**18**,2400746

[7] Chen, C.;Liu, B.;Liu, Y.;Liao, J.;Shan, X.;Wang, F.; Jin, D. Heterochromatic Nonlinear Optical Responses in Upconversion Nanoparticles for Super-Resolution Nanoscopy (2021). *Advanced Materials*.**33**,2008847

[8] Shang, Y.;Zhou, J.;Cai, Y.;Wang, F.;Fernandez-Bravo, A.;Yang, C.;Jiang, L.; Jin, D. Low threshold lasing emissions from a single upconversion nanocrystal (2020). *Nature communications*.**11**,6156

[9] Zhang, L.;Cao, C.;Kaushik, N.;Lai, R. Y.;Liao, J.;Wang, G.;Ariotti, N.;Jin, D.; Stenzel, M. H. Controlling the biological behaviors of polymer-coated Upconverting nanoparticles by adjusting the linker length of Estrone ligands (2022). *Biomacromolecules*.**23**,2572-2585

[10] Di, X.;Wang, D.;Su, Q. P.;Liu, Y.;Liao, J.;Maddahfar, M.;Zhou, J.; Jin, D. Spatiotemporally mapping temperature dynamics of lysosomes and mitochondria using cascade organelle-targeting upconversion nanoparticles (2022). *Proceedings of the National Academy of Sciences*.**119**,e2207402119

[11] Malhotra, K.;Kumar, B.;Piunno, P. A.; Krull, U. J. Cellular uptake of upconversion nanoparticles based on surface polymer coatings and protein corona (2024). *ACS Applied Materials & Interfaces*.**16**,35985-36001

[12] Liu, Q.;Feng, W.;Yang, T.;Yi, T.; Li, F. Upconversion luminescence imaging of cells and small animals (2013). *Nature protocols*.**8**,2033-2044

[13] Bolte, S.; Cordelières, F. P. A guided tour into subcellular colocalization analysis in light microscopy (2006). *Journal of microscopy*.**224**,213-232

[14] Tinevez, J.-Y.;Perry, N.;Schindelin, J.;Hoopes, G. M.;Reynolds, G. D.;Laplantine, E.;Bednarek, S. Y.;Shorte, S. L.; Eliceiri, K. W. TrackMate: An open and extensible platform for single-particle tracking (2017). *Methods*.**115**,80-90

[15] Tarantino, N.;Tinevez, J.-Y.;Crowell, E. F.;Boisson, B.;Henriques, R.;Mhlanga, M.;Agou, F.;Israël, A.; Laplantine, E. TNF and IL-1 exhibit distinct ubiquitin requirements for inducing NEMO–IKK supramolecular structures (2014). *Journal of Cell Biology*.**204**,231-245

[16] Monnier, N.;Barry, Z.;Park, H. Y.;Su, K.-C.;Katz, Z.;English, B. P.;Dey, A.;Pan, K.;Cheeseman, I. M.; Singer, R. H. Inferring transient particle transport dynamics in live cells (2015). *Nature methods*.**12**,838-840

Chapter 4 Synthesis, characterization and investigation of optical characteristics of single UCNPs with ideal volumetric scaling

4.1 Introduction

The application of luminescent materials as therapeutic and diagnostic materials in recent years has been thoroughly explored in previous chapters. With high photostability, no photobleaching, and no background autofluorescence via infrared lasing, lanthanide-doped nanocrystals are one such material with incredible clinical and diagnostic potential due to the rising demand for advanced tools for point-of-care diagnostics, super-resolution imaging, optical probing and sensing [1-3]. While growing interest in UCNPs ranging from 10-40 nm have been studied extensively for their potential for single-molecule level imaging and super-resolution imaging, surface-related losses in smaller UCNPs result in significantly darker nanoparticles due to intense surface quenching [4, 5]. However, surface-related losses can be mitigated in larger UCNPs through a reduction of surface area to volume ratio. Reports have demonstrated that ideal volumetric scaling for single UCNPs significantly enhances volume-normalized single particle brightness because of reduced surface quenching [6].

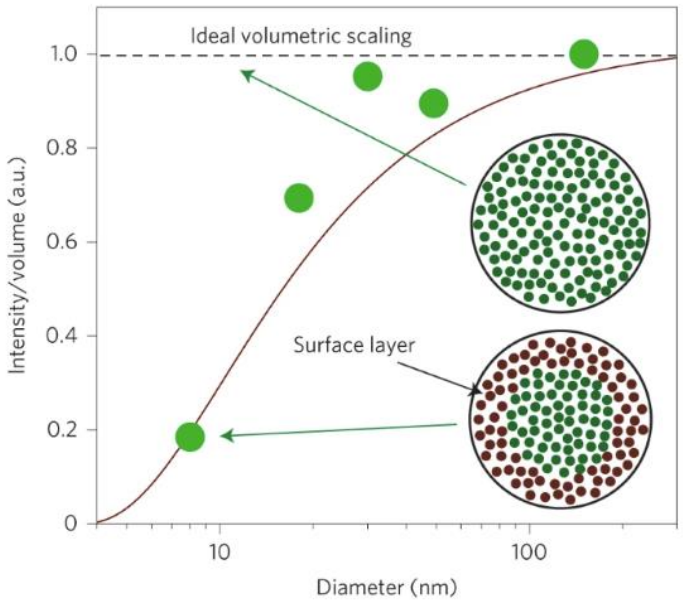

Figure 4.1 Single UCNP intensity normalized with ideal volumetric scaling with size considerations [6].

In an ideal particle, the saturation and emission intensity of a single UCNP should scale linearly with an increase in volume due to a proportional increase in emitter and sensitizer ions as volume increases. However, previous research performed by Garagas et al. demonstrated that ideal volumetric scaling only approaches a linear increase in optical properties for UCNPs with diameters at approximately 100 nm [6]. This is a result of a "dark" surface layer, where surface quenching results in a decrease in luminescence efficiency. However, the surface quenching dark layer remains the same regardless of UCNP volume as it is a surface-localized phenomenon, and an increase in UCNP size gradually minimizes the influence of a surface dark layer. As such, UCNPs with ideal volumetric scaling must approach a size at around 100 nm to mitigate the potential surface-related losses.

Despite evidence that larger up conversion nanoparticles can display enhanced single particle brightness due to diminished surface quenching, their optical properties have not been systematically explored at the single particle level. This gap in knowledge persists in part because the synthesis of lanthanide doped nanoparticles above 100 nm remains challenging using traditional coprecipitation methods. In this chapter, these limitations are addressed through a refined coprecipitation strategy that enables the controlled growth of large UCNPs by adjusting precursor concentrations during the Ostwald ripening process, thereby producing nanocrystals that approach volumetrically ideal dimensions. This advancement provides a foundation for examining their intrinsic optical behavior with single particle precision. While erbium doped systems have been thoroughly studied in previous research, thulium doped UCNPs demand further investigation due to their strong optical nonlinearity, which arises from fundamental differences in their electronic structure and energy transfer pathways. Given the potential of thulium-based nanoparticles for near infrared super resolution and other biomedical imaging applications, a deeper understanding of their photophysical mechanisms is essential. As such, this chapter investigates large volumetrically ideal UCNPs across varying sensitizer and thulium concentrations, revealing how these factors shape excited state populations, emission

efficiency and nonlinear behavior. Together, these developments contribute to the design of brighter and more efficient nanoprobes and establish a conceptual framework for future biological and optical applications.

The synthesis of UCNPs larger than 100 nm using the coprecipitation method has not been comprehensively documented in the current literature. Existing approaches capable of producing UCNPs in this size regime, including hydrothermal and thermal decomposition methods, each present notable limitation [30]. Hydrothermal synthesis requires extended reaction times in sealed and pressurized autoclave vessels, raising practical and safety concerns for routine or large scale production. This method also introduces hydroxyl groups into the reaction environment, which can generate structural defects that severely diminish luminescence efficiency. Thermal decomposition routes that rely on metal trifluoroacetates offer improved size control but pose significant hazards due to the possible release of hydrogen fluoride, trifluoroacetic acid and other corrosive fluorinated vapors under improper conditions.

In contrast, coprecipitation is widely regarded as a safer and more accessible technique that reliably produces highly uniform UCNPs within the 10 – 60 nm range. However, extending particle sizes beyond this range is inherently challenging because the rapid supersaturation characteristic of coprecipitation generates a large number of nuclei, depleting monomers and restricting subsequent particle growth. To address these limitations, this chapter introduces a modified coprecipitation strategy based on controlled adjustment of precursor concentrations to suppress excessive nucleation and promote sustained crystal growth. This approach enables the formation of larger UCNPs suitable for optical characterization under ideal volumetric conditions, thereby reducing the influence of surface related quenching.

Instead of investigating particle ensembles, this study aims to investigate single nanoparticle brightness to reveal the key up-conversion transfer mechanisms. The Gaussian point spread function of the widefield imaging system and the extreme optical sensitivity of UCNPs would result in data that does not correctly reflect on the optical properties of UCNPs during ensemble measurements, which is why an optical system for single particle imaging was constructed and designed in the first place. Additionally, a comparison between the optical properties at different sensitizers and emitter doping in nanoparticles

ensembles becomes inaccurate as the number of UCNPs is unknown due to the diffraction limit, and ensemble counting can only be achieved using electron microscopy.

In this chapter, our results demonstrate changes in optical properties based on differing emitter and sensitizer concentrations in a Yb^{3+}/Tm^{3+} co-doped system based on changes in excited electron occupation in single nanocrystals. The population distribution of excited electrons and energy transfer up-conversion processes are dictated via sensitizer and emitter concentrations which can result in tunable rise times and lifetimes with a range of two orders of magnitude dependent on sensitizer and emitter concentration. Highly Tm^{3+} doped UCNPs demonstrate a significant increase in cross relaxation and nonradiative transitions, as well as an increase in optical non-linearity as a result of the photon avalanche effect. These optical characteristics observed in single nanoparticles with ideal volumetric scaling provide further insight into the optical mechanism of lanthanide up-conversion.

4.2 Results and Discussion

4.2.1 Synthesis and morphological characterization of volumetrically ideal UCNPs

Morphological control of lanthanide-doped materials can significantly influence particle luminescence for enhanced sensitivity diagnostic applications [7, 8]. The luminescence mechanisms behind smaller lanthanide doped nanocrystals with higher emitter concentrations have been thoroughly explored in previous research [9-11]. Critically, in highly doped lanthanide nanocrystals, emission intensity scales linearly with particle volumes (>40 nm) at larger sizes due to decreasing effects based on surface-related losses [6, 12]. However, luminescent properties of super-large (>100 nm), differently doped lanthanide nanocrystals has not been explored. A reduction of surface-related losses, as well as an increase in emitter and sensitizer quantity within a single nanoparticle, makes 100 nm + nanoparticles significantly brighter while still being under resolution limit for conventional light microscopy techniques. As such, lanthanide-doped nanoparticles over 100 nm have been suggested to possess ideal volumetric scaling [6]. However, synthesis of lanthanide-doped materials with ideal-volumetric scaling have not been explored due to difficulties in synthesis procedures. The hydrothermal method was omitted due to the excess addition of hydroxyl defect groups with the addition of water. As shown in figure

4.2, our results demonstrate the production of 100+ nm nanoparticles via coprecipitation was a host dependent process that could be altered during the nucleation and crystallization process by changing the chemical equilibrium through precursor concentrations. An increase in size was therefore the result of reduced nucleation under lower precursor concentrations during the coprecipitation process.

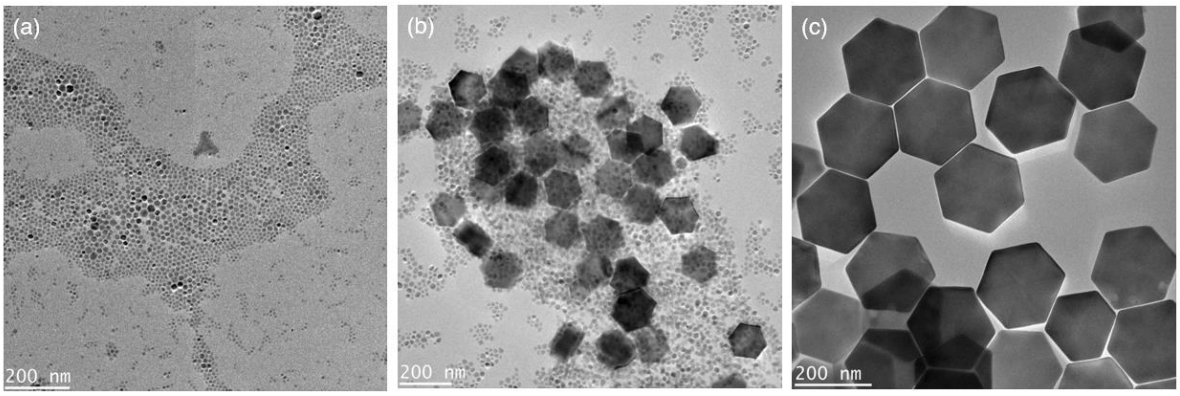

Figure 4.2 Synthesis of volumetrically ideal UCNPs via coprecipitation (a) Nanoparticle coalescence (b) Oswald ripening (c) Nanoparticle completion

The first step of coprecipitation involves the dissolution of lanthanide chloride-based salts and the formation of lanthanide oleate precursor complexes, which can be described as:

$$\mathrm{Ln}^{3+} + 3\mathrm{OA} \rightarrow \mathrm{Ln(OA)}_3$$

The formation of lanthanide-oleate complexes facilitates uniform precursor distribution and suppression of premature nucleation as lanthanide ions are solubilized in the nonpolar organic solution which allows for homogeneous mixing of metal ions throughout the reaction volume [13]. Afterwards, the addition of a methanol solution containing NaOH and NH_4F is added into the reaction for the dissolution of NH_4F and NaOH. This solution introduces both fluoride and hydroxide ions necessary for the formation of the fluoride crystal lattice [14]. The reaction mixture is heated to 110–150 °C under vacuum or inert gas flow to remove excess methanol and water. Following solvent removal, the reaction mixture is heated to approximately 300 °C to initiate nucleation and crystal growth. Nanoparticle formation is understood through the classical LaMer model, which separates the nucleation and growth phases into distinct time domains [15]. For the formation of nanocrystals, nucleation can be explained via the Lamer model:

$$S = \frac{C}{C_e}$$

With this model, nucleation begins once the concentration of dissolved solutes surpasses the critical supersaturation threshold, where super saturation (s) occurs when the actual concentration of the solute C is greater than the equilibrium solubility C_e, which is defined by the maximum amount of solute that can be dissolved under certain conditions. Therefore, nucleation occurs in conditions where over saturation occurs in the solution. In the case involving $NaYF_4$, the dissolution of NH_4F occurs at higher temperatures seen with

$$NH_4F \xrightarrow{\Delta} NH_3 \uparrow + HF \rightarrow H^+ + F^-$$

the reaction equation:

For the formation of $NaYF_4$ UCNPs, the decomposition and dissolution of NH_4F at elevated temperatures release free fluoride ions into the system [16]. The availability of fluoride and rare-earth cations leads to the precipitation of $NaYF_4$ crystals, as described by the overall reaction:

$$Y^{3+} + Na^+ + 4F^- \rightarrow NaYF_4 \downarrow (\text{nanoparticles})$$

As such, facilitating the dissolution of NH_4F through changes in temperature or increased NH_4F concentration can increase nucleation formation. Indeed, results demonstrate that a decrease of NH_4F ions resulted in an increase of UCNP size under identical synthesis conditions [17]. Our results demonstrate that after the rapid depletion of free ions through nucleation, the reduction in system supersaturation in the reaction results into a kinetically slower growth phase dominated by monomer deposition onto existing nuclei (Figure 4.2). Following nucleation, Oswald ripening of smaller nanocrystals and nuclei enables the formation of larger nanocrystals. In cases where nucleation is less due to reaction conditions, nanoparticles increase in size as monomers are deposited into a smaller quantity of nanoparticle nuclei. A simple model for nanoparticle growth can be explained by Lifshitz-Slyozov-Wagner Theory (LSW theory) where:

$$\langle a \rangle_t^3 - \langle a \rangle_{t=0}^3 = \frac{3}{4} \cdot \frac{C^{(P)} \gamma D \bar{V}^2}{kT} \cdot t$$

Related to the curvature effect of the Gibbs-Thomson rule, LSW theory depicts the size of the particle at time "*t*" compared to the initial time is dependent on a rate constant which is determined by the concentration of continuous phase molecules $C^{(P)}$, the interface energy (γ) as well as the diffusion coefficient (D) and volume of the occupied molecules in the solution $\bar{V}^2$. LSW theory further predicts a narrow size distribution as smaller particles equilibrate and diffuse into the local solution which are redeposited onto larger nanoparticles [18, 19]. Greater surface energy due to a higher surface area to volume ratio along with the curvature effect of the Gibbs-Thomson rule results in higher solubility of smaller nanoparticles which facilitates its deposition.

The ability to modulate particle morphology during coprecipitation is fundamentally governed by how reaction parameters shape the balance between nucleation and growth. Precursor concentration is one of the most critical determinants, as it directly sets the degree of supersaturation in the reaction mixture. High precursor concentrations rapidly push the system beyond the critical supersaturation threshold, resulting in a burst of homogeneous nucleation that produces numerous small nuclei and quickly depletes available monomers. Under these conditions, growth becomes severely limited, and particle sizes remain small. Conversely, lowering precursor concentrations suppresses excessive nucleation and permits a reduced number of nuclei to form. This shift enables sustained monomer availability during the subsequent ripening stage, promoting continued particle growth and ultimately yielding larger nanocrystals.

Temperature also plays a decisive role in shaping nucleation behavior by altering the solubility and diffusion kinetics of both rare earth and fluoride ions. Heating the reaction mixture accelerates the decomposition of ammonium fluoride, increases the mobility of ionic species and enhances ligand exchange between lanthanide oleate complexes and free ions. Rapid temperature ramps can therefore trigger intense nucleation, while slower or staged heating provides more controlled ion release and a prolonged growth period that favours the formation of larger particles. The solvent composition, particularly the ratio of

oleic acid to octadecene, further influences these dynamics by regulating the coordination strength of lanthanide ions and modifying surface energies of forming nuclei. Higher oleic acid content stabilizes smaller particles by strongly passivating their surfaces, whereas a reduced amount of coordinating ligands decreases surface passivation and enhances particle coalescence and Ostwald ripening.

Collectively, these parameters define the thermodynamic and kinetic landscape of the coprecipitation reaction. By precisely tuning precursor concentration, temperature profile and solvent composition, it is possible to suppress rapid nucleation, extend the growth phase and shift the system towards producing larger, more uniform nanocrystals. These mechanistic insights provide a clear rationale for the observed morphological control in this study and demonstrate how deliberate manipulation of reaction conditions enables the synthesis of volumetrically ideal UCNPs that would not otherwise emerge from conventional coprecipitation conditions.

Lattice fringes observed in the high-resolution TEM images correspond to the (100) planes of hexagonal NaYF4, confirming that the synthesized nanoparticles possess the expected hexagonal crystal phase (Figure 4.3). The clear and well defined spacing of these fringes reflects the high crystallinity of the nanocrystals and verifies that the coprecipitation method successfully produced phase pure hexagonal NaYF4. This structural confirmation is essential, as the hexagonal phase is known to support more efficient upconversion processes compared with the cubic counterpart, thereby validating the suitability of the synthesized nanoparticles for subsequent optical characterization and applications.

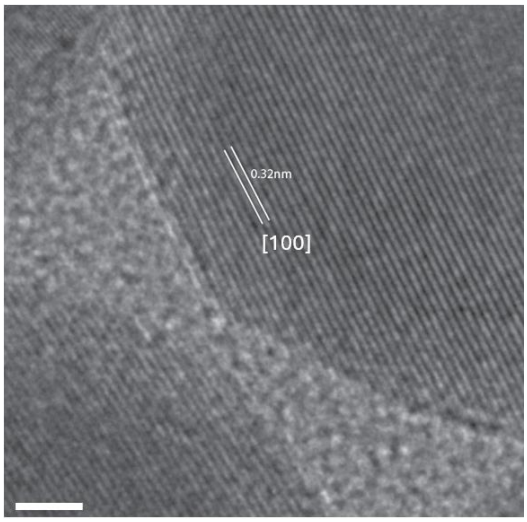

Figure 4.3 High Resolution TEM image of lattice fringes for $NaYF_4$ 40% Yb^{3+}/20%Tm^{3+} UCNPs. Scale bar:10 nm.

Afterwards, a series of hexagonal $NaYF_4$:Yb^{3+}/Tm^{3+} nanocrystals were synthesized following the method above. Size and morphology of UCNPs at different Tm^{3+} (40%Yb) via TEM imaging are displayed in figure 4.4. Tm^{3+} concentration ranging from 2% to 40% were synthesized and demonstrated possible ideal volumetric scaling regardless of Tm^{3+} doping via the coprecipitation method. The batches of these core nanoparticles were all above 90 nm, which is well over the ideal volumetric scaling reported in previous research [6].

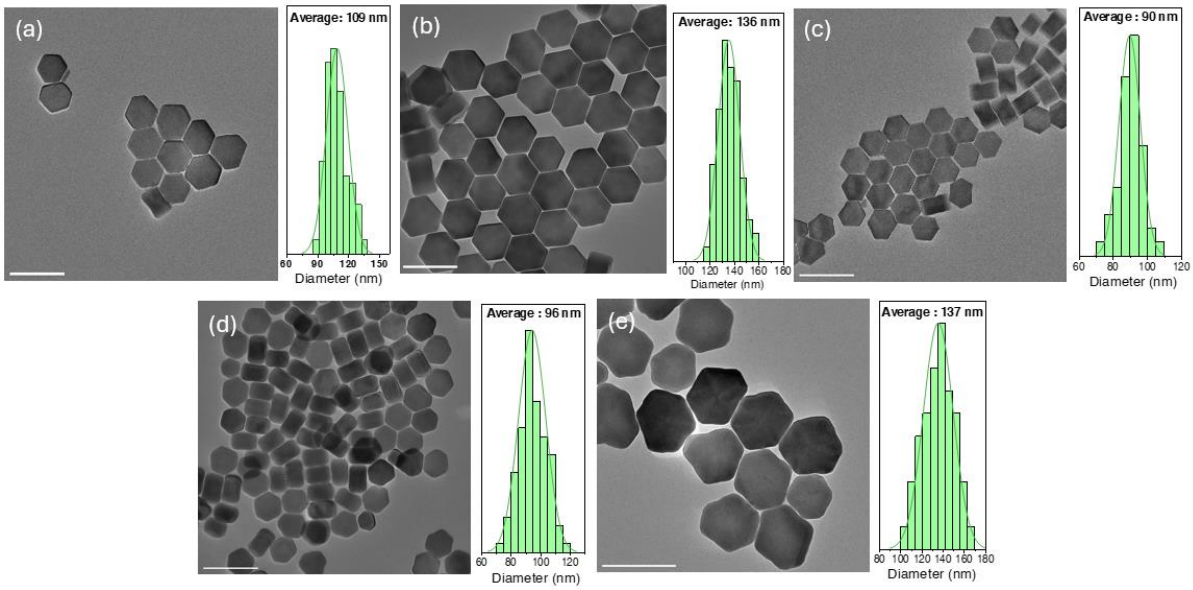

Figure 4.4 TEM images of $NaYF_4$:40% Yb^{3+} / x% Tm^{3+} UCNPs. **(a-e) 2%, 4%, 8%, 20%, 40%** Tm^{3+}. Scale Bar 200 nm.

Similarly, a series of hexagonal $NaYF_4$:Yb^{3+}/Tm^{3+} nanocrystals with different Yb^{3+} concentrations were synthesized with ideal volumetric scaling. A highly doped Tm^{3+} (20%) concentration was selected across all Yb^{3+} concentrations to ensure that populating the excited energy levels of Tm^{3+} ions could be observed at a greater scale with differing sensitizer concentrations.

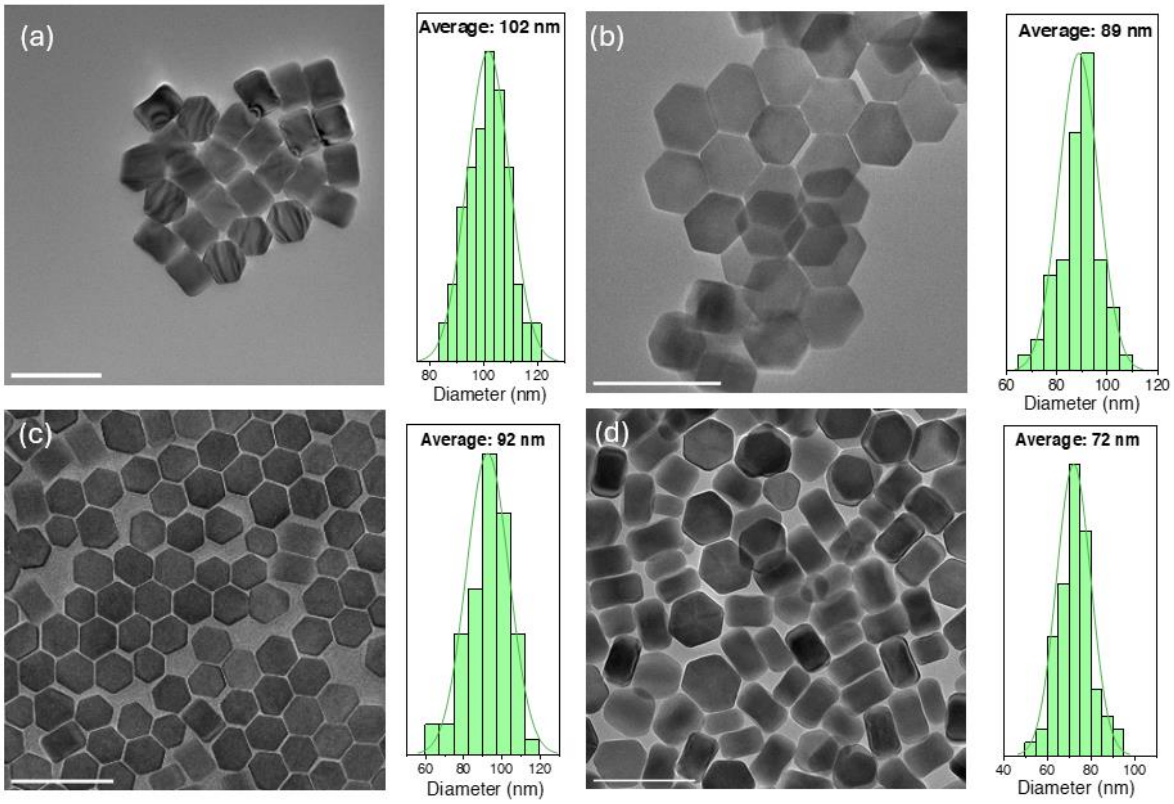

Figure 4.5 TEM images of $NaYF_4$:x% Yb^{3+} / 20% Tm^{3+} UCNPs. (a-d) 2%, 4%, 10%, 20% Yb^{3+}. Scale Bar 200 nm.

To determine if single nanoparticles with ideal volumetric scaling depict changes in optical characteristics after the addition of a core-shell structure, an inert $NaYF_4$ core-shell structure was synthesized onto the core nanoparticles. As illustrated in figure 4.6, the addition of a $NaYF_4$ layer on $NaYF_4$:40% Yb^{3+} / 20% Tm^{3+} resulted in an increase of average single nanoparticle size from 96 nm to 112 nm. Single nanoparticle power dependence measurements of 800 nm emissions under 980 nm laser excitation demonstrated that addition of an inert shell layer resulted in an increase in single particle luminescence as well as a left-ward shift of power dependence which can be attributed to a reduction of surface defects.

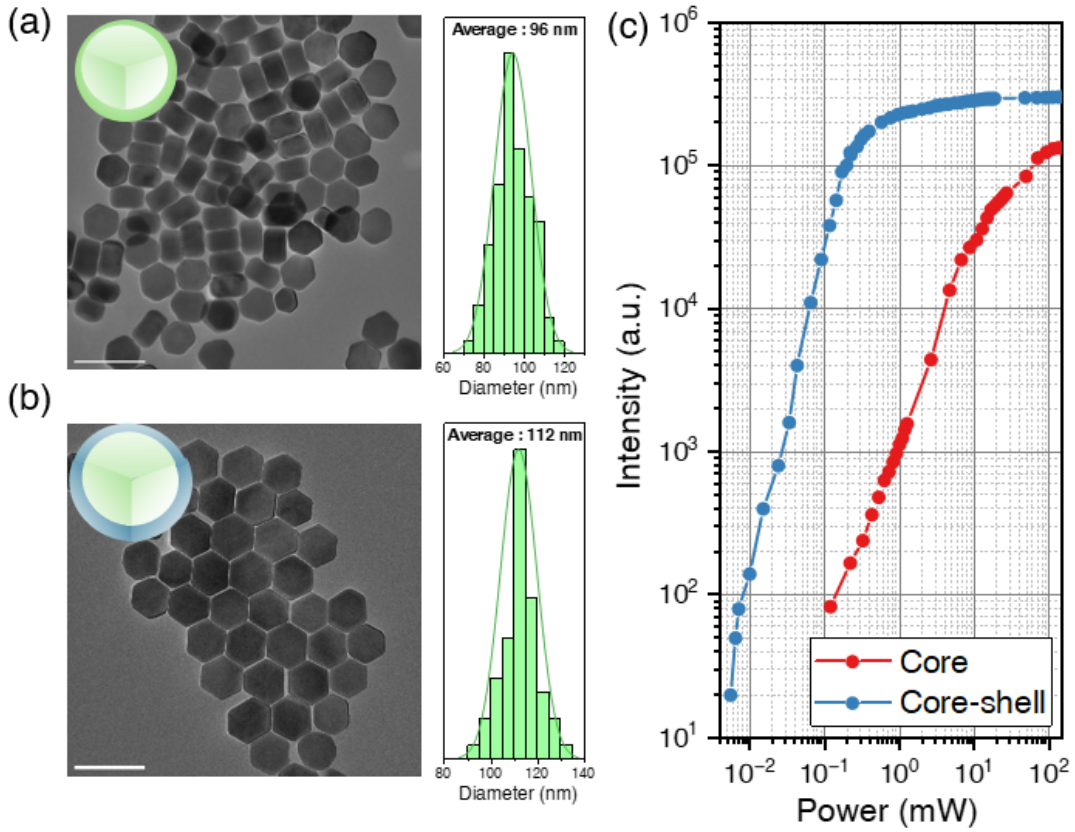

Figure 4.6 Core and core-shell nanoparticles and their power dependence. (a) $NaYF_4$:40% Yb^{3+} / 20% Tm^{3+} size and distribution. (b) $NaYF_4$:40% Yb^{3+} / 20% Tm^{3+}@$NaYF_4$ size and distribution. (c) 800nm power dependence emission of single UCNP. Scale bar 200 nm.

Given that core-shell structure improved the single particle brightness, a series of core-shell nanoparticles with differing sensitizer and emitter concentrations were synthesized using previous UCNPs with an inert $NaYF_4$ shell (Figure 4.7 & Figure 4.8).

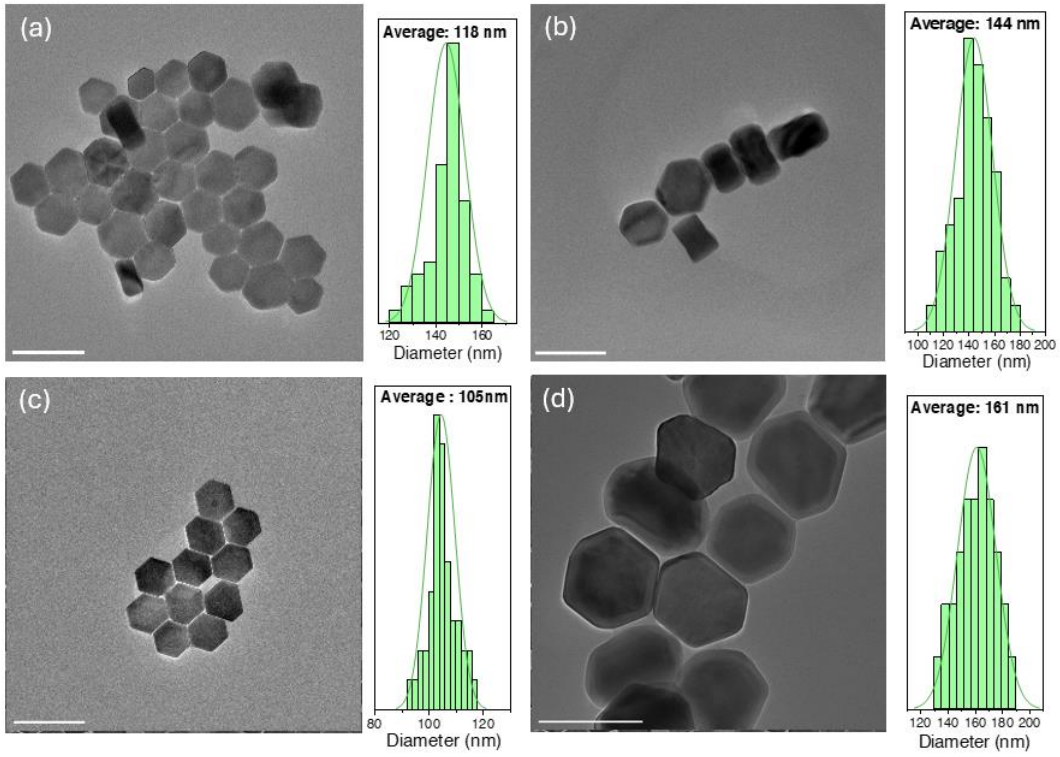

Figure 4.7 Core-shell nanoparticles (a) 2%Tm (b) 4%Tm (c) 8%Tm (d) 40% Tm. Scale bar 200 nm.

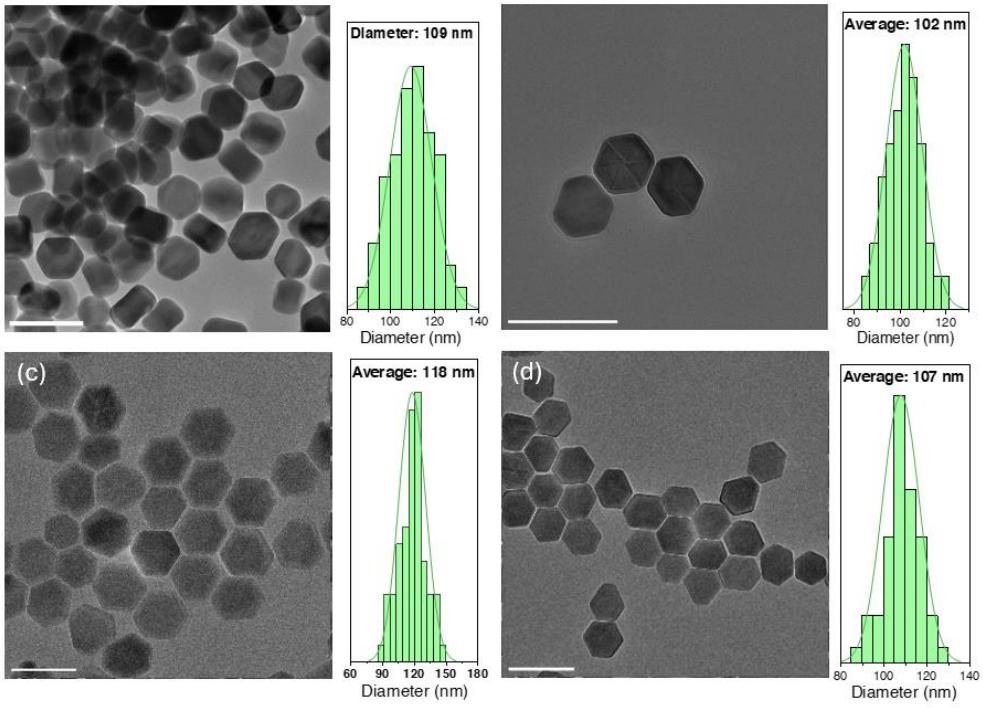

Figure 4.8 Core-shell nanoparticles (a) 2%Yb (b) 4%Yb (c) 10%Yb (d) 20% Tm. Scale bar 200 nm.

4.2.2 Optical properties of UCNPs with ideal volumetric scaling

Using the home-built optical characterization system and custom LABVIEW coding, the 800 nm emission intensity and power dependence of single nanoparticles across differing Tm^{3+} ion concentrations were measured under laser excitation using a 980 nm laser. As illustrated in figure 4.9, lower concentrations of Tm^{3+} resulted in earlier population saturation under 980 nm excitations. A decrease in single particle luminescence intensity at higher power for lower concentration single UCNPs is a result of the population of higher energy states, which is facilitated by cross relaxation between $^3H_4 \rightarrow {}^3F_4$ and $^1G_4 \rightarrow {}^1D_2$ transitions [20]. At higher Tm^{3+} concentrations, a decrease in 800 nm emissions is not observed due to cross relaxation occurring at lower energy levels between $^3H_4 \rightarrow {}^3F_4$ and $^3H_6 \rightarrow {}^3H_4$ [21].This is further evident via the emission spectrum in Figure 4.9b, where vastly lower $^1D_2 \rightarrow {}^3F_4$ emissions were observed at 20% Tm^{3+} concentration in comparison to 8% Tm^{3+}.

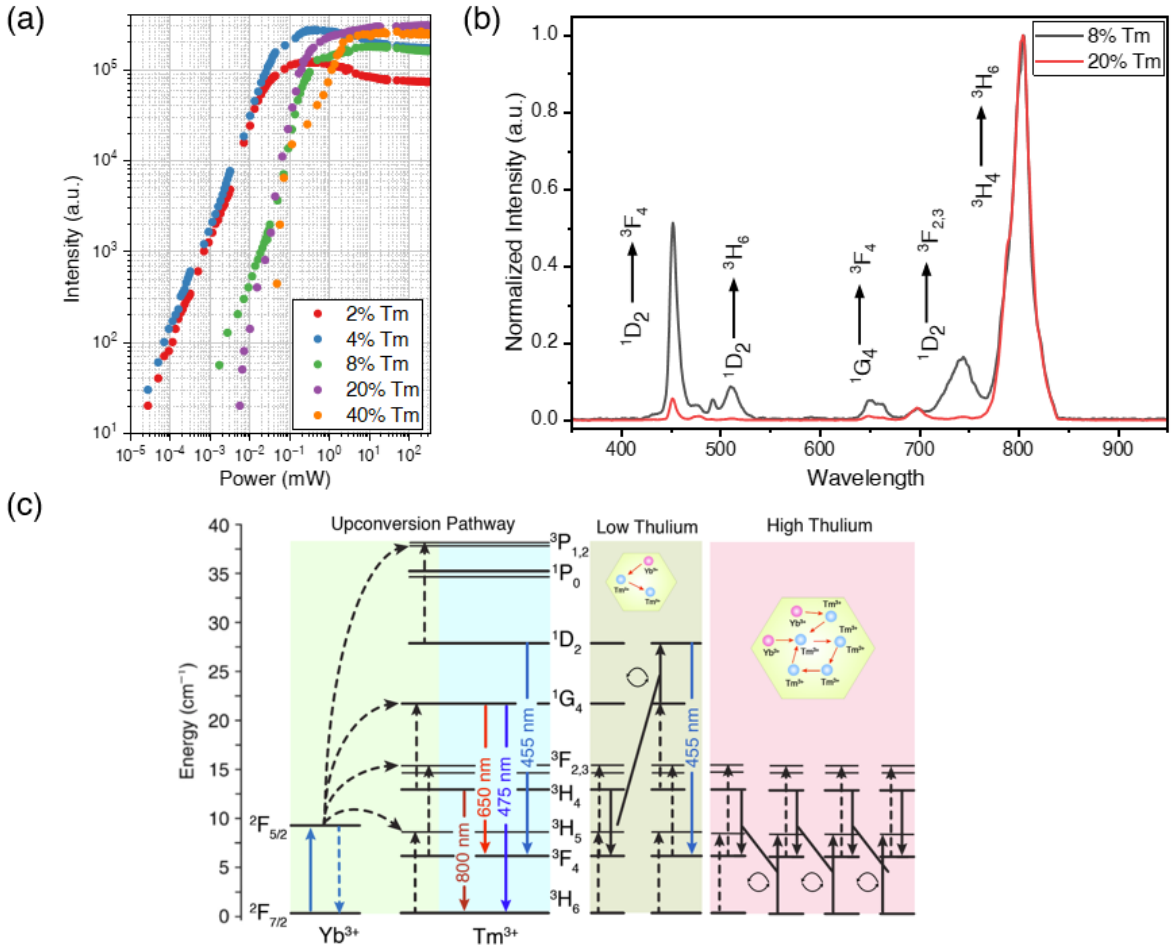

Figure 4.9 Optical characteristics of single core-shell UCNPs with Tm^{3+} doping. (a) Power dependence with changing Tm^{3+}. (b) Emission spectrum of 8% and 20% doped Tm^{3+} UCNPs. (c) Proposed schematic and excited population pathway under different Tm^{3+} concentrations.

Taking into account the potential difference in luminescence intensity due to slight size variation and Tm^{3+} concentration, a normalized power dependence graph illustrates an increase in saturation power as Tm^{3+} concentration increased as seen in figure 4.9. Furthermore, a decrease to up to 40% in 800 nm emissions are observed at lower concentrations of Tm^{3+}, further suggesting that excitation at higher energy levels is a result of internal energy transfer across emitter ions in single nanoparticles [22]. Additionally, an increase in optical non-linearity with a rise in Tm^{3+} concentration suggests a photon avalanche-based energy loop may occur in Tm^{3+}/Yb^{3+} systems with higher Tm^{3+} concentration under 980 nm excitation [23].

A decrease in saturation curve dynamics with increasing Tm^{3+} concentration further suggests that cross relaxation at lower energy levels significantly influences photon emission dynamics in single UCNPs. While the increase of luminescent intensity scales at higher nonlinearity, an increase in lasing power is required in order to facilitate single particle saturation at higher Tm^{3+} concentrations [21, 23].

Figure 4.9 Normalized Optical characteristics of single core-shell UCNPs with Tm^{3+} doping. (a) Normalized power dependence with changing Tm^{3+}. (b) Optical non-linearity with changing Tm^{3+}. (c) Normalized intensity at power ranging 0 – 30 mW. (d) Normalized intensity at power ranging 0 – 0.6 mW.

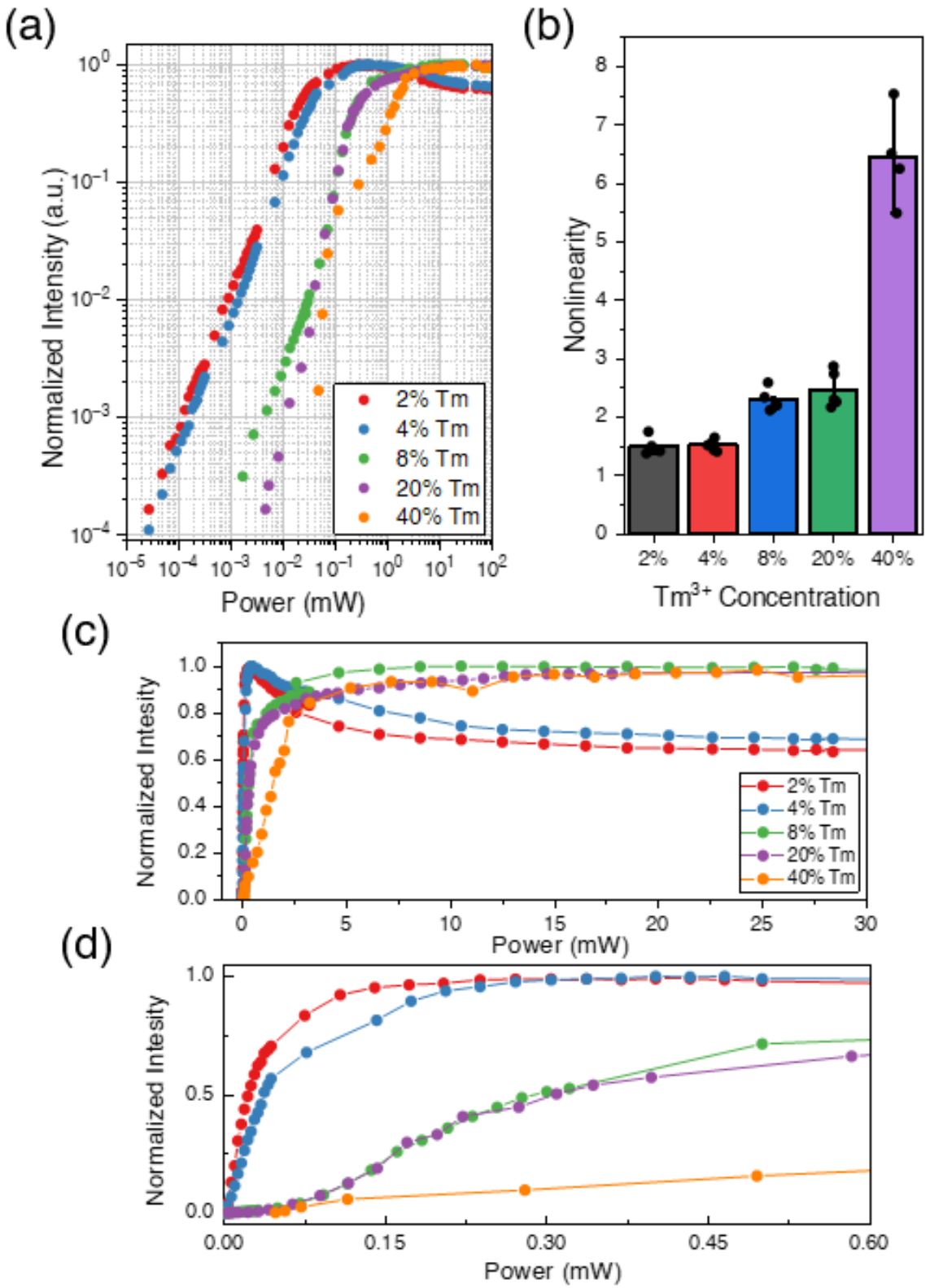
(a)
Normalized Intensity (a.u.)
Power (mW)
2% Tm
4% Tm
8% Tm
20% Tm
40% Tm
(b)
Nonlinearity
2%
4%
8%
20%
40%
Tm3+ Concentration
(c)
Normalized Intesity
Power (mW)
2% Tm
4% Tm
8% Tm
20% Tm
40% Tm
(d)
Normalized Intesity
Power (mW)

We next sought to uncover the population dynamics of single UCNPs through rise-time and lifetime measurements. As expected, a decrease in Tm^{3+} concentration depicted an increase in rise-time, with a rise time between 30-300 us across different Tm^{3+} concentrations. The massive difference in rise-time dynamics further suggests that higher Tm^{3+} (40%) concentrations facilitated a photon-avalanche like effect, which has been previously reported in Tm^{3+} ions [24]. The increase in rise-time, optical nonlinearity as well as threshold for luminescence (because of undetectable photon signals at lower thresholds observed in figure 4.9a), suggests that extremely high Tm^{3+} concentrations in Tm^{3+}/Yb^{3+} can facilitate a photon-avalanche effect in 980 nm lasing systems, which has immense potential for super-resolution imaging and bio diagnostic applications [25, 26].

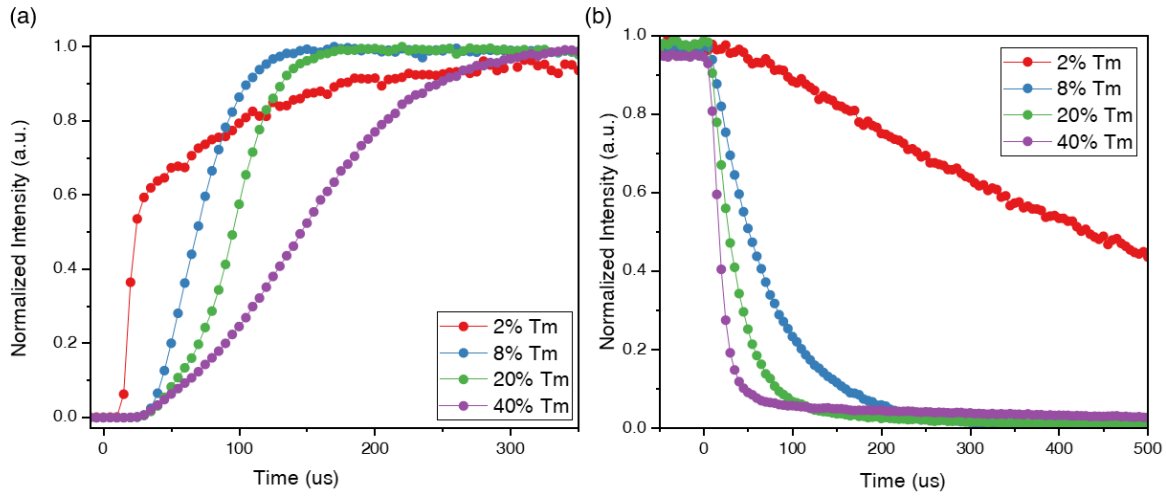

Figure 4.10 Rise-time and lifetime of single UCNPs (differing Tm^{3+}). (a) Rise-time (b) Lifetime.

An increase in luminescence lifetime was observed at lower Tm^{3+} concentrations. These results further suggests an increase in energy migration related quenching through cross-relaxation and non-radiative interactions [27]. As Tm^{3+} ions transfer energy to nearby Tm^{3+} ions, non-radiative depopulation of excited states results in lower lifetimes, which can also occur via multi-phonon relaxations [28].

Figure 4.11 Optical characteristics of single UCNPs with different Yb^{3+}. (a) Power dependence with differing Yb^{3+} concentrations. (b) Schematic proposing pathway and dynamics of energy up-conversion under 980 nm excitation in single UCNPs.

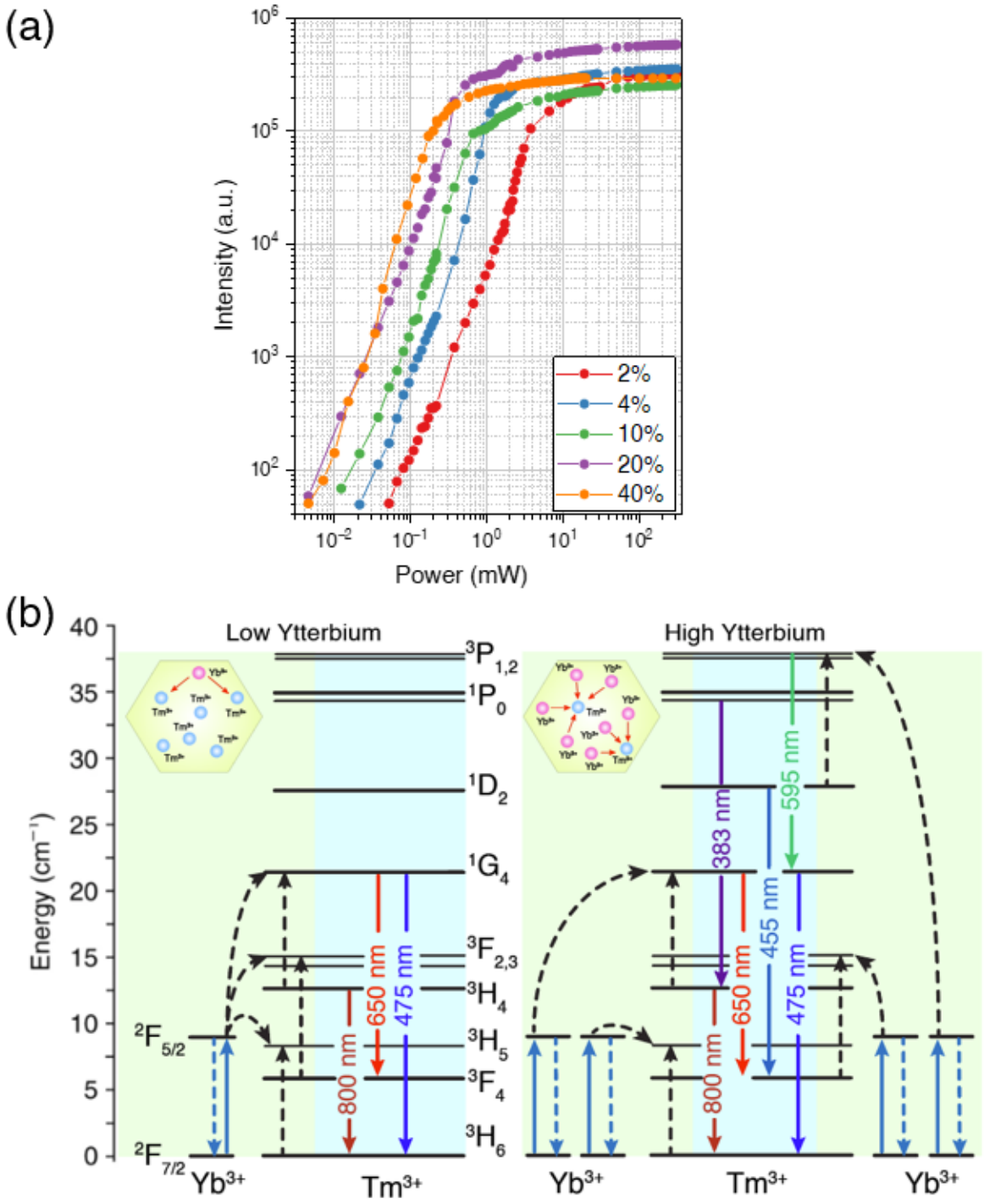

We next observed the saturation dynamics of UCNPs with differing sensitizer concentrations to unveil excitation dynamics related to sensitizer concentrations. Our results in Figure 4.11 demonstrate that lower Yb^{3+} concentrations result in an increase in single particle saturation requirements. However, while single particle saturation almost exhibits an almost linear rate of power saturation with increasing Yb^{3+} concentrations as a

result of sensitizer cross-section absorption under 980 nm emission, saturation efficiency plateaus between 20% and 40% Yb^{3+} concentration. Saturation efficiency is indeed the result of more efficient excited energy level population with an increase of sensitizers as depicted in the schematic 4.11b.

Our normalized power-dependence results further illustrate the role of Yb^{3+} concentrations in populating the Tm^{3+} energy levels by omitting potential differences caused by size variation. At lower lasing intensities, a 20-fold difference in Yb^{3+} concentrations can affect up-conversion efficiency up to 300-fold. These results suggest that excited Tm^{3+} populations are likely to de-populated before photon emissions due to the lack of Yb^{3+} ion induced up-conversion energy transfer. Furthermore, Yb^{3+} concentrations do not significantly influence the non-linearity in Tm^{3+}/Yb^{3+} systems, suggesting that non-linearity is solely an emitter/Tm^{3+} dependent process.

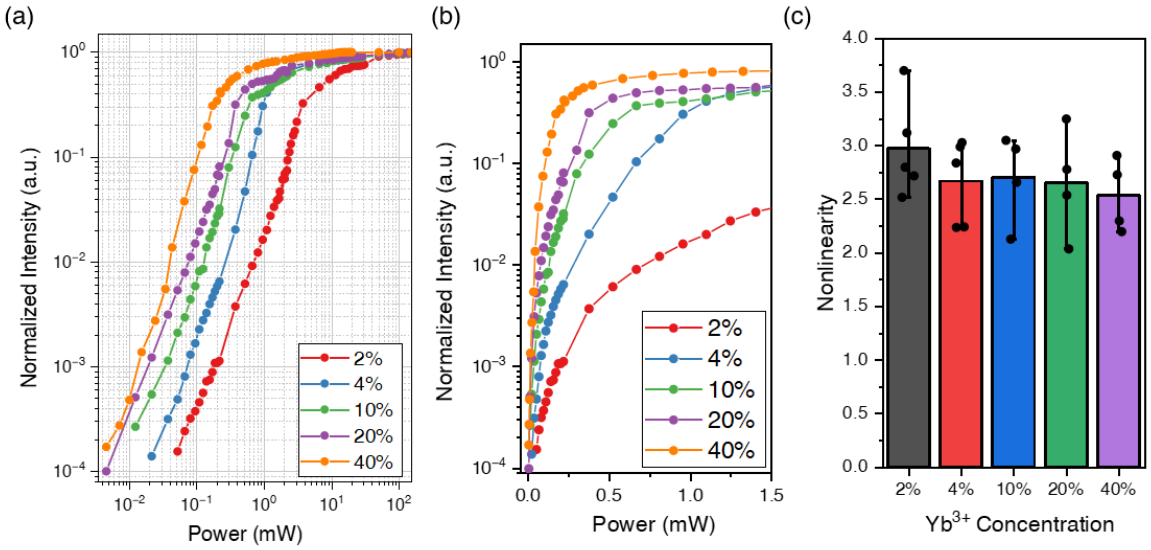

Figure 4.12 Normalized UCNPs properties with Yb^{3+} difference. (a) Normalized power dependence of single UCNPs with different Yb^{3+}. (b) Power dependence between the range of 0 – 1.5 mW. (c) Optical non-linearity with Yb^{3+} concentration.

Rise-time results further illustrate a catch-up process at low Yb^{3+} concentrations as Tm^{3+} ions de-populate during laser excitation. In Figure 4.13a, results illustrate an extreme increase in single particle luminescent rise time 2% Yb^{3+} concentration, and a decrease in rise-time as Yb^{3+} concentrations increase. Interestingly, decrease in Yb^{3+} concentration resulted in an increase in luminescent lifetime, which suggests that energy transfer between Tm^{3+} and Yb^{3+} can result in non-radiative interactions with an increased probability of multi-phonon relaxation [29].

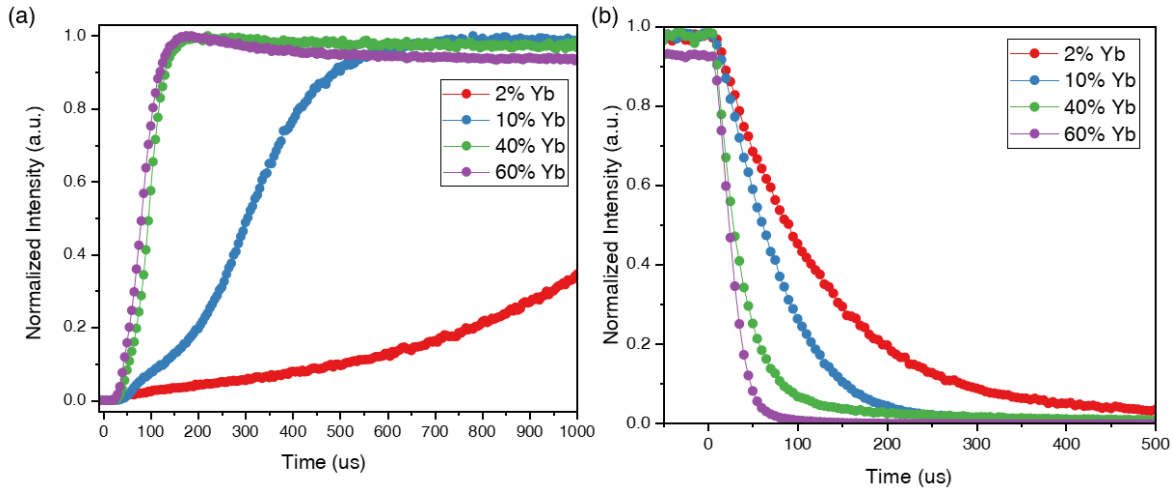

Figure 4.13 Rise-time and lifetime of single UCNPs (differing Yb^{3+}). (a) Rise-time (b) Lifetime.

4.3 Conclusion

In summary, the chapter investigated the optical characteristics of UCNPs with ideal volumetric scaling. By tuning single particle sizes via altering precursor composition, the method successfully altered nanoparticle growth kinetics to generate lanthanide-doped $NaYF_4$ at around ~100 nm via reduced nucleation rates. After the formation of core-shell structures via a precursor injection method, these nanoparticles depicted uniform size and morphological characteristics after TEM imaging. Furthermore, this chapter demonstrated the characterization capabilities of a home-built optical characterization setup which facilitated widefield and confocal scanning microscopy imaging, emission spectroscopy as well as single photon counting and lifetime measurement capabilities at a single nanoparticle level. Characterization of single UCNPs with ideal volumetric scaling and thulium doping reveals a wide range of differing optical properties dependent on both

emitter and sensitizer concentration, which are facilitated by the populating energy levels of both emitter and sensitizer ions. An increase of emitter ion Tm^{3+} reveals an increase of laser saturation power, as well as optical non-linearity as a result of the photon avalanche effect, which is evident by the increase of optical non-linearity as well as rise-time kinetics. These effects were not evident increase of sensitizer ion Yb^{3+} in single nanoparticles. However, changes in Yb^{3+} ions did significantly influence rise time and lifetime dynamics, where the rise time of single UCNPs differed over two orders of magnitudes as a result of less efficient up-conversion energy transfer. Future works using differing emitter ions will advance our understanding of energy transfer mechanisms in UCNPs.

4.4 References

[1] Zhang, Z.;Shikha, S.;Liu, J.;Zhang, J.;Mei, Q.; Zhang, Y. Upconversion nanoprobes: recent advances in sensing applications (2018). *Analytical Chemistry*.**91**,548-568

[2] Lingeshwar Reddy, K.;Balaji, R.;Kumar, A.; Krishnan, V. Lanthanide doped near infrared active upconversion nanophosphors: fundamental concepts, synthesis strategies, and technological applications (2018). *Small*.**14**,1801304

[3] Gu, Z.;Yan, L.;Tian, G.;Li, S.;Chai, Z.; Zhao, Y. Recent advances in design and fabrication of upconversion nanoparticles and their safe theranostic applications (2013). *Advanced Materials*.**25**,3758-3779

[4] Liu, Q.;Zhang, Y.;Peng, C. S.;Yang, T.;Joubert, L.-M.; Chu, S. Single upconversion nanoparticle imaging at sub-10 W cm− 2 irradiance (2018). *Nature photonics*.**12**,548-553

[5] Li, F.;Tu, L.;Zhang, Y.;Huang, D.;Liu, X.;Zhang, X.;Du, J.;Fan, R.;Yang, C.; Krämer, K. W. Size-dependent lanthanide energy transfer amplifies upconversion luminescence quantum yields (2024). *Nature Photonics*.**18**,440-449

[6] Gargas, D. J.;Chan, E. M.;Ostrowski, A. D.;Aloni, S.;Altoe, M. V. P.;Barnard, E. S.;Sanii, B.;Urban, J. J.;Milliron, D. J.; Cohen, B. E. Engineering bright sub-10-nm upconverting nanocrystals for single-molecule imaging (2014). *Nature nanotechnology*.**9**,300-305

[7] Muhr, V.;Würth, C.;Kraft, M.;Buchner, M.;Baeumner, A. J.;Resch-Genger, U.; Hirsch, T. Particle-size-dependent Forster resonance energy transfer from upconversion nanoparticles to organic dyes (2017). *Analytical Chemistry*.**89**,4868-4874

[8] Kraft, M.;Würth, C.;Muhr, V.;Hirsch, T.; Resch-Genger, U. Particle-size-dependent upconversion luminescence of NaYF4: Yb, Er nanoparticles in organic solvents and water at different excitation power densities (2018). *Nano Research*.**11**,6360-6374

[9] Siefe, C.;Mehlenbacher, R. D.;Peng, C. S.;Zhang, Y.;Fischer, S.;Lay, A.;McLellan, C. A.;Alivisatos, A. P.;Chu, S.; Dionne, J. A. Sub-20 nm core–shell–shell nanoparticles for bright upconversion and enhanced Förster Resonant Energy Transfer (2019). *Journal of the American Chemical Society*.**141**,16997-17005

[10] Ostrowski, A. D.;Chan, E. M.;Gargas, D. J.;Katz, E. M.;Han, G.;Schuck, P. J.;Milliron, D. J.; Cohen, B. E. Controlled synthesis and single-particle imaging of bright, sub-10 nm lanthanide-doped upconverting nanocrystals (2012). *ACS nano*.**6**,2686-2692

[11] Cai, Y.;Shang, Y.;Lu, M.;Jin, D.; Zhou, J. Polarized Upconversion of sub-100 nm Single Nanoparticles (2024). *Nano Letters*.**24**,10915-10920

[12] Quintanilla, M.;Hemmer, E.;Marques-Hueso, J.;Rohani, S.;Lucchini, G.;Wang, M.;Zamani, R. R.;Roddatis, V.;Speghini, A.; Richards, B. S. Cubic versus hexagonal–phase, size and morphology effects on the photoluminescence quantum yield of NaGdF 4: Er 3+/Yb 3+ upconverting nanoparticles (2022). *Nanoscale*.**14**,1492-1504

[13] Tang, S.-H.;Wang, J.;Yang, C.-X.;Dong, L.-X.;Kong, D.; Yan, X.-P. Ultrasonic assisted preparation of lanthanide-oleate complexes for the synthesis of multifunctional monodisperse upconversion nanoparticles for multimodal imaging (2014). *Nanoscale*.**6**,8037-8044

[14] Naccache, R.;Yu, Q.; Capobianco, J. A. The fluoride host: nucleation, growth, and upconversion of lanthanide-doped nanoparticles (2015). *Advanced Optical Materials*.**3**,482-509

[15] Whitehead, C. B.;Özkar, S.; Finke, R. G. LaMer's 1950 model for particle formation of instantaneous nucleation and diffusion-controlled growth: a historical look at the model's origins, assumptions, equations, and underlying sulfur sol formation kinetics data (2019). *Chemistry of Materials*.**31**,7116-7132

[16] Chen, B.; Wang, F. Recent advances in the synthesis and application of Yb-based fluoride upconversion nanoparticles (2020). *Inorganic Chemistry Frontiers*.**7**,1067-1081

[17] Wang, F.;Deng, R.; Liu, X. Preparation of core-shell NaGdF4 nanoparticles doped with luminescent lanthanide ions to be used as upconversion-based probes (2014). *Nature protocols*.**9**,1634-1644

[18] Vengrenovich, R.;Ivanskii, B.;Panko, I.;Yarema, S.;Kryvetskyi, V.; Stasyk, M. Ostwald ripening of the platinum nanoparticles in the framework of the modified LSW theory (2014). *Journal of Nanomaterials*.**2014**,821584

[19] Thanh, N. T.;Maclean, N.; Mahiddine, S. Mechanisms of nucleation and growth of nanoparticles in solution (2014). *Chemical reviews*.**114**,7610-7630

[20] Liu, Y.;Wen, S.;Wang, F.;Zuo, C.;Chen, C.;Zhou, J.; Jin, D. Population control of upconversion energy transfer for stimulation emission depletion nanoscopy (2023). *Advanced Science*.**10**,2205990

[21] Wen, S.;Li, D.;Liu, Y.;Chen, C.;Wang, F.;Zhou, J.;Bao, G.;Zhang, L.; Jin, D. Power-dependent optimal concentrations of Tm3+ and Yb3+ in upconversion nanoparticles (2022). *The Journal of Physical Chemistry Letters*.**13**,5316-5323

[22] Huang, D.;Li, F.;Ågren, H.; Chen, G. Inhibiting concentration quenching in Yb3+-Tm3+ upconversion nanoparticles by suppressing back energy transfer (2025). *Nature Communications*.**16**,4218

[23] Liu, Y.;Lu, Y.;Yang, X.;Zheng, X.;Wen, S.;Wang, F.;Vidal, X.;Zhao, J.;Liu, D.; Zhou, Z. Amplified stimulated emission in upconversion nanoparticles for super-resolution nanoscopy (2017). *Nature*.**543**,229-233

[24] Lee, C.;Xu, E. Z.;Liu, Y.;Teitelboim, A.;Yao, K.;Fernandez-Bravo, A.;Kotulska, A. M.;Nam, S. H.;Suh, Y. D.; Bednarkiewicz, A. Giant nonlinear optical responses from photon-avalanching nanoparticles (2021). *Nature*.**589**,230-235

[25] Liu, C.;Zhang, X.;Chen, X.; Liang, L. Emerging advances in lanthanide photon avalanche nanophotonics (2024). *Nano Letters*.**24**,15489-15500

[26] Szalkowski, M.;Kotulska, A.;Dudek, M.;Korczak, Z.;Majak, M.;Marciniak, L.;Misiak, M.;Prorok, K.;Skripka, A.; Schuck, P. J. Advances in the photon avalanche luminescence of inorganic lanthanide-doped nanomaterials (2025). *Chemical Society Reviews*.

[27] Zhang, M.;Wang, B.;Cai, Y.;Jin, D.; Zhou, J. Thermally prolonged NIR-II luminescence lifetimes by cross-relaxation (2024). *Nano Letters*.**24**,4877-4884

[28] Zhou, J.;Wen, S.;Liao, J.;Clarke, C.;Tawfik, S. A.;Ren, W.;Mi, C.;Wang, F.; Jin, D. Activation of the surface dark-layer to enhance upconversion in a thermal field (2018). *Nature Photonics*.**12**,154-158

[29] Wang, M.;Hu, C.; Su, Q. Luminescent lifetime regulation of lanthanide-doped nanoparticles for biosensing (2022). *Biosensors*.**12**,131

[30] Ye, X.;Collins, J. E.;Kang, Y.;Chen, J.;Chen, D. T.;Yodh, A. G.; Murray, C. B. Morphologically controlled synthesis of colloidal upconversion nanophosphors and their shape-directed self-assembly (2010). *Proceedings of the National Academy of Sciences*.**107**,22430-22435

Chapter 5 Investigation of UCNPs in biological systems

5.1 Preamble

Previous chapters have focused on the advanced medical applications with subcellular endoplasmic reticulum targeting nanomaterials. While these materials display immense potential, our current lack of understanding of the mechanisms dictating the trafficking of nanomaterials within the cell has become a major challenge for developing more efficient drug delivery systems. While existing ER targeted systems provide valuable insights into organelle specific delivery, they do not fully resolve how nanomaterials navigate the complex intracellular environment before reaching any organelle. The stochastic nature of endocytosis, the diversity of vesicular pathways, and the dynamic interactions within the endomembrane system represent major bottlenecks in our understanding of intracellular nanoparticle fate. Current luminescent probes often lack photostability, signal duration, and single particle brightness required to accurately monitor these early trafficking events over extended periods. As a result, the field still lacks a robust method for elucidating the mechanisms that govern vesicular transport, sorting, and retention prior to organelle level interactions.

These gaps directly motivate the work undertaken in this thesis, which focuses on the rational design and synthesis of stable and optically reliable up conversion nanoparticles that overcome the limitations associated with conventional luminescent probes. Building on these optimized materials, integrating the dynamic behavior of nanoparticles within the live cell environment, with a specific focus on cargo transport through the endomembrane system, provides an essential tool for observing how intracellular cargo moves, transforms, and interacts with the cytoskeleton and intracellular transport machinery. As such, this chapter aims to provide insights between fundamental nanoparticle movements and cellular metabolism for future biomedical applications.

5.2 Introduction

The previous chapters have demonstrated the unique optical properties of UCNPs and have highlighted immense potential for biological imaging due to their photostability, high brightness and chemical stability. Subsequently, this chapter will explore UCNPs as potential probes for understanding the intracellular dynamics within living cells. Near-infrared light (such as 976 nm), which are significantly less toxic due to minimal ROS generation, are much less capable of damaging critical biomolecules within the living cell such as DNA or amino acids [1, 2]. As such, NIR based up-conversion microscopy using non-photobleaching UCNPs can be an effective method for the long term live cell tracking due to a reduction in phototoxicity[3, 4]. The findings of lanthanide doping and particle brightness are taken into account in this chapter towards a method that reliably produces UCNPs for intracellular tracking using core-shell UCNPs. This chapter will first explore how surface modified UCNPs interact with living systems at a single cell level and their overall fate within cellular systems. Through the analysis of surface proteins via TEM and zeta potential, this section will also uncover the dynamic surface interactions of the protein corona before and after endocytosis and exocytosis to reveal nanoparticle fate at a single cellular level. Following the analysis of nanoparticle fate in living systems, this section will continue to observe the localization of nanoparticles in live cells via colocalization studies to understand nanoparticles are distributed in the cell. Finally, nanoparticle dynamics via SPT are performed to reveal distinct cargo populations through MSD and other methods, thereby providing a complete framework for the overall fate and dynamics of nanoparticles within living systems. This section therefore introduces a complete framework of the beginning, intermediate and final stages of nanoparticle fate through the analysis of particle surface chemistry and living cell cargo dynamics using transdisciplinary sciences, with a goal of gaining new insights into nanoparticles and cell interactions for future research.

5.3 Characterization of surface-modified UCNPs

The surfactant plays a critical role in maintaining the size, shape and uniformity of the particle during synthesis and particle coalescence [5, 6]. Oleic acid has been one of the most common surfactants to maintain uniformity across many nanomaterials [7]. However, oleic acid results in an extremely hydrophobic surface which results in severe nanoparticle aggregation in polar solutions such as water, which makes them difficult to be applied for biological applications. As such, ligand exchange from hydrophobic to hydrophilic PEG-based polymers are required to improve the biocompatibility and stability of nanoparticles in polar solvents, namely water [8, 9]. Given the quantity of UCNPs needed for numerous biological experiments, a new batch of UCNPs (Figure 5.3) were synthesized for surface-modification experiments. To facilitate biocompatibility for UCNPs, polymer-based surface exchange was conducted to coat the surface of UCNPs. As shown in figure 5.1, ligand exchange with polymers containing carboxylic acid groups (B12) and PLL depicted distinct peaks visible in FTIR spectroscopy. The addition of hydroxyl groups were visible via the absorbance between 3200 – 3500 nm, which are evident of polymer-based ligand exchange. These peaks were significantly decreased after electrostatic addition of PLL, resulting in a decrease in carboxyl groups due to electrostatic attraction [10]. Following PLL modification, new carbonyl bands become evident at 1730 nm, together with alkyl bands at 2900 nm and 2850 nm, confirming successful PLL coating of the nanoparticle surface [10].

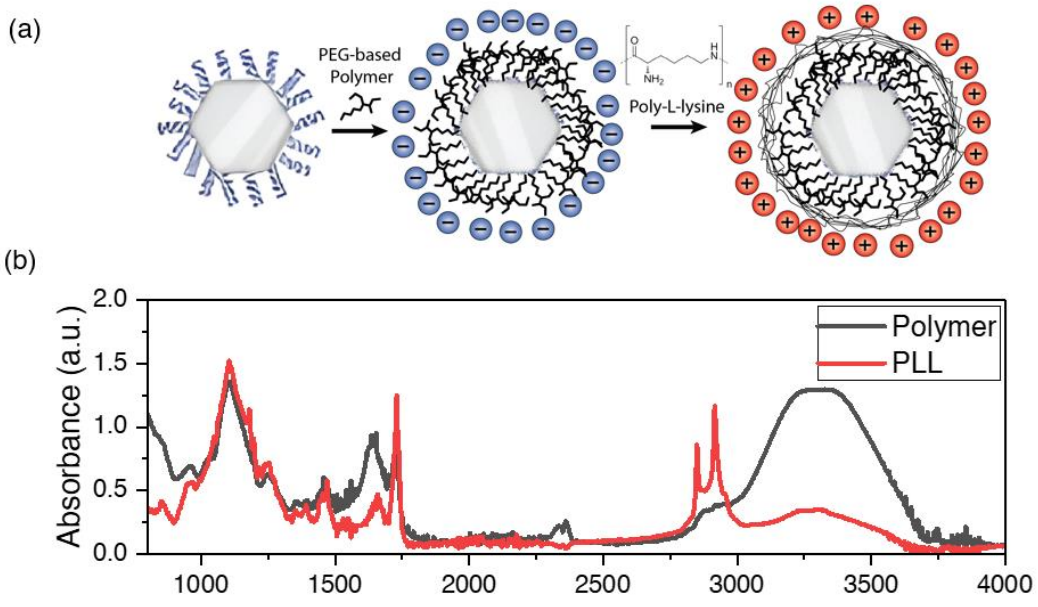

Figure 5.1 Ligand exchange for UCNPs. (a) Schematic for UCNPs surface modification (b) FTIR for surface-modified UCNPs.

Afterwards, the zeta potential of UCNPs were measured and compared between DI water and a biological state through RPMI and serum addition. As expected, UCNPs with carboxylic polymer-based modification (B12) possessed negative zeta potential as a result of deprotonation in water and the formation of carboxylate anions, while a positive surface potential after PLL surface modification was formed via ion protonation in water [11, 12]. Our results demonstrate a negative zeta potential for UCNPs regardless of carboxylic or amine polymer addition, which is likely the result of the formation of a protein corona within a biological environment [13, 14].

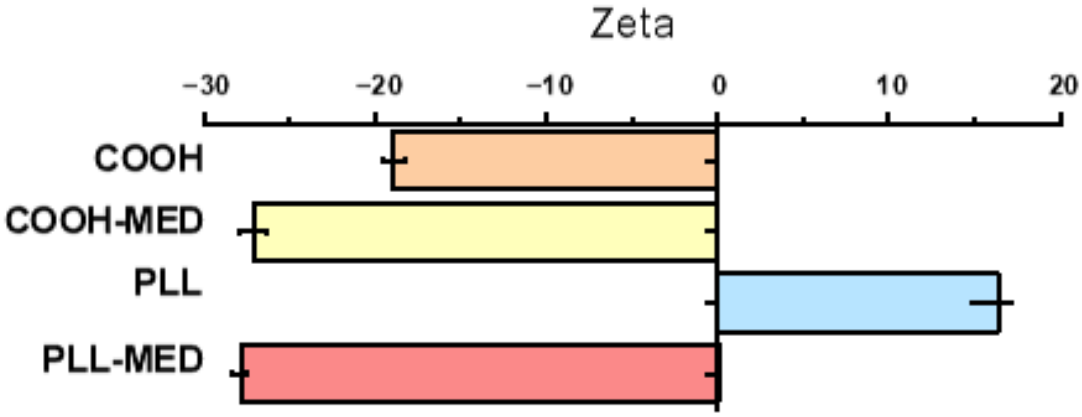

Figure 5.2 Zeta potential of UCNPs. COOH represents UCNPs with carboxylic acid surface modifications (PPEGMEMA$_{15}$-*b*-PMAA$_{12}$-*b*-PEGMP$_{3}$). COOH MED represents COOH-UCNPs after incubation with RPMI medium. Similarly, PLL and PLL-MED represent UCNPs with Poly-l-lysine surface modifications and UCNPs with PLL modification after RPMI incubation**.**

Results demonstrate that regardless of zeta potential or polymer surface, nanoparticles after FBS incubation resulted in negatively charged zeta potential, which can be attributed to the net negative charge albumin proteins contain at neutral pH presented in medium [15]. Similar zeta potential of both polymer and PLL surface modified nanoparticles further suggests that the binding affinity of the proteins arrives at an equilibrium when the surface of the nanoparticle equilibrates with the proteins in the external environment. To further demonstrate that protein corona formation is one of the critical interactions between

nanomaterials and the biological environment, TEM imaging experiments were performed with nanoparticles incubated with the RPMI containing protein corona. Indeed, TEM imaging reveals the formation of a protein corona at the surface of the nanoparticle that aligns with previous reports (Figure 5.3) [16, 17]. Furthermore, additional experiments were performed to observe the potential change in UCNP protein corona after cellular exocytosis. Our results demonstrate a vast change in UCNP structure and shape after cell exocytosis, which is attributed to the changes in pH via lysosomal storage within the cell, causing changes in polymer, protein corona and nanoparticle stability [18].

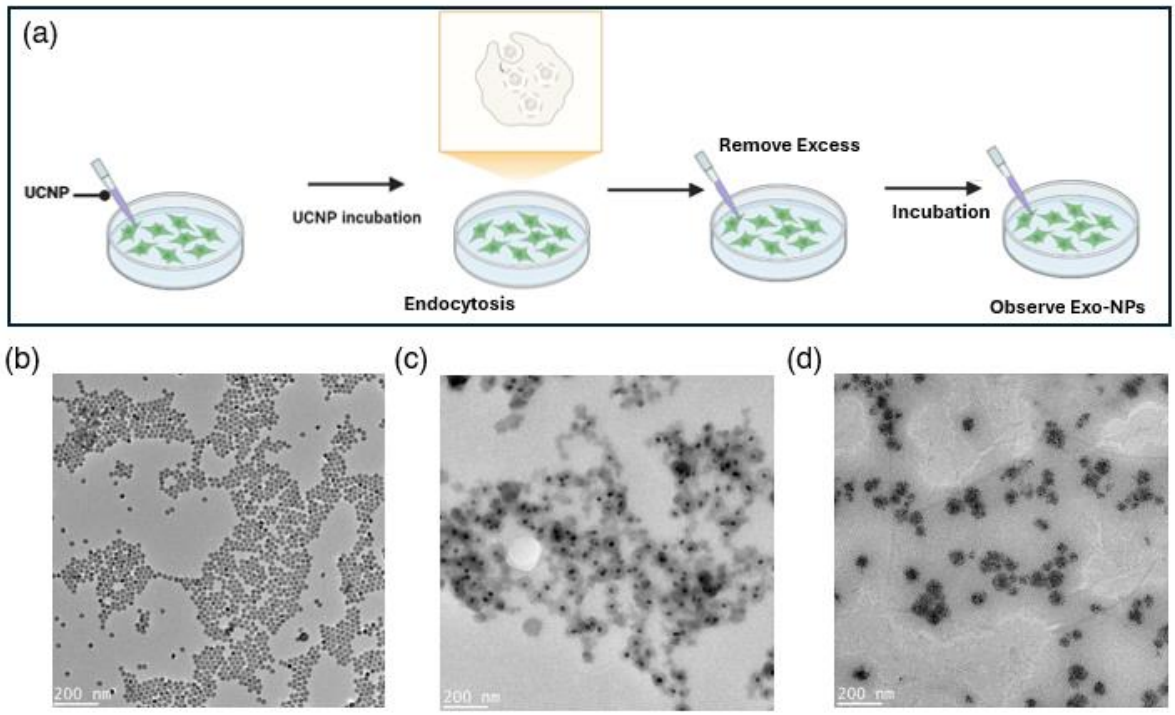

Figure 5.3 Biocompatible UCNPs in biological systems. (a) Schematic of experimental procedure. (b) UCNPs before entering a biological system in DI water. (c) Incubation of UCNPs in RPMI and FBS. (c) UCNPs observed after exocytosis.

Given that the nanoparticle state was vastly different after biological incubation, we next sought to determine if live cell endocytosis was the primary contributor to these interactions. Endocytosis is an active mechanism that occurs only in live cells, and has been generally recognized to be the primary method for nanoparticle entry into the cell [13]. To demonstrate that UCNP entry is indeed facilitated by an active pathway, cell fixation and permeation experiments were performed using Tm/Yb UCNPs and Er/Yb UCNPs (Figure

5.4). As expected, the widefield microscopy demonstrated that nanoparticle entry was not achieved under fixed cell conditions. Instead, the majority of nanoparticles were localized in the outer membrane of the cell, likely due to non-specific electrostatic interactions between the nanoparticle and the phospholipid bilayer of the cell [19, 20]. Given that fixed cells could not facilitate intracellular entry, live cell viability and imaging experiments were performed to determine the particle entry pathway and dynamics.

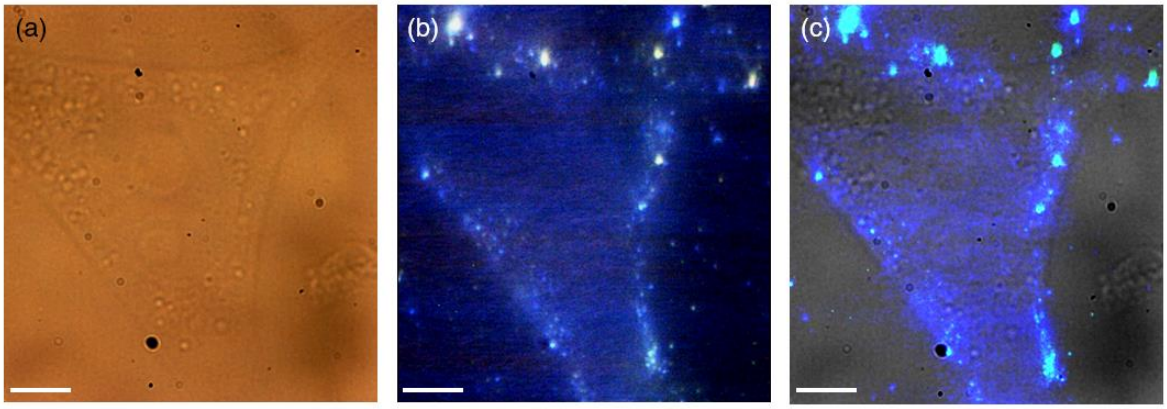

Figure 5.4 Biocompatible UCNPs and fixed cell interactions (a) Brightfield (b) Widefield under 980 nm excitation (c) merged. Scale bar 5 µm.

Before continuing further experiments to understand UCNPs and their biological interactions, an Alamar blue based cell viability test was conducted in order to determine the cytotoxicity and viability of surface-modified UCNPs within cells. Both B12 and PLL surface-modified UCNPs demonstrated no significant cytotoxicity at concentrations up to 200 µg/ml. The cell viability test via Alamar blue was conducted using both a normal cell line BV2 and cancer cell line A549. Given that our results implied no significant cytotoxicity of UCNPs in normal conditions, we next sought to determine if UCNPs after exocytosis can significantly influence the cellular viability.

As demonstrated via our schematic in 5.6a, UCNPs after exocytosis were incubated with a fresh batch of seeded A549 or BV2 cells. UCNPs exocytosed from cells (BV2, A549, Colo-794) previously incubated with B12-modified or PLL-modified nanoparticles were again incubated with fresh A549 and BV2 cells. Our results indicate an increase in overall cell viability across all UCNPs after exocytosis, which was similar to our results when cells were incubated with leftover control medium without UCNP exocytosis. These results suggest that UCNPs after exocytosis have no significant effect during live cell growth and

proliferation, and the increase in cell viability is attributed to growth factors potentially carried by the surface corona of nanoparticles [21-23].

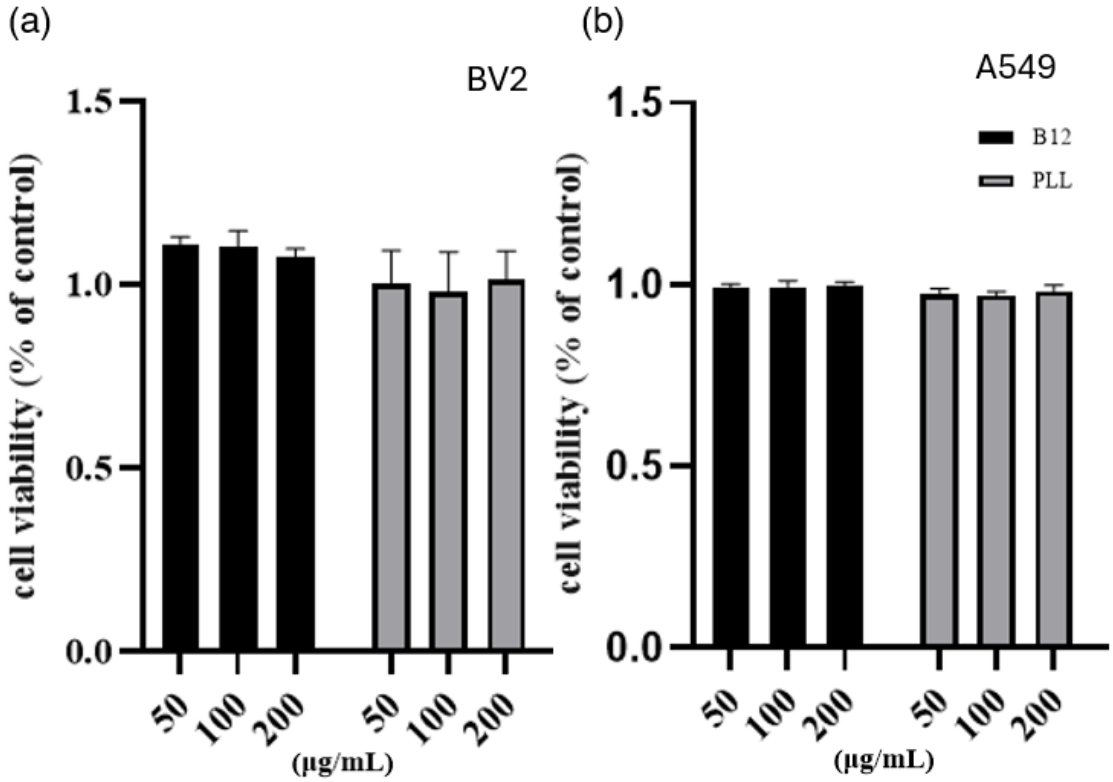

Figure 5.5 Cytotoxicity of UCNPs in biological systems. (a) Cell viability of UCNPs in BV2 cells. (b) Cell viability of UCNPs in A549 cells.

When UCNPs lose surface modification and the associated stabilizing interactions, strong van der Waals attraction in the absence of sufficient steric hindrance or surface charge leads to pronounced nanoparticle aggregation, which is readily observed in TEM images. In contrast, as shown in Figure 5.6, the UCNPs examined after exocytosis retain a well dispersed morphology, indicating that the surface modified particles remain stable and resist aggregation even following extended incubation in the cellular environment.

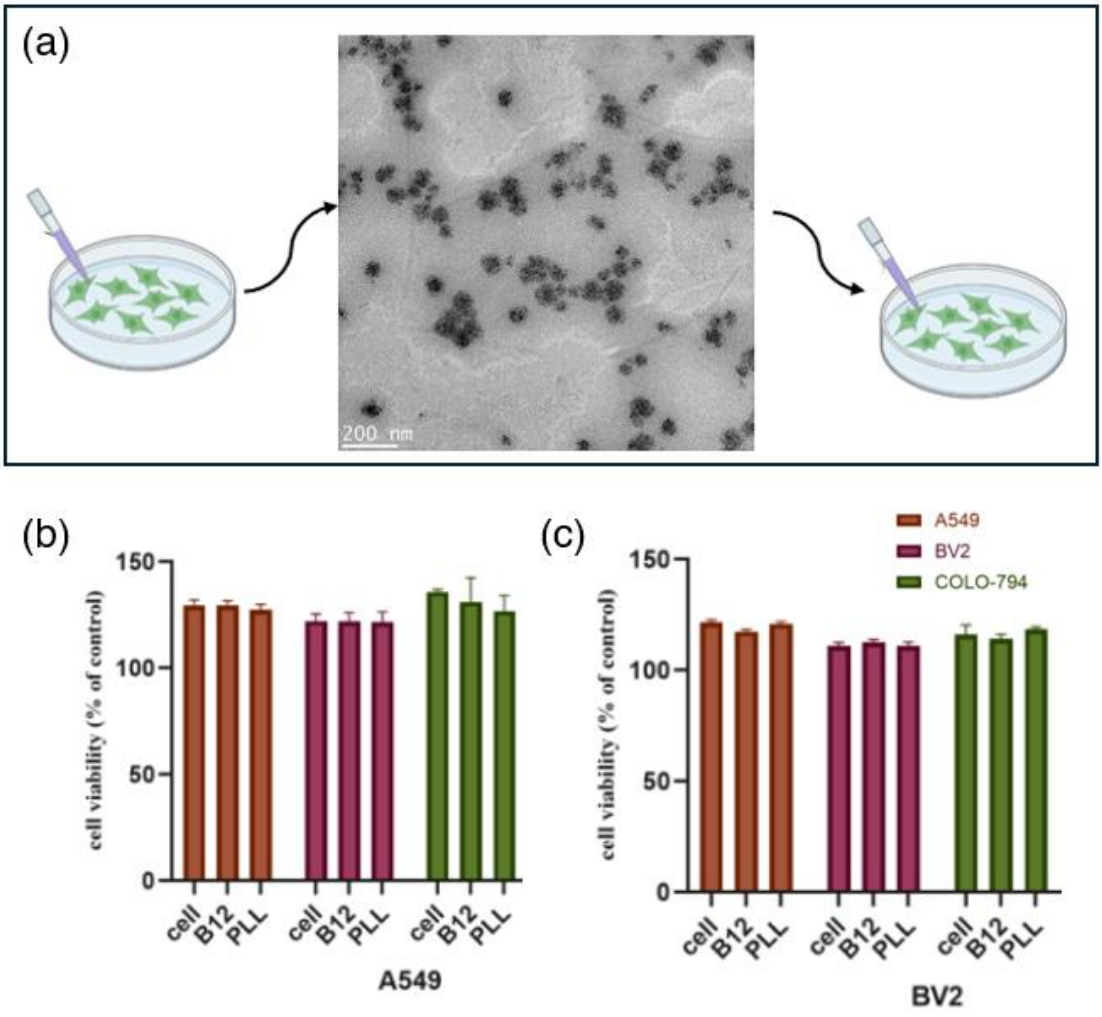

Figure 5.6 Cytotoxicity of UCNPs in biological systems after exocytosis. (a) Schematic of experimental procedure. (b) Cell viability of UCNPs in BV2 cells. (b) Cell viability of UCNPs in A549 cells.

To demonstrate that UCNPs were localized within the lysosome, a colocalization experiment was performed with Lysotracker dye to confirm the distribution of UCNPs as cargo within the lysosome. Indeed, our experiments demonstrate a significantly high Pearson value of 0.948, signifying strong localization within the lysosomes because of endocytosis. This is further reinforced by cell TEM images, which depict the localization of UCNPs both in the perinuclear region and cytoplasmic region. Furthermore, TEM images display the formation of tubular structures around nanoparticles at the surface of the cell, suggesting that UCNPs undergo active cellular transportation within live cells [24, 25].

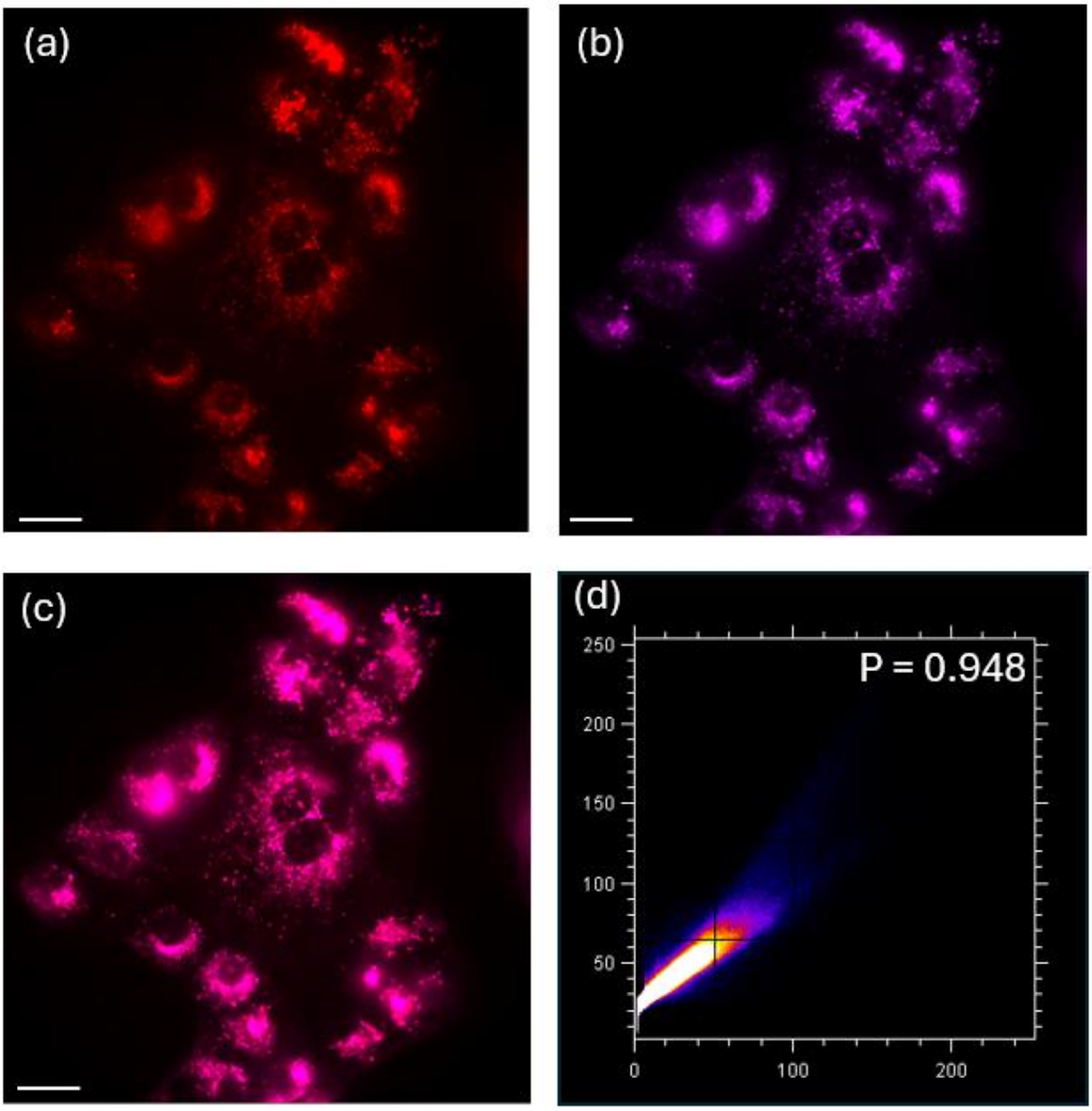

Figure 5.7 Colocalization of UCNPs and lysosome (a) UCNPs. (b) Lysotracker. (c) Merged (d) Pearson's coefficient value scale bar 30 µm.

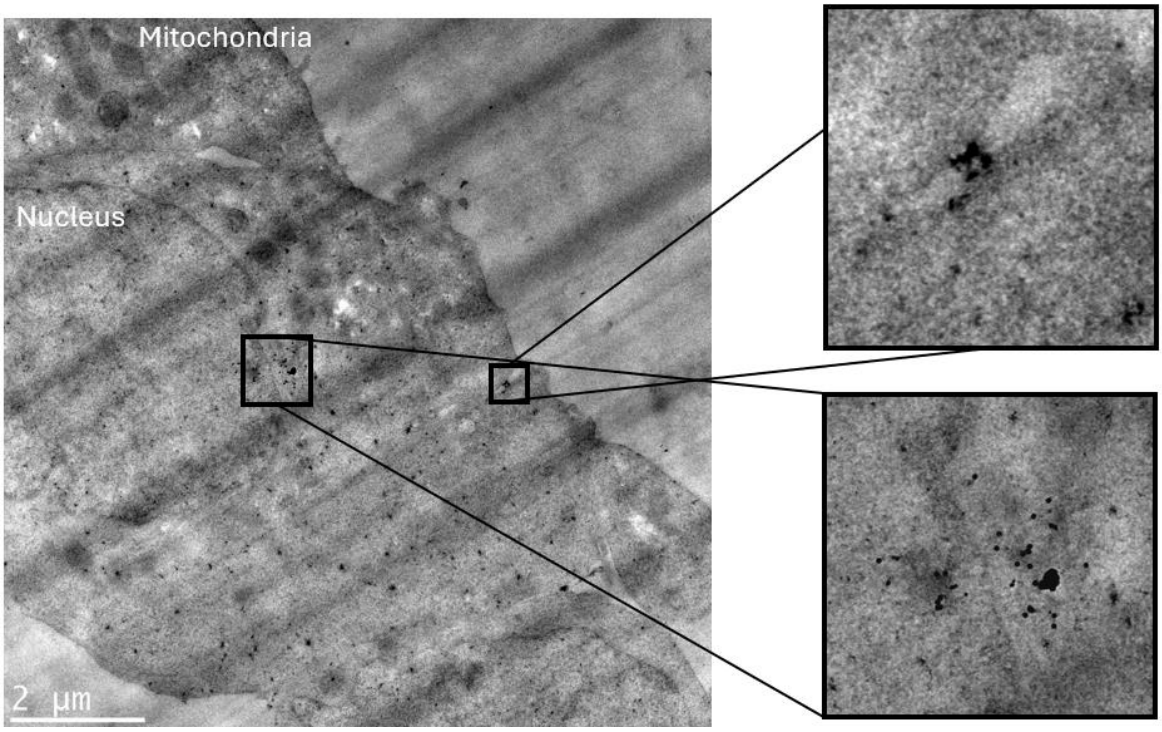

Figure 5.8 TEM images of UCNP endocytosis. Tubulation signifying active endocytosis are observed, as well as UCNPs surrounding the perinuclear region.

5.3 Live cell SPT using UCNPs

With evidence demonstrating the biocompatible nature of UCNPs within living cells, we next investigated the potential use for polymer-coated (B12) UCNPs for long term live cell tracking using the home-built widefield microscopy setup. Figure 5.8 illustrates the movement of UCNPs under 980nm excitation. With previous colocalization studies demonstrating strong co-localization within the lysosomes, movement observed under widefield microscopy is likely to be vesicles part of the lysosomal system after endocytosis. The MSD was computed for each trajectory over increasing lag times (Δt), with ensemble averaging performed across all valid trajectories to generate an average MSD curve. To improve tracking accuracy and suppress noise, trajectories shorter than a minimum frame threshold (e.g., 20 frames) were excluded. As expected, the MSD curve depicted an overall large standard deviation as the observed diffusion coefficients of singular tracks within the cell varied significantly, reflecting the diverse environments experienced by UCNPs once internalized.

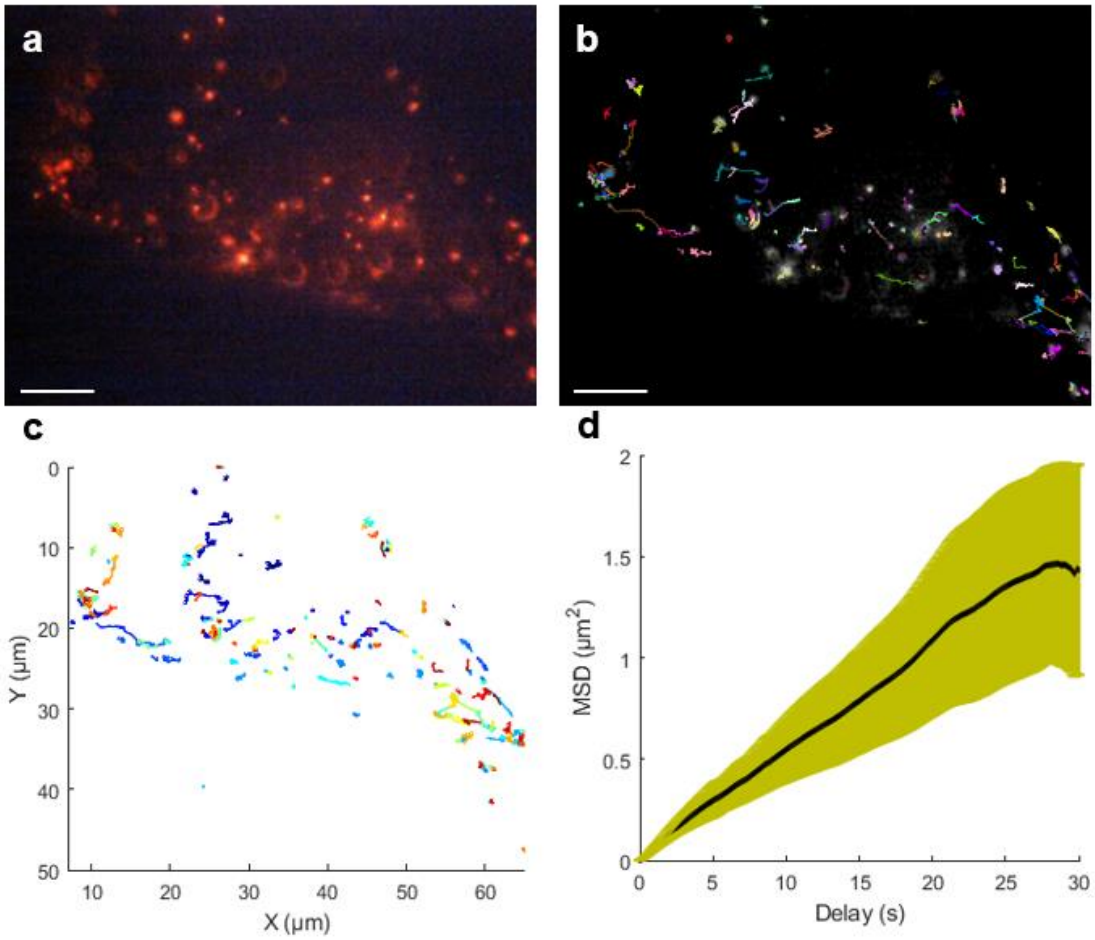

Figure 5.8 Live cell cargo tracking using UCNPs (a) Widefield imaging of HeLa cells under 980nm lasing under widefield microscopy. Scale bar: 10 µm (b) Dynamic tracks after 30 seconds of image recording. Scale bar: 10 µm (c) Coordination graph of (b). (d) Average MSD all tracked cargo and the standard deviation.

Next, a measurement of particle displacement relative to cell position was calculated with estimated nucleus locations based on widefield images. As seen in figure 5.9, a statistically significant difference ($p < 0.05$) between the total particle displacement and the nuclear region and cytoplasmic region was observed. The difference between total particle displacement was attributed to lysosomal tethering occurring at the endoplasmic reticulum region surrounding the nucleus, resulting in decreased cargo motility [26]. On the other hand, an increase in total particle displacement at the cytoplasmic region was a result of active cargo transport along the cytoskeletal network of the cell which can be observed in figure 5.9a [27].

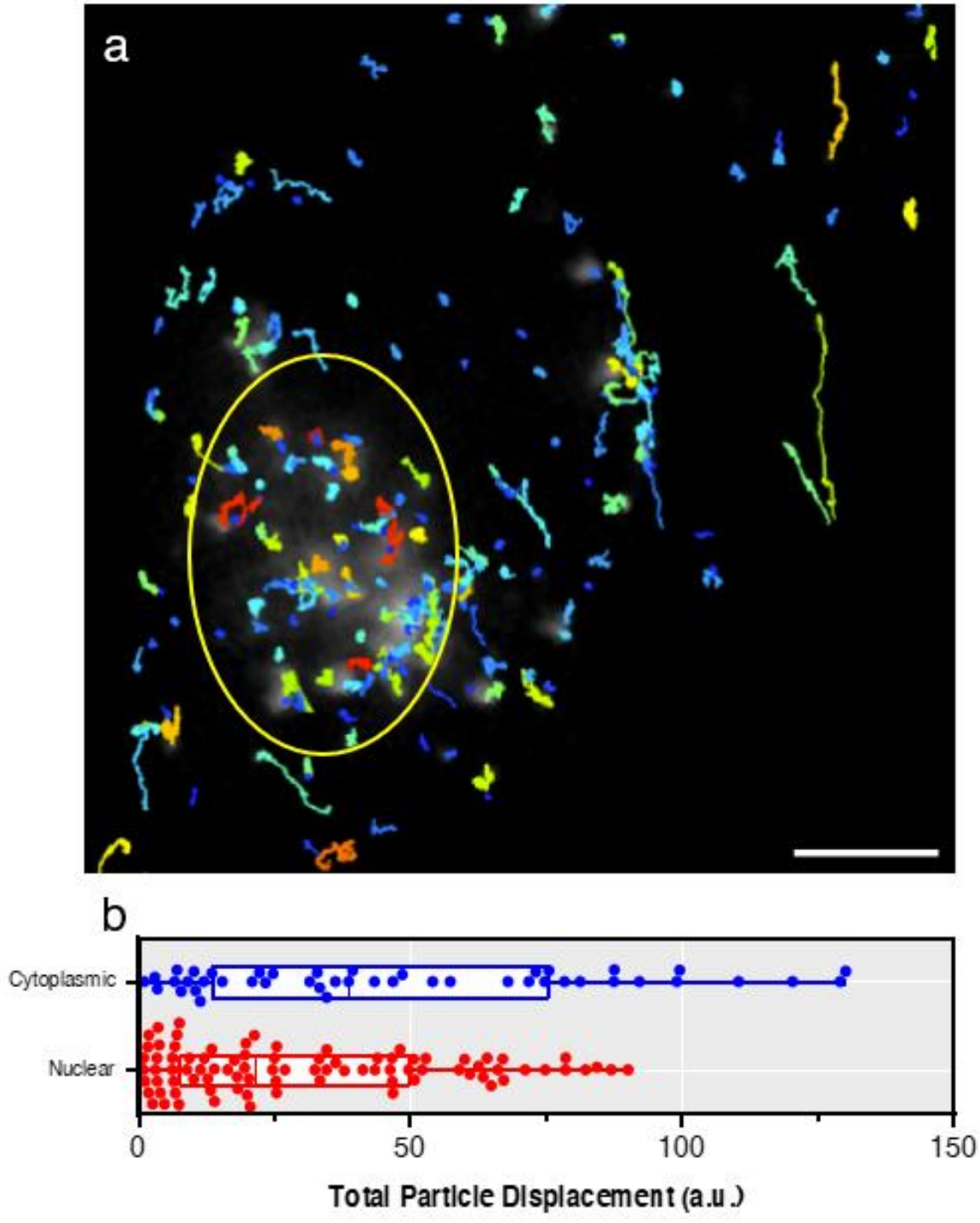

Figure 5.9 Cargo movements relative to intracellular position (a) Single cell cargo tracks with yellow oval representing perinuclear separation. Scale bar: 10 µm (b) Total cargo displacement between nuclear and cytoplasmic region.

Following the observation of the population of cargo within a cell, singular cargo dynamics were observed to highlight the distinct cargo states in a live cell using UCNPs. As seen in figure 5.10b, the MSD of singular cargo varied significantly depending on the total movement and displacement of the cargo. A rapid rise of the MSD for the blue track in figure 5.10b was a result of a rapid change between particle movement, likely the result of changing cargo states due to cellular signaling [4]. While rapid changes between confined and active movement can be detected via rapid changes in MSD, subtle changes between particle trafficking dynamics required further analysis. Using a Hidden Markov Model, a singular cargo track seen in figure 5.10c depicted changes between Brownian motion and active transport likely result of inner cellular trafficking [28]. The HMM-Bayes package was applied to single-particle UCNP trajectories in live cells, modeling each as a time

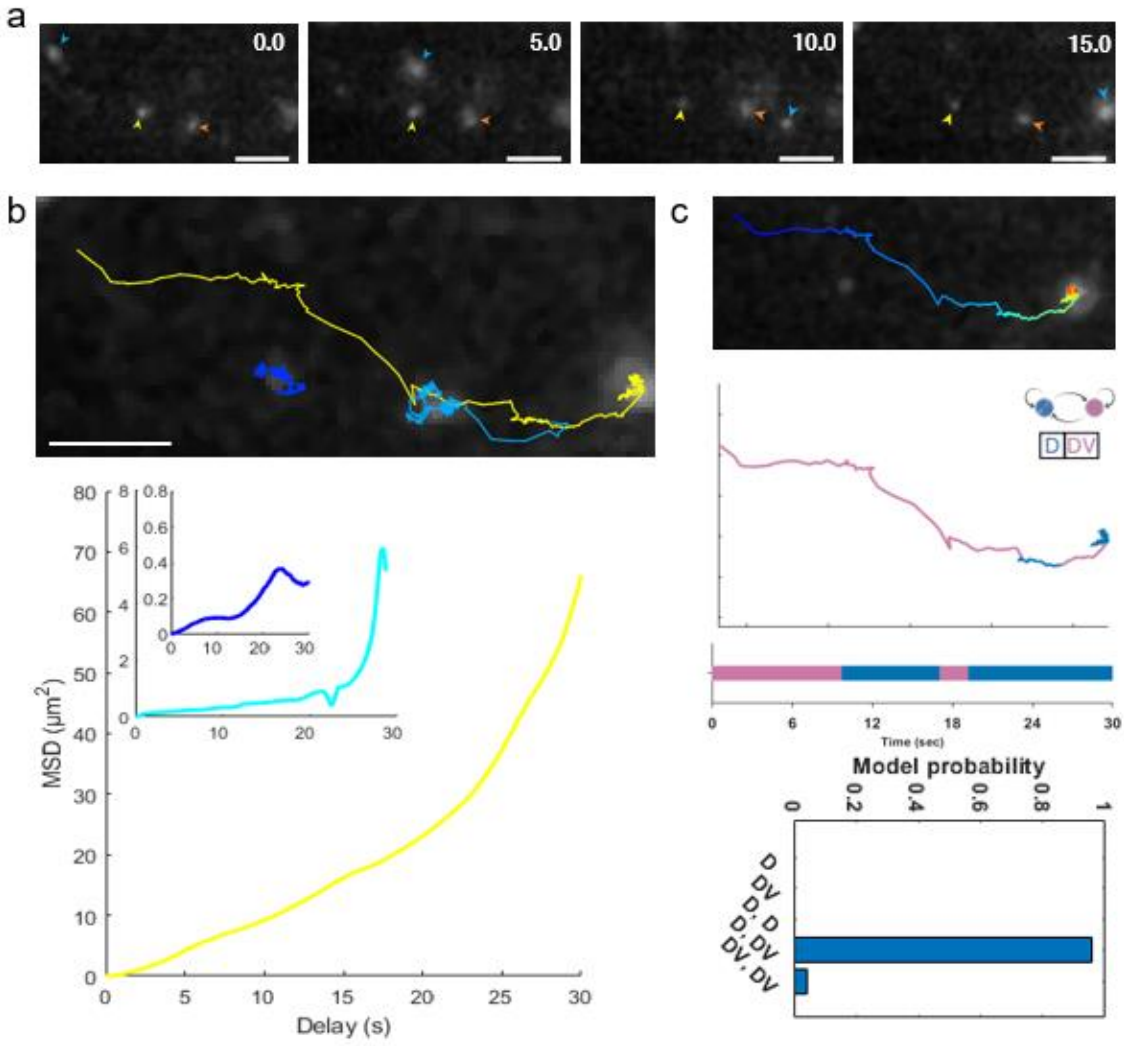

Figure 5.10 Single particle tracking within live cells (a) Selected single cargo vesicles over 30 seconds. Scale bar: 10 μm (b) MSD of single tracks (color-coded) seen in (a). (c) hidden Markov modeling for single track.

series of two-dimensional displacements and empirically determining, via the Bayesian Information Criterion, that the data were best described by two to four underlying motility states [28]. Active transport of the single particle mostly occurred between 0–11 seconds, while slower movement due to inner cellular tethering occurred between 11–17 seconds as well as 19–30 seconds. Fast movement between 17–19 seconds is suggested to be a brief re-engagement of motor-protein transport as a result of actin–microtubule handoff or a transient tug-of-war resolution [29, 30]. After the slow segment from 11–18 seconds, reattachment to the microtubule and produced a short, directed run between 18–19 seconds before detaching again which enabled the motion to return to a slow/diffusive from 19–30 seconds.

Afterwards, classification across a population of cargo within the cell was described via a non-linear relationship between the MSD and time, which can be depicted by:

$$\langle r^2(\tau)\rangle = K_\alpha \tau^\alpha$$

Brownian motion, which can be classified as a random walk with no memory, should result in statistically independent steps which result in linear MSD. In the equation above, Ka is generalized coefficient, while τ represents time. Described via the power law, classification between different movements via MSD is defined by α, where a nonlinear relationship between the MSD and time can therefore be classified as non-Brownian motion, which is the result of external factors such as motor proteins or a crowded environment within an organelle.

To further elucidate the intracellular dynamics within the cell, over 800 cargo tracks over multiple cells were observed using MSD analysis. Further computed MSD curves revealed multiple distinct motion regimes among intracellular UCNPs (Figure 5.11). A subset of particles exhibited linear MSD curves on a log–log scale with slopes (α) close to 1 (± 0.2), indicative of normal Brownian diffusion which were likely loosely bound lysosome vesicles containing UCNPs. Other particles showed sublinear growth (slope < 1), consistent

with confined or anomalous diffusion typically observed in vesicle-bound or cytoskeletal-restricted motion. Particles displaying confined diffusion were likely sequestered in endosomes or lysosomes while tethered to the endoplasmic reticulum or other organelles, while superdiffusive tracks (slope > 1) aligned with directed motion along microtubules, suggesting motor protein involvement [31, 32].

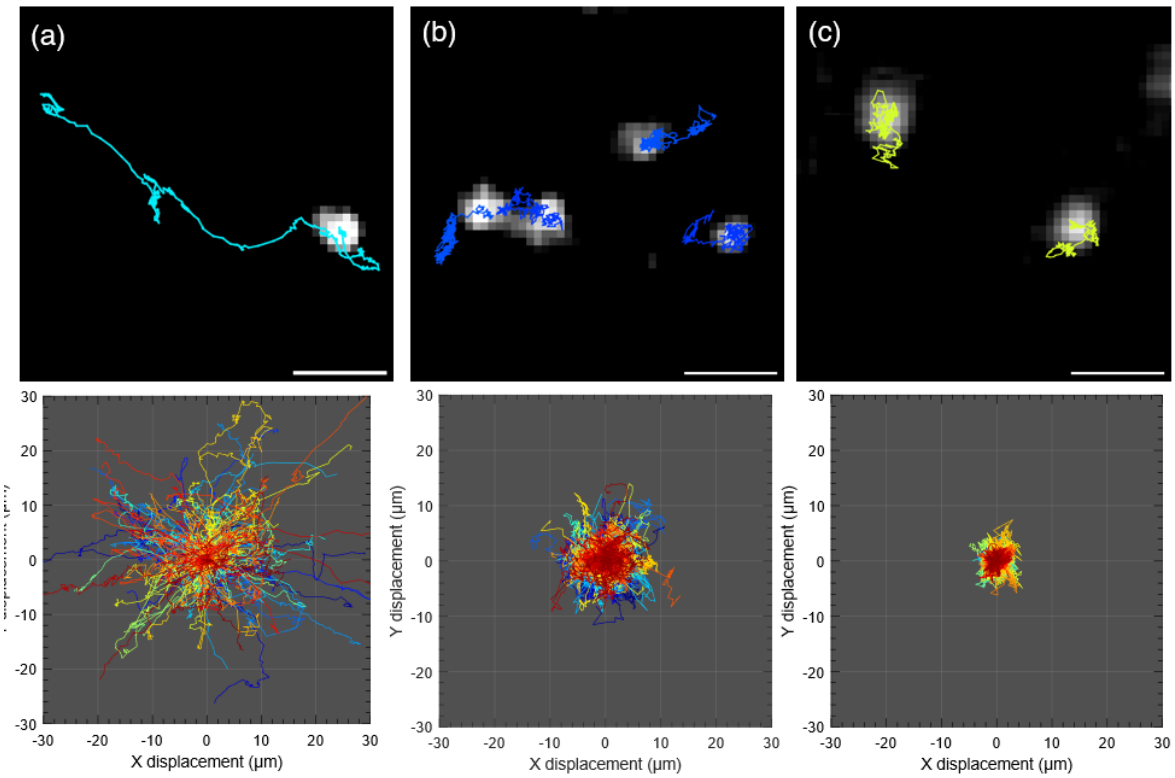

Figure 5.11 MSD analysis over a population of cargo tracks (a) active transport/super diffusive transport. (b) Brownian motion (c) Confine cargo/anomalous diffusion.

Importantly, the presence of multimodal distributions suggested the coexistence of multiple transport regimes rather than a uniform motion profile. These observations were reproducible across different cells and experimental replicates, confirming their biological relevance rather than noise artifacts.

To evaluate if UCNPs within live cells could be used to detect a change in cargo displacement as a result of changing conditions, a population-level analysis was performed under differing conditions. Three conditions along with a control were selected including hydrogen peroxide for inducing cellular stress, palmitate for inducing endoplasmic reticulum stress, as well as ammonium chloride (AC) for its effects on enlarging endosomal

organelles [33-35]. Our results demonstrated only a difference in cargo displacement after hydrogen peroxide addition in live cells (Figure 5.12). Furthermore, a recovery of single cargo displacement was observed after 2 hours of hydrogen peroxide addition. Increased cargo displacement after 2 hours of hydrogen peroxide suggests that the recovery of oxidative stress was possible after extended time periods, but further investigations are required to reveal the mechanisms utilized to combat oxidative stress in single cells [36, 37]. Although H_2O_2 is rapidly degraded in cell culture media by catalase, glutathione peroxidase and peroxiredoxins, giving it a half-life on the order of minutes, our results indicate that H_2O_2 can still drive long term cellular responses despite its brief stability [42]. The re-emergence of active transport approximately two hours after hydrogen peroxide treatment suggests that intracellular trafficking is restored once cells initiate compensatory antioxidant pathways that reverse the earlier oxidative suppression of motility. Hydrogen peroxide is rapidly buffered in the cytosol by enzymatic systems including catalase, glutathione peroxidases, and peroxiredoxins, each of which reduces H_2O_2 to water while undergoing catalytic turnover [43]. Notably, the timescale of transport recovery aligns with the expected kinetics of glutathione replenishment, where oxidative stress transiently depletes reduced GSH pools, and de novo GSH synthesis via glutamate–cysteine ligase (GCL) typically restores intracellular redox balance quickly following moderate oxidative stress [44]. This synthesis window coincides with the observed recovery of cargo displacement, suggesting that restoration of the GSH:GSSG ratio may be a key threshold enabling motor protein activity and cytoskeletal reorganization to resume.

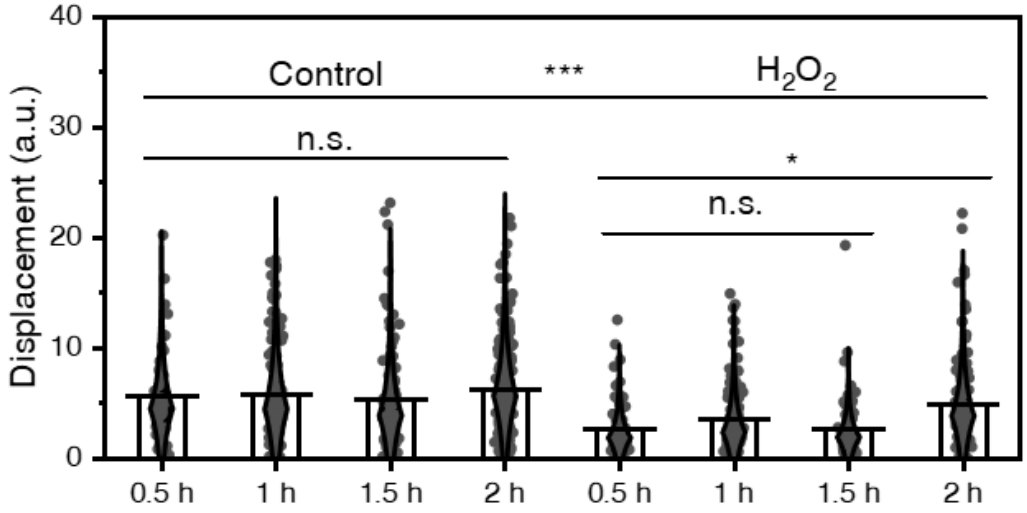

Figure 5.12 Complete population displacement after hydrogen peroxide treatment across 2 hours. Population level analysis in Hela cells on cargo displacement in 30 seconds. H_2O_2, concentration at 100 µM. (n>5). (* < 0.05, ***<0.0005)

Analysis on the population distribution of single cargo trajectories under different conditions through MSD slope α. Trajectories were classified into three categories based on their α values: subdiffusive motion ($\alpha < 0.8$), consistent with constrained or hindered movement; normal diffusion ($0.8 \leq \alpha \leq 1.2$), indicative of Brownian motion; and superdiffusive or active transport ($\alpha > 1.2$), typically associated with motor-driven movement along cytoskeletal tracks. Results (Figure 5.13) reveal a substantial decrease in active transport after hydrogen peroxide addition, which is replaced by subdiffusive trajectories within the cell. Aligning with previous research, it is evident that oxidative stress through hydrogen peroxide addition results in decreased active transport across live cells as a result of protein oxidation, which generates aggregates, stress granules, and swollen organelles, all of which increase macromolecular crowding and reduce cargo trafficking [38]. Furthermore, oxidation of motor proteins, tubulin networks, actin and actin binding proteins affect cytoskeletal stability, resulting in reduced vesicle binding for effective cargo transport [27, 39-41].

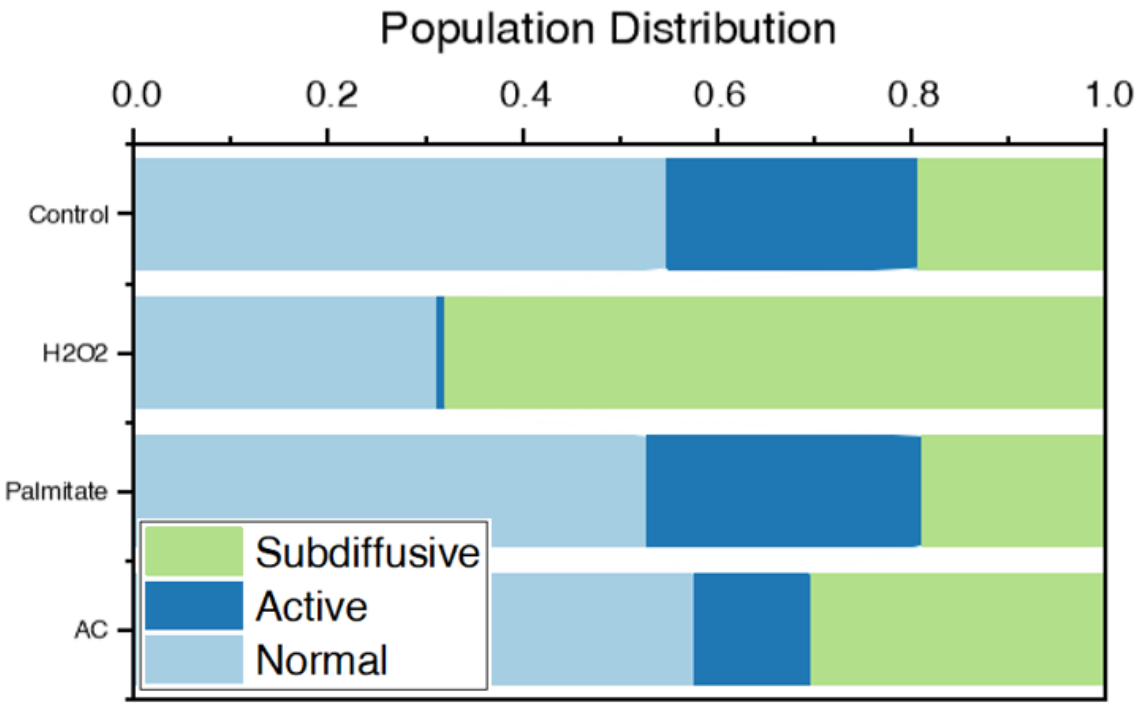

Figure 5.13 Population distribution of single cargo across different conditions. Single cargo analysis with different treatment options, including H_2O_2, (100 μM) Palmitate (200 μM) and Ammonium Chloride (20 mM) (n>5). After treatment, cells were observed after 1 hour, with cargo dynamics classified based on MSD to Subdiffusive, active and normal transport.

5.4 Conclusion

In conclusion, we applied UCNPs with surface modified polymers for enhanced biocompatibility to enable intracellular cargo tracking under NIR lasing with a homebuilt widefield microscopy system. This chapter thoroughly evaluated the biological interactions between biocompatible UCNPs under biological conditions. Results demonstrate that surface-modified UCNPs are significantly influenced by the protein corona in biological conditions, and cellular endocytosis results in UCNPs localization within the lysosomal system. With no photobleaching and strong photostability and good biocompatibility, UCNPs proved to be useful tools for single cargo tracking in live cells, with trajectory analysis through MSD and HMM modelling demonstrating distinct diffusion states within the live cell cargo trafficking. Furthermore, under different chemical stimuli, differences in complete population displacement were observed, which is attributed towards a natural cellular reaction against external factors.

These results highlight the immense potential of UCNPs as potential tools for further understanding of intracellular dynamics and interactions, which could greatly benefit clinical diagnostics and therapeutic applications. Future investigations using UCNPs can study the intricate mechanisms of organelle-based interactions, such as lysosomal tethering, ER and mitochondrial crosstalk as well as organelle kiss-and-run interactions.

5.5 References

[1] George, S.;Hamblin, M. R.; Abrahamse, H. Effect of red light and near infrared laser on the generation of reactive oxygen species in primary dermal fibroblasts (2018). *Journal of Photochemistry and Photobiology B: Biology*.**188**,60-68

[2] Golovynska, I.;Golovynskyi, S.; Qu, J. Comparing the impact of NIR, visible and UV light on ROS upregulation via photoacceptors of mitochondrial complexes in normal, immune and cancer cells (2023). *Photochemistry and Photobiology*.**99**,106-119

[3] F. Shida, J. o.;Ma, K.;Toll, H. W.;Salinas, O.;Ma, X.; Peng, C. S. Multicolor long-term single-particle tracking using 10 nm upconverting nanoparticles (2024). *Nano letters*.**24**,4194-4201

[4] Peng, C. S.;Zhang, Y.;Liu, Q.;Marti, G. E.;Huang, Y.-W. A.;Suedhof, T. C.;Cui, B.; Chu, S. Nanometer-resolution tracking of single cargo reveals dynein motor mechanisms (2025). *Nature Chemical Biology*.**21**,648-656

[5] Song, T.;Gao, F.;Guo, S.;Zhang, Y.;Li, S.;You, H.; Du, Y. A review of the role and mechanism of surfactants in the morphology control of metal nanoparticles (2021). *Nanoscale*.**13**,3895-3910

[6] Holmberg, K. Surfactant-templated nanomaterials synthesis (2004). *Journal of Colloid and Interface Science*.**274**,355-364

[7] Mourdikoudis, S.;Menelaou, M.;Fiuza-Maneiro, N.;Zheng, G.;Wei, S.;Pérez-Juste, J.;Polavarapu, L.; Sofer, Z. Oleic acid/oleylamine ligand pair: a versatile combination in the synthesis of colloidal nanoparticles (2022). *Nanoscale Horizons*.**7**,941-1015

[8] Rabanel, J.-M.;Hildgen, P.; Banquy, X. Assessment of PEG on polymeric particles surface, a key step in drug carrier translation (2014). *Journal of Controlled Release*.**185**,71-87

[9] D'souza, A. A.; Shegokar, R. Polyethylene glycol (PEG): a versatile polymer for pharmaceutical applications (2016). *Expert opinion on drug delivery*.**13**,1257-1275

[10] Mecozzi, M.; Sturchio, E. Computer assisted examination of infrared and near infrared spectra to assess structural and molecular changes in biological samples exposed to pollutants: a case of study (2017). *Journal of Imaging*.**3**,11

[11] Honary, S.; Zahir, F. Effect of zeta potential on the properties of nano-drug delivery systems-a review (Part 1) (2013). *Tropical journal of pharmaceutical research*.**12**,255-264

[12] Honary, S.; Zahir, F. Effect of zeta potential on the properties of nano-drug delivery systems-a review (Part 2) (2013). *Tropical journal of pharmaceutical research*.**12**,265-273

[13] Bilardo, R.;Traldi, F.;Vdovchenko, A.; Resmini, M. Influence of surface chemistry and morphology of nanoparticles on protein corona formation (2022). *Wiley Interdisciplinary Reviews: Nanomedicine and Nanobiotechnology*.**14**,e1788

[14] Richtering, W.;Alberg, I.; Zentel, R. Nanoparticles in the biological context: surface morphology and protein corona formation (2020). *Small*.**16**,2002162

[15] Kubiak-Ossowska, K.;Jachimska, B.;Al Qaraghuli, M.; Mulheran, P. A. Protein interactions with negatively charged inorganic surfaces (2019). *Current opinion in colloid & interface science*.**41**,104-117

[16] Liang, L.;Everest-Dass, A. V.;Kostyuk, A. B.;Khabir, Z.;Zhang, R.;Trushina, D. B.; Zvyagin, A. V. The surface charge of polymer-coated upconversion nanoparticles determines protein corona properties and cell recognition in serum solutions (2022). *Cells*.**11**,3644

[17] Miclăuş, T.;Beer, C.;Chevallier, J.;Scavenius, C.;Bochenkov, V. E.;Enghild, J. J.; Sutherland, D. S. Dynamic protein coronas revealed as a modulator of silver nanoparticle sulphidation in vitro (2016). *Nature Communications*.**7**,11770

[18] Ovais, M.;Mukherjee, S.;Pramanik, A.;Das, D.;Mukherjee, A.;Raza, A.; Chen, C. Designing stimuli-responsive upconversion nanoparticles that exploit the tumor microenvironment (2020). *Advanced Materials*.**32**,2000055

[19] Schulz, M.;Olubummo, A.; Binder, W. H. Beyond the lipid-bilayer: interaction of polymers and nanoparticles with membranes (2012). *Soft Matter*.**8**,4849-4864

[20] Balog, S.;de Almeida, M. S.;Taladriz-Blanco, P.;Rothen-Rutishauser, B.; Petri-Fink, A. Does the surface charge of the nanoparticles drive nanoparticle–cell membrane interactions? (2024). *Current Opinion in Biotechnology*.**87**,103128

[21] Bashiri, G.;Padilla, M. S.;Swingle, K. L.;Shepherd, S. J.;Mitchell, M. J.; Wang, K. Nanoparticle protein corona: from structure and function to therapeutic targeting (2023). *Lab on a Chip*.**23**,1432-1466

[22] Wolfe, R.;Wu, R.; Sato, G. Epidermal growth factor-induced down-regulation of receptor does not occur in HeLa cells grown in defined medium (1980). *Proceedings of the National Academy of Sciences*.**77**,2735-2739

[23] Hutchings, S. E.; Sato, G. H. Growth and maintenance of HeLa cells in serum-free medium supplemented with hormones (1978). *Proceedings of the National Academy of Sciences*.**75**,901-904

[24] Wei, Y.;Tang, T.; Pang, H.-B. Cellular internalization of bystander nanomaterial induced by TAT-nanoparticles and regulated by extracellular cysteine (2019). *Nature communications*.**10**,3646

[25] Firdessa, R.;Oelschlaeger, T. A.; Moll, H. Identification of multiple cellular uptake pathways of polystyrene nanoparticles and factors affecting the uptake: Relevance for drug delivery systems (2014). *European journal of cell biology*.**93**,323-337

[26] Kümmel, D.; Ungermann, C. Principles of membrane tethering and fusion in endosome and lysosome biogenesis (2014). *Current opinion in cell biology*.**29**,61-66

[27] Cabukusta, B.; Neefjes, J. Mechanisms of lysosomal positioning and movement (2018). *Traffic*.**19**,761-769

[28] Monnier, N.;Barry, Z.;Park, H. Y.;Su, K.-C.;Katz, Z.;English, B. P.;Dey, A.;Pan, K.;Cheeseman, I. M.; Singer, R. H. Inferring transient particle transport dynamics in live cells (2015). *Nature methods*.**12**,838-840

[29] Hancock, W. O. Bidirectional cargo transport: moving beyond tug of war (2014). *Nature reviews Molecular cell biology*.**15**,615-628

[30] Osunbayo, O.;Butterfield, J.;Bergman, J.;Mershon, L.;Rodionov, V.; Vershinin, M. Cargo transport at microtubule crossings: evidence for prolonged tug-of-war between kinesin motors (2015). *Biophysical journal*.**108**,1480-1483

[31] Schirripa Spagnolo, C.; Luin, S. Trajectory analysis in single-particle tracking: From mean squared displacement to machine learning approaches (2024). *International Journal of Molecular Sciences*.**25**,8660

[32] Simon, F.;Weiss, L. E.; Van Teeffelen, S. A guide to single-particle tracking (2024). *Nature Reviews Methods Primers*.**4**,66

[33] Sies, H. Hydrogen peroxide as a central redox signaling molecule in physiological oxidative stress: Oxidative eustress (2017). *Redox biology*.**11**,613-619

[34] Lakadamyali, M.;Rust, M. J.; Zhuang, X. Ligands for clathrin-mediated endocytosis are differentially sorted into distinct populations of early endosomes (2006). *Cell*.**124**,997-1009
[35] Karaskov, E.;Scott, C.;Zhang, L.;Teodoro, T.;Ravazzola, M.; Volchuk, A. Chronic palmitate but not oleate exposure induces endoplasmic reticulum stress, which may contribute to INS-1 pancreatic β-cell apoptosis (2006). *Endocrinology*.**147**,3398-3407
[36] Shang, F.; Taylor, A. Oxidative stress and recovery from oxidative stress are associated with altered ubiquitin conjugating and proteolytic activities in bovine lens epithelial cells (1995). *Biochemical Journal*.**307**,297-303
[37] Eisenstark, A.;Yallaly, P.;Ivanova, A.; Miller, C. Genetic mechanisms involved in cellular recovery from oxidative stress (1995). *Archives of insect biochemistry and physiology*.**29**,159-173
[38] Saffi, G. T.;Tang, E.;Mamand, S.;Inpanathan, S.;Fountain, A.;Salmena, L.; Botelho, R. J. Reactive oxygen species prevent lysosome coalescence during PIKfyve inhibition (2021). *PLoS One*.**16**,e0259313
[39] Bakker, N.;Jongsma, M. L.; Neefjes, J. Engine breakdown of lysosomes and related organelles and the resulting physiology (2025). *Frontiers in Cell and Developmental Biology*.**13**,1575571
[40] Yap, Y. W.;Llanos, R. M.;La Fontaine, S.;Cater, M. A.;Beart, P. M.; Cheung, N. S. Comparative Microarray analysis identifies commonalities in neuronal injury: evidence for oxidative stress, dysfunction of calcium signalling, and inhibition of autophagy–lysosomal pathway (2016). *Neurochemical research*.**41**,554-567
[41] Spang, A. Membrane tethering complexes in the endosomal system (2016). *Frontiers in cell and developmental biology*.**4**,35
[42] Imlay, J. A. Cellular defenses against superoxide and hydrogen peroxide (2008). *Annu. Rev. Biochem.***77**,755-776
[43] Winterbourn, C. C. Biological production, detection, and fate of hydrogen peroxide (2018). *Antioxidants & redox signaling*.**29**,541-551
[44] Jiang, X.;Chen, J.;Bajić, A.;Zhang, C.;Song, X.;Carroll, S. L.;Cai, Z.-L.;Tang, M.;Xue, M.; Cheng, N. Quantitative real-time imaging of glutathione (2017). Nature communications.8,16087

Chapter 6. Conclusion, perspectives and future work

6.1 Conclusions

This thesis aims to utilize UCNPs to reveal cargo dynamics within single cells. The project involved many aspects of the physical and biological sciences, demonstrating the importance of transdisciplinary sciences for future research (Figure 6.1). The synthesis of inorganic nanoparticles and their modification with organic polymers to enable hydrophilicity and biocompatibility involved many chemical aspects. Similarly, the setup of a home-built optical characterization device, and the optical characterization of UCNPs was used to study the photonic and physical properties of singular nanoparticles. Finally, utilizing the optical properties of biocompatible UCNPs and the home-built optical system, live cell dynamics were investigated under different physiological conditions.

As such, the outcomes of this thesis include:

Synthesis of UCNPs with ideal volumetric scaling. The key to synthesizing UCNPs at 100 nm involved the delicate management of precursor concentration in order to decrease nucleation and promote Ostwald ripening for larger uniform nanocrystals.

The design and setup of a characterization system, which enabled both widefield and confocal scanning microscopy using a flip mirror between a CCD and SPAD. Additionally, UCNP emission spectroscopy was achieved by switching the optical fiber to a spectrometer. Other optical characteristics such as power dependence, luminescence rise-time and lifetime were achieved with custom LabVIEW and MATLAB programming using SPAD.

Optical characterization of UCNPs at a single particle level. The power dependence of single nanoparticles was significantly influenced by the emitter and sensitizer concentration, which facilitated differences in excited state population under different lasing conditions. Single particle characterization of UCNPs with ideal volumetric scaling also revealed tunable rise-time dynamics that ranged up to two orders of magnitudes (20 μs to 2 ms).

Interactions between single nanoparticles and a biological environment revealed the significance of the protein corona. Additionally, nanoparticle exocytosis revealed significant changes in nanoparticle surface chemistry due to lysosomal acidification.

Single cargo tracking within live cells reveals dynamic trajectories localized within the lysosomal compartments. Cargo that acted as confined, Brownian and super diffusive motion could be interpreted as tethered, loosely bound and active transport within the live cell. Further analysis with the MSD and HMM model reveals constant changes in singular trajectories, as well as changes in the population of diffusive states under different chemical conditions.

Overall, this thesis demonstrates the remarkable potential of UCNPs by developing and studying the optical characteristics of ideally volumetric UCNPs, as well as the potential for UCNPs as tools for studying cargo trafficking in live cells, which can be key to solving key issues such as:

(1) The morphological control and design of different nanomaterials.
(2) The development of further luminescent materials and probes for bio-imaging and super-resolution applications.
(3) Understanding the transportation and localization of nanotherapeutics for cancer therapy and diagnostics.
(4) Studying cargo dynamics and organelle tethering for metabolic or motor neuron diseases.

Specifically, key and novel outcomes of this study include:

(1) The design of an optical platform with widefield and scanning functionalities.
(2) Synthesizing 100 nm UCNPs through a coprecipitation method through precursor modulation.
(3) Single-particle optical characterization of volumetrically optimized thulium-based UCNPs, designed to suppress surface-defect contributions, demonstrated lifetimes that varied by two orders of magnitude with different sensitizer concentrations.
(4) A novel method for the analysis of intracellular state using UCNPs, which revealed distinct changes in cargo population based on trajectory classification.

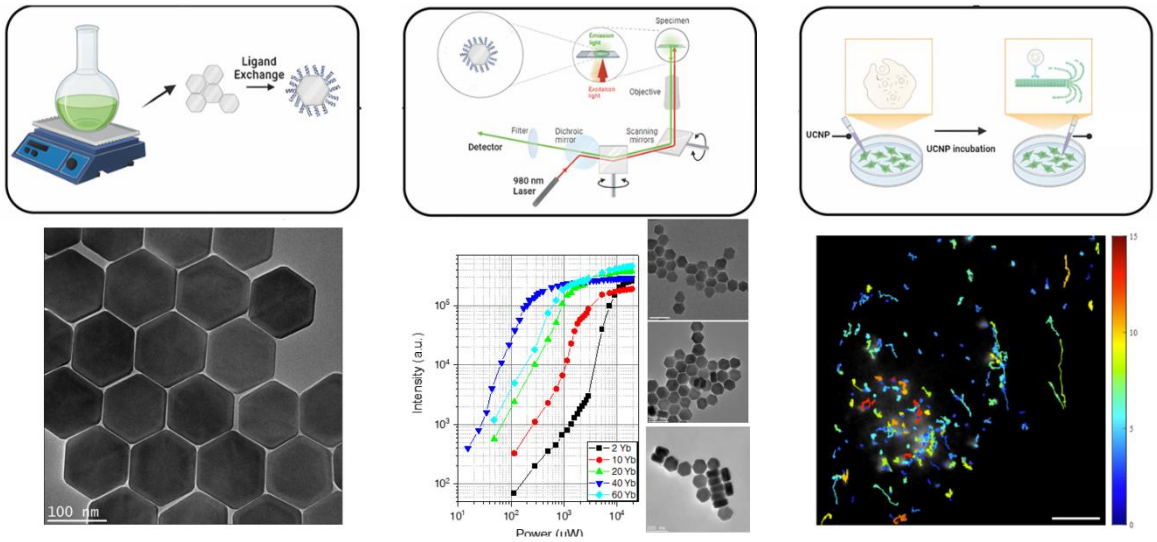

Figure 6.1 Chemical, Physical and biological aspects of this project.

6.2 Perspectives and future work

Given the immense potential and optical properties of UCNPs explored throughout this thesis, this section will describe the potential of future work, as well as additional investigations carried out during this thesis.

6.2.1 Single layer nano-ensembles using UCNPs

Advances in the synthesis and directed assembly of monodisperse colloidal nanocrystals have immense utility in electronics, optics and information technology [1-3]. Beyond immediate applications, superlattices offer a clean platform for fundamental studies that bridge single particle physics and condensed matter. They allow systematic variation of dimensionality, coupling strength, and anisotropy while holding disorder and defect density low, which enables rigorous tests of theory and clear identification of structure–property relationships. Superlattice films with well-defined size, shape, and surface chemistry also provide a controlled context for evaluating biological interactions and environmental safety, addressing an important prerequisite for responsible development and use of nanoscale materials. Using the solvent evaporation deposition method (Figure 6.2), single layer nano-ensembles of UCNPs could be produced [4, 5]. These single layer ensembles of UCNPs have immense potential for the fabrication of highly sensitive optical devices, such as

charged devices, avalanche-diodes and spectrometers, as well as energy-related biotechnological applications.

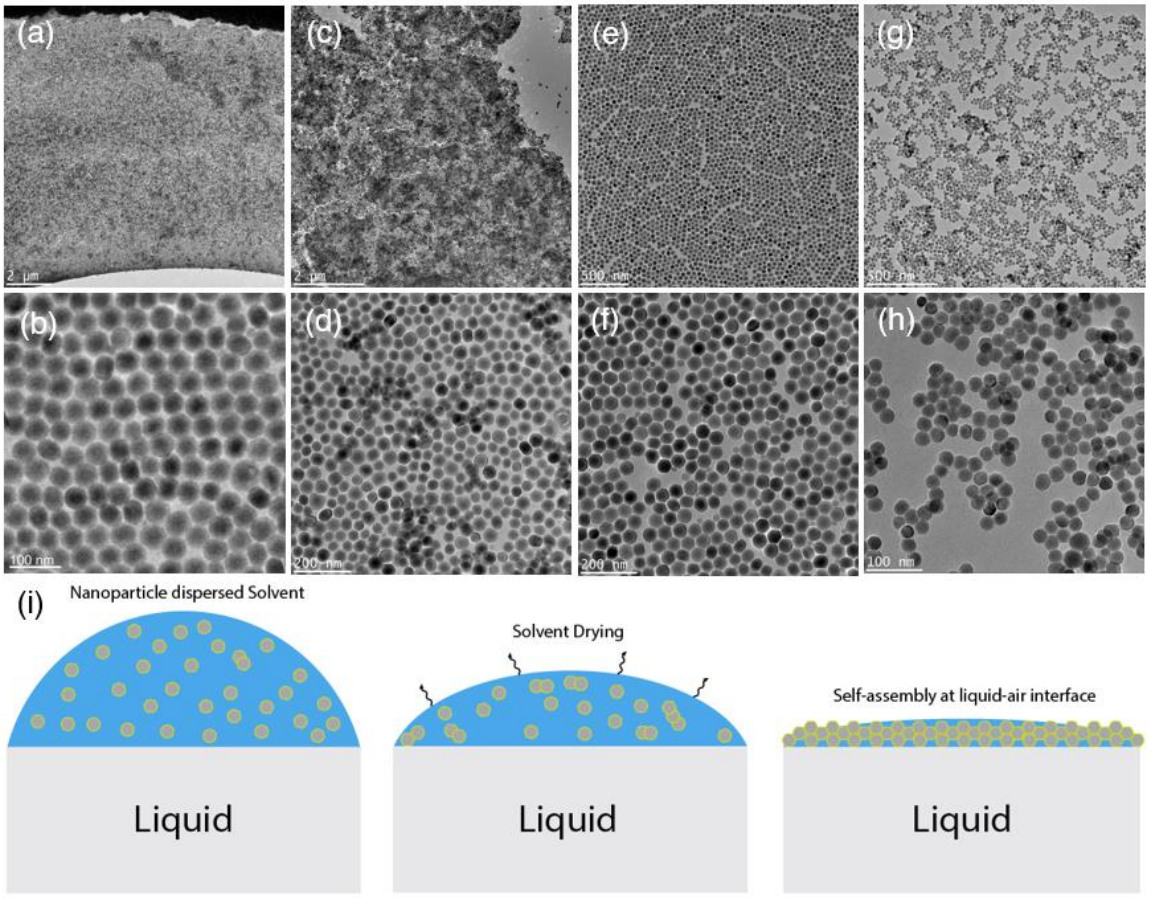

Figure 6.2 Single layer nano ensembles using UCNPs (a)(b) Cyclohexane drying over di-ethylene glycol (c)(d) Drying over ethylene glycol. (e)(f) Cyclohexane individual drying. (g)(h) Drying over water. **(**i) Schematic representation of self-assemby at liquid air interface

6.2.2 Simulation of power dependence in single UCNPs

The design of UCNPs with ideal volumetric scaling should theoretically eliminate the loss of luminescence intensity in single nanoparticles [6]. Furthermore, a core-shell structure should further eliminate the loss of energy due to surface defects. As such, ideally volumetric UCNPs should approach theoretical simulations due to elimination of defects.

As expected, custom MATLAB code reveals similar simulated values of 800 nm emission under 980 nm excitation (Figure 6.3) for the experimental power dependence for 40%Yb/20%Tm $NaYF_4$ Core-shell structure. Therefore, future experiments and

investigations dedicated to comparing the experimental and simulated optical luminescence of UCNPs under different emitter and sensitizer concentrations should reveal key insights into the energy transfer mechanisms in lanthanide doped nanoparticles. Additionally, a comparison between the optical properties of different sized UCNPs that share the same sensitizer and emitter concentration at a single particle level may reveal further insights towards the naturally occurring surface defects in UCNPs. Future work with quantitative measurements of emission intensity and lifetime, under different lasing conditions with normalized optical luminescence can reveal how power saturation through the up-conversion pathway is influenced via size.

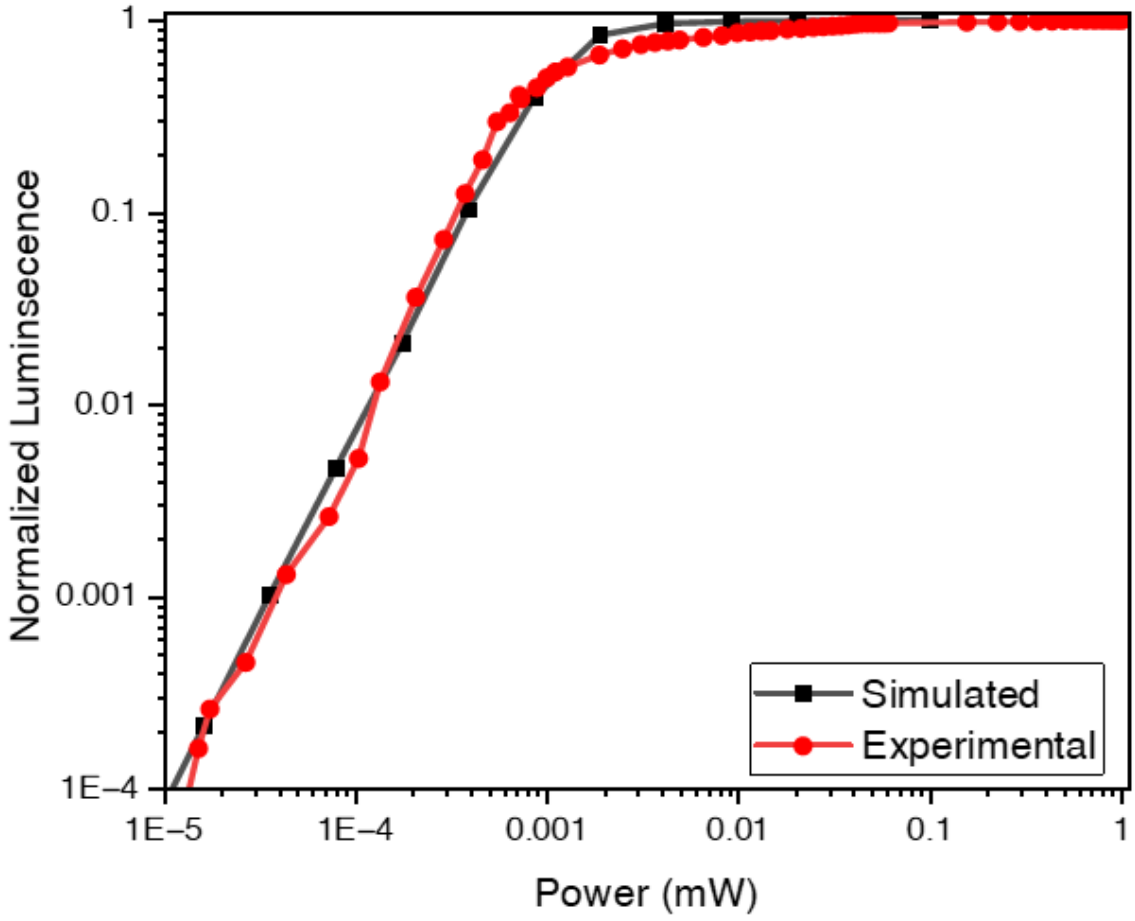

Figure 6.3 Simulated power dependence and experimental power dependence for 40%Yb/20%Tm $NaYF_4$ Core-shell structure.

6.2.3 Intracellular directionality through multi-color UCNP cargo tracking.

While studying the generalized population and trajectory of cargo within a live cell, the vector coordinates and trajectories of a single cell require further investigation. As demonstrated in figure 6.4, a key factor not investigated in current trajectory studies involves cargo directionality. The anterograde and retrograde transport of cargo within the live cell depict two opposite functions within the cell corresponding to the export and import of cellular cargo. Once placed on a vector graph, the position of the nanoparticle which could originate from either the cytoplasmic or perinuclear region is not considered. Therefore, the import and export of cargo cannot be effectively studied.

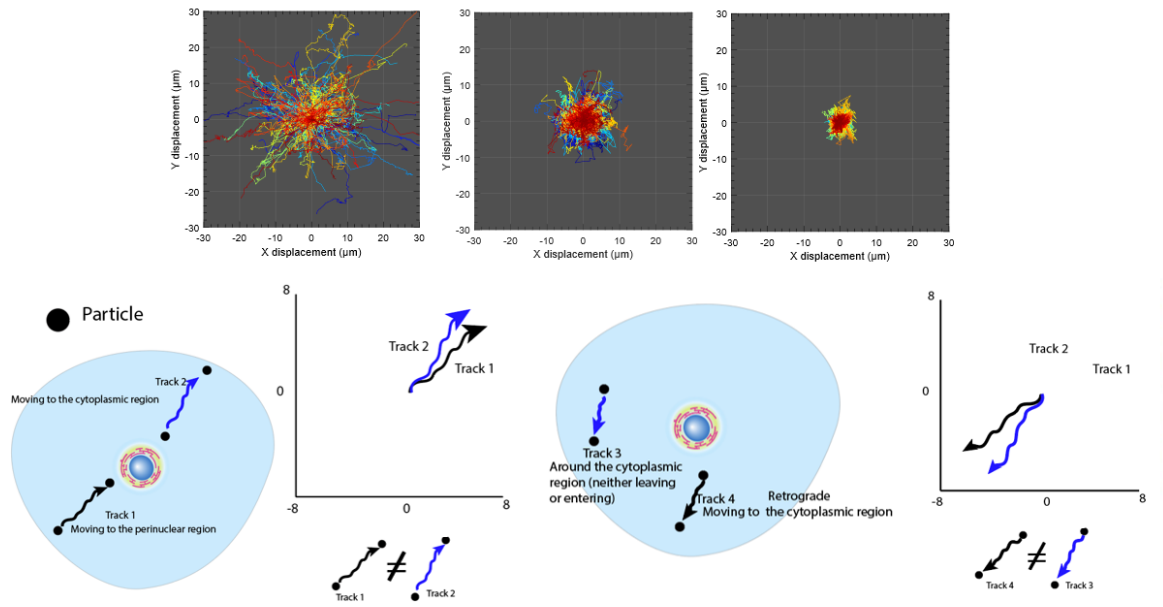

Figure 6.4 Schematic explanation of the directionality of cargo transport.

A solution to this type of conundrum could be achieved via pulse chase experiments with different emitters and emission UCNPs. Forgoing the requirement of multiple lasers for different emission wavelengths, 980 nm excitations of UCNPs can facilitate different emission wavelengths, which can also be tuned depending on emitter concentration (figure 6.5). As such, future experiments involve a pulse chase procedure (in order to separate the cargo) can further investigate the directionality of nanoparticles by observing the different color emissions and their respective cargo dynamics at different time periods (Figure 6.6).

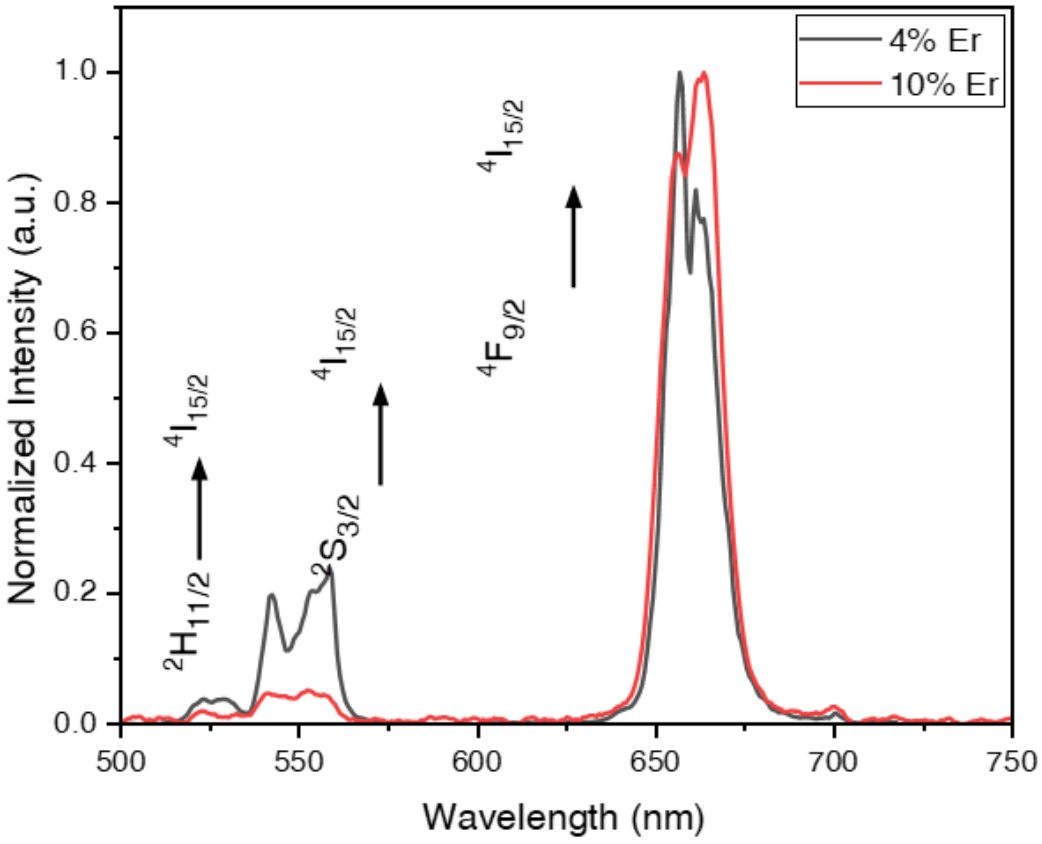

Figure 6.5 Different emission spectrums based on emitter concentration for 40%Yb/X%ER UCNPs.

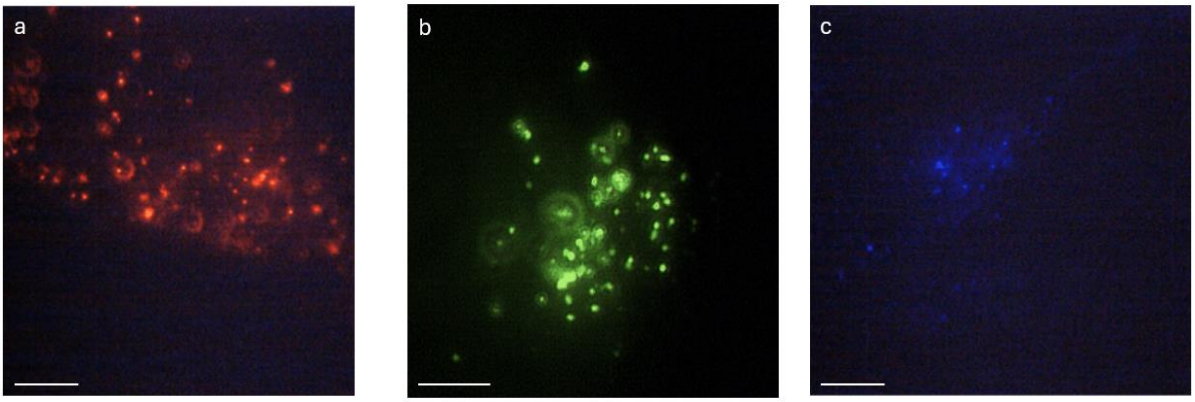

Figure 6.6 Different coloured UCNPs in live cell (a)10% ER-UCNP (b) 4% ER-UCNP (c) 2% TM-UCNP

6.3 References

[1] Sun, S.;Murray, C. B.;Weller, D.;Folks, L.; Moser, A. Monodisperse FePt nanoparticles and ferromagnetic FePt nanocrystal superlattices (2000). *science*.**287**,1989-1992

[2] Tao, A.;Sinsermsuksakul, P.; Yang, P. Tunable plasmonic lattices of silver nanocrystals (2007). *Nature nanotechnology*.**2**,435-440

[3] Talapin, D. V.; Murray, C. B. PbSe nanocrystal solids for n-and p-channel thin film field-effect transistors (2005). *Science*.**310**,86-89

[4] Ye, X.;Collins, J. E.;Kang, Y.;Chen, J.;Chen, D. T.;Yodh, A. G.; Murray, C. B. Morphologically controlled synthesis of colloidal upconversion nanophosphors and their shape-directed self-assembly (2010). *Proceedings of the National Academy of Sciences*.**107**,22430-22435

[5] Dong, A.;Chen, J.;Vora, P. M.;Kikkawa, J. M.; Murray, C. B. Binary nanocrystal superlattice membranes self-assembled at the liquid–air interface (2010). *Nature*.**466**,474-477

[6] Gargas, D. J.;Chan, E. M.;Ostrowski, A. D.;Aloni, S.;Altoe, M. V. P.;Barnard, E. S.;Sanii, B.;Urban, J. J.;Milliron, D. J.; Cohen, B. E. Engineering bright sub-10-nm upconverting nanocrystals for single-molecule imaging (2014). *Nature nanotechnology*.**9**,300-305